An integrated assessment of nutrient loadings to Baffin Bay, Texas

Final Report

CMP project # 21-060-017-C677
August 2023

Prepared by:

Michael S. Wetz, Principal Investigator; David Felix, Ph.D., Dorina Murgulet, Ph.D., Hussain Abdulla, Ph.D., Mohamed Ahmed, Ph.D., Co-Investigators
Texas A&M University-Corpus Christi
6300 Ocean Dr., Unit 5869
Corpus Christi, Texas 78412
Phone: 361-825-2132
Email: michael.wetz@tamucc.edu

Submitted to:

Texas General Land Office
1700 Congress Ave.
Austin, TX 78701-1495

This report was funded in part through a grant from the Texas General Land Office (GLO) providing Gulf of Mexico Energy Security Act of 2006 funding made available to the State of Texas and awarded under the Texas Coastal Management Program. The views contained herein are those of the authors and should not be interpreted as representing the views of the GLO or the State of Texas.

Table of Contents

Executive Summary *1*
Task 1: Quantification and Source Tracking of Surficial Nutrients *2*
Task 2: Quantification and Source Tracking of Groundwater Nutrients *54*
Task 3: Quantifying Benthic Fluxes of Inorganic and Organic Nutrients *105*
Task 4: Modelling Freshwater Inflow, Nutrient and Sediment Loads *149*
Task 5: Education and Outreach Activities *195*
Management Recommendations 200

Executive Summary

Baffin Bay is considered the "jewel" of the Texas coast, providing critical habitat for important fish species. However, it currently exhibits symptoms of water quality degradation that threaten the health of the bay and its valuable fishery. Earlier studies showed that the concentration of dissolved organic nitrogen (DON), linked to brown tide algal blooms, is 2-3-fold higher in Baffin Bay than other Texas estuaries, and that Baffin Bay has undergone a long-term increase (since 1970's) in chlorophyll *a* (a proxy for algal biomass). These findings argue that nutrient pollution is a major factor in the declining water quality and ecosystem health of Baffin Bay.

In order to improve Baffin Bay ecosystem health, it is clear that large-scale watershed restoration aimed at reducing nutrient loads is needed. To do this, a reasonable accounting of nutrient sources must be in place. Here, a multidisciplinary team of researchers propose to quantify nutrient loadings to Baffin Bay from surficial, groundwater/benthic and atmospheric sources. The project goal is to identify the main source(s) of nutrients to help prioritize watershed restoration activities.

Results from high spatial resolution sampling in watershed creeks showed hot spots of nutrient enrichment, primarily at sites downstream of wastewater treatment plants, but also showed a general pattern of high nutrient levels (e.g., total nitrogen $\geq$ 100 µM) at nearly all locations sampled. Sampling conducted over wet-dry periods provided further evidence for the role of point sources (i.e., wastewater) in delivering nutrients to San Fernando Creek, while suggesting the possibility of both point- and nonpoint sources for Petronila Creek. In terms of dissolved inorganic nitrogen (DIN) sources, atmospheric deposition contributed roughly 3.7 kg N/(ha*yr) to the bay through rainfall. Stable isotope approaches determined that in the airshed, agriculture and vehicles were the primary NH_3 emission sources; vehicle and intermittent sources (i.e., biomass burning and lightning) were the main NOx emission sources; vehicle, fertilizer, and marine sources were the dominant organic nitrogen emission sources. For the watershed creeks, wastewater was found to be a dominant source of DIN. However, DIN was only about 5% of total dissolved nitrogen (TDN) in Baffin Bay, which displayed high mean dissolved organic nitrogen (DON) concentrations year-round. The sum of allochthonous contributions (i.e., wastewater, manure, and wet deposition) to Baffin Bay represented over 60% of DON sources. Likewise, in tributaries, allochthonous sources contributed ~60-80% of DON and autochthonous source contributed ~20-40%. Aside from atmospheric and surficial nutrient loadings, input of nutrients from sediment porewater and groundwater were found to be a significant, if not dominant source of nutrients to Baffin Bay. Both contained very high nutrient concentrations; groundwater NO_3^- averaged ~1064 µM and DON averaged ~64 µM concentrations while porewater NH_4^+ averaged ~325 µM. A dual isotope mixing model indicated that sewage and agriculture-derived NH_4^+ were the dominant sources to the NO_3^- in the groundwater.

Watershed nutrient reduction plans should be tailored according to the features of different regions in the watershed, as they may be subjected to varying nitrogen sources and processing. Based on the results of this study and available literature, nitrogen mitigation in both the watershed (incl. surficial creeks and groundwater) and airshed should focus particular attention on sources such as wastewater and septic sewage, followed by agricultural and animal sources as well as vehicles. A comprehensive list of nutrient reduction plans can be found in a soon-to-be released Watershed Protection Plan, which can be found here: https://baffin.twri.tamu.edu/

Task 1:

Quantification and Source Tracking of Surficial Nutrients

Prepared by:

Yixi Qiu, Ph.D.

J. David Felix, Ph.D.

Michael S. Wetz, Ph.D.

Summary

Baffin Bay has undergone eutrophication associate with nutrient enrichment over the past 3-4 decades, resulting in negative impacts to ecosystem health. This task utilized two complementary approaches to quantify potential nutrient sources to Baffin Bay via surface waters and atmospheric deposition. Results from high spatial resolution sampling in watershed creeks showed hot spots of nutrient enrichment, primarily at sites downstream of wastewater treatment plants, but also showed a general pattern of high nutrient levels (e.g., total nitrogen ≥ 100 μM) at nearly all locations sampled. Sampling conducted over wet-dry periods provided further evidence for the role of point sources (i.e., wastewater) in delivering nutrients to San Fernando Creek, while suggesting the possibility of both point- and nonpoint sources for Petronila Creek. In terms of dissolved inorganic nitrogen (DIN), atmospheric deposition contributed roughly 3.7 kg N/(ha*yr) to the bay through rainfall, while the creeks had relatively high but variable DIN concentrations whose loadings would be dependent on rainfall conditions. Stable isotope approaches determined that in the airshed, agriculture and vehicles were the primary NH_3 emission sources; vehicle and intermittent sources (i.e., biomass burning and lightning) were the main NO_x emission sources; vehicle, fertilizer, and marine sources were the dominant organic nitrogen emission sources. For the watershed creeks, wastewater was found to be a dominant source of DIN. However, DIN were only about 5% of total dissolved nitrogen (TDN) in Baffin Bay, which displayed high mean DON concentrations year-round. This was possibly because DIN had faster turnover rates than DON. A stable isotope mixing model suggested that the sum of allochthonous contributions (i.e., wastewater, manure, and wet deposition) to Baffin Bay represented over 60% of DON sources. Likewise, in tributaries, allochthonous sources contributed ~60-80% of DON and autochthonous source contributed ~20-40%. Recommendations are presented that highlight the need to address both sewage and non-point sources (incl. from the land and atmosphere) in order to reduce nitrogen inputs to Baffin Bay.

1. Background

Over the last 3-4 decades there has been a decline in Baffin Bay's water quality and ecosystem health. Symptoms include episodic hypoxia, a multidecadal increase in chlorophyll levels that are now ~3 fold higher than nearly every other estuary in Texas, and recurring, persistent blooms of the HAB species *Aureoumbra lagunensis* ("Brown tide") (Wetz et al. 2017; Bugica et al. 2020). In addition, dissolved organic nitrogen (N) levels (mostly in organic form) are consistently high in the system and are 2-3-fold higher than other estuaries in Texas (Wetz et al. 2017). Taken as a whole, these water quality indicators highlight the enrichment of Baffin Bay from a nutrient standpoint. While nutrient ratios indicate alternating nitrogen and phosphorus limitation of phytoplankton growth in the system, nutrient bioassays have shown that nitrogen is the main growth limiting element in Baffin Bay (e.g., Wetz et al. 2017). Accompanying the water quality degradation are growing indications that impacts to ecosystem health are taking hold. For instance, significant seagrass die-off has occurred, primarily resulting from the *A. lagunensis* blooms that greatly decrease light penetration (Onuf 1996, 2000). In addition, hypoxia that co-occurred with algal blooms was linked to large fish kills in 2007, 2010, 2012, and 2015 that involved recreationally and/or commercially important species (i.e., trout, red drum, black drum) (unpubl. Texas Parks & Wildlife Spills & Kills Team reports).

Based on the aforementioned trends in water quality indicators, it is clear that large-scale watershed restoration aimed at reducing nutrient loads is needed for Baffin Bay. To do this, a

reasonable accounting of nutrient sources must be in place. A first order understanding of nutrient sources is derived from a U.S. Geological Survey SPAtially Referenced Regression On Watershed attributes (SPARROW) model, which estimates annual average nutrient loads at a watershed's outlet and relative contributions from sources, and was applied to the Baffin Bay watershed in 2002 (Rebich et al. 2011). From the 2002 model, N and P loadings were ascribed to fertilizers (~30%), wastewater (~10%), manure (~20%), urban runoff (~10%) and atmospheric deposition (~30%). However, results from a recent isotope-based nutrient source tracking study found a significant contribution of human sewage to nitrogen loads to Baffin Bay that exceeded the contribution from agricultural sources (Felix and Campbell 2019). There are several documented municipal wastewater treatment plants that have been cited for discharging minimally treated or even raw sewage to the creeks that flow into Baffin Bay, especially during rain events, and it has been estimated that approximately 1,363 septic tanks out of ~9,086 total located in the watershed that need to be replaced because of age or poor functioning (San Fernando and Petronila Creek Watershed Protection Plan 2023). Thus, there is clearly a need for additional work to refine nutrient load source apportionment in Baffin Bay and its watershed.

One effective method to determine N sources is the use of stable isotope techniques. Stable isotope techniques utilize distinct N isotope composition ($\delta^{15}N$) and the known systematic alteration of this composition through fractionation to trace N sources and investigate potential processing (Hu et al., 2019). These isotope techniques have been widely applied to dissolved inorganic nitrogen (DIN) studies (Jiang et al., 2020; Wells et al., 2016; Yu et al., 2020; Zhong et al., 2020). However, few studies have employed the isotope approach to dissolved organic nitrogen (DON) because of analytical difficulties, limited knowledge about the fractionation factors associated with DON processing and the scarce inventory of DON isotope source signatures. Nevertheless, the stable isotope approach may be more applicable to DON source tracing as DON is relatively stable in redox environments and some DON forms are not directly available for the uptake of microorganisms (Osterholz et al., 2015; Schmidt et al., 2011). As a result, less isotope fractionation would occur, and the isotope signatures of DON sources may be better preserved when reaching the watershed.

The goal of this task was to identify "hot spots" of nutrient enrichment and identify potential surficial nutrient sources to both Baffin Bay and its feeder creeks. Results contribute to our understanding of priority nutrient sources/source locations in support of watershed restoration efforts.

2. Method

2.1 Study area

2.1.1 Baffin Bay watershed

Baffin Bay (27.255877° N, 97.51638° W) is a shallow estuary isolated from the Gulf of Mexico by the Padre Island barrier island (Figure 1) (Simms et al., 2010). Watershed land use is dominated by agriculture (primarily cotton farming; 44%), followed by scrub (35%) and grassland (8%) (NOAA Coastal Change Assessment Program). Human development is relatively limited within the watershed, with the city of Kingsville being the largest populated area (pop. 26,213). The riverine discharges of the feeder creeks (i.e., Petronila, Los Olmos, and San Fernando Creek) are variable and intermittent (from 0 m^3/s to 2.2 m^3/s during the sampling period) (USGS, 2021a; b; c). There are 18 permitted wastewater treatment plants (WWTP) draining into BB watershed and

794 septic tanks found within the coastal zone boundary of Cayo del Grullo (CDG) and Alazan Bay (AB), two sub-watersheds of BB (Figure 1b and c). Rain events contribute 60 to 80 cm of precipitation per year, which is half of the annual evapotranspiration rate. BB shows common characteristics of semi-arid estuaries, with water residence times exceeding one year and salinities from 40 to 60 (An and Gardner, 2002).

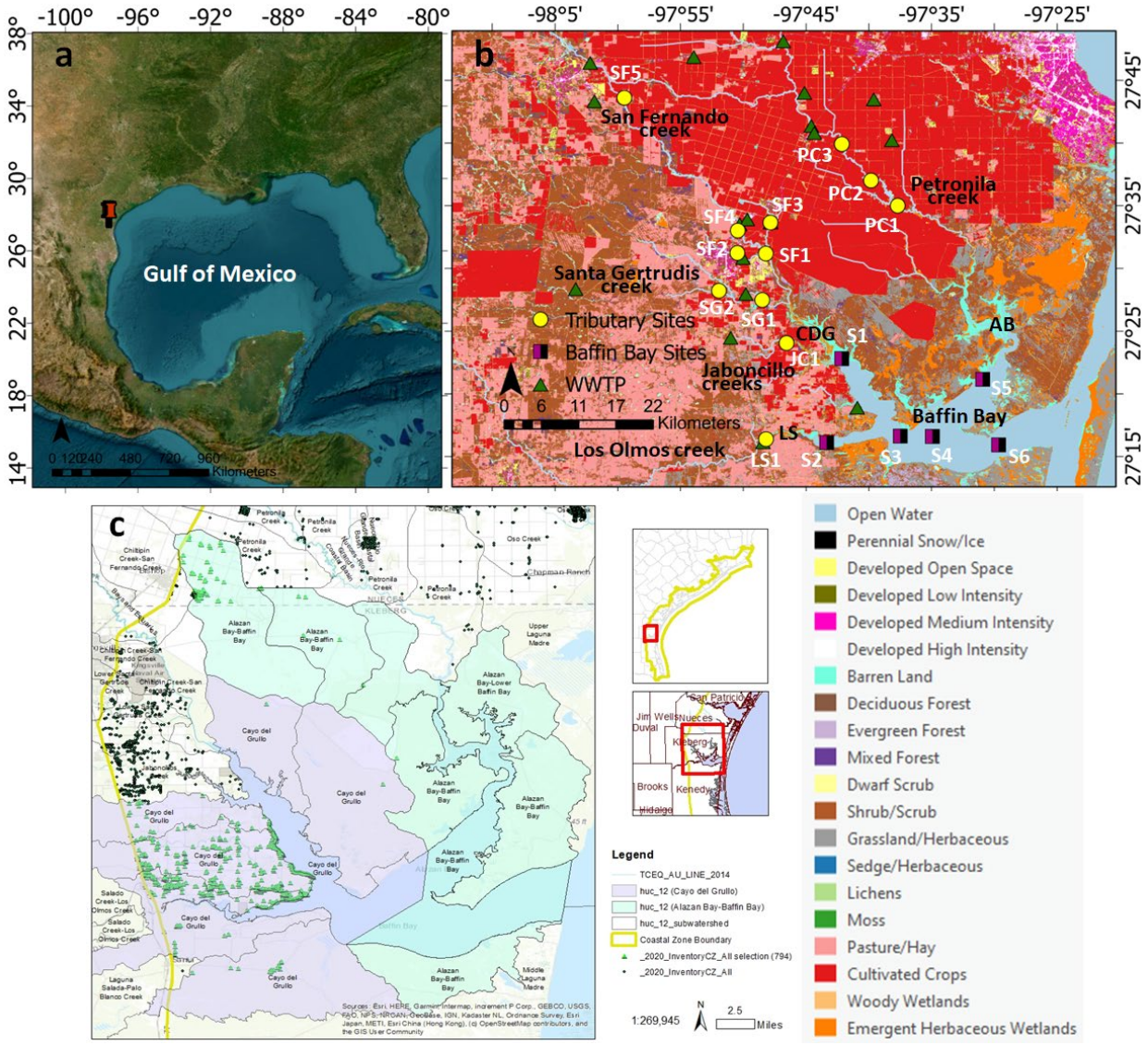

Figure 1. *a) Location of Baffin Bay, indicated by the red pin, along the western Gulf of Mexico. b) Baffin Bay map depicting land cover and land use layer (USGS, 2022). Green triangles indicate permitted wastewater treatment facilities. Purple/black squares indicate the sampling locations of surface water in the bay. Yellow dots indicate sampling sites of Baffin Bay tributaries (i.e., Los Olmos, Petronila, Jaboncillo, San Fernando and Santa Gertrudis creek) draining into Alazan Bay (AB), Laguna Salada (LS) and Cayo del Grullo (CDG) sub-watersheds. c) Map of septic systems in the Baffin Bay watershed. Green triangles indicate 794 septic systems within the coastal zone boundary of CDG and AB, and black dots indicate the septic systems outside the coastal zone but within the Baffin Bay watershed. Map was created by Texas A&M AgriLife with data collected from contract # 582-20-10160 funded by the Environmental Protection Agency (EPA) Clean Water*

Act (CWA) Section 319(h) funds through the Texas Commission on Environmental Quality (TCEQ), titled "Coastal Zone Act Reauthorization Amendments (CZARA) - On-Site Sewage Facilities (OSSFs) Coastal Inventory and Chocolate Bayou OSSF Inspections.

2.1.2 Airshed

The atmospheric deposition (i.e., wet deposition) was collected at a nearby city (i.e., Corpus Christi) of Baffin Bay watershed. The rain collector was located at the Texas A&M University – Corpus Christi weather station (27.71 N, -97.32 W) on Ward Island (Figure 2a). Based on airmass trajectories of rain events collected during this project (Figure 2b-e), most of the airmasses over this site either come from the airshed of Baffin Bay or the Gulf of Mexico, which is also a major source to the airshed of Baffin Bay. Thus, the N concentrations and isotope compositions over the airshed of Corpus Christi was used as a reference to study the N deposition and emission sources over the airshed of Baffin Bay.

Corpus Christi is a coastal city located in southern Texas, USA with a population of 317,863 in 2020. Based on the UN-DESA urban area classification, Corpus Christi is defined as a small-sized city (United States Census Bureau, 2020). This city is surrounded by agricultural land to the north, west and south and it borders, Nueces Bay, Corpus Christi Bay, and Laguna Madre (Berner and Felix, 2020). Metropolitan Corpus Christi area is a home to 332,346 acres of planted cropland, 10,414 head of cattle (USDA, 2017), four petrochemical refineries, three operating natural gas power plants, and two industrial gas manufacturing plants (Berner and Felix, 2020). The weather station is located 13.5 km southeast of downtown Corpus Christi and 16 km west of the Gulf of Mexico on Ward Island (or the TAMU-CC campus), on Corpus Christi Bay shoreline and near Oso Bay discharge mouth (Figure 2a). This site borders a marshland that displays intermittent flooding to the west. It is also adjacent to a four-lane-two-way road with 27,640 daily traffic counts in 2018 (Corpus Christi MPO, 2018).

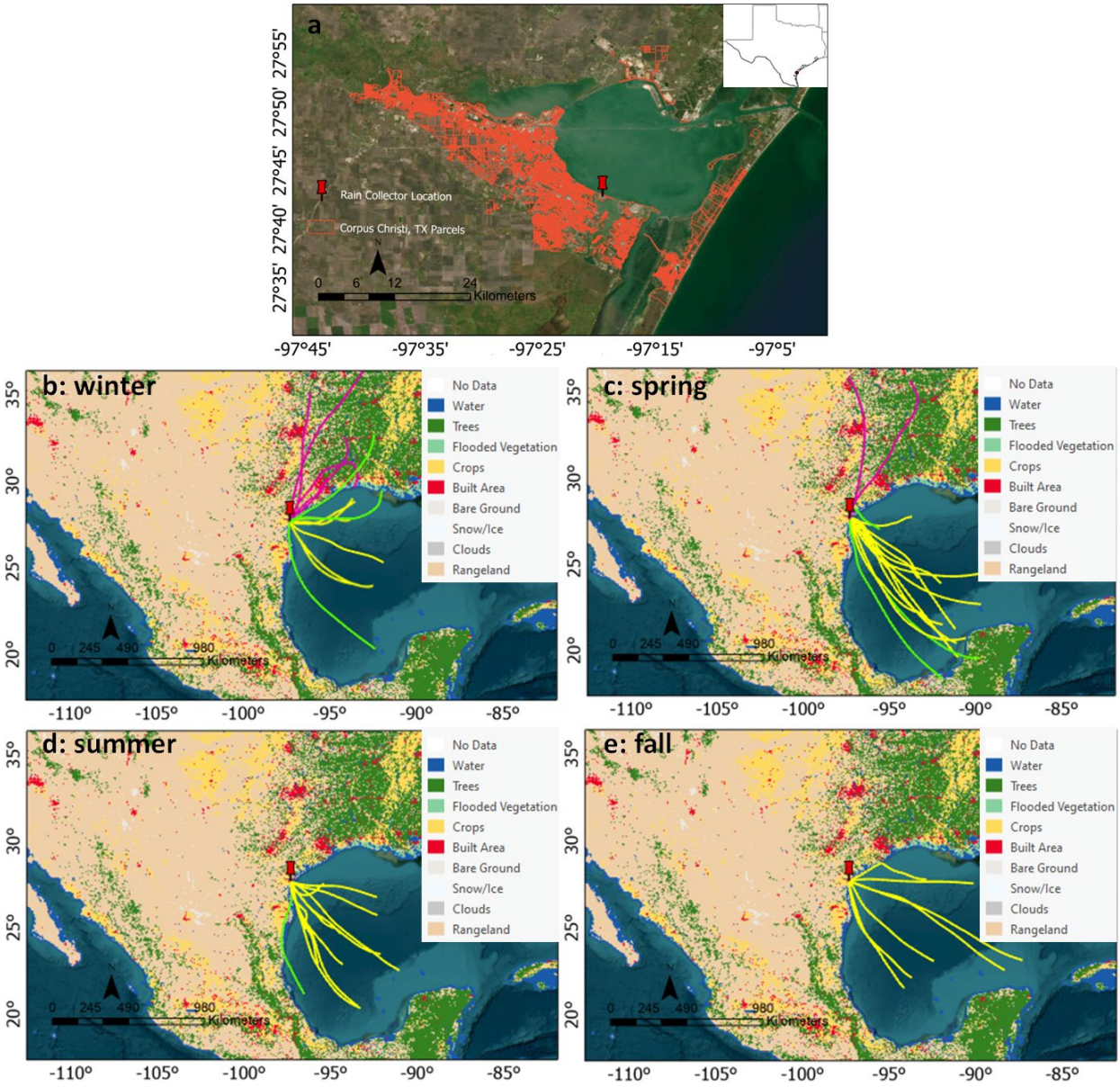

Figure 2. *Map of study airshed and air mass back trajectories. a) Corpus Christi airshed. Red pin indicates the location of the rainwater collector. b) 24-hour air mass trajectories in winter (i.e., December, January, and February). c) 24-hour air mass trajectories in spring (i.e., March, April, and May). d) 24-hour air mass trajectories in summer (i.e., June, July, and August). e) 24-hour air mass trajectories in fall (i.e., September, October, and November). Purple trajectories indicate continental air masses, yellow trajectories indicate marine air masses, and green trajectories indicate mixed (i.e., continental and marine) air masses (USGS, 2022).*

2.2 Field and isotope sample collection

Baffin Bay surface water (S1-6) were collected monthly from November 2020 to June 2022 (Figure 1b). The surface water samples of tributaries that drain into BB sub-watersheds (i.e., Laguna Salada (LS), CDG and AB) (Figure 1b) were collected six times before (dry period) and after (wet period) the rain events that occurred in spring 2021, fall 2021 and spring 2022. Salinity,

temperature, pH and dissolved oxygen (DO) were measured by a multi-probe YSI ProPlus. All watershed samples, collected in 1 L HPDE bottles previously acid-washed and rinsed with 18.2 MΩ cm water and finally triple rinsed with sample water, were placed in ice until transported back to the lab.

Rainwater samples (n = 51) were collected on an event-basis from January 2021 to June 2022 using an N-CON automated wet/dry atmospheric deposition sampler. Rainwater was collected in a 4 L glass beaker which was rinsed with Milli-Q water and combusted in a muffle furnace at 450 ℃. Rain was collected directly after the event's culmination within 12 hours. Rainwater pH was measured in situ using the Extech Waterproof Palm pH Meter. Rainwater was filtered through 0.2 µm pore-sized hydrophilic polycarbonate membranes and frozen until further analysis. HYSPLIT online transport model was used to simulate the 24-hour air mass backward trajectory at 500 m altitude of each rain event (Figure 2b-e). The 24-hour time frame was selected since NO_x and NH_3 have a short lifespan in the atmosphere (Dammers et al., 2019; Romer et al., 2016). Although organic nitrogen compounds have varied atmospheric lifetimes, 24-hour was able to comprise the lifespan of most nitrogen compounds and was considered as the best representative time frame in this study (Borduas et al., 2016). Rain events were categorized as continental, marine and mixed events based on the transport of air masses. Out of 51 trajectories, 9 originated from and transported over continental areas (continental), 35 originated from and transported over the Gulf of Mexico (marine), and 7 traveled over both continental and marine areas (mixed).

Watershed sample processing

Prior to subsampling from 1-L amber bottles, the bottles were gently inverted several times to homogenize the water and materials contained therein. For chlorophyll *a* determination, a known volume of sample water was gently filtered (≤ 5 mm Hg) through 25 mm Whatman GF/F filters. Filters were stored frozen (-20ºC) in sealed Vacutainers until analysis. Chlorophyll a was extracted from the filters by soaking for 18-24 hours in 90% HPLC-grade acetone at -20ºC, after which chlorophyll a was determined fluorometrically with a Turner Trilogy fluorometer without acidification according to EPA method 445.0. Inorganic nutrients were determined using the filtrate of water samples that were passed through a 25 mm GF/F filter and stored frozen (-20ºC) until analysis. After thawing to room temperature, samples were analyzed on a Seal QuAAtro autoanalyzer. Standard curves with five different concentrations were run daily at the beginning of each run. Fresh standards were made prior to each run by diluting a primary standard with low nutrient surface seawater. Deionized water (DIW) was used as a blank, and DIW blanks were run at the beginning and end of each run, as well as after every 8-10 samples to correct for baseline shifts. Dissolved organic carbon (DOC) and total dissolved nitrogen (TDN) were determined using the filtrate of water samples that were passed through precombusted 25 mm GF/F filters and stored frozen (-20ºC) until analysis. Total organic carbon (TOC) and total nitrogen (TN) were determined from whole water samples. Samples were subsequently analyzed using the High Temperature Catalytic Oxidation method on a Shimadzu TOC-Vs analyzer with nitrogen module. Standard curves were run twice daily using a DIW blank and five concentrations of either acid potassium phthalate solution or potassium nitrate for DOC and TDN, respectively. Three to five subsamples were taken from each standard and water sample and injected in sequence. Reagent grade glucosamine was used as a laboratory check standard and inserted throughout each run, as were Certified Reference Material Program (CRMP) deep-water standards of known DOC/TDN concentration. Dissolved organic nitrogen (DON) was determined by subtracting dissolved inorganic nitrogen (ammonium, N+N) from TDN.

2.3. Isotope source tracking data analysis

For results and discussion sections, seasons were divided meteorologically with spring referred to as March to May, summer as June to August, fall as September to November, and winter as December to February. The sampling period from November 2020 to May 2021 was categorized as a dry period and June 2021 to July 2022 was categorized as a wet period based on the salinities of BB and the amount of precipitation this watershed received (Figure 3 and Table 1). Watershed tributary sites PC1, PC2, and PC3 were referred as AB; JC1, SG1, SG2, SF1, SF2, SF3, SF4, and SF5 were referred as CDG; LS1 was referred as LS. The comparisons of concentrations and isotope compositions among samples/seasons/wet-dry periods/groups/events were conducted using the analysis of variance (ANOVA). When the p value was lower than 0.05, the result was significantly/statistically different; when the p value was higher than 0.05, the result was not different. The correlations between analytes were conducted by Pearson Correlation method.

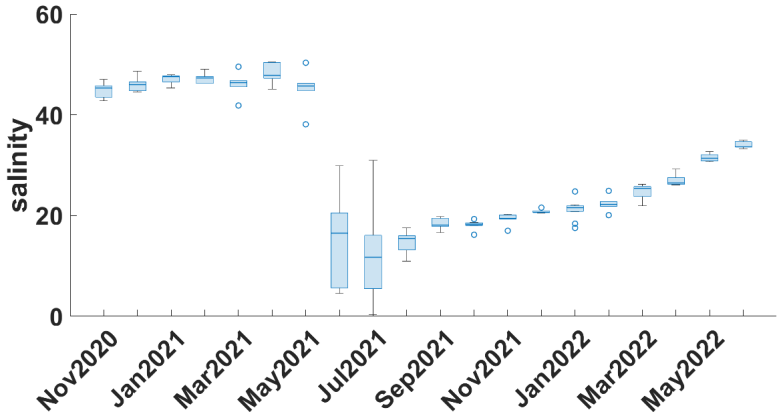

Figure 3. *Salinities of Baffin Bay surface water from November 2020 to June 2022.*

Table 1. *Precipitation amount (inches) in Kingsville from November 2020 to June 2022.*

	Jan	Feb	Mar	Apr	May	Jun	Jul	Aug	Sep	Oct	Nov	Dec
2020											1.19	0.29
2021	1.79	0.64	0.18	0.46	20.94	7.07	4.76	0.58	4.00	0.49	1.22	0.28
2022	1.03	1.12	0.18	0.28	3.00	0.02						

2.4 Concentration analysis and flux calculation

The NO_3^-/NO_2^- concentrations of watershed samples were measured by a colorimetric method (Tsikas, 2007). After NO_2^- was measured, NO_3^- was reduced to NO_2^- using the cadmium reduction method (Tsunogai et al., 2008) and concentrations were calculated by subtracting NO_2^- from the measured $NO_3^- + NO_2^-$. The NO_3^-/NO_2^-, Cl^- and SO_4^2 concentrations of airshed samples were measured by a Dionex Aquion Ion Chromatography 4000i, equipped with an AS-AP autosampler and AS4A separation column. Throughout the sampling period, NO_2^- was not detected in rainwater. The NH_4^+ concentrations of watershed and airshed samples were measured using the o-phthalaldehyde (OPA) fluorometric method (Holmes et al., 1998). DON concentrations were calculated by subtracting DIN from TDN. First, NH_4^+ was removed from each sample through NH_4^+ diffusion by increasing the pH to 10 (Holmes et al., 1998). This NH_4^+ removal step was to

reduce the error involved with DON concentration and isotope back calculations. TDN was then oxidized to NO_3^- by the persulfate oxidation method, followed by reduction to NO_2^- via the cadmium reduction method and further analysis by the colorimetric method (Tsunogai et al., 2008). DON concentrations were calculated by subtracting previously measured NO_3^- + NO_2^- from the TDN pool. Representative DON standards (i.e., urea, glycine, N-acetyl-D-glucosamine) were oxidized and reduced alongside samples to confirm quantitative conversion (>90%) of TDN to NO_2^-. Urea was used as a DON standard since it is a common component in fertilizers and accounts for about 50% of N uptake in many coastal regions (Sipler and Bronk, 2015). Glycine was used to represents dissolved free amino acids (DFAA) which are expected to be 1.2 to 12.5% of the total DON pool (Sipler and Bronk, 2015). N-acetyl-D-glucosamine represented N-acetyl amino polysaccharides (N-AAPs), which are important to the semi-labile DON pool (Aluwihare et al., 2005).

The volume-weighted mean (VWM) concentrations of each species in rainwater were calculated using the following equation:

$$\text{VWM } (\mu\text{M}) = \sum_{i=1}^{N} C_i p_i \,/\, \sum_{i=1}^{N} p_i \qquad (1)$$

where c_i is the species concentration of ith rain event (μM); p_i is the precipitation amount of ith rain event (mm); and N is the total number of rain events. VWM was used in discussion sections rather than the arithmetic average because of the bias imposed by varied precipitation amounts.

The wet deposition flux of each species in rainwater was calculated using the following equation:

$$D_w = P_{t2021} \times VWM_{2021} \times 14/\ 100000 \qquad (2)$$

where D_w is the wet deposition flux (kg N/(ha*yr)); P_t is the total rainfall in 2021 (mm); VWM_{2021} is the VWM concentration of rain events collected in 2021; 14/1000 is a unit conversion factor. In the annual wet deposition flux calculation, only data collected from January through December 2021 was used. To prevent seasonal bias and maintain accuracy in the annual flux calculation, rain collected from January to June 2022 was excluded from this calculation.

2.5 N and O isotope composition analysis

The N and O isotope composition ($\delta^{15}N$/ $\delta^{18}O$) was denoted by the following equation and was reported in permil (‰):

$$\delta_{sample}\,(‰) = (R_{sample}/R_{standard} - 1) * 1000 \qquad (3)$$

where R is the ratio of $^{15}N/^{14}N$ or $^{18}O/^{16}O$, respectively. The isotopic composition of NO_3^-/NO_2^- ($\delta^{15}N\text{-}NO_3^-/NO_2^-$ and $\delta^{18}O\text{-}NO_3^-/NO_2^-$) was measured by the denitrifier bacteria method at the University of California, Davis Stable Isotope Facility (Sigman et al., 2001). Internationally recognized standards (USGS32, USGS34, USGS35, IAEA-N3) were measured during sample analysis to provide known $\delta^{15}N\text{-}NO_3^-$ and $\delta^{18}O\text{-}NO_3^-$ references for data correction. Average standard deviations for $\delta^{15}N\text{-}NO_3^-$ and $\delta^{18}O\text{-}NO_3^-$ reference materials were 0.2 and 0.2‰, respectively. Rainwater stable isotopes of $\delta^{18}O$ and δD were measured at Stable Isotope Geosciences Facility - Texas A&M University, using a Picarro L2120-I cavity ringdown spectrometer with uncertainties of 0.1‰ for $\delta^{18}O$ and 1‰ for δD. Oxygen and hydrogen isotope abundances were measured relative to the accepted international standard, the Vienna Standard Mean Oceanic Water (VSMOW). The average $\delta^{18}O\text{-}H_2O$ values were found to be -3.1 ± 3.2‰.

To measure $\delta^{15}N\text{-}NH_4^+$, NH_4^+ was oxidized to NO_2^- before isotope analysis (Felix et al., 2013; Zhang et al., 2007). Then the $\delta^{15}N$-DIN (NH_4^+, NO_3^-, and NO_2^-) was measured by the denitrifier bacteria method and $\delta^{15}N\text{-}NH_4^+$ was back calculated using equation 4:

$$\delta^{15}N\text{-DIN} = f_{NH4+} \times \delta^{15}N\text{-}NH_4^+ + f_{NO3-/NO2-} \times \delta^{15}N\text{-}NO_3^-/NO_2^- \quad (4)$$

where f_{NH4+} is the fraction of NH_4^+ in the DIN pool and $f_{NO2-/NO3-}$ is the fraction of NO_2^- and NO_3^- in the DIN pool. Solutions of international $\delta^{15}N\text{-}NH_4^+$ standards USGS25 and USGS26 were prepared, oxidized, and analyzed in the same manner as the samples for data normalization and to test the efficiency of the coupled method oxidation and denitrifier method. Average standard deviations for the standards were 0.9‰.

To measure $\delta^{15}N$-TDN, first NH_4^+ was removed from the TDN pool via diffusion (Holmes et al., 1998). Then the remaining TDN (i.e., NO_3^-, NO_2^- and DON) was oxidized to NO_3^- via the persulfate oxidation method. Analyses of $\delta^{15}N$-TDN were conducted using the denitrifier bacteria method (Knapp et al., 2005). $\delta^{15}N$-DON was back calculated using equation 5:

$$\delta^{15}N\text{-TDN} = f_{DON} \times \delta^{15}N\text{-DON} + f_{DIN} \times \delta^{15}N\text{-DIN} \quad (5)$$

where f_{DON} and f_{DIN} are the fraction of DON and NO_2^- and NO_3^-, respectively, in the TDN pool.

2.6 Nitrogen isotope fractionation during HNO_3 formation in the airshed

After emission, NO_x undergoes isotope fractionation during atmospheric transformations thus changing the $\delta^{15}N\text{-}NO_3^-$ rain value compared to its NO_x source. The nitrogen isotope fractionation was simplified and summarized using the following equation (Li et al., 2020):

$$\delta(NO_2) - \delta(NO_x) = \frac{A(\alpha 2 - \alpha 1) + (\alpha(NO_2 - NO) - 1)}{A+1} \times \left(1 + \delta(NO_2)\right) \times \left(1 - f(NO_2)\right) \quad (6)$$

$$A = \frac{k_2[O_3]}{k_1[NO_2]} \quad (7)$$

where $\delta(NO_2)$ and $\delta(NO_x)$ were $\delta^{15}N\text{-}NO_2$ and $\delta^{15}N\text{-}NO_x$, respectively. α_1 and α_2 were fractionation factors of NO + O_3 and NO + NO_2 reactions. ($\alpha_2 - \alpha_1$) was predicted as -10‰ and $\alpha(NO_2 - NO)$ was experimentally determined as 1.0289 (Li et al., 2020). $f(NO_2)$ was the fraction of NO_2 in NO_x pool. A was determined by Equation 7 where k_1 was the rate constant for NO + NO_2 reaction (8.14 x 10^{-14} cm^3 s^{-1}), k_2 was the rate constant for NO + O_3 reaction (1.73 x 10^{-14} cm^3 s^{-1}), [O_3] was the concentration of O_3 and [NO_2] was the concentration of NO_2 (Atkinson et al.; Sharma et al., 1970). [O_3] and [NO_2] over the airshed were detected by a Teledyne T400 ozone analyzer and a Teledyne T500 NO_x analyzer located at the City of Corpus Christi air monitoring site 7 km away from the rain collector. The calculated $\delta(NO_2)$ - $\delta(NO_x)$ ranged from -4.1 to 12.5‰ with a mean of 2.0‰.

The $\delta^{15}N\text{-}NO_3^-$ of rainwater should also inherit the $\delta^{15}N$ values of $NO_3^-{}_{(p)}$ and $HNO_{3(g)}$, as both are water-soluble and can be effectively washed out of the atmosphere (Li et al., 2019b). Here fractionation was assumed to be negligible when NO_2 was transferred to HNO_3 and $\delta^{15}N\text{-}NO_2$ equaled to the measured $\delta^{15}N\text{-}NO_3^-$ of rainwater (Felix and Murgulet, 2020; Li et al., 2019b; Passos et al., 2022). Fractionation to $NO_3^-{}_{(p)}$ was also assumed to be negligible, as comprehensive quantification of potential fractionation is still pending, and we lack additional measured parameters for estimation.

2.7 Isotope mixing model

Due to the principal characteristics of the watershed described in 2.1, a five-end member isotope mixing model to estimate DON source contributions was developed using N isotope signatures of four primary sources including wastewater, manure and wet deposition as allochthonous sources and particle organic nitrogen (PON) (i.e., phytoplankton and zooplankton) as an autochthonous source (Table 2) (Qiu et al., in prep-b). The mixing model was constructed using the Stable Isotope Analysis in R (SIAR) package, which employs Bayesian statistical techniques (Parnell et al., 2010). The Bayesian statistics incorporated N sources isotope signatures, uncertainties and the fractionation factor to produce source contribution probabilities, which was run through 200,000 iterations in the mixing model to provide its best estimate of the source apportionments (Parnell et al., 2010). The study observed a significant linear correlation between δ^{15}N-DON and ln[DON] with slopes of 4.2 and 2.6 in the BB surface water and three tributaries during dry period, indicating DON assimilation and coupled PON/DON remineralization with a fractionation factor of 4.2‰ and 2.6‰, respectively (Figure 4), which was applied in the mixing model for dry period samples. The mixing model can be simply described as below:

$$\delta^{15}\text{N-DON}_{bay} = \sum_{i=1}^{i} f_i(\delta^{15}\text{N}_i + C_i) \quad (8)$$

where: δ^{15}N-DON$_{bay}$ is the DON isotopic composition of surface samples; f_i is the fraction of the ith source (e.g., wastewater, manure, wet deposition and PON); δ^{15}N$_i$ is the DON isotopic composition of the ith source; C_i is the fractionation factor applied on the ith source.

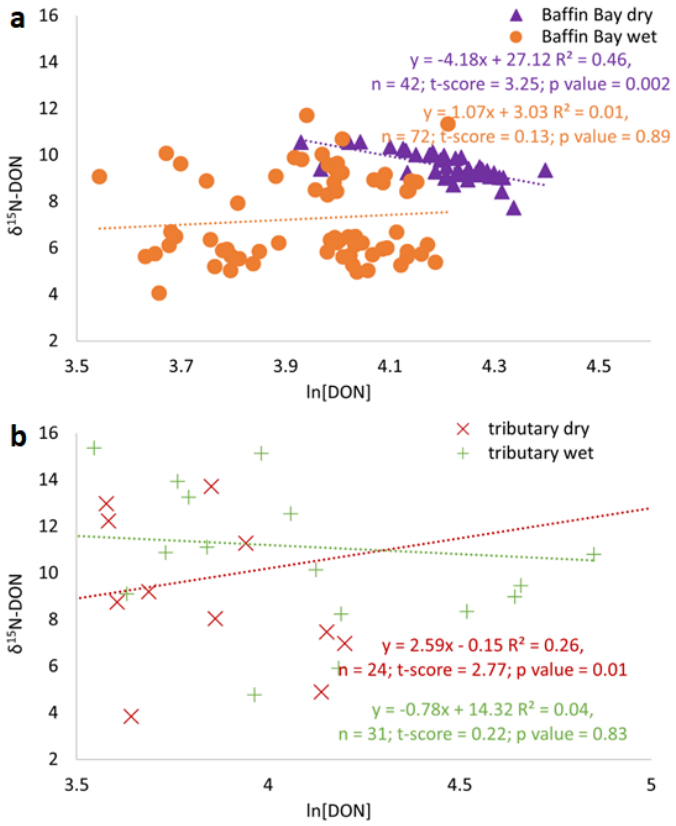

Figure 4. *The linear correlations of δ^{15}N-DON and ln[DON] in Baffin Bay surface water (a) and three watersheds (b) during dry (purple triangles and red crosses) and wet (orange dots and green pluses) periods.*

Table 2. *N Isotope signatures of potential sources to watersheds.*

Source Type	DON isotope signature	DON assimilation/remineralization fractionation in dry period
Wastewater (Qiu et al., in prep-b)	+22.3 ± 7.9‰*	4.2‰ [c] /2.6‰ [d]
Manure (Campbell, 2018)	+3.9 ± 0.2‰ *, [a]	4.2‰ [c] /2.6‰ [d]
Wet deposition (Russell et al., 1998)	+5.0 ± 5.5‰	4.2‰ [c] /2.6‰ [d]
PON (Wetz, unpublished work)	+3.9 ± 1.4‰*, [b]	4.2‰ [c] /2.6‰ [d]

Note. * means local δ^{15}N-PON/δ^{15}N-DON/δ^{15}N-TDN. [a] is the δ^{15}N-TDN of cattle, which was the most populated livestock in study region (USDA, 2017). This δ^{15}N-TDN value could reflect cattle manure DON isotope signature as DIN concentrations in these cattle manure samples were measured to be less than 2% of the TDN pool and δ^{15}N-DIN values could have negligible influence on the δ^{15}N-TDN value (Choi et al., 2006). [b] is the δ^{15}N-PON of BB surface water collected in 2020. The fractionation of PON breakdown to DON was reported to be negligible (Sigman and Fripiat, 2019). [c] is the DON assimilation fractionation observed in the BB surface water during dry the period. [d] is the PON/DON remineralization fractionation observed in the tributaries' surface water during the dry period.

Dual isotope mixing models have been employed in many nitrate studies (He et al., 2022; Li et al., 2019a; Liu et al., 2018). Here we employ the mixing model summarized as Equation 9 and 10, respectively for tributary samples.

$$\delta^{15}\text{N-NO}_3^-{}_{\text{samples}} = \sum_{i=1}^{i} f_i(\delta^{15}\text{N}_i + C_i) \quad (9)$$

$$\delta^{18}\text{O-NO}_3^-{}_{\text{samples}} = \sum_{i=1}^{i} f_i(\delta^{18}\text{O}_i + C_i) \quad (10)$$

where: δ^{15}N-$NO_3^-{}_{\text{samples}}$ and δ^{18}O-$NO_3^-{}_{\text{samples}}$ are the N and O isotopic compositions of tributary NO_3^-, respectively; f_i is the fraction of the ith source (e.g., wastewater NH_4^+, wastewater NO_3^-, fertilizer NH_4^+, fertilizer NO_3^-, and soil NO_3^- in Table 3); $\delta^{15}N_i/\delta^{18}O_i$ is the δ^{15}N/δ^{18}O value of the ith source; C_i is the fractionation factor applied on the ith source.

Table 3. *Primary sources and potential fractionations of NO_3^- stable isotope mixing model for tributaries.*

	δ^{15}N (Nikolenko et al., 2018; Xue et al., 2009)	δ^{18}O (Onodera et al., 2021; Xue et al., 2009)	Nitrification fractionation on N-NO_3^- (Granger and Wankel, 2016)	Denitrification fractionation on N-NO_3^- and O-NO_3^- (Granger and Wankel, 2016)
Fertilizer NH_4^+	0 ± 3‰	5 ± 5‰	-15 ± 10‰	15 ± 10‰
Wastewater NH_4^+	3.9 ± 2.8	5 ± 5‰	-15 ± 10‰	15 ± 10‰
Fertilizer NO_3^-	0 ± 3‰	21 ± 4‰		15 ± 10‰
Soil NO_3^-	4 ± 4‰	3 ± 3‰		15 ± 10‰
Wastewater/Manure NO_3^-	14.9 ± 3.5	19.3 ± 4.6		15 ± 10‰

Note. Due to the lack of tributary δ^{18}O-H_2O, the δ^{18}O generated by nitrification is from reported literature (Xue et al., 2009).

The mixing model for rainwater can be described below:

$$\delta^{15}N_{rain} = \sum_{i=1}^{N} \delta^{15}N_i f_i \quad (11)$$

where $\delta^{15}N_{rain}$ was the N isotope composition of NH_4^+, corrected NO_3^-, or DON in the rain; $\delta^{15}N_i$ was the nitrogen isotope composition of the *i*th NH_3, NO_x, or ON source; f_i was the fraction of the *i*th source.

After emission, NH_3 and NH_4^+ reached equilibrium over the airshed and both were entrained in the rain. Therefore, the equilibrium fractionation was considered insignificant and the $\delta^{15}N$-NH_4^+ of the rain was believed to reflect the isotope signatures of the NH_3 emission sources. The NH_3 and NH_4^+ might be unequally entrained, which could further lead to fractionation. However, without the knowledge of NH_3/NH_4^+ ratios, using the $\delta^{15}N$-NH_4^+ values of rainwater to represent N isotope compositions of both NH_3 and NH_4^+ is the most straightforward and feasible approach. For the NH_4^+ mixing model, fertilizer, livestock waste and vehicle were selected as continuous potential NH_4^+ sources (Table 4). As previously mentioned, the study area is surrounded by agricultural land to the north, west and south. Agriculture is estimated to be responsible for 85% of NH_3 emissions (55% from volatilized livestock waste and 30% from volatilized fertilizer) in the USA (Berner and Felix, 2020; EPRI, 2015). Also, the study site is directly adjacent to a four-lane-two-way road that 27,640 counts of vehicles passed through every day in 2018 (Corpus Christi MPO, 2018). Vehicles emit NH_3 as a byproduct and NH_3 emission during heavy traffic can be significant (Felix et al., 2013). The air-sea flux of NH_3 is a recognized source and sink of NH_3 (Johnson et al., 2021) but its significance and timing as an emission source during the study period is unknown and depends on many physical and chemical factors (e.g., temperature, salinity, pH, wind, $[NH_4^+]_{(aq)}$, $NH_{3(g)}$). Due to gaps in knowledge and the potential role of water bodies to be primarily a sink for NH_3 (Altieri et al., 2022), a marine source is not included as a significant source in our source apportionment but deserves further attention in future coastal studies. Over the sampling period, NOAA Hazard Mapping System Fire and Smoke Product detected many fire events (e.g., agricultural waste burning, forest fires, grassland fires, etc.) in Mexico and Central America. Biomass burning could significantly affect the concentration and isotope composition of NH_4^+ in the rain. Whether biomass burning was a potential source in single rain events was determined by the coupled implementation of HYSPLIT airmass trajectory and Hazard Mapping System Fire and Smoke Product (Qiu et al., in prep-a). When the total fire radiative power of biomass burning events within the back trajectory radius of the rain event was higher than 100 MJ/s, the biomass burning emission was about the same magnitude of estimated vehicle emission according to National Emissions Inventory (EPA, 2020) and the rain event would be classified into the biomass burning (BB) group for the NH_4^+ isotope mixing model. The rest would be categorized into the not affected (NA) group.

For the NO_3^- mixing model, vehicle, natural gas combustion and soil biogenic emission were selected as continuous potential NO_x sources (Table 4). Vehicle emissions became the dominant anthropogenic NO_x source in the USA after mitigating the direct emission from industry (McDonald et al., 2012). Natural gas combustion and biogenic soil emission were selected as focal points due to the prevalence of natural gas as the primary fuel utilized by energy generating units and industries in southeast Texas. Additionally, biogenic soil gases are emitted continuously, potentially contributing substantially to NO_x emissions (Felix and Murgulet, 2020). Furthermore, lightning is one of the largest natural NO_x sources, while biomass burning was estimated to be responsible for 25% of global NO_x emissions (Galloway et al., 2004; Jin et al., 2021). These two

sources are important but also intermittent. This study used HYSPLIT airmass trajectory, NOAA Geostationary Lightning Mapper and NOAA Hazard Mapping System Fire and Smoke Product to determine if lightning or biomass burning may be potential NO_x sources in single rain events (Qiu et al., in prep-a). The rain events were categorized based on specific criteria; it classified as belonging to the biomass burning (BB) group when the total fire radiative power of biomass burning events within the back trajectory radius of the rain event was higher than 100 MJ/s. Similarly, when the total number of lightning strikes within the back trajectory radius of the rain event was more than two hundred, the lightning emission was about the same magnitude of estimated vehicle emission according to National Emissions Inventory (EPA, 2020) and the rain event was classified as part of the lightning (L) group. In instances where the rain event met the signature requirements for both L and BB, it was classified into the lightning and biomass burning (LBB) group. Any rain events that did not meet the criteria for these groups were categorized as belonging to the NA group.

For the DON mixing model, vehicle, fertilizer, marine, and biomass burning were chosen as potential DON sources (Table 4). Biomass burning is an intermittent source and can yield a large amount of ON aerosol (Ito et al., 2015). Whether biomass burning was a potential source in single rain events was determined by the coupled implementation of the HYSPLIT airmass trajectory and Hazard Mapping System Fire and Smoke Product (Qiu et al., in prep-a). When the total fire radiative power of biomass burning events within the back trajectory radius of the rain event was higher than 100 MJ/s, the rain event would be classified into biomass burning (BB) group for the DON isotope mixing model. The rest would be categorized into not affected (NA) group. Vehicle, fertilizer, and marine, on the other hand, could continuously release DON. The study site was in a coastal area and can be significantly affected by marine source, which releases DON through sea spray or ocean surface microlayer (Mace et al., 2003; Miyazaki et al., 2011). The use of commercial/organic fertilizer can be a source of urea and other ON emission and vehicles can contribute to the majority emission of LMW-DON (Chen et al., 2010).

Table 4. *Reported N source isotope signatures. Marine may also be a NH_3 source; however, the NH_3 flux over the air-water interface is bidirectional. Marine was not included as a NH_3 source here as the mechanism behind the bidirectional flux was unconstrained.*

	NH_3	NO_x	DON
Vehicle (Elliott et al., 2019; Walters et al., 2020; Wu et al., 2020)	+6.4 ± 1.7‰	-2 ± 4‰	+12.3 ± 0.3‰
Biomass burning (Elliott et al., 2019; Kawashima and Kurahashi, 2011; Wu et al., 2020)	+12‰	+1 ± 4‰	+1.7 ± 0.3‰
Fertilizer (Bhattarai et al., 2021; Wu et al., 2021)	-28.3 ± 5.8‰		-2.4 ± 2.1‰
Livestock waste (Bhattarai et al., 2021)	-18.3 ± 7.7‰		
Lightning (Hoering, 1957)		0‰	
Natural gas (Walters et al., 2015)		-17.9 ± 1‰	
Soil "biogenic" (Elliott et al., 2019)		-35 ± 10‰	
Marine (Altieri et al., 2016; Wu et al., 2020)			+11.0 ± 0.3‰

3. Results

3.1 Watershed

3.1.1 Spatial and Temporal Variability of Watershed Nutrients

The various nutrient indicators showed a high degree of spatial variability. For example, relatively high mean ammonium concentrations that exceed Texas' designated screening level for impairment (≥23.6 µM) were observed at SF3 (146.9 ± 79.1 µM, n=6), JC1 (40.4 ± 73.0 µM, n=7), and SG1 (30.0 ± 34.9 µM, n=7), while concentrations ≤ 23.6 µM were observed at the other sites (Figure 5). Relatively high mean nitrate + nitrite concentrations (> 20 µM) were observed at all

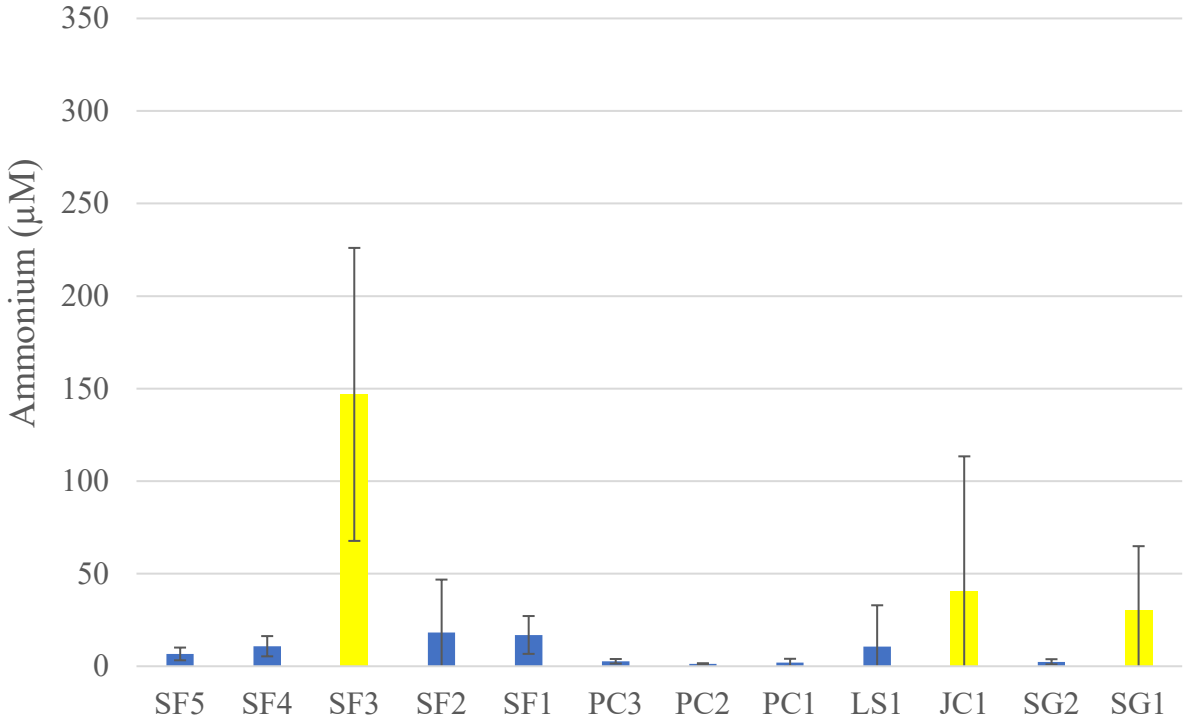

Figure 5. *Ammonium concentration at watershed sites. Yellow bars indicate exceedance of state water quality criteria.*

sites but PC1, LS1, JC1, and SG2 (Figure 6). Exceptionally high concentrations, approaching 100 µM, were observed at SF5 (93.8 ± 93.3 µM, n=6), SF4 (94.3 ± 73.8 µM, n=6), and PC3 (98.5 ± 93.5 µM, n=7). Based on the nitrate concentration designated as indicative of impaired waters by Texas (≥ 139.3 µM), none of the sites would be considered impaired. However, in general, the established screening level is well above a level that would typically lead to harmful impacts on aquatic ecosystems. High mean DON (> 20 µM) concentrations were observed at all sites (Figure 7), with notably high concentrations exceeding those typically found in Baffin Bay itself being observed at SF3 (121.5 ± 25.0 µM, n=6), LS1 (191.1 ± 73.3 µM, n=7), JC1 (167.2 ± 161.6 µM, n=7), and SG2 (115.5 ± 48.4 µM, n=7). Unfortunately, Texas does not have an established screening level that includes organic nitrogen (such as DON in this case), even though it can be utilized for algal growth and, as shown here, is often a dominant form of nitrogen found in watershed creeks. Mean TN concentrations exceeded 100 µM at all but one site (PC1)(Figure 8), indicative of nitrogen enrichment. Texas does not have an established screening level for TN in

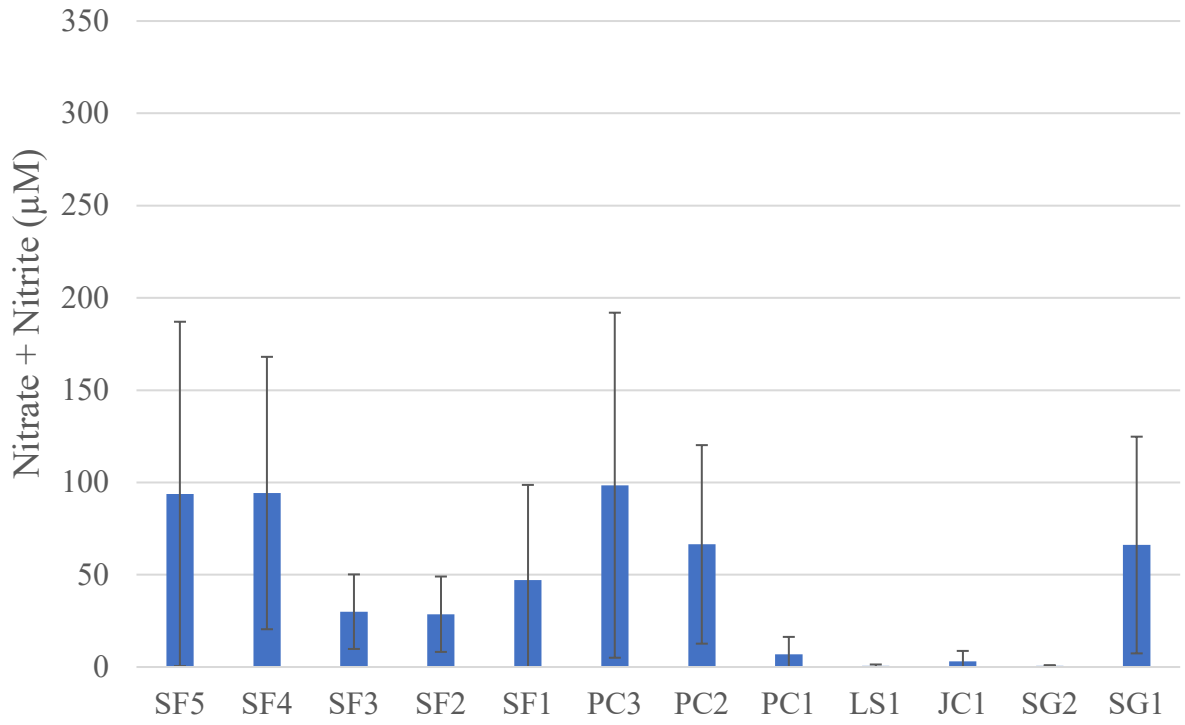

Figure 6. *Nitrate + nitrite concentration at watershed sites.*

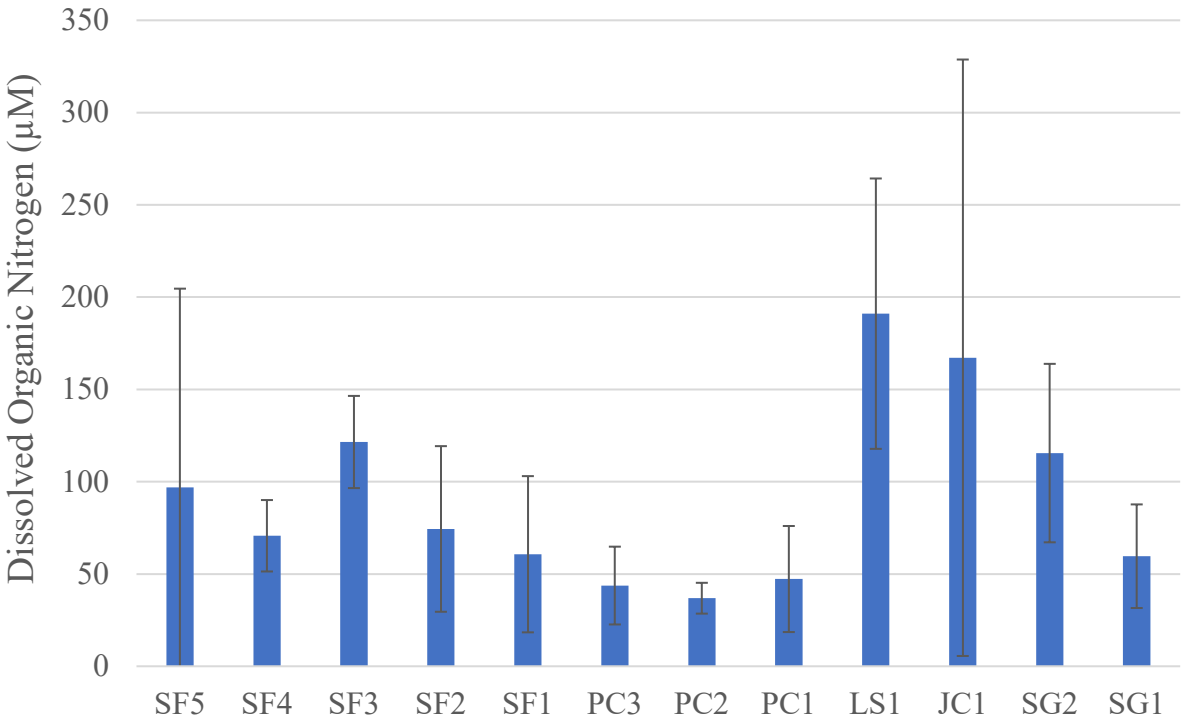

Figure 7. *DON concentration at watershed sites.*

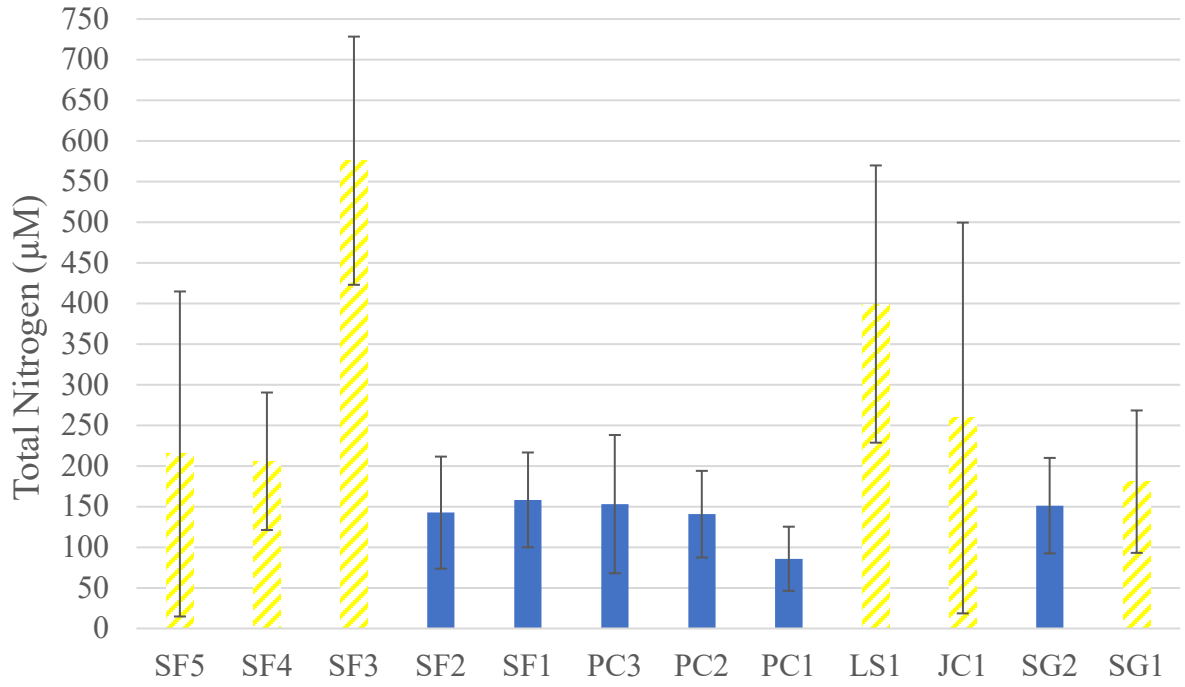

Figure 8. *TN concentration at watershed sites. Yellow bars indicate exceedance of median criteria level established for European rivers.*

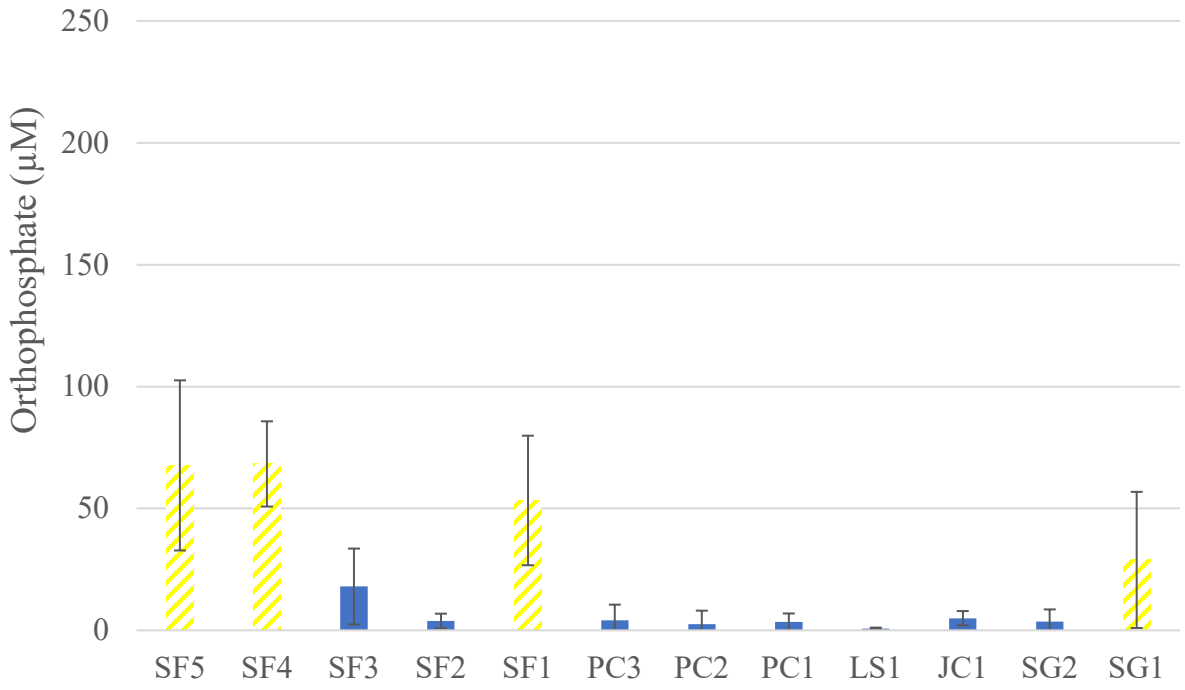

Figure 9. *Orthophosphate concentration at watershed sites. Yellow bars indicate state screening level for total phosphorus.*

rivers. However, if we apply the median TN level to designate impairment in European rivers (178.6 µM; Poikane et al. 2019), sites SF5, SF4, SF3, LS1, JC1 and SG1 would be considered impaired. Mean orthophosphate concentrations were spatially variable, with most sites have relatively low concentrations (<5 µM; SF2, PC3, PC2, PC1, LS1, JC1, SG2) and a few sites having very high concentrations including SF5 (67.6 ± 34.9 µM, n=6), SF4 (68.3 ± 17.5 µM, n=6), SF1 (53.3 ± 26.6 µM, n=7), and SG1 (28.9 ± 27.9 µM, n=7)(Figure 9). Although Texas does not have a screening level for orthophosphate, it does have a screening level for total phosphorus (22.3 µM) that would include both orthophosphate and organic phosphorus. In this case, the orthophosphate concentrations alone would exceed the screening level at SF5, SF4, SF1, and SG1. Aside from these direct nutrient measurements, chlorophyll *a* is frequently used as an indicator of nutrient enrichment, as it represents algal biomass that would utilize nutrients and perhaps mask their appearance in the environment (at least in the case of dissolved nutrients). Here, chlorophyll exceeded Texas' screening level (21 µg/L for the tidal LS1, 14.1 µg/L for all other sites) at all sites except SF 5 and SF4 (Figure 10). SF3 had a notably high mean chlorophyll level (649.6 µg/L).

Temporal variability in the various nutrient indicators was also pronounced, primarily in response to rainfall events. Two pre- and post-rainfall sampling events yielded instructive data on potential nutrient sources to each of the two main creeks (PC, SF) that eventually flows to Baffin Bay. The first sampling event was conducted from 5/13/21-6/23/21. Ammonium concentrations were initially high at SF1 (35.4 ± 0.2 µM) on 5/13/21 during dry weather, decreased dramatically to 1.6 ± 0.1 µM on 5/20 after a major flood event, and then increased to 16.0 ± 0.0 µM on 6/23/21 after a period of dry weather (Figure 11). The opposite pattern was observed at PC1, where ammonium concentrations were initially low (1.10 ± 0.1 µM), increased to 6.2 ± 0.1 µM after the flood, and

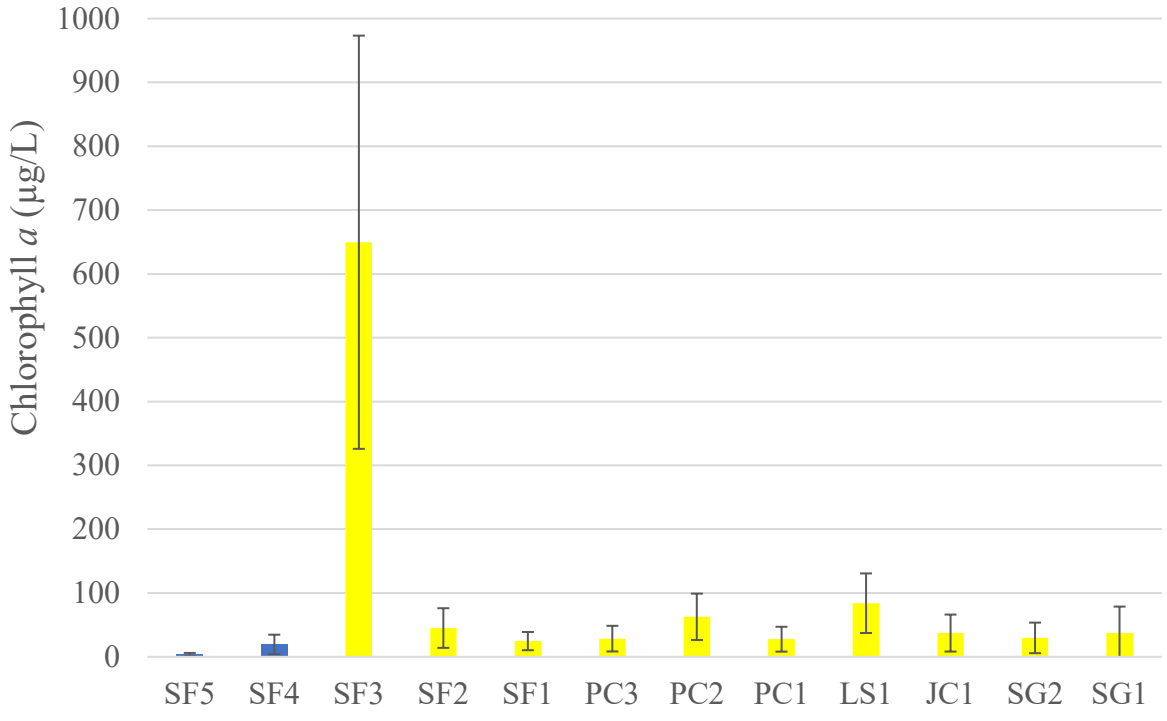

Figure 10. *Chlorophyll a concentration at watershed sites. Yellow bars indicate exceedance of state water quality criteria.*

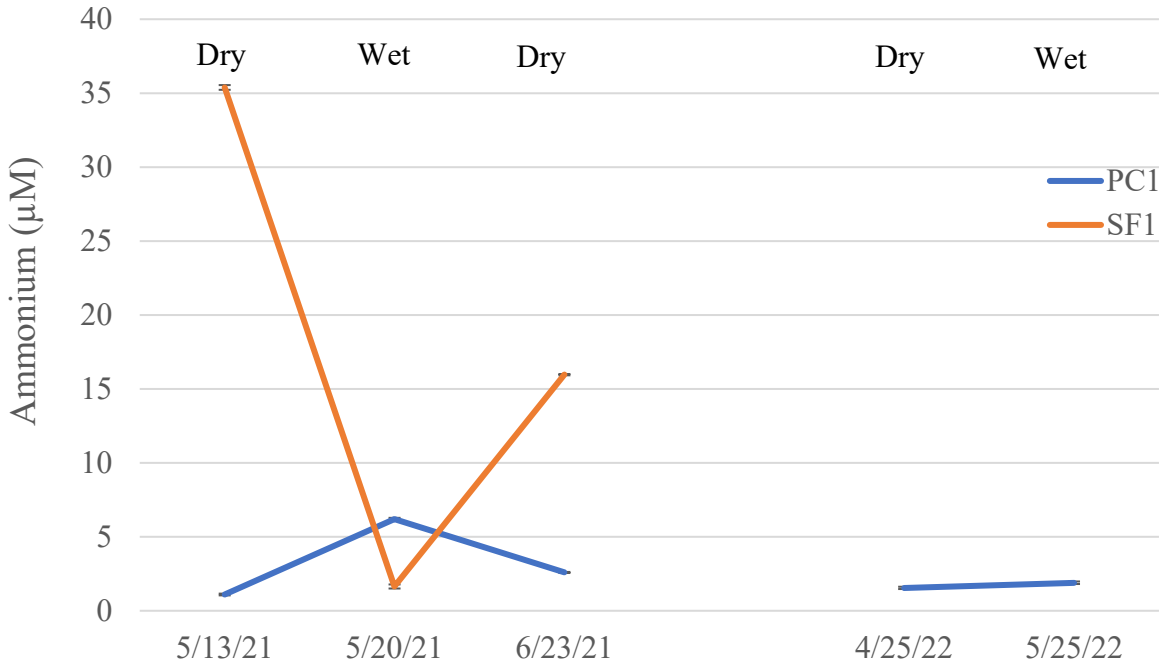

Figure 11. *Temporal variability in Ammonium at downstream creek sites.*

then subsequently decreased again to 2.59 ± 0.0 µM. However, there was minimal change in ammonium during a dry-wet transition in April-May 2022 (Figure 11). Nitrate + nitrite concentration was initially 17.9 ± 0.1 µM at SF1 on 5/13/21 during dry weather, decreased to 13.3 ± 0.2 µM on 5/20 after a major flood event, and then increased dramatically to 161.5 ± 0.2 µM on 6/23/21 after a period of dry weather (Figure 12). The opposite pattern was observed at PC1, where

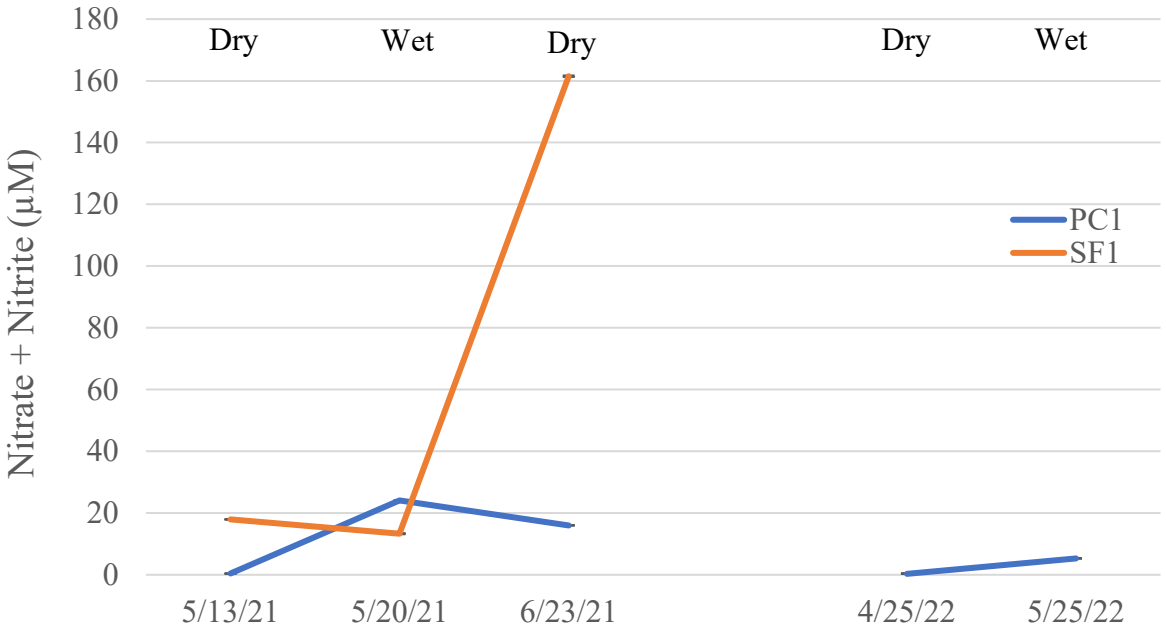

Figure 12. *Temporal variability in Nitrate + Nitrite at downstream creek sites.*

nitrate + nitrite concentrations were initially low during the dry weather sampling on 5/13/21 (0.4 ± 0.0 µM), increased to 24.1 ± 0.1 µM on 5/20/21 after the flood, and then subsequently decreased to 16.0 ± 0.1 µM on 6/23/21 after dry weather. Likewise, during a second sampling event that started 4/25/22 during a dry period, nitrate + nitrate was 0.3 ± 0.2 µM at PC1 but subsequently increased to 5.3 ± 0.1 µM during a post-rain sampling on 5/25/22. DON concentration was initially 102.8 ± 1.8 µM at SF1 on 5/13/21 during dry weather, decreased to 23.4 ± 1.1 µM on 5/20 after a major flood event, and continued to decrease to 6.0 ± 12.9 µM on 6/23/21 after a period of dry weather (Figure 13). A similar pattern was observed at PC1, where DON concentrations were

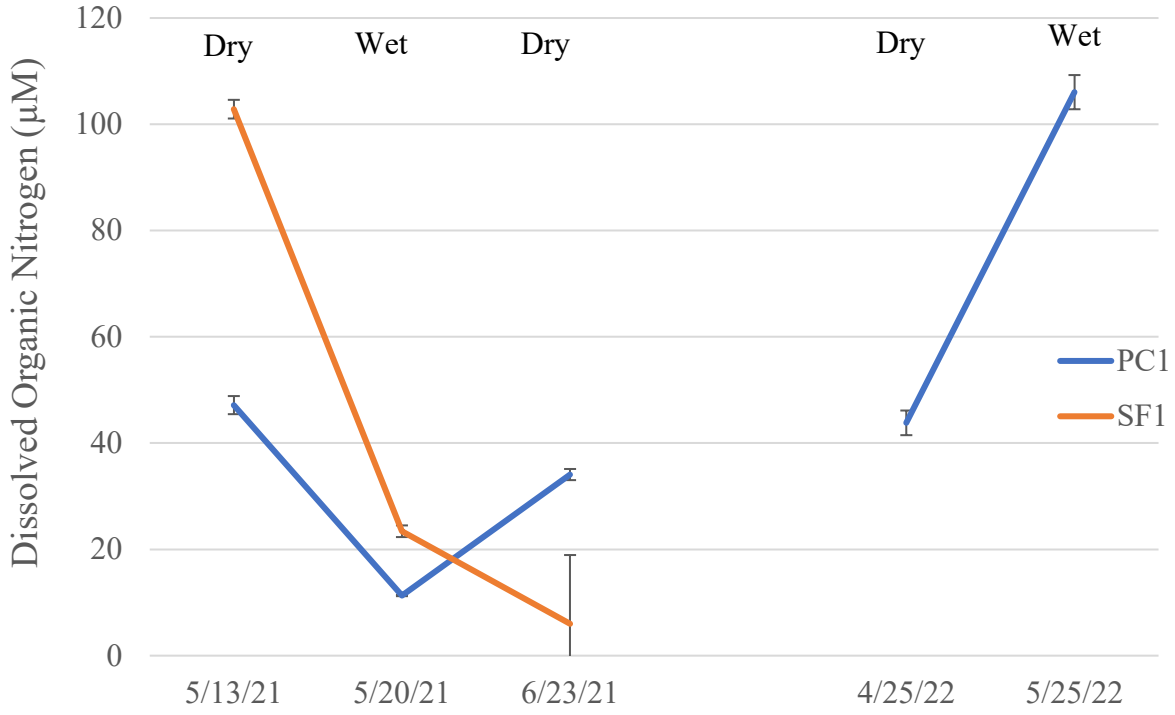

Figure 13. *Temporal variability in DON at downstream creek sites.*

initially 47.2 ± 1.7 µM, decreased to 11.3 ± 0.1 µM after the flood, and then subsequently increased to 34.1 ± 1.1 µM. In contrast, the opposite pattern was observed at PC1 during the second sampling event. On 4/25/22 during a dry period, DON was 43.8 ± 2.3 µM but subsequently increased to 106.1 ± 3.2 µM during a post-rain sampling on 5/25/22. TN concentrations were initially high at SF1 (206.4 ± 0.9 µM) on 5/13/21 during dry weather, decreased dramatically to 57.9 ± 4.1 µM on 5/20 after a major flood event, and then increased to 210.6 ± 15.4 µM on 6/23/21 after a period of dry weather (Figure 14). At PC1, TN concentrations were initially 82.8 ± 1.6 µM on 5/13/21 but decreased thereafter to 68.1 ± 3.6 µM on 5/20/21 after the flood and then to 63.2 ± 13.4 µM by 6/23/21. In contrast, during the second sampling event that started 4/25/22 during a dry period, TN was 70.9 ± 6.3 µM at PC1 but subsequently increased to 173.6 ± 4.0 µM during a post-rain sampling on 5/25/22. Orthophosphate concentrations were initially high at SF1 (41.9 ± 0.0 µM) on 5/13/21 during dry weather, decreased dramatically to 5.4 ± 0.1 µM on 5/20 after a major flood event, and then increased to 55.8 ± 0.5 µM on 6/23/21 after a period of dry weather (Figure 15). At PC1, orthophosphate concentrations were initially low during dry weather (0.2 ± 0.0 µM), then subsequently increased to 3.8 ± 0.0 µM after the flood and continued increasing to 10.1 ± 0.0 µM by 6/23/21. Likewise, during the second sampling event that started 4/25/22 during a dry period,

orthophosphate was 2.2 ± 2.2 µM at PC1 and increased slightly to 3.2 ± 0.3 µM during a post-rain sampling on 5/25/22.

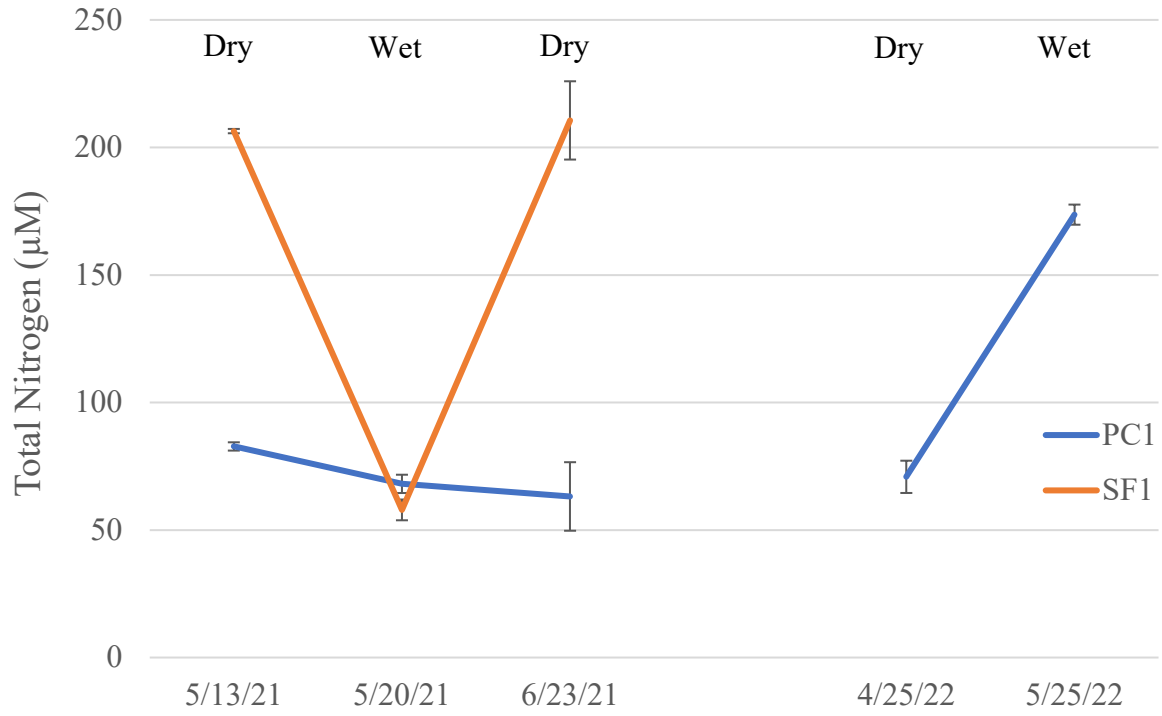

Figure 14. *Temporal variability in TN at downstream creek sites.*

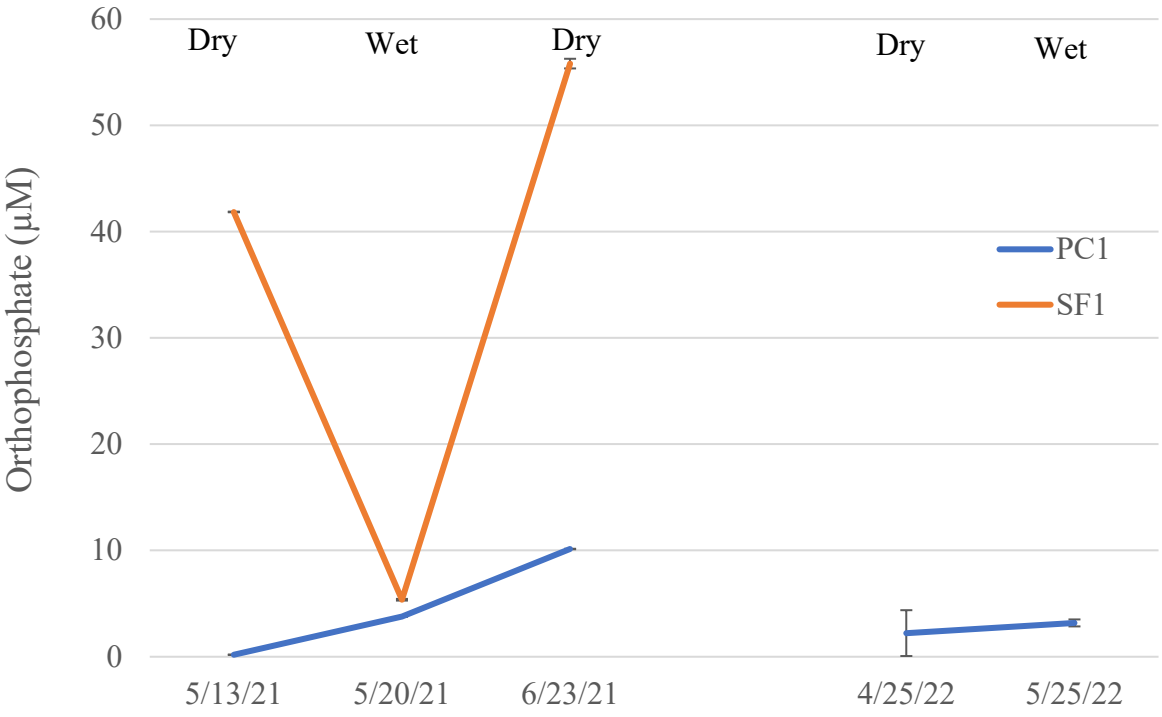

Figure 15. *Temporal variability in orthophosphate at downstream creek sites.*

3.1.2 Spatial and Temporal Variations of tributary NH_4^+ and $\delta^{15}N\text{-}NH_4^+$

Among tributary sites, higher concentrations were found in CDG ($\bar{x}$: 40.7 ± 62.3 µM, n = 51) ($p < 0.05$) while concentrations in LS ($\bar{x}$: 3.3 ± 4.0 µM, n = 7) and AB ($\bar{x}$: 4.1 ± 5.2 µM, n = 20) were not significantly different ($p = 0.7$) (Figure 16). Temporal variations were not detected among tributaries ($p = 0.8$). In Baffin Bay, although spatial variations were not observed ($p = 0.6$), lower surface water concentrations were observed in the dry period ($\bar{x}$: 0.1 ± 0.4 µM, n = 42) than the wet period ($\bar{x}$: 3.5 ± 3.6 µM, n = 78) ($p < 0.05$).

Tributary $\delta^{15}N\text{-}NH_4^+$ values were 46.9 ± 33.3‰ at AB (n = 3), 52.0 ± 64.3‰ at CDG (n = 27), and 1.0‰ at LS (n = 1) without displaying significant spatial ($p = 0.7$) or temporal ($p = 0.6$) variation (Figure 16). Baffin Bay surface $\delta^{15}N\text{-}NH_4^+$ values were 9.7 ± 4.4‰ (n = 36) without displaying significant spatial ($p = 0.7$) or temporal ($p = 1.0$) variations.

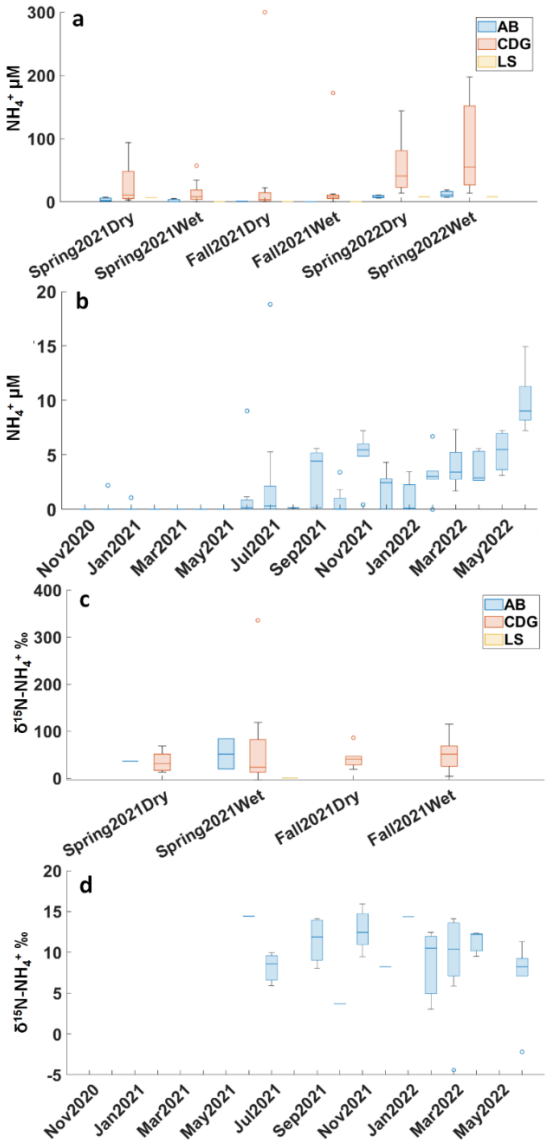

Figure 16. *NH_4^+ concentrations and $\delta^{15}N\text{-}NH_4^+$ values of tributaries (a and c) and Baffin Bay surface water (b and d) over the sampling period.*

3.1.3 Spatial and Temporal Variations of tributary NO_3^- and $\delta^{15}N\text{-}NO_3^-$

Among tributary sites, NO_3^- concentrations were 40.1 ± 60.9 µM at AB (n = 20), 36.9 ± 56.4 µM at CDG (n = 51), and 0.4 ± 0.7 µM at LS (n = 6) (Figure 17). Spatial (p = 0.2) or temporal (p = 0.2) variations were not observed among tributaries. The average NO_3^- concentration of Baffin Bay surface water was 0.7 ± 1.6 µM (n = 120) and did not display significant spatial (p = 0.2) or temporal (p = 0.5) variations.

As Baffin Bay surface water and LS tributary samples did not have samples that exceed isotope method detection limit (3 µM), $\delta^{15}N\text{-}NO_3^-$ values were not available. Values of $\delta^{15}N\text{-}NO_3^-$ in AB ($\bar{x}$: 17.3 ± 5.3‰, n = 8) and CDG ($\bar{x}$: 16.5 ± 8.1‰, n = 24) were not significantly different (p = 0.8) (Figure 17). Temporal isotopic variations were not observed in tributaries (p = 0.1).

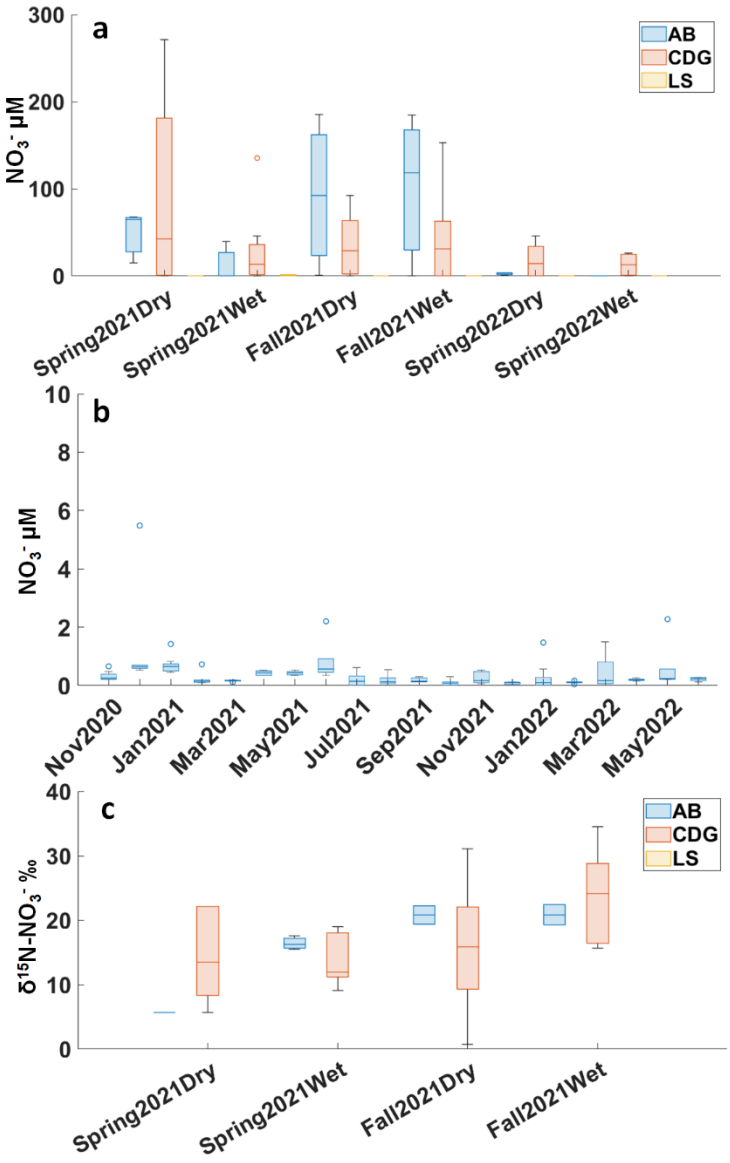

Figure 17. *NO_3^- concentrations and $\delta^{15}N\text{-}NO_3^-$ values of tributaries (a and c) and Baffin Bay surface water (b) over the sampling period.*

3.1.4 Spatial and Temporal Variations of tributary DON and δ^{15}N-DON

Baffin Bay surface water had higher DON concentrations ($\bar{x}$: 56.1 ± 11.0 µM, n = 120) than tributary samples (LS $\bar{x}$: 48.1 ± 15.6 µM, n = 6; AB $\bar{x}$: 43.9 ± 22.8 µM, n = 20; CDG $\bar{x}$: 40.1 ± 44.9 µM, n = 51) ($p < 0.05$) (Figure 18). Tributary DON concentrations did not display significant spatial ($p = 0.8$) or temporal ($p = 0.4$) variations. Baffin Bay surface water had higher DON concentrations during the dry sampling period ($\bar{x}$: 67.3 ± 6.0 µM, n = 42) but lower concentrations during the wet period ($\bar{x}$: 51.5 ± 9.2 µM, n = 78) ($p < 0.05$).

Surface water ($\bar{x}$: 8.2 ± 1.9‰, n = 120) had higher δ^{15}N-DON values than the tributary draining into LS ($\bar{x}$: 6.3 ± 2.7‰, n = 6) ($p < 0.05$) but lower than AB ($\bar{x}$: 12.1 ± 3.2‰, n = 20) and CDG tributaries ($\bar{x}$: 10.1 ± 4.0‰, n = 51) (Figure 18). Higher Baffin Bay surface δ^{15}N-DON values were found in the dry period ($\bar{x}$: 9.5 ± 0.6‰, n = 42) than the wet ($\bar{x}$: 7.2 ± 1.8‰, n = 78) ($p < 0.05$), while higher tributary δ^{15}N-DON values occurred in the wet period ($\bar{x}$: 11.5 ± 3.6‰, n = 30) and lower in the dry ($\bar{x}$: 8.8 ± 3.9‰, n = 24) ($p < 0.05$).

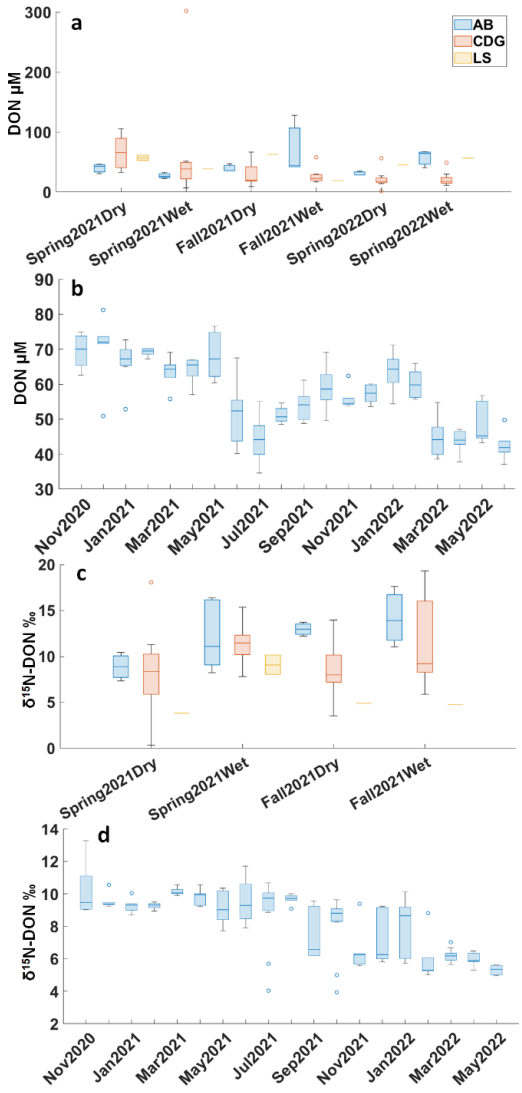

Figure 18. *DON concentrations and δ^{15}N-DON values of tributaries (a and c) and Baffin Bay surface water (b and d) over the sampling period.*

3.1.5 DON and NO_3^- Source Apportionments

The results of DON mixing model indicated allochthonous and autochthonous sources contributed ~60-70% and ~30-40% of DON, respectively, in the BB surface water for the duration of the study (Figure 19). Higher wastewater (dry: 12 ± 10%; wet: 15 ± 11%) and manure (dry: 20 ± 15%; wet: 30 ± 20%) contributions were found in the wet period ($p < 0.05$) while higher wet deposition (dry: 29 ± 20%; wet: 25 ± 18%) and PON (dry: 39 ± 24%; wet: 31 ± 20%) contributions were found in the dry period ($p < 0.05$).

In tributaries, allochthonous and autochthonous sources contributed ~60-80% and ~20-40% of DON, respectively (Figure 19). Higher wastewater (dry: ~10-20%; wet: ~20-30%) contributions were found in the wet period at AB, CDG and LS ($p < 0.05$) while higher wet deposition contributions (dry: ~30-50%; wet: ~25%) were observed in the dry period at CDG and LS ($p < 0.05$). The contribution of wet deposition at AB (dry: 24 ± 18%; wet: 24 ± 18%) during the dry period was not significantly different from the wet period ($p = 0.3$). Manure had higher contributions during the wet period at CDG (dry: 23 ± 16%; wet: 25 ± 18%) and LS (dry: 14 ± 10%; wet: 30 ± 21%) ($p < 0.05$) while higher manure contributions were observed during the dry period at AB (dry: 33 ± 23%; wet: 25 ± 17%) ($p < 0.05$). PON contributions were higher in the wet period at LS (dry: 26 ± 22%; wet: 29 ± 19%) ($p < 0.05$) while were higher in the dry period at AB (dry: 26 ± 18%; wet: 19 ± 13%) and CDG (dry: 37 ± 22%; wet: 20 ± 14%) ($p < 0.05$).

Wastewater NH_4^+ was the dominant NO_3^- source in both AB and CDG during both the dry (AB: 78 ± 8%; CDG: 67 ± 11%) and wet period (AB: 73 ± 9%; CDG: 78 ± 8%) (Figure 20).

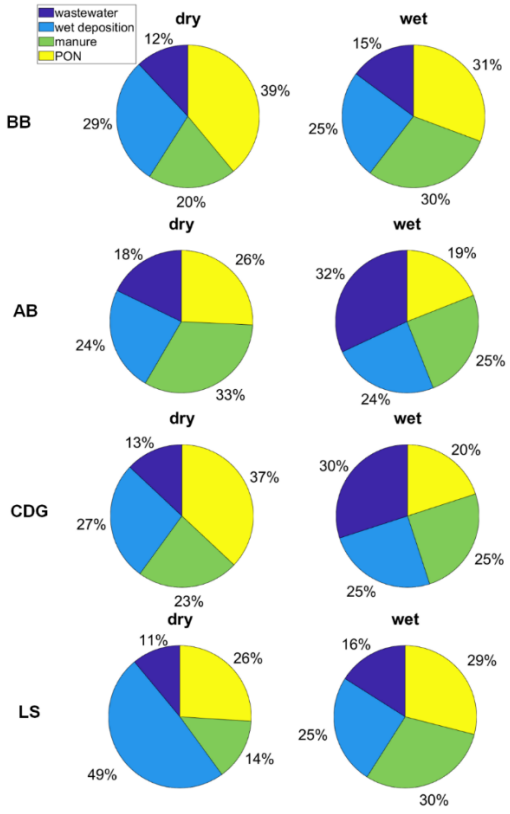

Figure 19. *The DON source apportionments of Baffin Bay and tributaries draining into AB, CDG and LS during the dry/wet periods.*

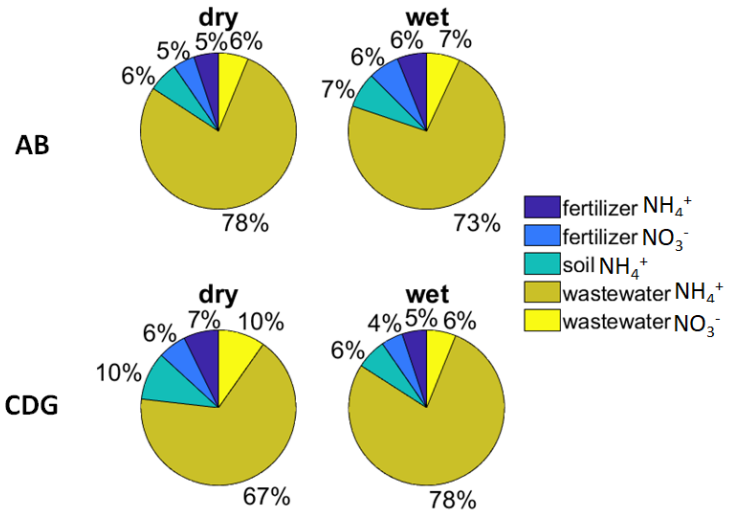

Figure 20. *The NO_3^- source apportionments of tributaries draining into AB and CDG during the dry/wet periods.*

3.2 Airshed

3.2.1 NH_4^+ concentration, isotope, and source apportionment variation

The VWM and arithmetic average NH_4^+ concentration during the sampling period were 17.9 and 26.9 ± 30.9 µM (n = 51), respectively, with both higher in winter (12.9 and 29.1 ± 16.5 µM, n = 16) and spring (34.6 and 45.8 ± 45.4 µM, n = 16) and lower in summer (5.7 and 9.6 ± 6.9 µM, n = 12) and fall (6.9 and 8.6 ± 7.2 µM, n = 7) ($p < 0.05$) (Figure 10). Mixed events (10.9 and 51.5 ± 66.4 µM, n = 7) had lower VWM but higher arithmetic average concentrations than marine (18.7 and 18.3 ± 18.2 µM, n = 35) and continental events (38.6 and 41.3 ± 12.2 µM, n = 9) ($p < 0.05$). Lower VWM and arithmetic average NH_4^+ concentrations were observed in the NA group (11.2 and 18.6 ± 15.7 µM, n = 33) compared to the BB group (32.9 and 42.2 ± 44.2 µM, n = 18) ($p < 0.05$). The annual NH_4^+ wet deposition flux was 2.4 kg N/(ha*yr) (Table 5). The VWM and arithmetic average $\delta^{15}N\text{-}NH_4^+$ during the sampling period was -3.8‰ and -3.1 ± 4.0‰ (n = 42), respectively. The $\delta^{15}N\text{-}NH_4^+$ values did not vary insignificantly between seasons ($p = 0.4$), event type ($p = 0.1$) or groups ($p = 0.6$) (Figure 21).

Table 5. *Annual wet deposition flux of NH_4^+, NO_3^-, and DON.*

	NH_4^+	NO_3^-	DON
Annual wet deposition flux (kg N/(ha*yr))	2.4	1.3	1.5

The isotope mixing model results indicated higher vehicle contribution to NH_3 than agriculture in winter (vehicle: 48 ± 15%; fertilizer + livestock waste: 37 ± 11%) ($p < 0.05$) and summer (vehicle: 61 ± 14%; fertilizer + livestock waste: 34 ± 11%) ($p < 0.05$), and higher agriculture contribution to NH_3 than the vehicle in fall (vehicle: 44 ± 15%; fertilizer + livestock waste: 47 ± 13%) ($p < 0.05$) (Figure 22). While vehicle and agriculture contributions were not significantly different in spring (vehicle: 42 ± 16%; fertilizer + livestock waste: 42 ± 13%) ($p = 0.9$), higher biomass burning contributions were found in winter (15 ± 8%) and spring (16 ± 8%) compared to summer (5 ± 3%) and fall (9 ± 4%) ($p < 0.05$). Among event types, the lowest agriculture contribution was observed

in marine events (fertilizer + livestock waste: 38 ± 11%) ($p < 0.05$). In comparison, the highest agriculture (fertilizer + livestock waste: 47 ± 14%) and the lowest biomass burning contributions (8 ± 5%) were found in continental events ($p < 0.05$). The most prevalent source in the NA group was vehicle (60 ± 13%) and agriculture was the dominant source in the BB group (fertilizer + livestock waste: 40 ± 12%).

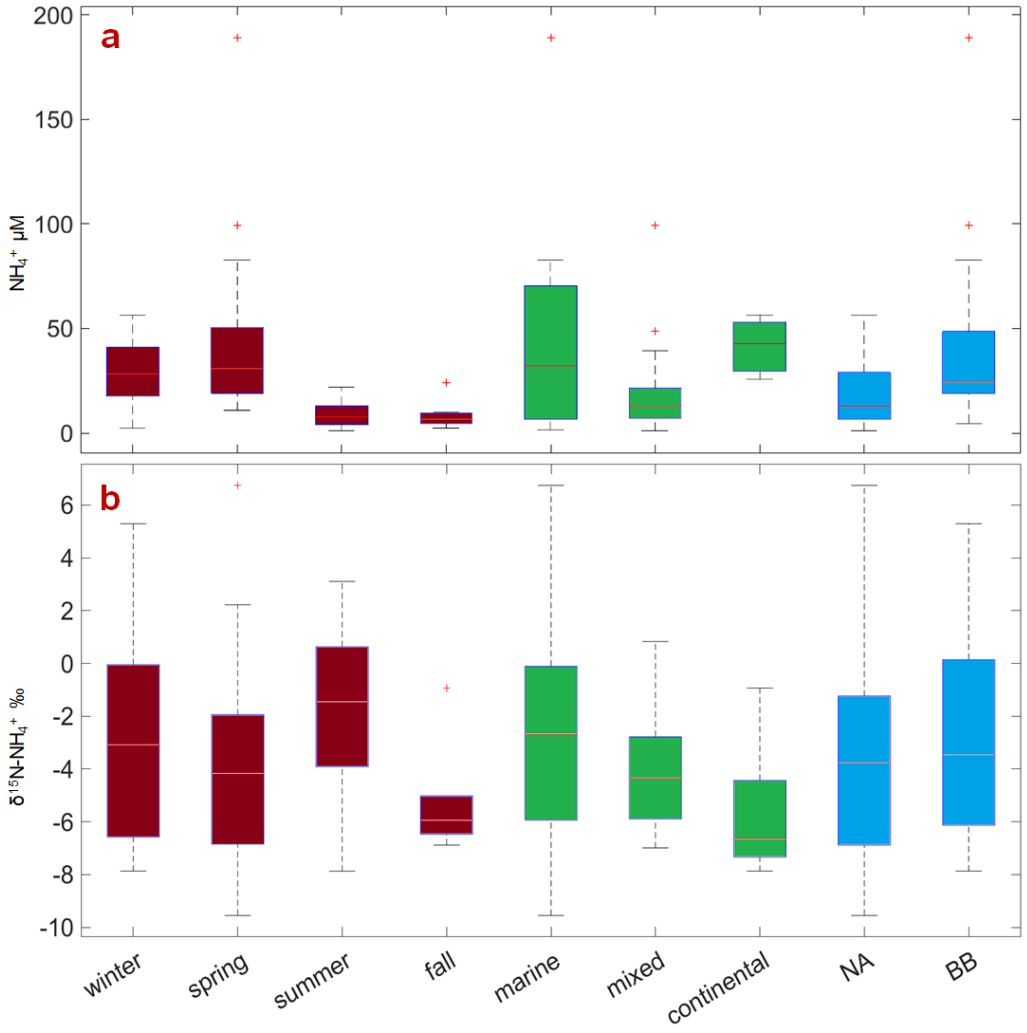

Figure 21. *Variations of NH_4^+ concentrations (a) and $\delta^{15}N\text{-}NH_4^+$ values (b) between seasons (red), event types (green), and source groups (blue). Winter refers to December, January, and February. Spring refers to March, April, and May. Summer refers to June, July, and August. Fall refers to September, October, and November. Marine refers to events with airmasses transported over the Gulf of Mexico. Mixed refers to events with airmasses transported over both continental and marine areas. Continental refers to events with airmasses transported over continental regions. NA refers to events that were not affected by biomass burning emissions. BB refers to events that were influenced by biomass burning emissions.*

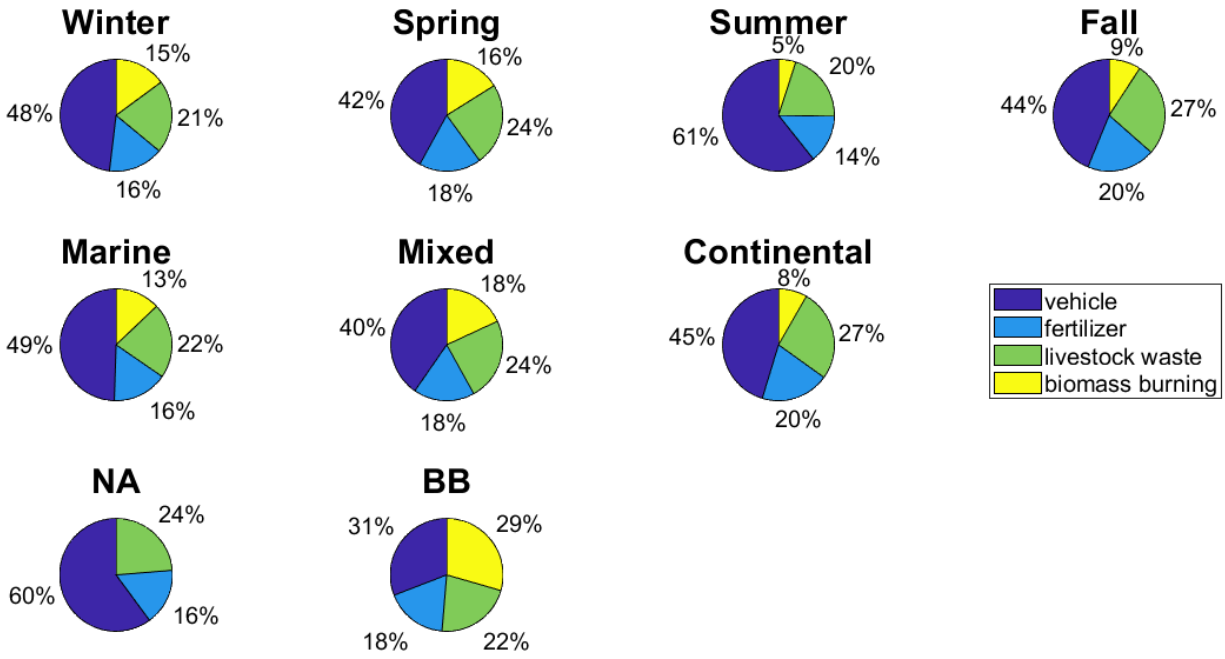

Figure 22. *NH_4^+ source apportionments in wet deposition. Winter refers to events in December, January, and February. Spring refers to events in March, April, and May. Summer refers to events in June, July, and August. Fall refers to events that happened in September, October, and November. Marine refers to events with airmasses transported over the Gulf of Mexico. Mixed refers to events with airmasses transported over both continental and marine areas. Continental refers to events with airmasses transported over continental areas. NA refers to events that were not affected by biomass burning emissions. BB refers to events that were influenced by biomass burning emissions.*

3.2.2 NO_3^- concentration, isotope, and source apportionment variation

The VWM and arithmetic average of NO_3^- concentrations were 9.7 and 17.4 ± 20.2 µM (n = 51), respectively. While NO_3^- concentrations did not exhibit significant seasonal variation ($p = 0.5$), higher VWM was observed in continental events (26.2, n = 9) compared to marine (9.9, n = 35) and mixed (6.2, n = 7) events (Figure 23). Among the groups, the highest VWM and arithmetic average NO_3^- concentration was found in the BB group (22.5 and 27.9 ± 21.1 µM, n = 7), followed by the LBB (10.7 and 26.6 ± 32.6 µM, n = 11) ($p < 0.05$) (Figure 23). The annual NO_3^- wet deposition flux was 1.3 kg N/(ha*yr) (Table 5).

Spring displayed the highest $\delta^{15}N\text{-}NO_3^-$ (1.7‰ and 0.4 ± 4.6‰, n = 16) ($p < 0.05$) and the lowest $\delta^{18}O\text{-}NO_3^-$ (57.4‰ and 61.2 ± 9.0‰, n = 16) though not significantly ($p = 0.1$) among seasons (Figure 23). Winter had lower $\delta^{15}N\text{-}NO_3^-$ (-3.6‰ and -3.3 ± 1.9‰, n = 12) ($p < 0.05$) than spring and the highest $\delta^{18}O\text{-}NO_3^-$ (71.6‰ and 71.3 ± 6.0‰, n = 12) ($p < 0.05$). $\delta^{15}N\text{-}NO_3^-$ did not exhibit significant differences among continental, mixed, and marine events ($p = 0.2$). While the highest $\delta^{18}O\text{-}NO_3^-$ (71.8‰ and 70.8 ± 7.4‰, n = 8) was found in continental events ($p < 0.05$). Although the arithmetic average $\delta^{18}O\text{-}NO_3^-$ values of the mixed (62.9 ± 10.1‰, n = 6) and the marine events (63.3 ± 6.5‰, n = 30) were not significantly different, the lowest VWM $\delta^{18}O\text{-}NO_3^-$ was found in the mixed events (54.1‰, n = 6). Among the groups, higher VWM $\delta^{15}N\text{-}NO_3^-$ (0.3‰, n = 22) and lower VWM $\delta^{18}O\text{-}NO_3^-$ (57.6‰, n = 22) were measured in the L group.

The isotope mixing model indicated that seasonally winter (biomass burning: 19 ± 11%; lightning: 15 ± 10%) and spring (biomass burning: 23 ± 13%; lightning: 17 ± 12%) had higher biomass burning contributions compared with summer (biomass burning: 2 ± 2%; lightning: 33 ± 20%) and fall (biomass burning: 10 ± 5%; lightning: 39 ± 18%) ($p < 0.05$), which displayed higher lightning contributions ($p < 0.05$) (Figure 24). Summer also had the highest soil "biogenic" emissions (10 ± 7%) ($p < 0.05$). Among event types, continental events had the highest lightning contribution (30 ± 19%) ($p < 0.05$). Among groups, the NA group (77 ± 11%) had the highest vehicle contribution followed by the L group (45 ± 22%) ($p < 0.05$). BB (45 ± 24%) while the LBB (33 ± 20%) group had biomass burning as the primary NO_3^- contributor.

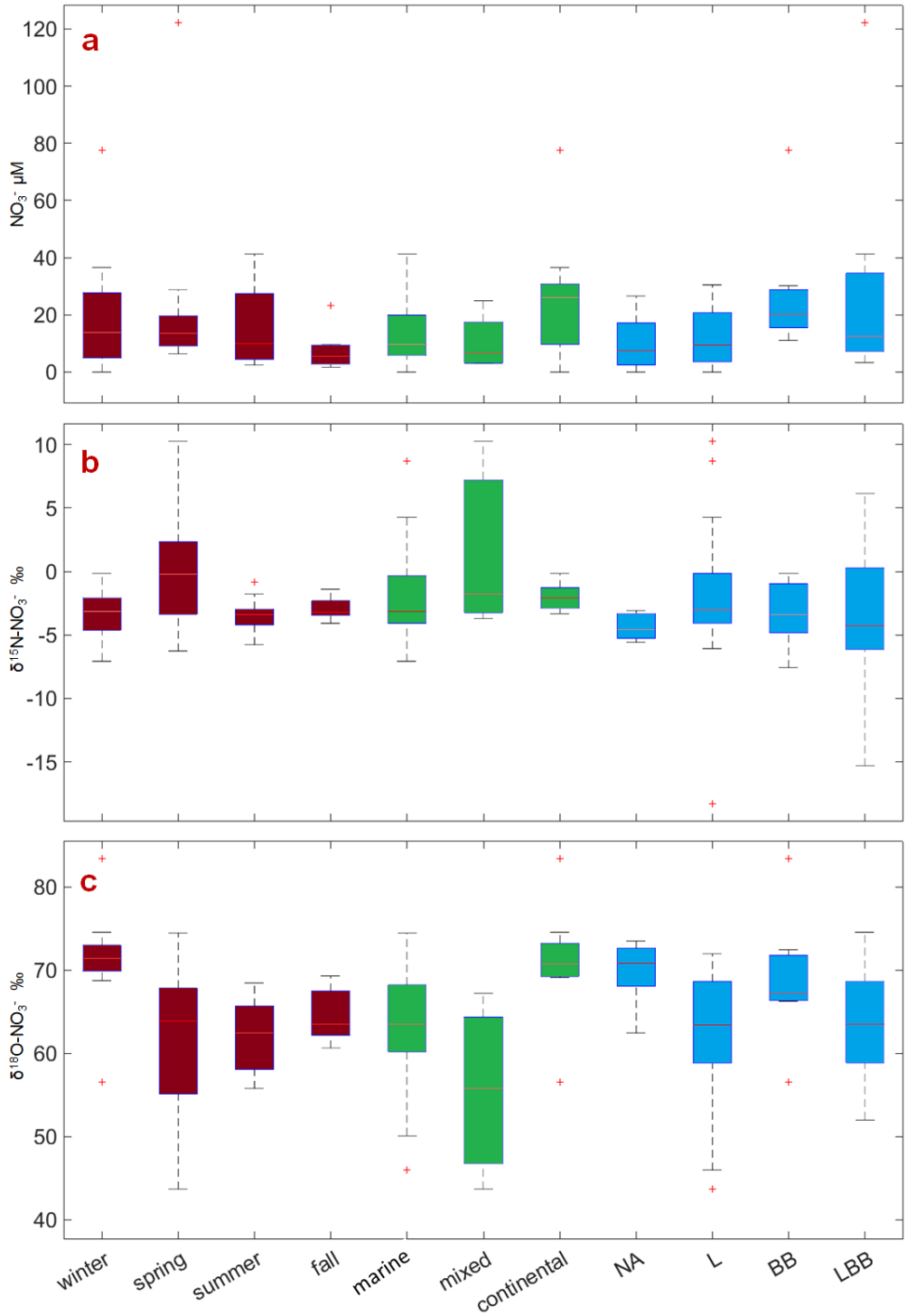

Figure 23. *NO_3^- concentrations (a), $\delta^{15}N$-NO_3^- (b), and $\delta^{18}O$-NO_3^- (c) variations between seasons (red), event types (green), and source groups (blue). Winter refers to December, January and February. Spring refers to March, April and May. Summer refers to June, July and August. Fall refers to September, October and November. Marine refers to airmasses transported over the Gulf of Mexico. Mixed refers to airmasses transported over both continental and marine areas. Continental refers to airmasses transported over continental areas. NA refers to events that were*

not affected by either lightning or biomass burning emissions. L refers to events that were affected by lightning emissions. BB refers to events that were influenced by biomass burning emissions. LBB refers to events influenced by lightning and biomass burning emissions.

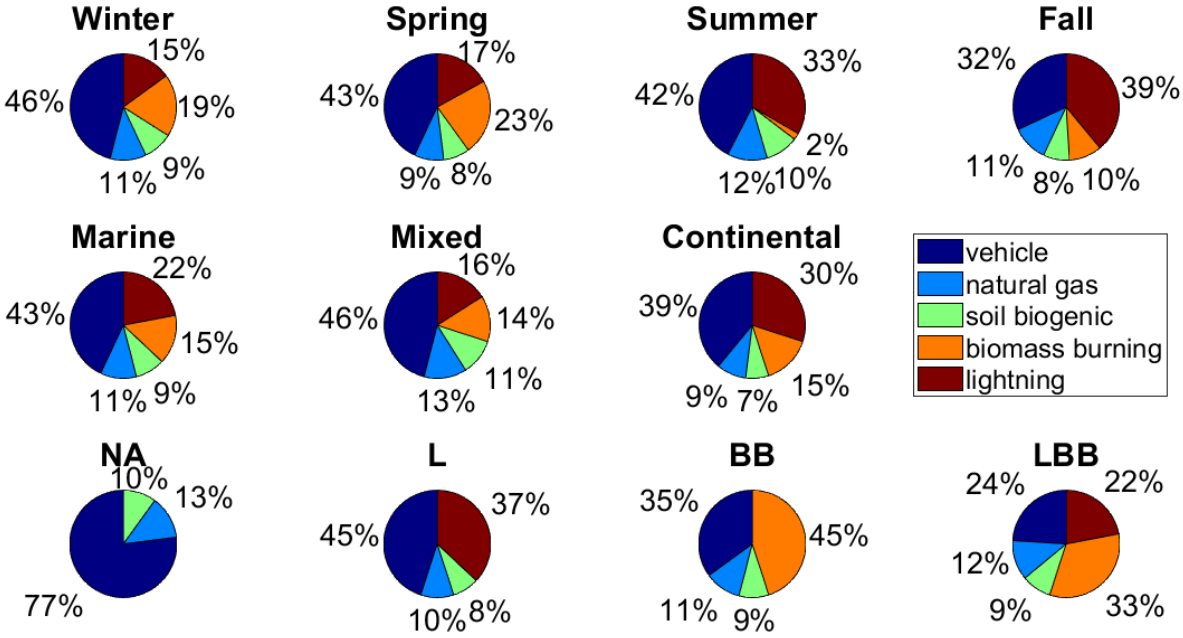

Figure 24. *NO_3^- source apportionments in wet deposition. Winter refers to December, January and February. Spring refers to March, April and May. Summer refers to June, July and August. Fall refers to September, October and November. Marine refers to airmasses transported over the Gulf of Mexico. Mixed refers to airmasses transported over both continental and marine areas. Continental refers to airmasses transported over continental areas. NA refers to events that were not affected by either lightning or biomass burning emissions. L refers to events that were affected by lightning emissions. BB refers to events that were influenced by biomass burning emissions. LBB refers to events influenced by lightning and biomass burning emissions.*

3.2.3 DON concentration, isotope, and source apportionment variation

The DON concentration ranged from below detection limit to 35.8 μM with a VWM and arithmetic average of 11.5 and 10.6 ± 7.6 μM (n = 42), respectively. Although arithmetic average DON concentration did not display significant seasonal variation ($p = 0.2$), the highest and lowest VWM DON concentration were observed in spring (16.1 μM, n = 13) and fall (7.6 μM, n = 7), respectively (Figure 25). Although significant variations of arithmetic average DON concentration were also not observed among marine, continental, and mixed events ($p = 0.1$), continental events exhibited the highest VWM DON concentration (18.7 μM, n = 6). The DON concentration of the NA group (11.3 μM and 12.0 ± 7.8 μM, n = 28) was not significantly different from the BB group (12.0 μM and 8.6 ± 6.4 μM, n = 14) ($p = 0.2$). The annual DON wet deposition flux was 1.5 kg N/(ha*yr) (Table 5).

The δ^{15}N-DON ranged from -7.3 to 17.5‰ with a VWM and arithmetic average of 10.6‰ and 8.5 ± 5.3‰ (n = 36), respectively. Higher δ^{15}N-DON values were found in summer (12.6 and 12.7 ± 3.6 ‰, n = 9) and fall (11.8‰ and 10.4 ± 4.6‰, n = 7) than winter (9.1‰ and 4.6 ± 5.5‰, n = 10) and spring (8.2‰ and 7.2 ± 3.6‰, n = 10) ($p < 0.05$) (Figure 25). Marine (10.6‰ and 9.7 ± 4.4‰,

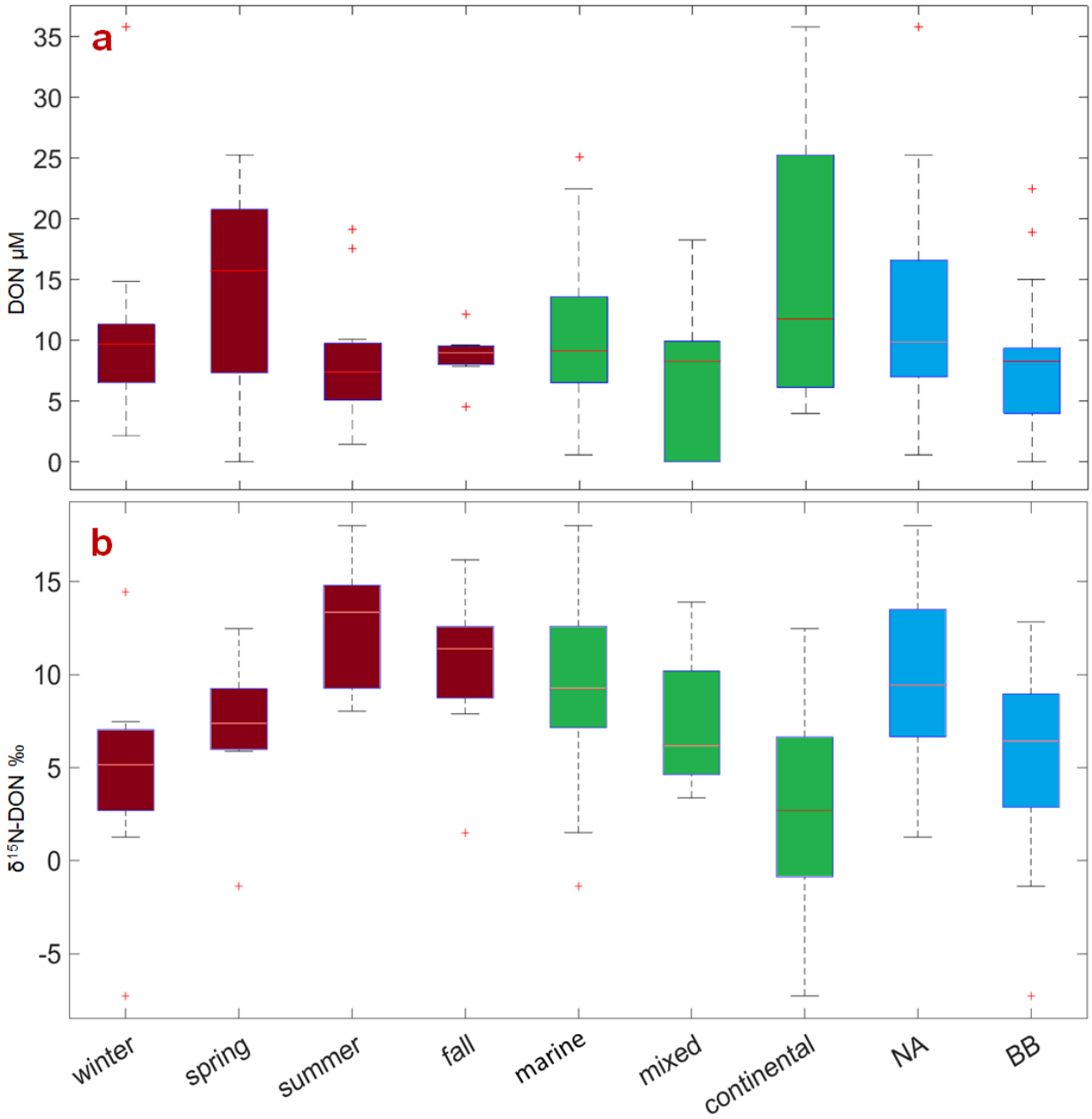

Figure 25. *DON concentrations (a) and δ^{15}N-DON (b) variations between seasons (red), event types (green), and source groups (blue). Winter refers to events in December, January, and February. Spring refers to events in March, April, and May. Summer refers to events in June, July, and August. Fall refers to events happened in September, October, and November. Marine refers to events with airmasses transported over the Gulf of Mexico. Mixed refers to events with airmasses transported over both continental and marine areas. Continental refers to events with airmasses transported over continental areas. NA refers to events that were not affected by biomass burning emissions. BB refers to events that were influenced by biomass burning emissions.*

n = 27) and mixed (11.4‰ and 7.4 ± 4.5‰, n = 4) events both displayed higher δ^{15}N-DON than continental events (5.8‰ and 2.8 ± 7.1‰, n = 5) ($p < 0.05$). The δ^{15}N-DON of the NA group (11.1‰ and 9.8 ± 4.5‰, n = 25) was higher than the BB group (9.1‰ and 5.3 ± 5.8‰, n = 11) ($p < 0.05$).

Overall, the isotope mixing model results suggested vehicle (36 ± 14%) was the dominant DON source followed by marine (32 ± 18%), fertilizer (24 ± 4%), and biomass burning (8 ± 3%). Fertilizer and biomass burning contributions were significantly higher in winter (fertilizer: 36 ± 6%; biomass burning: 20 ± 6%) and spring (fertilizer: 30 ± 5%; biomass burning: 8 ± 4%) than summer (fertilizer: 9 ± 1%; biomass burning: 0%) and fall (fertilizer: 18 ± 2%; biomass burning: <1%) (Figure 26). Marine (52 ± 25%) and vehicle (59 ± 17%) exhibited the highest contribution in summer and fall, respectively. Among event types, marine (37 ± 19%) and mixed (31 ± 21%) events displayed higher marine contribution than continental (9 ± 5%) events. In NA group, vehicle (38 ± 16%) and marine (38 ± 20%) were the two primary DON sources. While marine contribution (18 ± 11%) decreased significantly in BB group, in which vehicle (31 ± 10%) was the dominant DON source.

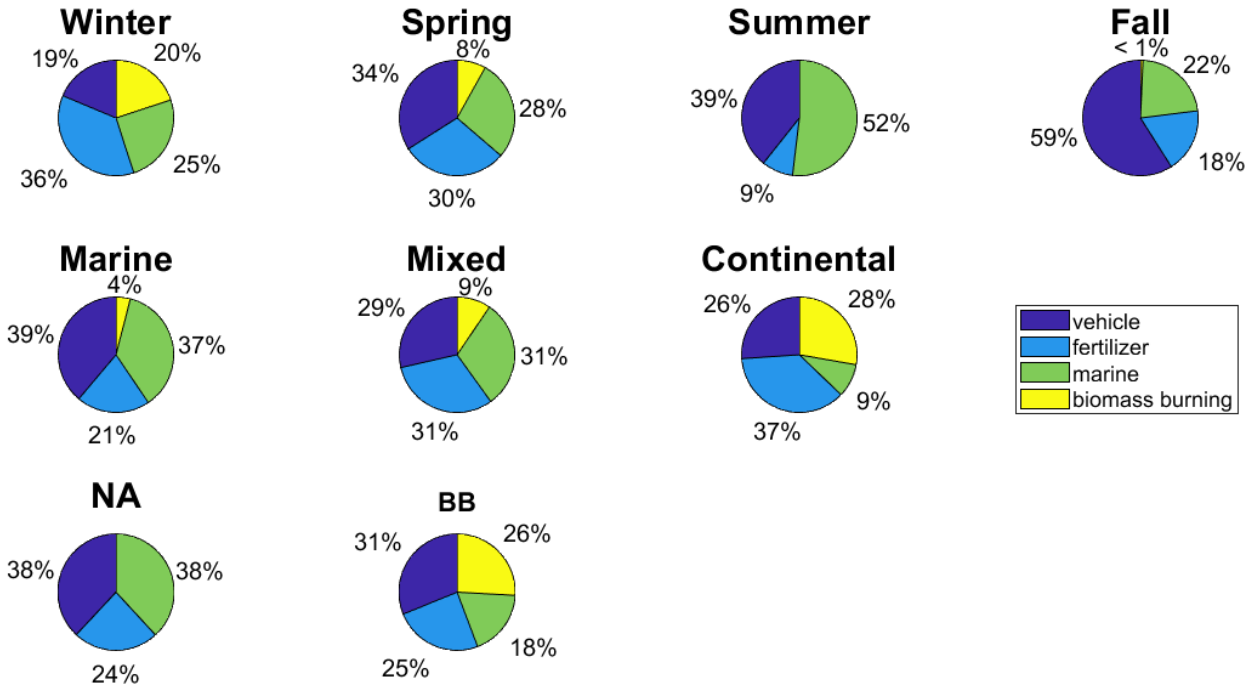

Figure 26. *DON source apportionments in wet deposition. Winter refers to December, January, and February. Spring refers to March, April, and May. Summer refers to June, July, and August. Fall refers to September, October, and November. Marine refers to events with airmasses transported over the Gulf of Mexico. Mixed refers to events with airmasses transported over both continental and marine areas. Continental refers to events with airmasses transported over continental areas. NA refers to events that were not affected by biomass burning emissions. BB refers to events that were influenced by biomass burning emissions.*

4. Discussion

This task utilized two complementary approaches to quantify potential nutrient sources to Baffin Bay via surface waters and atmospheric deposition. The first approach involved high spatial resolution sampling of nutrient indicators from watershed creeks under dry and wet conditions. This approach was complemented by isotope source tracking to hone in on the dominant nitrogen sources.

4.1. Spatial-temporal distribution of nutrients in the Baffin Bay watershed

Results from the spatial mapping of watershed creek nutrient indicators highlighted several locations of concern. For example, nearly all of the nutrient indicators were notably high and/or exceeded screening levels for impairment at sites SF3 and SG1, both of which are downstream of municipal wastewater treatment facilities. Likewise, TN was very high at SF5, SF4, JC1 and LS1. SF5 and SF4 are both also downstream of municipal and/or industrial wastewater treatment facilities. LS1 is still tidal, often seeing very high salinities. Thus it is difficult to know whether the high TN values observed there are from internal production (i.e., algal biomass which was high, release from sediments) or external sources. It is worth noting that LS1 is downstream of a wastewater plant outfall, but there has been anecdotal evidence that bat guano may also contribute to nitrogen there. JC1 was an abnormal site in the sense that it is frequently choked, i.e., it does not connect directly with Baffin Bay unless heavy rains occur. It is also unclear what the potential nutrient sources to it might be.

Nutrient indicators displayed considerable temporal variability that was linked to the presence or absence of previous rainfall. Coincidentally, this variability provides an additional glimpse into the dominant nutrient sources to the two main tributary creeks, Petronila and San Fernando Creek. For example, during the May-June 2021 sampling in San Fernando Creek, there was a consistent pattern of decreasing concentrations of ammonium, N+N, DON, TN and orthophosphate during wet/high rainfall conditions, which suggests that there was a dilution effect occurring. Typically this would also indicate dominance of the nutrients in the creek by point sources (as opposed to non-point sources). In contrast, several of the nutrient indicators (ammonium, N+N, orthophosphate) increased in Petronila Creek during wet/high rainfall conditions, suggestive of non-point sources. Less clear were impacts of rainfall on DON and TN in Petronila Creek, as during one event both decreased with rainfall, while during a second event they increased. This perhaps indicates that a mix of point and non-point sources contribute to nutrient loads to Petronila Creek.

4.2.1 NH_4^+ processing and sources in Baffin Bay and tributaries

Tributary LS (3.3 ± 4.0 μM) and AB (4.1 ± 5.2 μM) both had low NH_4^+ concentrations (Figure 16). LS only had one $\delta^{15}N\text{-}NH_4^+$ value (1.0‰) available (Figure 16), which resembled the reported fertilizer isotope signature (Nikolenko et al., 2018). The single data point does not allow for determining possible processing to further confirm the NH_4^+ source. AB had higher $\delta^{15}N\text{-}NH_4^+$ values (46.9 ± 33.3‰) presumably indicating nitrification and assimilation. Like in LS, AB only had a few (n =3) $\delta^{15}N\text{-}NH_4^+$ data available. The lack of $\delta^{15}N\text{-}NH_4^+$ data and correlation of $\delta^{15}N\text{-}NH_4^+$ to $NH_4^+/\ln[NH_4^+]$ prevented further NH_4^+ source identification. Nevertheless, CDG had higher NH_4^+ concentrations (40.7 ± 62.3 μM) and $\delta^{15}N\text{-}NH_4^+$ values (52.0 ± 64.3‰) (Figure 5). The high $\delta^{15}N\text{-}NH_4^+$ values (52.0 ± 64.3‰) might be a result of nitrification. However, some samples with high $\delta^{15}N\text{-}NH_4^+$ values had relatively low NH_4^+ concentrations that were ~10% of NO_3^- and the sensitivity test indicated if there was a 0.2‰ increase/decrease on the measured $\delta^{15}N\text{-}NO_3$, which was the systematic error for the isotope analysis, the back calculated $\delta^{15}N\text{-}NH_4^+$ values would fluctuate up to 10%. This fluctuation could make our observed $\delta^{15}N\text{-}NH_4^+$ higher than the actual values. CDG NH_4^+ concentrations had significant negative correlations with $\ln[NO_3^-]$ in both dry and wet periods (Figure 27), suggesting nitrification may significantly affect the concentration variations of NH_4^+ and NO_3^-. This was consistent with NO_3^- mixing model results

that nitrification of fertilizer and wastewater derived NH_4^+ contributed to over 70% of NO_3^- in CDG (Figure 20).

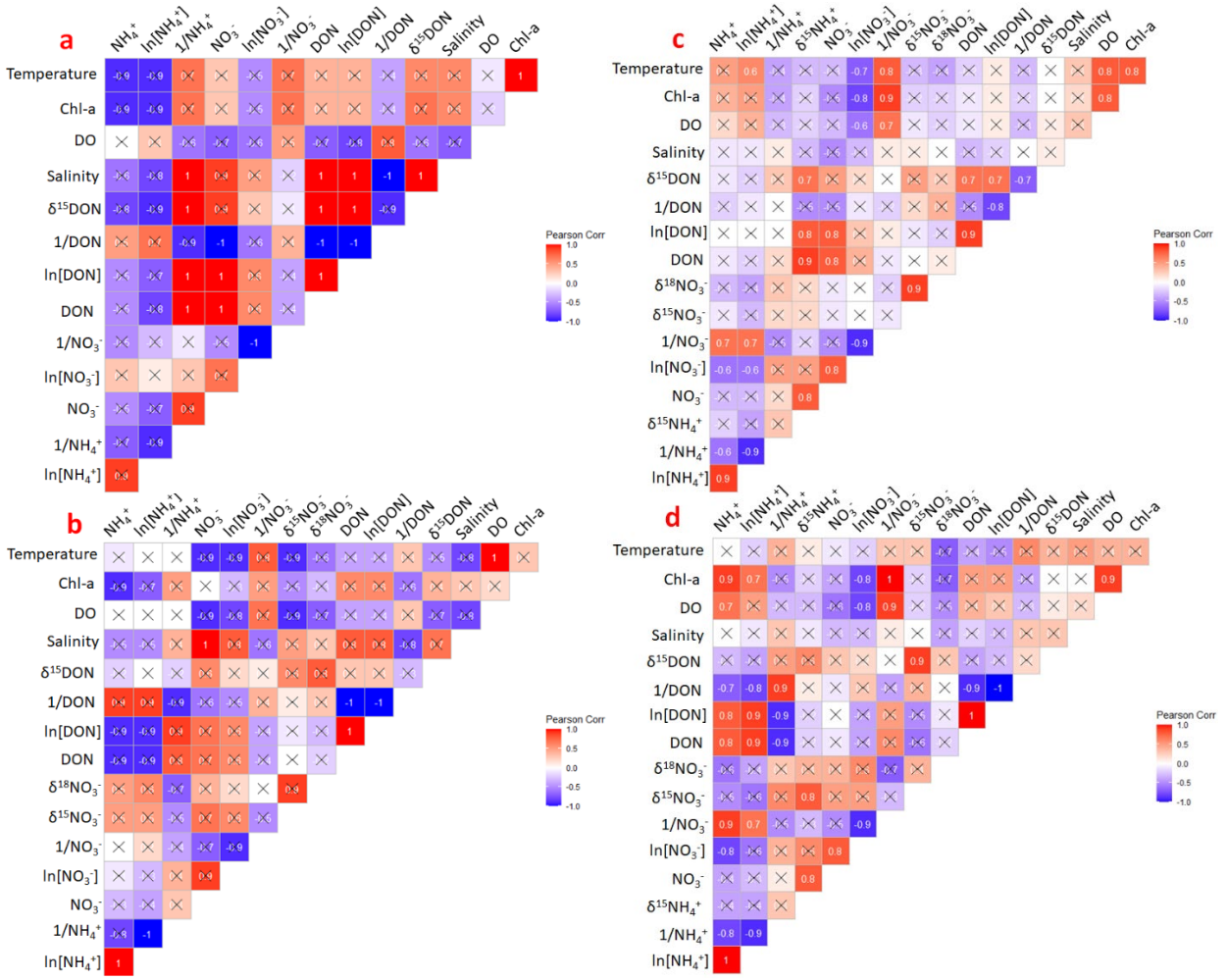

Figure 27. *Correlation heatmaps of tributary AB (dry: a; wet: b) and CDG (dry: c; wet: d). p value <0.05 indicates a significant correlation. When it is not significant, the correlation value is marked with the black cross.*

Baffin Bay surface water displayed higher NH_4^+ concentrations in the wet period (3.5 ± 3.6 μM) ($p < 0.05$) when more nutrients were delivered to the bay via wet deposition and surface/subsurface flow (Figure 16). The NH_4^+ flux at the water-sediment interface was assumed to be substantial because porewater is typically an important NH_4^+ source. However, the long residence time in arid/semi-arid estuaries led to the extended processing and prolonged mixing in Baffin Bay, which let the phytoplankton-favored N form (i.e., NH_4^+) be preferentially and substantially utilized. The growth cycle of phytoplankton further made NH_4^+ either stored in the sediment as NH_4^+/PON/DON or recirculated back to the surface water as NH_4^+/DON, presumably resulting in the low NH_4^+ but high DON concentrations in Baffin Bay surface water (Figure 16 and 18).

4.2.2 NO_3^- processing and sources in Baffin Bay and tributaries

Baffin Bay surface water (0.7 ± 1.6 μM) and tributary LS (0.4 ± 0.7 μM) have low NO_3^- concentrations and did not display temporal variations (Baffin Bay surface water $p = 0.5$; tributary LS $p = 0.2$) (Figure 17). High NO_3^- concentrations have been found in tributary AB (40.1 ± 60.9 μM) and CDG (36.9 ± 56.4 μM). Tributary AB and CDG had high $\delta^{15}N\text{-}NO_3^-$ (AB: 17.3 ± 5.3‰ and CDG: 16.5 ± 8.1‰) values, which could be a result of coupled nitrification and denitrification. A five-endmember NO_3^- dual stable isotope mixing model was built for tributary AB and CDG (Table 3) and the results found AB and CDG received the highest NO_3^- contribution from the nitrification of wastewater NH_4^+ (AB $\bar{x}$: 76 ± 9%; CDG $\bar{x}$: 73 ± 10%) (Figure 20). Both creeks receive effluent from municipal wastewater treatment facilities, although the permitted discharge to CDG is about an order of magnitude higher than to AB. Nonetheless, there are also numerous colonias that lack proper sewage treatment located in and around Petronila Creek (AB).

4.2.3 DON processing and sources in Baffin Bay and tributaries

Baffin Bay surface water had lower DON concentrations in the wet period (51.9 ± 8.2 μM) (Figure 18). However, this did not mean less nitrogen was discharged to the bay. Instead, increased rainfall would recharge the water table, and raise riverine discharge rate and runoff, which could bring more nitrogen into estuaries. It was the high freshwater input following the rainfall that diluted the concentrations and decreased the residence time in the wet period. The increased rainfall with relatively low wet deposition $\delta^{15}N\text{-}DON$ (5.0 ± 5.5‰) (Russell et al., 1998) was presumed to be one of the factors decreasing the $\delta^{15}N\text{-}DON$ value of Baffin Bay surface water during the wet period (7.2 ± 1.8‰) (Figure 7). The linear correlation between surface water $\delta^{15}N\text{-}DON$ and ln[DON] was observed in the dry period with a slope of -4.2 ($p < 0.05$) (Figure 4), indicating $\delta^{15}N\text{-}DON$ increased when DON concentration decreased with a fractionation factor of ~4.2‰, which was similar to the few reported isotope effects associated with DON consumption (4.9 to 6.9‰) (Knapp et al., 2018; Qiu et al., in prep-b; Thibodeau et al., 2017; Westbrook, 2021; Zhang et al., 2020). However, in the wet period, there was no significant correlation indicating DON consumption (e.g., $\delta^{15}N\text{-}DON$ versus ln[DON]) ($p = 0.9$), possibly due to the extensive source mixing and flushing following the increased rainfall and surface/subsurface runoff that masked the signal of DON consumption.

Tributaries displayed higher $\delta^{15}N\text{-}DON$ in wet periods (Figure 18). This was consistent with their higher wet period wastewater DON contribution (Figure 19), which was reported to have high $\delta^{15}N\text{-}DON/TDN$ (Curt et al., 2004; Qiu et al., in prep-b). In dry periods, tributaries had a significant positive-correlation between $\delta^{15}N\text{-}DON$ and ln[DON] (Figure 4), presumably indicating coupled PON and DON mineralization. Dry periods received limited rainfall and possibly had stratified water columns, which was reported to favor mineralization (Hou et al., 2021). Coupled PON and DON mineralization could increase the DON pool and was reported to increase the residual $\delta^{15}N\text{-}DON$ by 3-5‰ (Sigman and Fripiat, 2019). The linear correlation of $\delta^{15}N\text{-}DON$: ln[DON] had a slope of 2.6, suggesting a DON fractionation factor of 2.6‰, which was consistent with the reported increase of 3-5‰ (Sigman and Fripiat, 2019).

The mixing model results indicated autochthonous contribution (31-39%) was lower than the sum of allochthonous contributions (~61-69%) to DON (Figure 19). It is important to note that while fertilizer was not considered as a direct DON source, here the autochthonous apportionment could include contribution from sources such as e.g., inorganic N fertilizer, that was assimilated by algae that ultimately contribute to the DON pool. The autochthonous source was the primary *individual* source DON contributor to Baffin Bay over the sampling period, the dominant contributor to CDG

in dry period, and one of the primary contributors to LS in the wet period. Lower PON contributions were observed in the wet period at Baffin Bay, AB, and CDG presumably due to the increased allochthonous inputs following the high rainfall and subsequent surface/subsurface runoff. LS, on the other hand, displayed higher PON contributions in the wet period. LS is the tributary that has the lowest riverine discharge rate (~0.03 m^3/s) (USGS, 2021b) and is almost dry during the sampling period. However, rainfall could increase the flow, which might cover the sediment that was once exposed to the air. This could favor the release of autochthonous DON to the water column. Additionally, LS had lower Chl-a concentrations in the wet period compared to dry period ($p < 0.05$) while Baffin Bay had higher Chl-a concentrations in the wet period ($p < 0.05$) (Figure 28). Although not significantly, AB and CDG also had higher Chl-a concentrations in the wet period. This lower Chl-a concentrations at LS might not be only a result of rainwater dilution but could also be due to the declined biomass of phytoplankton, which was further degraded and released to the water column as DON, contributing to the higher PON contributions in the wet period at LS.

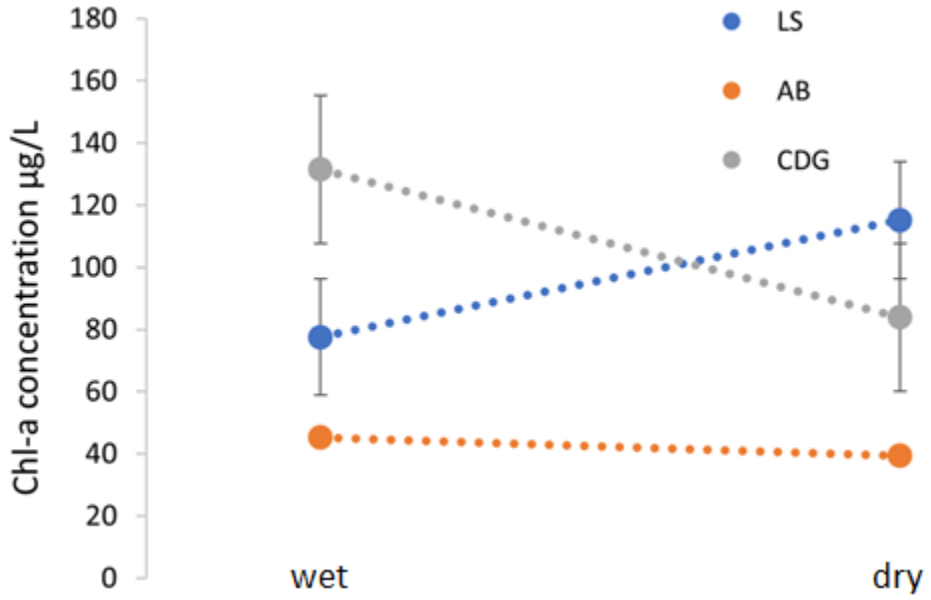

Figure 28. Chl-a concentrations of tributary surface water in the dry and wet periods.

Higher wet deposition contributions were not observed in the wet period at both Baffin Bay and tributaries (Figure 19). This was possibly because of the increased surface/subsurface runoff following the rainfall, which could recharge the subsurface aquifer and increase the SGD and riverine discharge rates. The increased SGD and riverine discharge rates could transport more wastewater and manure derived N to the watershed. As a result, higher wastewater contributions were found in the wet period in both Baffin Bay and tributaries, resulting in wastewater as the dominant DON source at AB and CDG in the wet period. Similarly higher manure contributions were observed in the wet period at Baffin Bay, CDG, and LS.

4.3 Airshed

4.3.1 NH_4^+ wet deposition and sources

The VWM NH_4^+ concentration during the sampling period was 17.9 μM and the annual NH_4^+ wet deposition flux in 2021 was 2.4 kg N/(ha*yr) (Table 5), which was similar to the reported NH_4^+ deposition flux in the eastern US (2.3 kg N/(ha*yr)), Canadian coastal sites (0.2-3.9 kg N/(ha*yr)) and remote Chinese areas (0.7-5.9 kg N/(ha*yr)) but lower than Canadian agricultural sites (2.3-6.5 kg N/(ha*yr)) and Chinese developing and developed cities (19.5-21.4 kg N/(ha*yr)) (Chen et al., 2022; Cheng and Zhang, 2017; Feng et al., 2021; Liu et al., 2015; NADP, 2019). This study found higher NH_4^+ concentration in winter (12.9 μM) and spring (34.6 μM) with lower concentrations in summer (5.7 μM) and fall (6.9 μM) (Figure 21), which was probably due to the timing of fertilizer application. Fertilizer application starts from late fall through early spring in the study area (USDA, 2007) to reduce the N loss via volatilization in warmer months. However, while the timing of fertilizer application leads to lower losses, it could become a more important source of NH_3 to the ambient air in winter than in summer.

Agriculture (i.e., fertilizer and livestock waste) has long been regarded as the primary contributor to NH_3 emissions (Paulot et al., 2014). However, recent research reported vehicles as an important NH_3 source that may outcompete agriculture emission in urban areas (Felix et al., 2014; Felix et al., 2023; Fenn et al., 2018). Here, the $\delta^{15}N\text{-}NH_4^+$ values ranged from -9.5 to 6.7‰ (Figure 21), with more observations clustered at the positive end of the range than observations from other areas that identified agriculture as the primary NH_4^+ source (southern Korea: -15.9 to 2.9‰; southern China: -12.4 to -0.6‰; North America: -9.3 to -2.3‰). It fell into the reported $\delta^{15}N\text{-}NH_4^+$ range of areas that found combustion sources as dominant NH_4^+ sources (southwestern China: -28.7 to 6.6‰; eastern China: -20.2 to 19.9‰) (Chen et al., 2022; Jia and Chen, 2010; Lee et al., 2012; Liu et al., 2017; Nanus et al., 2018). This study observed a higher contribution of vehicle sources than agriculture in winter (vehicle: 48 ± 15%; fertilizer + livestock waste: 37 ± 11%) and summer (vehicle: 61 ± 14%; fertilizer + livestock waste: 34 ± 11%) (Figure 11), stressing the importance of vehicles on NH_3 emission in urban areas.

Continental events had the lowest proportion of biomass burning (8 ± 5%) and the highest local sources (vehicle + fertilizer + livestock waste: 92 ± 14%) contribution compared with marine and mixed events (Figure 22). The high local source contribution could result from the low precipitation amount (0.3 ± 0.3 cm) observed in continental events over the study period (Table 6). Below-cloud scavenging can quickly remove NH_3/NH_4^+ in the ambient air compared with in-cloud scavenging, with the former potentially playing a dominant role in removing atmospheric constituents in small-volume rain events (i.e., continental events) (Bayramoğlu Karşı et al., 2018; Bertrand et al., 2008). Most local sources (i.e., vehicle and agriculture), while not long-range sources (i.e., biomass burning), could be deposited via below-cloud scavenging, leading to the high vehicle + fertilizer + livestock waste contribution (92 ± 14%) in continental events (Figure 11).

The NA group had vehicle contributions to be 60 ± 13% (Figure 22). BB group had a lower vehicle contribution (31 ± 19%) while the same agriculture apportionment (fertilizer + livestock waste: 40 ± 23%) as the NA group (fertilizer + livestock waste: 40 ± 11%). In comparison, the BB group (32.9 μM) had higher NH_4^+ concentrations than the NA group (11.2 μM) (Figure 21). The same agriculture apportionments found in these two groups suggest a higher release of NH_3 from agriculture sources in the BB group. Thus, the observed biomass burning incidents in BB group might not be just wildfires but associated with agriculture.

Table 6. Ancillary data of each rain event. NA indicates not available.

Date	Collection time	pH	$[Cl^-]$ μM	$[SO_4^{2-}]$ μM	Precipitation amount cm	$[NH_4^+]/[NO_3^- + 0.5*SO_4^{2-}]$
1/10/2021	18:00	NA	134.1	5.8	3.3	0.5
1/20/2021	20:00	NA	285.5	33.9	0.1	2.3
2/11/2021	20:00	NA	NA	NA	0.1	NA
2/18/2021	10:00	NA	405.2	47.4	0.4	0.9
3/1/2021	23:00	NA	336.1	46.5	0.2	1.6
3/17/2021	11:00	NA	337.8	88.9	0.2	1.2
3/28/2021	10:00	NA	528.3	76.9	5.9	1.7
4/17/2021	17:00	NA	241.1	22.2	1.1	1.4
4/30/2021	15:00	3.50	60.0	13.9	3.9	1.9
5/1/2021	18:00	3.40	75.7	9.1	8.9	2.3
5/12/2021	6:00	3.38	103.2	14.1	1.5	0.9
5/16/2021	12:00	3.43	149.5	9.7	3.5	0. 8
5/18/2021	6:00	NA	40.3	21.6	1.3	0.7
5/19/2021	9:20	6.60	114.8	13.4	9.7	1.1
5/29/2021	14:00	6.26	132.5	11.3	0.3	0.6
6/1/2021	9:30	6.45	125.8	9.2	1.5	0. 9
6/3/2021	20:30	5.87	34.9	8.1	1.9	1.0
6/21/2021	3:10	NA	841.2	156.6	0.4	0.2
7/1/2021	10:10	NA	183.5	17.4	2.4	0.4
7/4/2021	13:20	NA	136.6	24.0	0.1	0.5
7/5/2021	13:30	6.50	117.4	19.6	0.5	0.1
7/6/2021	16:30	5.22	103.1	10.5	4.8	0.4
7/7/2021	16:00	5.91	115.7	13.3	11.4	0.1
7/8/2021	8:00	5.26	147.9	6.7	2.9	0.4
7/9/2021	8:00	6.30	125.4	9.6	4.5	0.8
7/14/2021	6:00	5.71	196.3	20.5	1.2	0.4
8/27/2021	12:00	4.83	145.4	10.0	1.1	0.2
9/12/2021 TS Nicholas	16:00	5.21	314.7	12.9	1.9	0.2
9/13/2021 TS Nicholas	6:00	6.70	282.2	15.2	3.0	0.7
9/13/2021 TS Nicholas	8:00	6.79	333.4	11.2	3.0	0.6
9/29/2021	12:00	6.10	117.2	9.2	3.9	0.6
10/1/2021	10:00	6.38	83.6	17.6	9.4	0.4
10/14/2021	13:00	6.33	130.6	17.2	2.7	0.7
11/4/2021	4:00	6.74	92.2	18.9	0.5	0.7
12/13/2021	10:00	5.87	61.9	9.7	0.2	1.1
12/14/2021	4:00	5.05	428.3	14.5	1.2	0.8

12/19/2021	17:00	5.30	235.2	25.3	0.1	1.5
12/20/2021	1:00	5.44	363.5	44.1	0.1	1.0
1/7/2022	22:00	4.79	160.9	21.7	0.2	1.0
1/9/2022	14:00	5.13	122.6	14.1	0.8	1.1
1/21/2022	5:00	6.24	254.1	35.3	0.4	1.0
1/24/2022	12:00	5.28	35.2	5.2	1.3	1.7
1/28/2022	11:00	4.16	209.0	29.3	0.4	0.5
1/31/2022	12:00	5.54	39.5	2.6	4.1	0.7
2/7/2022	4:00	5.09	141.1	11.4	0.2	0.8
2/26/2022	8:00	4.52	163.1	21.7	0.3	0.7
3/22/2022	4:00	6.43	265.1	39.3	0.3	1.0
4/11/2022	6:00	7.19	1013.1	202.8	0.2	0.8
4/25/2022	23:00	5.43	603.0	85.5	0.4	0.7
5/22/2022	10:30	5.20	69.5	7.0	5.5	2.0
5/24/2022	2:00	4.91	161.2	16.4	0.9	1.4

4.3.2 NO_3^- wet deposition and sources

The wet deposition NO_3^- concentration has been decreasing since the implementation of the Clean Air Act (NADP, 2019). The VWM NO_3^- concentration in this study was 9.7 μM and was within the range of the reported NO_3^- concentration in Texas (6.5-12.9 μM) by NADP in 2019 (NADP, 2019) (Figure 23). This study did not observe seasonal variations in NO_3^-, but higher concentrations were found in continental events (26.2 μM). The airmasses of continental events may transport through populated areas and entrain concentrated anthropogenic NO_3^-. Marine airmasses, on the other hand, have been treated as unpolluted and had relatively lower NO_3^- concentrations (Altieri et al., 2013), which possibly contributed to the lower NO_3^- concentrations in marine (9.9 μM) and mixed (6.2 μM) events compared with continental events (26.2 μM).

The average $\delta^{15}N\text{-}NO_3^-$ in this study (-1.9 ± 3.5‰) was within the reported range of averages in the North America (urban: -0.5 ± 1.9‰; non-urban: -1.9 ± 2.1‰) (Figure 23) (Song et al., 2021). The highest $\delta^{15}N\text{-}NO_3^-$ (1.7‰) observed in spring, when compared to other seasons ($p < 0.05$), was presumably attributed to the higher frequency of biomass burning incidents in southeastern Mexico due to spring's dry conditions and prevalent agricultural activities (Carabalí et al., 2019). The L group (0.3‰) had a higher VWM $\delta^{15}N\text{-}NO_3^-$ value than the BB (-2.1‰). This was likely caused by the slightly higher natural gas (BB group: 11 ± 7%; L group: 10 ± 6%) and soil "biogenic" (BB group: 9 ± 6%; L group: 8 ± 6%) contribution found in the BB group than the L group (Figure 24). Natural gas (-17.9 ± 1‰) and soil "biogenic" (-35 ± 10‰) derived NO_3^- were reported to be depleted in ^{15}N (Elliott et al., 2019; Walters et al., 2015). The higher contributions of sources with low $\delta^{15}N\text{-}NO_3^-$ values may cause the lower BB group signature compared to the L. The L group also had the lowest VWM $\delta^{18}O\text{-}NO_3^-$ (57.6‰) among the groups (Figure 23), implying the contribution of peroxyl radicals ($RO_2^{\cdot}$).

Higher biomass burning contributions were observed in winter (19 ± 11%) and spring (23 ± 13%) (Figure 24), presumably a result of the higher frequency of biomass burning incidents during those seasons. Among the 16 rain events that occurred in each winter and spring, 6 and 9 of them,

respectively, were found to be significantly affected by biomass burning. Of the 12 summer rain events, 10 were found to be significantly affected by lightning emission. In addition, all 7 fall rain events were affected considerably by lightning emission. The higher frequency of lightning incidents occurring over land is also likely to highly contribute to the continental events (30 ± 19%) in which 7 of the 9 rain events were lightning affected. However, while 13 out of the 16 spring events were affected by lightning, the lightning contribution was relatively low (17 ± 12%). There is a high probability that the increased NO_x emissions in spring from other potential sources (e.g., biomass burning) have decreased the proportion of lightning contribution. In the NA group, vehicle sources contributed 77 ± 11% of NO_3^- in the rain (Figure 24). When biomass burning or/and lightning incidents happened, vehicle contribution significantly decreased to 24-45%, making the non-fossil fuel sources responsible for 55-76% of the NO_3^- in the rain. This demonstrated the competing inputs of NO_x from intermittent biomass burning and lightning emissions with vehicle emissions. This is also consistent with the finding that non-fossil fuel sources could contribute 55 ± 13% of atmospheric NO_x in the North America (Song et al., 2021).

4.3.3 DON wet deposition and sources

The DON wet deposition flux was calculated to be 1.5 kg N/(ha*yr) (Table 5) and constituted 29% of the TDN deposition. This was within the reported range from 17 to 41% (Altieri et al., 2016; Lee et al., 2012; Liu et al., 2017; Russell et al., 1998; Yan and Kim, 2015). The VWM DON concentration of this study was 11.5 μM, which was similar to a coastal area of Korea (13 μM) (Yan and Kim, 2015), but higher than Bermuda (1.9 ± 2.7 μM) and Chesapeake Bay (6.2 μM) (Altieri et al., 2016; Russell et al., 1998), USA region and lower than metropolises of China (78.6 μM) and Korea (21 to 34 μM) (Lee et al., 2012; Liu et al., 2017). The δ^{15}N-DON of this study ranged from -7.3 to 17.5‰ (Figure 25), which was wider and higher than the reported rainwater δ^{15}N-DON in either rural or agricultural areas (-7.5 to 7.5‰; 0.6 ± 5.8‰; -7.9 to 3.8‰) (Altieri et al., 2016; Cornell et al., 1995; Lee et al., 2012) but was similar to Chesapeake Bay, USA region reported values (-1 to 15‰) (Russell et al., 1998) and fell in the range of an urban area in China (-32.5 to 26.6‰) (Liu et al., 2017).

DON concentrations did not display significant variations between seasons/events/groups, while lower δ^{15}N-DON values were found in winter (9.1‰ and 4.6 ± 5.5‰) and spring (8.2‰ and 7.2 ± 3.6‰) (Figure 25). The low δ^{15}N-DON presumably reflected the fertilization activities in winter and spring. Fertilizer and manure emit DON via volatilization (Schade and Crutzen, 1995). The isotopic signature of fertilizer DON is lower than other primary sources and due to the preferential volatilization of ^{14}N, volatilized DON could be even more depleted in δ^{15}N. The study region normally starts fertilizer application from late fall to early spring to reduce the nitrogen lost via volatilization in warmer seasons (USDA, 2007). Due to the higher temperatures in spring, volatilization rates increased and more DON with low δ^{15}N values could be released to the atmosphere, leading to the low δ^{15}N-DON in the rain. Marine (10.6‰ and 37 ± 17%) and mixed (11.4‰ and 31 ± 21%) events had higher δ^{15}N-DON and higher marine DON contribution compared with continental (5.8‰ and 9 ± 5%) events (Figure 25 and 26). The air masses of marine and mixed events travelled through the open ocean and can entrain more marine ON aerosols. Marine (11.0 ± 0.3‰) was reported to have relatively higher ON isotope compositions and the higher marine DON contributions could result in the higher δ^{15}N-DON in marine and mixed events (Altieri et al., 2016; Wu et al., 2020).

Among the identified DON sources, agricultural activities (e.g., fertilizer application) were reported to have the lowest δ^{15}N-DON of -2.4 ± 2.1‰ (Wu et al., 2021; Wu et al., 2020). However, there was one rain event in January 2022 which had a δ^{15}N-DON value of -7.3‰, even lower than the reported fertilizer isotope signature. This likely resulted from secondary DON formation. Secondary DON is formed through the reaction between non-N-containing organic compounds and inorganic N aerosols, predominantly NH_4^+ (Altieri et al., 2016; Liu et al., 2017). NH_4^+ sources (e.g. volatilized fertilizer and livestock waste) were reported to have much lower nitrogen isotope compositions (Bhattarai et al., 2021), which could lower δ^{15}N-DON values through secondary DON formation. To investigate secondary DON formation, the DON stable isotope mixing model was further developed assuming the δ^{15}N-NH_4^+ and δ^{15}N-NO_3^- values reflect δ^{15}N values of organic amines and organic nitrates of secondary DON sources contributing to bulk DON. Results of this modified mixing model indicated secondary DON might not be the dominant contributors but can be significant (Figure 29).

Figure 29. Corrected DON source apportionments. This assumes the observed rainwater δ^{15}N-NH_4^+ (-3.1 ± 4.0‰) and δ^{15}N-NO_3^- (-1.9 ± 3.5‰) values were approximately equivalent to the δ^{15}N values of organic amine and nitrate, which were added into the DON isotope mixing model as two potential sources.

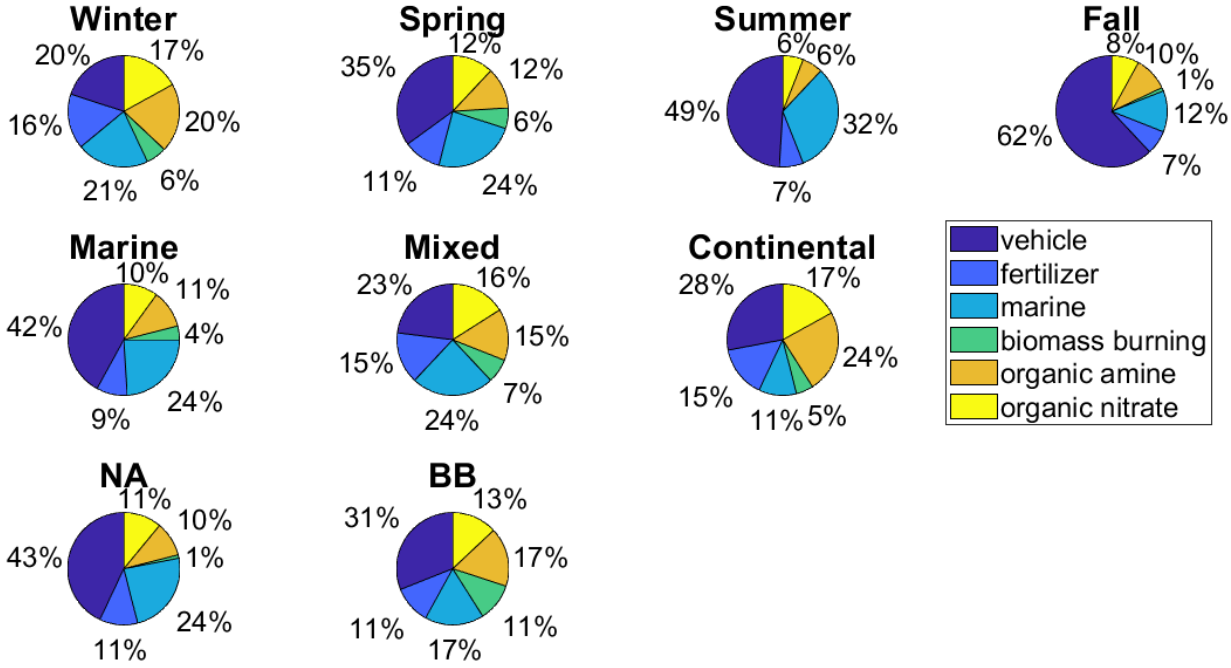

Conclusions/recommendations

This project sampled the surface water of Baffin Bay and its tributaries and collected rainwater to constrain the N profiles and source apportionments in watershed creeks and the bay. In terms of DIN, atmospheric deposition contributed roughly 3.7 kg N/(ha*yr) to the bay through rainfall, while most tributaries had relatively high but variable DIN concentrations whose loadings would be dependent on rainfall conditions. Stable isotope approaches determined that in the airshed, agriculture and vehicle were the primary NH_3 emission sources; vehicle and intermittent sources (i.e., biomass burning and lightning) were the main NO_x emission sources; vehicle, fertilizer, and

marine were the dominant organic nitrogen emission sources. For the watershed creeks, wastewater was found to be a dominant source of DIN. However, DIN were only about 5% of total dissolved nitrogen (TDN) in Baffin Bay, which displayed high mean DON concentrations year-round. This was possibly because DIN had faster turnover rates than DON. A stable isotope mixing model suggested that the sum of allochthonous contributions (i.e., wastewater, manure, and wet deposition) to Baffin Bay represented over 60% of DON sources. Likewise, in tributaries, allochthonous sources contributed ~60-80% of DON and autochthonous source contributed ~20-40%.

Watershed nutrient reduction plans should be tailored according to the features of different regions in the watershed, as they may be subjected to varying N sources and processing. Based on the results of this study and available literatures, the following are examples of suggestions for N mitigation in both the watershed and airshed:

1) Routine monitoring of wastewater treatment plant compliance with regulatory requirements is strongly encouraged and, in cases where sewage treatment is not adequate, repairs and/or replacement of treatment plants may be necessary.

2) Other potential sources of sewage should also be considered, including septic tanks. Regular inspection of septic tanks, especially where the soil is highly permeable, is strongly encouraged. Conventional septic systems located where there are inadequate soils and/or water table is shallow should be removed or replaced with alternative options such as aerobic treatment units or recirculating sand filter systems.

3) Agricultural producers are encouraged to avoid overfertilization, lowering the probability or degree of N reaching the bay through surface/subsurface runoff and rainfall, and employ NRCS approved practices wherever practicable.

4) Regular vehicle emission testing is encouraged to examine the operation of catalysts to ensure that N emission is not excessive.

A more comprehensive list of nutrient reduction plans can be found in a soon-to-be released Watershed Protection Plan, which can be found here: https://baffin.twri.tamu.edu/

References

Altieri, K.E., Fawcett, S.E., Peters, A.J., Sigman, D.M. and Hastings, M.G. 2016. Marine biogenic source of atmospheric organic nitrogen in the subtropical North Atlantic. Proceedings of the National Academy of Sciences 113(4), 925-930.

Altieri, K.E., Hastings, M.G., Gobel, A.R., Peters, A.J. and Sigman, D.M. 2013. Isotopic composition of rainwater nitrate at Bermuda: The influence of air mass source and chemistry in the marine boundary layer. Journal of Geophysical Research: Atmospheres 118(19), 11,304-311,316.

Aluwihare, L.I., Repeta, D.J., Pantoja, S. and Johnson, C.G. 2005. Two Chemically Distinct Pools of Organic Nitrogen Accumulate in the Ocean. Science 308(5724), 1007-1010.

Arar, E.J. and Collins, G.B. 1997 Method 445.0 In Vitro Determination of Chlorophyll a and Pheophytin ain Marine and Freshwater Algae by Fluorescence, U.S. Environmental Protection Agency, Washington, DC.

Atkinson, R., Baulch, D.L., Cox, R.A., Hampson, J., R F, Kerr, J.A. and Troe, J. Evaluated kinetic and photochemical data for atmospheric chemistry. Journal of Physical and Chemical Reference Data; (United States) 21:6, Medium: X; Size: Pages: 1125-1568 2009-1112-1117.

Bayramoğlu Karşı, M.B., Yenisoy-Karakaş, S. and Karakaş, D. 2018. Investigation of washout and rainout processes in sequential rain samples. Atmospheric Environment 190, 53-64.

Berner, A.H. and Felix, J. 2020. Investigating ammonia emissions in a coastal urban airshed using stable isotope techniques. Science of The Total Environment 707, 134952.

Bertrand, G., Celle-Jeanton, H., Laj, P., Rangognio, J. and Chazot, G. 2008. Rainfall chemistry: long range transport versus below cloud scavenging. A two-year study at an inland station (Opme, France). Journal of Atmospheric Chemistry 60(3), 253-271.

Bhattarai, N., Wang, S., Pan, Y., Xu, Q., Zhang, Y., Chang, Y. and Fang, Y. 2021. δ15N-stable isotope analysis of NHx: An overview on analytical measurements, source sampling and its source apportionment. Frontiers of Environmental Science & Engineering 15(6), 126.

Borduas, N., Abbatt, J.P.D., Murphy, J.G., So, S. and da Silva, G. 2016. Gas-Phase Mechanisms of the Reactions of Reduced Organic Nitrogen Compounds with OH Radicals. Environmental Science & Technology 50(21), 11723-11734.

Borsari, V. and Assunção, J.V.d. 2017. Ammonia emissions from a light-duty vehicle. Transportation Research Part D: Transport and Environment 51, 53-61.

Buskey, E.J., Montagna, P.A., Amos, A.F. and Whitledge, T.E. 1997. Disruption of grazer populations as a contributing factor to the initiation of the Texas brown tide algal bloom. Limnology and Oceanography 42(5part2), 1215-1222.

Campbell, J. (2018) Investigating the isotopic composition of reactive nitrogen in a South Texas estuary (Baffin Bay), Texas A&M University-Corpus Christi, Corpus Christi, Texas.

Carabalí, G., Ríos, B., Florean-Cruz, L., Estévez, H., Valdés-Barrón, M., Bonifaz, R. and Riveros-Rosas, D. 2019. Aerosol Optical Characteristics During the Biomass Burning Season in Southeastern Mexico. Water, Air and Soil Pollution 230(10), 1-18.

Chen, H.-Y., Chen, L.-D., Chiang, Z.-Y., Hung, C.-C., Lin, F.-J., Chou, W.-C., Gong, G.-C. and Wen, L.-S. 2010. Size fractionation and molecular composition of water-soluble inorganic and organic nitrogen in aerosols of a coastal environment. Journal of Geophysical Research: Atmospheres 115(D22).

Chen, Z., Huang, X., Huang, C., Yang, Y., Yang, H., Zhang, J. and Huang, T. 2022. High atmospheric wet nitrogen deposition and major sources in two cities of Yangtze River Delta: Combustion-related NH3 and non-fossil fuel NOx. Science of The Total Environment 806, 150502.

Cheng, I. and Zhang, L. 2017. Long-term air concentrations, wet deposition, and scavenging ratios of inorganic ions, HNO3, and SO2 and assessment of aerosol and precipitation acidity at Canadian rural locations. Atmos. Chem. Phys. 17(7), 4711-4730.

Choi, W.J., Arshad, M.A., Chang, S.X. and Kim, T.H. 2006. Grain 15N of crops applied with organic and chemical fertilizers in a four-year rotation. Plant and Soil 284(1), 165-174.

Cornell, S., Randell, A. and Jickells, T. 1995. Atmospheric inputs of dissolved organic nitrogen to the oceans. Nature 376(6537), 243-246.
Corpus Christi MPO 2018.

Curt, M.D., Aguado, P., Sánchez, G., Bigeriego, M. and Fernández, J. 2004. Nitrogen Isotope Ratios of Synthetic and Organic Sources of Nitrate Water Contamination in Spain. Water, Air and Soil Pollution 151(1-4), 135-142.

Dammers, E., McLinden, C.A., Griffin, D., Shephard, M.W., Van Der Graaf, S., Lutsch, E., Schaap, M., Gainairu-Matz, Y., Fioletov, V., Van Damme, M., Whitburn, S., Clarisse, L., Cady-Pereira, K., Clerbaux, C., Coheur, P.F. and Erisman, J.W. 2019. NH3 emissions from large point sources derived from CrIS and IASI satellite observations. Atmos. Chem. Phys. 19(19), 12261-12293.

Davidson, E.A., De Abreu SÁ, T.D., Reis Carvalho, C.J., De Oliveira Figueiredo, R., Kato, M.d.S.A., Kato, O.R. and Ishida, F.Y. 2008. An integrated greenhouse gas assessment of an alternative to slash-and-burn agriculture in eastern Amazonia. Global Change Biology 14(5), 998-1007.

Elliott, E.M., Yu, Z., Cole, A.S. and Coughlin, J.G. 2019. Isotopic advances in understanding reactive nitrogen deposition and atmospheric processing. Science of The Total Environment 662, 393-403.
EPA 2020 2020 National Emissions Inventory (NEI) Data.

EPRI 2015 Long-term Emissions and Air Quality Trends in the United States, Electric Power Research Institute, Palo Alto, CA.

Felix, J., Elliott, E.M., Gish, T., Maghirang, R., Cambal, L. and Clougherty, J. 2014. Examining the transport of ammonia emissions across landscapes using nitrogen isotope ratios. Atmospheric Environment 95, 563-570.

Felix, J., Elliott, E.M., Gish, T.J., McConnell, L.L. and Shaw, S.L. 2013. Characterizing the isotopic composition of atmospheric ammonia emission sources using passive samplers and a combined oxidation-bacterial denitrifier approach. Rapid Communications in Mass Spectrometry 27(20), 2239-2246.

Felix, J. and Murgulet, D. 2020. Nitrate isotopic composition of sequential Hurricane Harvey wet deposition: Low latitude NOx sources and oxidation chemistry. Atmospheric Environment, 117748.

Felix, J.D., Berner, A., Wetherbee, G.A., Murphy, S.F. and Heindel, R.C. 2023. Nitrogen isotopes indicate vehicle emissions and biomass burning dominate ambient ammonia across Colorado's Front Range urban corridor. Environmental Pollution 316, 120537.

Feng, J., Vet, R., Cole, A., Zhang, L., Cheng, I., O'Brien, J. and Macdonald, A.-M. 2021. Inorganic chemical components in precipitation in the eastern U.S. and Eastern Canada during 1989–2016: Temporal and regional trends of wet concentration and wet deposition from the NADP and CAPMoN measurements. Atmospheric Environment 254, 118367.

Fenn, M.E., Bytnerowicz, A., Schilling, S.L., Vallano, D.M., Zavaleta, E.S., Weiss, S.B., Morozumi, C., Geiser, L.H. and Hanks, K. 2018. On-road emissions of ammonia: An underappreciated source of atmospheric nitrogen deposition. Science of The Total Environment 625, 909-919.

Galloway, J.N., Dentener, F.J., Capone, D.G., Boyer, E.W., Howarth, R.W., Seitzinger, S.P., Asner, G.P., Cleveland, C.C., Green, P.A., Holland, E.A., Karl, D.M., Michaels, A.F., Porter, J.H., Townsend, A.R. and Vöosmarty, C.J. 2004. Nitrogen Cycles: Past, Present, and Future. Biogeochemistry 70(2), 153-226.

Granger, J. and Wankel, S.D. 2016. Isotopic overprinting of nitrification on denitrification as a ubiquitous and unifying feature of environmental nitrogen cycling. Proceedings of the National Academy of Sciences 113(42), E6391-E6400.

He, S., Li, P., Su, F., Wang, D. and Ren, X. 2022. Identification and apportionment of shallow groundwater nitrate pollution in Weining Plain, northwest China, using hydrochemical indices, nitrate stable isotopes, and the new Bayesian stable isotope mixing model (MixSIAR). Environmental Pollution 298, 118852.

Hoagland, P., Anderson, D.M., Kaoru, Y. and White, A.W. 2002. The Economic Effects of Harmful Algal Blooms in the United States: Estimates, Assessment Issues, and Information Needs. Estuaries 25(4), 819-837.

Hoering, T. 1957. The isotopic composition of the ammonia and the nitrate ion in rain. Geochimica et Cosmochimica Acta 12(1), 97-102.

Holmes, R.M., McClelland, J.W., Sigman, D.M., Fry, B. and Peterson, B.J. 1998. Measuring 15N–NH4+ in marine, estuarine and fresh waters: An adaptation of the ammonia diffusion method for samples with low ammonium concentrations. Marine Chemistry 60(3), 235-243.

Hou, Y., Liu, X., Chen, S., Ren, J., Bai, L., Li, J., Gu, Y. and Wei, L. 2021. Effects of Seasonal Thermal Stratification on Nitrogen Transformation and Diffusion at the Sediment-Water Interface in a Deep Canyon Artificial Reservoir of Wujiang River Basin. Water 13(22), 3194.

Hou, Y., Velthof, G.L. and Oenema, O. 2015. Mitigation of ammonia, nitrous oxide and methane emissions from manure management chains: a meta-analysis and integrated assessment. Global Change Biology 21(3), 1293-1312.

Hu, M., Liu, Y., Zhang, Y., Dahlgren, R.A. and Chen, D. 2019. Coupling stable isotopes and water chemistry to assess the role of hydrological and biogeochemical processes on riverine nitrogen sources. Water Research 150, 418-430.

Ito, A., Lin, G. and Penner, J.E. 2015. Global modeling study of soluble organic nitrogen from open biomass burning. Atmospheric Environment 121, 103-112.

Jia, G. and Chen, F. 2010. Monthly variations in nitrogen isotopes of ammonium and nitrate in wet deposition at Guangzhou, south China. Atmospheric Environment 44(19), 2309-2315.

Jiang, H., Lan, W., Li, T., Xu, Z., Liu, W. and Pan, K. 2020. Isotopic Composition Reveals the Impact of Oyster Aquaculture on Pelagic Nitrogen Cycling in a Subtropical Estuary. Water Research 187, 116431.

Jin, X., Zhu, Q. and Cohen, R.C. 2021. Direct estimates of biomass burning NOx emissions and lifetimes using daily observations from TROPOMI. Atmos. Chem. Phys. 21(20), 15569-15587.

Kawashima, H. and Kurahashi, T. 2011. Inorganic ion and nitrogen isotopic compositions of atmospheric aerosols at Yurihonjo, Japan: Implications for nitrogen sources. Atmospheric Environment 45(35), 6309-6316.

Knapp, A.N., McCabe, K.M., Grosso, O., Leblond, N., Moutin, T. and Bonnet, S. 2018. Distribution and rates of nitrogen fixation in the western tropical South Pacific Ocean constrained by nitrogen isotope budgets. Biogeosciences 15(9), 2619-2628.

Knapp, A.N., Sigman, D.M. and Lipschultz, F. 2005. N isotopic composition of dissolved organic nitrogen and nitrate at the Bermuda Atlantic Time-series Study site. Global Biogeochemical Cycles 19(1).

Lee, K.-S., Lee, D.-S., Lim, S.-S., Kwak, J.-H., Jeon, B.-J., Lee, S.-I., Lee, S.-M. and Choi, W.-J. 2012. Nitrogen isotope ratios of dissolved organic nitrogen in wet precipitation in a metropolis surrounded by agricultural areas in southern Korea. Agriculture, Ecosystems & Environment 159, 161-169.

Li, C., Li, S.-L., Yue, F.-J., Liu, J., Zhong, J., Yan, Z.-F., Zhang, R.-C., Wang, Z.-J. and Xu, S. 2019a. Identification of sources and transformations of nitrate in the Xijiang River using nitrate isotopes and Bayesian model. Science of The Total Environment 646, 801-810.

Li, J., Zhang, X., Orlando, J., Tyndall, G. and Michalski, G. 2020. Quantifying the nitrogen isotope effects during photochemical equilibrium between NO and NO2: implications for δ15N in tropospheric reactive nitrogen. Atmospheric Chemistry and Physics 20(16), 9805-9819.

Li, Z., Walters, W.W., Hastings, M.G., Zhang, Y., Song, L., Liu, D., Zhang, W., Pan, Y., Fu, P. and Fang, Y. 2019b. Nitrate Isotopic Composition in Precipitation at a Chinese Megacity: Seasonal Variations, Atmospheric Processes, and Implications for Sources. Earth and Space Science 6(11), 2200-2213.

Liu, S., Wu, F., Feng, W., Guo, W., Song, F., Wang, H., Wang, Y., He, Z., Giesy, J.P., Zhu, P. and Tang, Z. 2018. Using dual isotopes and a Bayesian isotope mixing model to evaluate sources of nitrate of Tai Lake, China. Environmental Science and Pollution Research 25(32), 32631-32639.

Liu, X.-Y., Xiao, H.-W., Xiao, H.-Y., Song, W., Sun, X.-C., Zheng, X.-D., Liu, C.-Q. and Koba, K. 2017. Stable isotope analyses of precipitation nitrogen sources in Guiyang, southwestern China. Environmental Pollution 230, 486-494.

Liu, Y.W., Xu, R., Wang, Y.S., Pan, Y.P. and Piao, S.L. 2015. Wet deposition of atmospheric inorganic nitrogen at five remote sites in the Tibetan Plateau. Atmospheric Chemistry and Physics 15(20), 11683-11700.

Mace, K.A., Duce, R.A. and Tindale, N.W. 2003. Organic nitrogen in rain and aerosol at Cape Grim, Tasmania, Australia. Journal of Geophysical Research: Atmospheres 108(D11).

Maftuah, E. and Wakhid, N. 2019. Replacing slash and burn practices with slash and composting to reduce carbon dioxide emissions from degraded peatland. Indonesian J. Agricultural Sci. 20(1), 9.

McDonald, B.C., Dallmann, T.R., Martin, E.W. and Harley, R.A. 2012. Long-term trends in nitrogen oxide emissions from motor vehicles at national, state, and air basin scales. Journal of Geophysical Research: Atmospheres 117(D21).
Meijide, A., Díez, J.A., Sánchez-Martín, L., López-Fernández, S. and Vallejo, A. 2007. Nitrogen oxide emissions from an irrigated maize crop amended with treated pig slurries and composts in a Mediterranean climate. Agriculture, Ecosystems & Environment 121(4), 383-394.

Miyazaki, Y., Kawamura, K., Jung, J., Furutani, H. and Uematsu, M. 2011. Latitudinal distributions of organic nitrogen and organic carbon in marine aerosols over the western North Pacific. Atmospheric Chemistry and Physics 11(7), 3037.

Montagna, P.A., Stockwell, D.A. and Kalke, R.D. 1993 Dwarf surfclam Mulinia lateralis (Say, 1822) populations and feeding during the Texas brown tide event.
NADP 2019 National Trends Network Animated Maps.

Nanus, L., Campbell, D.H., Lehmann, C.M.B. and Mast, M.A. 2018. Spatial and temporal variation in sources of atmospheric nitrogen deposition in the Rocky Mountains using nitrogen isotopes. Atmospheric Environment 176, 110-119.

Nikolenko, O., Jurado, A., Borges, A.V., Knöller, K. and Brouyère, S. 2018. Isotopic composition of nitrogen species in groundwater under agricultural areas: A review. Science of The Total Environment 621, 1415-1432.

NOAA 2019 Land Cover: 2010. Coastal Change Analysis Program (C-CAP) Regional Land Cover, NOAA Office for Coastal Management.

Onodera, T., Komatsu, K., Kohzu, A., Kanaya, G., Mizuochi, M. and Syutsubo, K. 2021. Evaluation of stable isotope ratios (δ15N and δ18O) of nitrate in advanced sewage treatment processes: Isotopic signature in four process types. Science of The Total Environment 762, 144120.

Onuf, C.P. 1996. Seagrass responses to long-term light reduction by brown tide in upper Laguna Madre, Texas: distribution and biomass patterns. Marine Ecology Progress Series 138, 219-231.

Osburn, C.L., Handsel, L.T., Peierls, B.L. and Paerl, H.W. 2016. Predicting Sources of Dissolved Organic Nitrogen to an Estuary from an Agro-Urban Coastal Watershed. Environmental Science & Technology 50(16), 8473-8484.

Osterholz, H., Niggemann, J., Giebel, H.-a., Simon, M. and Dittmar, T. 2015. Inefficient microbial production of refractory dissolved organic matter in the ocean. Nature Communications 6, 7422.

Pan, B., Lam, S.K., Mosier, A., Luo, Y. and Chen, D. 2016. Ammonia volatilization from synthetic fertilizers and its mitigation strategies: A global synthesis. Agriculture, Ecosystems & Environment 232, 283-289.

Parnell, A.C., Inger, R., Bearhop, S. and Jackson, A.L. 2010. Source Partitioning Using Stable Isotopes: Coping with Too Much Variation. PLoS ONE 5, e9672.

Passos, R.G., Matiatos, I., Monteiro, L.R., Almeida, R.S.S.P., Lopes, N.P., Carvalho Filho, C.A. and Cota, S.D.S. 2022. Imprints of anthropogenic air pollution sources on nitrate isotopes in precipitation in a tropical metropolitan area. Atmospheric Environment 288, 119300.

Paulot, F., Jacob, D.J., Pinder, R.W., Bash, J.O., Travis, K. and Henze, D.K. 2014. Ammonia emissions in the United States, European Union, and China derived by high-resolution inversion of ammonium wet deposition data: Interpretation with a new agricultural emissions inventory (MASAGE_NH3). Journal of Geophysical Research: Atmospheres 119(7), 4343-4364.

Poikane, S., Kelly, M.G., Herrero, F.S., Pitt, J., Jarvie, H.P., Claussen, U., Leujak, W., Solheim, A.L., Teixeira, H., and Phillips, G. 2019. Nutrient criteria for surface waters under the European Water Framework Directive: current state of the art challenges and future outlook. Sci. Tot. Environ. 695: 133888

Qiu, Y., Felix, J.D., Murgulet, D. and Abdulla, H. in prep-a. NOx and NH3 Emission Source Apportionment in an Urban Coastal Airshed Using Stable Isotopes and a Novel Approach to Interment Sources

Qiu, Y., Felix, J.D., Murgulet, D., Wetz, M. and Abdulla, H. in prep-b. Isotopic compositions of organic and inorganic nitrogen reveal processing and source dynamics at septic influenced and undeveloped estuary sites

Romer, P.S., Duffey, K.C., Wooldridge, P.J., Allen, H.M., Ayres, B.R., Brown, S.S., Brune, W.H., Crounse, J.D., de Gouw, J., Draper, D.C., Feiner, P.A., Fry, J.L., Goldstein, A.H., Koss, A., Misztal, P.K., Nguyen, T.B., Olson, K., Teng, A.P., Wennberg, P.O., Wild, R.J., Zhang, L. and Cohen, R.C. 2016. The lifetime of nitrogen oxides in an isoprene-dominated forest. Atmospheric Chemistry and Physics 16, 7623.

Russell, K.M., Galloway, J.N., Macko, S.A., Moody, J.L. and Scudlark, J.R. 1998. Sources of nitrogen in wet deposition to the Chesapeake Bay region. Atmospheric Environment 32(14), 2453-2465.

Schade, G.W. and Crutzen, P.J. 1995. Emission of aliphatic amines from animal husbandry and their reactions: Potential source of N2O and HCN. Journal of Atmospheric Chemistry 22(3), 319-346.

Schmidt, F., Koch, B.P., Elvert, M., Schmidt, G., Witt, M. and Hinrichs, K.-U. 2011. Diagenetic Transformation of Dissolved Organic Nitrogen Compounds under Contrasting Sedimentary Redox Conditions in the Black Sea. Environmental Science & Technology 45(12), 5223-5229.

Sharma, H.D., Jervis, R.E. and Wong, K.Y. 1970. Isotopic exchange reactions in nitrogen oxides. The Journal of Physical Chemistry 74, 923-933.

Sigman, D.M., Casciotti, K.L., Andreani, M., Barford, C., Galanter, M. and Böhlke, J.K. 2001. A Bacterial Method for the Nitrogen Isotopic Analysis of Nitrate in Seawater and Freshwater. Analytical Chemistry 73(17), 4145-4153.

Sigman, D.M. and Fripiat, F. (2019) Encyclopedia of Ocean Sciences (Third Edition). Cochran, J.K., Bokuniewicz, H.J. and Yager, P.L. (eds), pp. 263-278, Academic Press, Oxford.

Simms, A., ARYAL, N., MILLER, L. and YOKOYAMA, Y. 2010. The incised valley of Baffin Bay, Texas: a tale of two climates. Sedimentology 57(2), 642-669.

Sipler, R.E. and Bronk, D.A. (2015) Biogeochemistry of Marine Dissolved Organic Matter (Second Edition). Hansell, D.A. and Carlson, C.A. (eds), pp. 127-232, Academic Press, Boston.

Song, W., Liu, X.-Y., Hu, C.-C., Chen, G.-Y., Liu, X.-J., Walters, W.W., Michalski, G. and Liu, C.-Q. 2021. Important contributions of non-fossil fuel nitrogen oxides emissions. Nature Communications 12(1), 243.

Sun, M.M., Sun, J., Qiu, J.W., Jing, H. and Liu, H. 2012. Characterization of the proteomic profiles of the brown tide alga Aureoumbra lagunensis under phosphate- and nitrogen-limiting conditions and of its phosphate limitation-specific protein with alkaline phosphatase activity. Appl Environ Microbiol 78(6), 2025-2033.

Thibodeau, B., Bauch, D. and Voss, M. 2017. Nitrogen dynamic in Eurasian coastal Arctic ecosystem: Insight from nitrogen isotope. Global Biogeochemical Cycles 31(5), 836-849.

Ti, C., Xia, L., Chang, S.X. and Yan, X. 2019. Potential for mitigating global agricultural ammonia emission: A meta-analysis. Environmental Pollution 245, 141-148.

Tsikas, D. 2007. Analysis of nitrite and nitrate in biological fluids by assays based on the Griess reaction: Appraisal of the Griess reaction in the l-arginine/nitric oxide area of research. Journal of Chromatography B 851(1-2), 51-70.

Tsunogai, U., Kido, T., Hirota, A., Ohkubo, S.B., Komatsu, D.D. and Nakagawa, F. 2008. Sensitive determinations of stable nitrogen isotopic composition of organic nitrogen through chemical conversion into N2O. Rapid Communications in Mass Spectrometry 22(3), 345-354.

United States Census Bureau 2020.

USDA 2007 Tailored Reports: Crop Production Practices.

USDA 2017 Census of Agriculture 2017 Census Volume 1, Chapter 2: County Level Data.

USGS 2021a USGS 08211900 San Fernando Ck at Alice, TX, National Water Information System: Web Interface.

USGS 2021b USGS 08212400 Los Olmos Ck nr Falfurrias, TX, National Water Information System: Web Interface.

USGS 2021c USGS 08212820 Petronila Ck at FM 665 nr Driscoll, TX, National Water Information System: Web Interface.

USGS 2022 USA NLCD Land Cover.

Walters, W.W., Song, L., Chai, J., Fang, Y., Colombi, N. and Hastings, M.G. 2020. Characterizing the spatiotemporal nitrogen stable isotopic composition of ammonia in vehicle plumes. Atmos. Chem. Phys. 20(19), 11551-11567.

Walters, W.W., Tharp, B.D., Fang, H., Kozak, B.J. and Michalski, G. 2015. Nitrogen Isotope Composition of Thermally Produced NOx from Various Fossil-Fuel Combustion Sources. Environmental Science & Technology 49(19), 11363-11371.

Wells, N.S., Hakoun, V., Brouyère, S. and Knöller, K. 2016. Multi-species measurements of nitrogen isotopic composition reveal the spatial constraints and biological drivers of ammonium attenuation across a highly contaminated groundwater system. Water Research 98, 363-375.

Westbrook, H. (2021) Dissolved Nitrogen Cycling in the Eastern Canadian Arctic Archipelago From Stable Isotopic Data, University of South Carolina.

Wetz, M. unpublished work.

Wu, L., Yue, S., Shi, Z., Hu, W., Chen, J., Ren, H., Deng, J., Ren, L., Fang, Y., Yan, H., Li, W., Harrison, R.M. and Fu, P. 2021. Source forensics of inorganic and organic nitrogen using δ15N for tropospheric aerosols over Mt. Tai. npj Climate and Atmospheric Science 4(1), 8.

Wu, Y., Huang, X., Jiang, Z., Liu, S. and Cui, L. 2020. Composition and sources of aerosol organic matter in a highly anthropogenic influenced semi-enclosed bay: Insights from excitation-emission matrix spectroscopy and isotopic evidence. Atmospheric Research 241, 104958.

Xue, D., Botte, J., De Baets, B., Accoe, F., Nestler, A., Taylor, P., Van Cleemput, O., Berglund, M. and Boeckx, P. 2009. Present limitations and future prospects of stable isotope methods for nitrate source identification in surface- and groundwater. Water Research 43(5), 1159-1170.

Yan, G. and Kim, G. 2015. Sources and fluxes of organic nitrogen in precipitation over the southern East Sea/Sea of Japan. Atmospheric Chemistry and Physics 15, 2761.

Yu, L., Zheng, T., Zheng, X., Hao, Y. and Yuan, R. 2020. Nitrate source apportionment in groundwater using Bayesian isotope mixing model based on nitrogen isotope fractionation. Science of The Total Environment 718, 137242.

Zhang, L., Altabet, M.A., Wu, T. and Hadas, O. 2007. Sensitive Measurement of NH4+ 15N/14N (δ15NH4+) at Natural Abundance Levels in Fresh and Saltwaters. Analytical Chemistry 79(14), 5297-5303.

Zhang, R., Wang, X.T., Ren, H., Huang, J., Chen, M. and Sigman, D.M. 2020. Dissolved Organic Nitrogen Cycling in the South China Sea From an Isotopic Perspective. Global Biogeochemical Cycles 34(12), e2020GB006551.

Zhong, X., Yan, M., Ning, X., Yan, Z. and Xin, Y. 2020. Nitrate processing traced by nitrate dual isotopic composition in the early spring in the Changjiang (Yangtze River) Estuary and adjacent shelf areas. Marine Pollution Bulletin 161, 111699.

Task 2:

Quantification and Source Tracking of Groundwater Nutrients

Prepared by:

Dorina Murgulet, Ph.D.

Cody Lopez

Yixi Qiu, Ph.D.

Sean Majors

J. David Felix, Ph.D.

Summary

This study found groundwater had NO_3^-, porewater had NH_4^+, and surface water had DON as the primary form of nitrogen species. Groundwater had high NO_3^- (~1064 μM) and DON (~64 μM) concentrations. The nitrogen and oxygen isotopic compositions of NO_3^- suggested nitrification and denitrification co-existed in groundwater group I and II and group III was mainly controlled by nitrification. The dual isotope mixing model results indicated wastewater- and agriculture-derived NH_4^+ were the dominant sources to the NO_3^- in the groundwater. Porewater had high NH_4^+ concentrations (~325 μM) and had average $\delta^{15}N\text{-}NH_4^+$ values of 4.1‰. Lower $\delta^{15}N\text{-}NH_4^+$ values were observed in summer 2021 (-3.8‰) indicating a temperature- and/or solar radiation-dependent processing (e.g., mineralization and photo-ammonification in the euphotic zone). Despite of the high NO_3^- and NH_4^+ concentrations in the groundwater and porewater, surface water had low DIN (~3 μM) but high DON (~50 μM) concentrations. The work detailed in the report revolves around the study of Submarine Groundwater Discharge (SGD) and nutrient fluxes in Baffin Bay, Texas. The study was conducted over a period of two years, from October 2020 to March 2022. The report provides a comprehensive analysis of SGD rates, nutrient concentrations, and their implications for remediation efforts. The SGD rates were measured using radium and radon isotopes, as well as Darcy's law. The highest SGD rate was measured in January 2022 at 95.7 cm/day, and the lowest in January 2021 at 6.7 cm/day. The SGD rates varied seasonally, with higher rates following the large Spring-Summer 2021 rain events implying that aquifer recharge leads to significant increases in fluxes to the bay. The associated nutrient fluxes were determined with two different nutrient sources, either the concentration of nutrients in groundwater or that of porewater. When using the most conservative SGD rates (e.g., radium-derived) and average nutrient concentrations of groundwater and porewater as the endmembers, the maximum flux of NH_4^+ across all events was 18,790 $\mu M \cdot m^{-2} \cdot d^{-1}$, the average was 9,518 $\mu M \cdot m^{-2} \cdot d^{-1}$, and the minimum was 2,475 $\mu M \cdot m^{-2} \cdot d^{-1}$. Fluxes of NOx reached a maximum of 19,052 $\mu M \cdot m^{-2} \cdot d^{-1}$, an average of 9,652 $\mu M \cdot m^{-2} \cdot d^{-1}$, and a minimum of 251 $\mu M \cdot m^{-2} \cdot d^{-1}$. Fluxes of DOC were between 3 to 34 times higher than those of TDN (NO_x+NH_4^+). The lowest DOC fluxes occurred in January 2021 (average 2,765 $\mu M \cdot m^{-2} \cdot d^{-1}$), and the highest in November 2021 (average 346,789 $\mu M \cdot m^{-2} \cdot d^{-1}$). Fluxes of DON were up to two orders of magnitude lower than DOC but followed a similar trend, with the lowest magnitudes in January 2021 (15 $\mu M \cdot m^{-2} \cdot d^{-1}$) and the highest in November 2021 (2,563 $\mu M \cdot m^{-2} \cdot d^{-1}$). The study's findings have significant implications for remediation efforts. The high SGD rates and nutrient fluxes indicate a high volume of nutrients arriving around the bay, particularly in Cayo del Grullo, which can have a significant impact on the bay's water quality. The detailed understanding of SGD and associated nutrient sources as well as its variability in response to environmental conditions, hydrological events, and geographic location can help in designing effective remediation strategies.

Background

In the estuarine and coastal ocean setting, groundwater can be a significant source of inorganic N to local ecosystems and may provide up to 30% of the non-recycled N in the nutrient budget (Matson 1993, Paerl 1997, Chaillou, Couturier et al. 2014). Giblin and Gaines (1990) found that N inputs from groundwater were similar in magnitude to riverine inputs in a river-dominated estuary. In bays with limited freshwater inflows and poor connection to a larger body of water, or rainfall that is significantly less than the local evaporation rate, submarine groundwater discharge (SGD) could influence the salinity of the local environment (Jolly, McEwan et al. 2008) in addition to being an important source of nutrients. SGD, as described by (Moore 2010), is “any and all flow

of water on continental margins from the seabed to the coastal ocean, with scale lengths of meters to kilometers, regardless of fluid composition or driving force." Thus, SGD includes terrestrial groundwater and recirculated seawater (Santos, Cook et al. 2012).

Semi-arid estuarine systems are in general characterized by longer residence times, due to limited riverine inflows, and are known to cycle N for prolonged periods of time. In the absence of nutrient inputs from surface runoff, SGD could control primary productivity and lead to excessive algal growth or harmful algal blooms, especially in systems with long residence times (Hu, Muller-Karger et al. 2006, Kroeger, Swarzenski et al. 2007, Jolly, McEwan et al. 2008). In addition, even under low magnitudes of groundwater input, recirculated seawater can be a significant source of nutrients and anoxic waters to the water column (Santos, Cook et al. 2012). Development of anoxic conditions in the porewater could lead to the buildup of ammonium (NH_4^+) (Schulz, Dahmke et al. 1994, Prokopenko, Sigman et al. 2011) that, later, can be released to the water column through SGD (including both groundwater and recirculated seawater) (Moore 1996, Brock 2001). Increasing salinity levels in porewater is also very common in semi-arid estuaries (Bighash and Murgulet 2015). Previous studies indicate that salinity levels affect the N cycle of estuaries (Giblin and Gaines 1990, Holmes, Peterson et al. 2000, Conley, Paerl et al. 2009). For instance, NH_4^+ release from sediment is dependent on salinity, with lower salinities effectively storing NH_4^+ in sediments and higher salinities releasing NH_4^+, which may enhance summertime primary production (Holmes, Peterson et al. 2000, Giblin, Weston et al. 2010). The extent of SGD input is not fully known, but given the high enrichment of porewater and groundwater in nutrients, it is recognized to play a significant role in coastal ocean chemistry, even when volumetric inputs are low (Krest, Moore et al. 2000, Santos, Cook et al. 2012).

Nitrogen enters estuarine systems through a variety of pathways including: atmospheric deposition, surface runoff (land and riverine), biological fixation, remineralization of decaying organic matter, and SGD (Figure 1) (Paerl 1997, Santos, Cook et al. 2012, Fowler, Coyle et al. 2013, WSDE 2017). This study focused on determining and quantifying the sources and processing of nutrients along transport paths to the bay, accomplished by analysis of stable nitrogen isotopic composition in combination with groundwater tracers and submarine groundwater discharge rates (SGD) in groundwater, bay water, and porewater. The distinct isotopic ratios of nitrogen (nitrate: NO_3^-, NH_4^+, DON) sources were used to fingerprint and quantify nutrient sources (i.e., nutrients entering groundwater from atmospheric deposition or fertilizer, sewage, etc.) and processing mechanisms (i.e., remineralization) in estuaries, bays, oceans, and rivers (Hadas, Altabet et al. 2009, Schlarbaum, Daehnke et al. 2010, Knapp, Sigman et al. 2011).

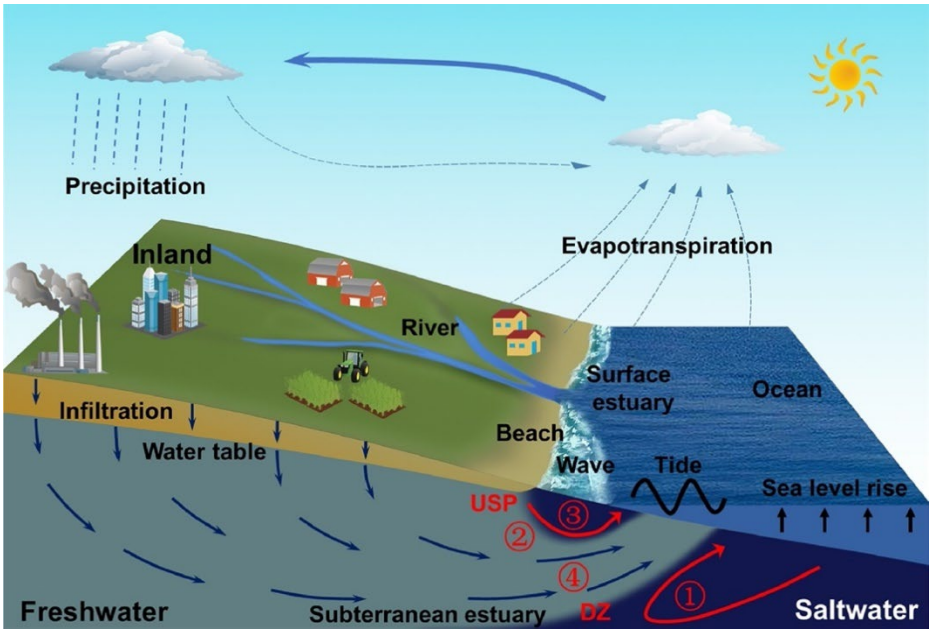

Figure 1: Conceptual diagram showing the interaction between a coastal unconfined aquifer and surface water including major flow processes: (1) density-driven recirculation, (2) tide-induced recirculation, (3) wave-driven recirculation and (4) terrestrial fresh groundwater discharge. The subterranean estuary (STE) is associated with the dispersion zone (DZ) of the saltwater wedge and the upper saline plume (USP); from Robinson, Xin et al. (2018).

The results of this study will pave the way to a greater understanding of nutrients sources to Texas estuaries, an important step in meeting the overarching goal of the Coastal Zone Act Reauthorization Amendments (CZARA or §6217) to "protect coastal waters" by "control" of NPS pollution. The results are a step forward in the development and implementation of management measures leading to better control of nonpoint pollution sources and improved water budgets.

Methods

Water Sample Collection

Groundwater, porewater and surface water samples were collected in November 2020, January 2021, June 2021, July 2021, October 2021, January 2022, March 2022 and July 2022. Field parameters, which were collected before sampling, including salinity, dissolved oxygen (DO), pH and specific conductivity, were measured using a multi-probe YSI ProDSS. Groundwater was sampled at the wellhead using a peristaltic pump after purging three well volumes and after field parameters stabilized. Surface water samples were collected with a Van Dorn bottle deployed to the desired depth and given a few minutes for circulation according to standard operating procedure (TCEQ 2012). Porewater was sampled, from 0.3-1.6 m below the sediment-water interface with a push-piezometer sampler attached to a peristaltic pump, after stabilization of field parameters (RCRA SOP 2009). All water samples, collected in 1 L HPDE bottles previously acid-washed with 20% hydrochloride acid and rinsed with 18.2 MΩ cm water and finally triple rinsed with sample water, were placed in ice until transported back to the lab and filtered through 0.2 µm pore-sized polycarbonate membranes within 24-48 hours. Samples were then frozen until analysis.

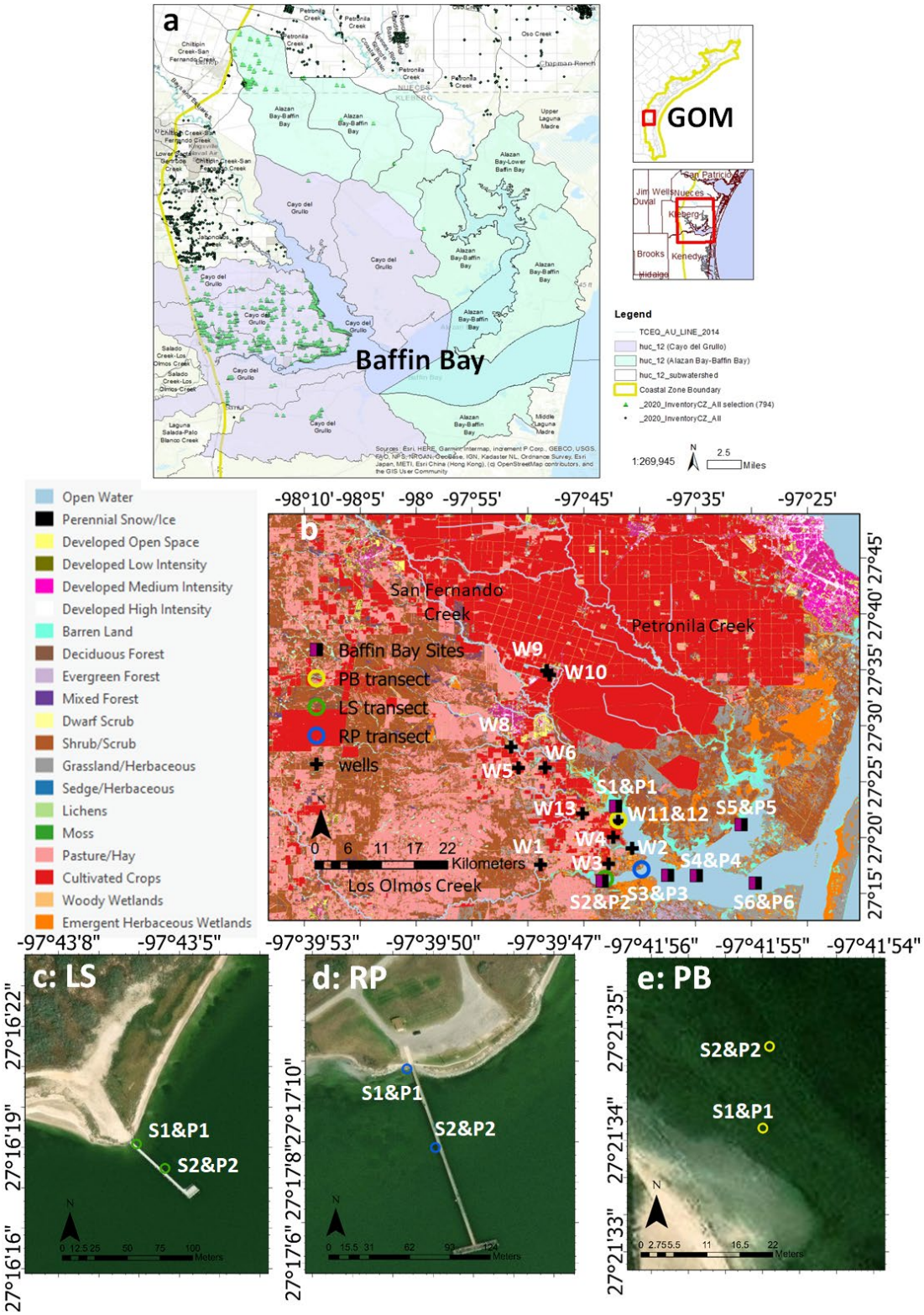

Figure 2. May of study area. a) The location of Baffin Bay, which is along the western coastline of Gulf of Mexico (GOM). The green triangles indicate 794 septic systems within the coastal zone boundary of Cayo del Grullo (CDG) and Alazan Bay (AB), two sub-watersheds of Baffin Bay and

black dots indicate the septic systems outside the coastal zone but within the Baffin Bay watershed. The count of those septic systems is not available yet. This map was created by Texas A&M AgriLife Extension OSSF Team with data collected from contract # 582-20-10160 funded by the Environmental Protection Agency (EPA) Clean Water Act (CWA) Section 319(h) funds through the Texas Commission on Environmental Quality (TCEQ), titled "Coastal Zone Act Reauthorization Amendments (CZARA) - On-Site Sewage Facilities (OSSFs) Coastal Inventory and Chocolate Bayou OSSF Inspections. b) Baffin Bay map depicting land cover and land use layer (USGS 2022). The black crosses indicate the sampling locations of groundwater. The purple/black squares indicate the sampling locations of surface water and porewater in the bay. The green (c), blue (d) and yellow (e) circles indicate LS, RP and PB sampling transects where the surface water and porewater were collected on the beach. S: surface water; W: well/groundwater; P: porewater.

Nitrogen concentration analysis

Measurements of NH_4^+ and NO_3^-/NO_2^- were conducted using the o-phthalaldehyde (Dutta, Kumar et al.) fluorometric (Holmes, Aminot et al. 1999) and colorimetric methods, respectively (Tsikas 2007). After NO_2^- was measured, NO_3^- was reduced to NO_2^- using the cadmium reduction method (Tsunogai, Kido et al. 2008) and concentrations were calculated by subtracting NO_2^- from the measured $NO_3^- + NO_2^-$. Sulfamic acid solution was added to samples that had NO_2^- concentrations over 2% of NO_3^- to remove NO_2^- for isotope analysis of $\delta^{15}N\text{-}NO_3^-$ (Granger and Sigman 2009).

DON concentrations were calculated by subtracting DIN from TDN. First, NH_4^+ was removed from each sample through NH_4^+ diffusion by increasing the pH to 10 (Holmes, McClelland et al. 1998). This NH_4^+ removal step was to reduce the error involved with DON concentration and isotope back calculations. TDN was then oxidized to NO_3^- by the persulfate oxidation method, followed by reduction to NO_2^- via the cadmium reduction method and further analysis by the colorimetric method (Tsunogai, Kido et al. 2008). DON concentrations were calculated by subtracting previously measured $NO_3^- + NO_2^-$ from the TDN pool. Representative DON standards (i.e., urea, glycine, N-acetyl-D-glucosamine) were oxidized and reduced alongside samples to confirm quantitative conversion (>90%) of TDN to NO_2^-. Urea was used as a DON standard since it is a common component in fertilizers and accounts for about 50% of N uptake in many coastal regions (Sipler and Bronk 2015). Glycine was used to represents dissolved free amino acids (DFAA) which are expected to be 1.2 to 12.5% of the total DON pool (Sipler and Bronk 2015). N-acetyl-D-glucosamine represented N-acetyl amino polysaccharides (N-AAPs), which are important to the semi-labile DON pool (Aluwihare, Repeta et al. 2005).

Nitrogen and Oxygen isotope composition analysis

The N and O isotope composition ($\delta^{15}N$/ $\delta^{18}O$) was denoted by the following equation and was reported in permil (‰):

$$\delta_{sample}\,(‰) = (R_{sample}/R_{standard} - 1) * 1000 \quad (4)$$

where R is the ratio of $^{15}N/^{14}N$ or $^{18}O/^{16}O$, respectively. The isotopic composition of NO_3^-/NO_2^- ($\delta^{15}N\text{-}NO_3^-/NO_2^-$ and $\delta^{18}O\text{-}NO_3^-/NO_2^-$) was measured by the denitrifier bacteria method at the University of California, Davis Stable Isotope Facility (Sigman, Casciotti et al. 2001). Internationally recognized standards (USGS32, USGS34, USGS35, IAEA-N3) were measured during sample analysis to provide known $\delta^{15}N\text{-}NO_3^-$ and $\delta^{18}O\text{-}NO_3^-$ references for data correction. Average standard deviations for $\delta^{15}N\text{-}NO_3^-$ and $\delta^{18}O\text{-}NO_3^-$ reference materials were 0.2 and 0.2‰, respectively. The measurement of groundwater $\delta^{18}O\text{-}H_2O$ was done at the Texas A&M University,

College Station. Groundwater $\delta^{18}O\text{-}H_2O$ was reported relative to the Vienna Standard Mean Ocean Water (VSMOW) with uncertainties of 0.1‰.

To measure $\delta^{15}N\text{-}NH_4^+$, NH_4^+ was oxidized to NO_2^- before isotope analysis (Zhang, Altabet et al. 2007, Felix, Elliott et al. 2013). Then the $\delta^{15}N$-DIN (NH_4^+, NO_3^-, and NO_2^-) was measured by the denitrifier bacteria method and $\delta^{15}N\text{-}NH_4^+$ was back calculated using Equation 5:

$$\delta^{15}N\text{-DIN} = f_{NH4+} \times \delta^{15}N\text{-}NH_4^+ + f_{NO3-/NO2-} \times \delta^{15}N\text{-}NO_3^-/NO_2^- \quad (5)$$

where f_{NH4+} is the fraction of NH_4^+ in the DIN pool and $f_{NO2-/NO3-}$ is the fraction of NO_2^- and NO_3^- in the DIN pool. Solutions of international $\delta^{15}N\text{-}NH_4^+$ standards USGS25 and USGS26 were prepared, oxidized, and analyzed in the same manner as the samples for data normalization and to test the efficiency of the coupled method oxidation and denitrifier method. Average standard deviations for the standards were 0.9‰.

To measure $\delta^{15}N$-TDN, first NH_4^+ was removed from the TDN pool via diffusion (Holmes, McClelland et al. 1998). Then the remaining TDN (i.e., NO_3^-, NO_2^- and DON) was oxidized to NO_3^- via the persulfate oxidation method. Analyses of $\delta^{15}N$-TDN were conducted using the denitrifier bacteria method (Knapp, Sigman et al. 2005). $\delta^{15}N$-DON was back calculated using Equation 6:

$$\delta^{15}N\text{-TDN} = f_{DON} \times \delta^{15}N\text{-DON} + f_{DIN} \times \delta^{15}N\text{-DIN} \quad (6)$$

where f_{DON} and f_{DIN} are the fraction of DON and NO_2^- and NO_3^-, respectively, in the TDN pool.

Isotope mixing model

Dual isotope mixing models have been employed in many nitrate studies (Liu, Wu et al. 2018, Li, Li et al. 2019, He, Li et al. 2022). Here we employ the mixing model summarized as Equation 8 and 9, respectively for groundwater samples and is further detailed in Table 1.

$$\delta^{15}N\text{-}NO_3^-{}_{samples} = \sum_{i=1}^{i} f_i(\delta^{15}N_i + C_i) \quad (8)$$

$$\delta^{18}O\text{-}NO_3^-{}_{samples} = \sum_{i=1}^{i} f_i(\delta^{18}O_i + C_i) \quad (9)$$

where: $\delta^{15}N\text{-}NO_3^-{}_{samples}$ and $\delta^{18}O\text{-}NO_3^-{}_{samples}$ are the N and O isotopic compositions of groundwater NO_3^-, respectively; f_i is the fraction of the ith source (e.g., fertilizer NH_4^+, fertilizer NO_3^-, manure NH_4^+, and septic NH_4^+ for groundwater samples); $\delta^{15}N_i/\delta^{18}O_i$ is the $\delta^{15}N/\delta^{18}O$ value of the ith source; C_i is the fractionation factor applied on the ith source.

Table 1. Primary sources and potential fractionations of NO_3^- stable isotope mixing model for groundwater (Xue, Botte et al. 2009, Granger and Wankel 2016, Nikolenko, Jurado et al. 2018). Groundwater NH_4^+ concentrations were below detection limit during the sampling period indicating nitrification process was thorough and the fractionation should be negligible if nitrification occurred. [a] is the estimated $\delta^{18}O\text{-}NO_3^-$ generated through nitrification following $\delta^{18}O\text{-}NO_3^- = \delta^{18}O\text{-}O_2/3 + 2*\delta^{18}O\text{-}H_2O/3$. [b] is the reported denitrification oxygen fractionation applied to group I, which is the same as nitrogen fractionation (Granger and Wankel 2016). [c] is the denitrification oxygen fractionation applied to group II, which is the fifth of nitrogen fractionation as the slope of $\delta^{18}O\text{-}NO_3^-$: $\delta^{15}N\text{-}NO_3^-$ is 0.2 (Figure 6b). Denitrification fractionation is not applied to group III as it displays a weak $\delta^{18}O\text{-}NO_3^-$: $\delta^{15}N\text{-}NO_3^-$ correlation, suggesting denitrification is insignificant in this system (Figure 6b).

	$\delta^{15}N$ (Xue, Botte et al. 2009, Nikolenko, Jurado et al. 2018)	$\delta^{18}O$ (Xue, Botte et al. 2009, Nikolenko, Jurado et al. 2018)	Denitrification fractionation on $N\text{-}NO_3^-$ (Granger and Wankel 2016)	Denitrification fractionation on $O\text{-}NO_3^-$ (Granger and Wankel 2016)
Fertilizer NH_4^+	0 ± 3‰	5.2 ± 0.4‰[a]	15 ± 10‰	15 ± 10‰[b]; 3 ± 2‰[c]
Fertilizer NO_3^-	0 ± 3‰	21 ± 4‰	15 ± 10‰	15 ± 10‰[b]; 3 ± 2‰[c]
Manure NH_4^+	7.4 ± 3.8‰	5.2 ± 0.4‰[a]	15 ± 10‰	15 ± 10‰[b]; 3 ± 2‰[c]
Septic NH_4^+	4.4 ± 4.6‰	5.2 ± 0.4‰[a]	15 ± 10‰	15 ± 10‰[b]; 3 ± 2‰[c]

Submarine Groundwater Discharge Estimates

SGD rates were calculated using Darcy's law, time-series ^{222}Rn, and radium activities, as described below.

Darcy Discharge Rate Estimates

Darcy's law estimates of groundwater velocity (*v*, Darcy's Law formulas below) of "local" shallow, brackish to hypersaline SGD were derived using water level data from the groundwater monitoring wells (Figure 3). Hydraulic conductivity data was estimated from a series of well core data collected at the installation of each monitoring site. Different soil types have distinct hydrologic properties, with certain regions more susceptible to surface infiltration and aquifer recharge and, thus, nutrient inputs. To account for this, a subsurface profile for each well was created and the gaps were filled with interpolations using a fence diagram. Sedimentary layer information was determined from these diagrams. This field analysis provided knowledge about how grain size, sorting, composition, and porosity changed with depth. The subsequent soil layers were categorized into clay, clay with sand, sand, sandy clay, and vertisol. With these categories

and an idea of where the water table lies, base hydraulic conductivity values ranged between 10^{-4} to 10^{-6} cm/s, as dependent on the sedimentary make-up of the conductive saturated layer using standard values from Fetter (2001).

Darcy's Law analysis was performed using the true or seepage velocity formula: $v = K \cdot i/n$; where K is the hydraulic conductivity, i is the hydraulic gradient, and n is effective porosity.

The distance used to calculate the hydraulic gradient came from estimated flow paths on a groundwater elevation interpolation map (Fig 3). The calculations focus on three major flow paths drawn in Figure 3 around the study site. Due to their proximity to Flow Paths 1, 2, and 3, groundwater elevation levels from Wells 9, 8 and 1 were used for the calculations, respectively. Flow Paths 1 and 2 discharge to the Cayo del Grullo, while Flow Path 3 discharges to the Laguna Salada. Tidal activity was subtracted from the seasonal groundwater level at each well to get a true idea of the water's change in distance. An effective porosity ranging from 0.05 to 0.15 was used for velocity estimates.

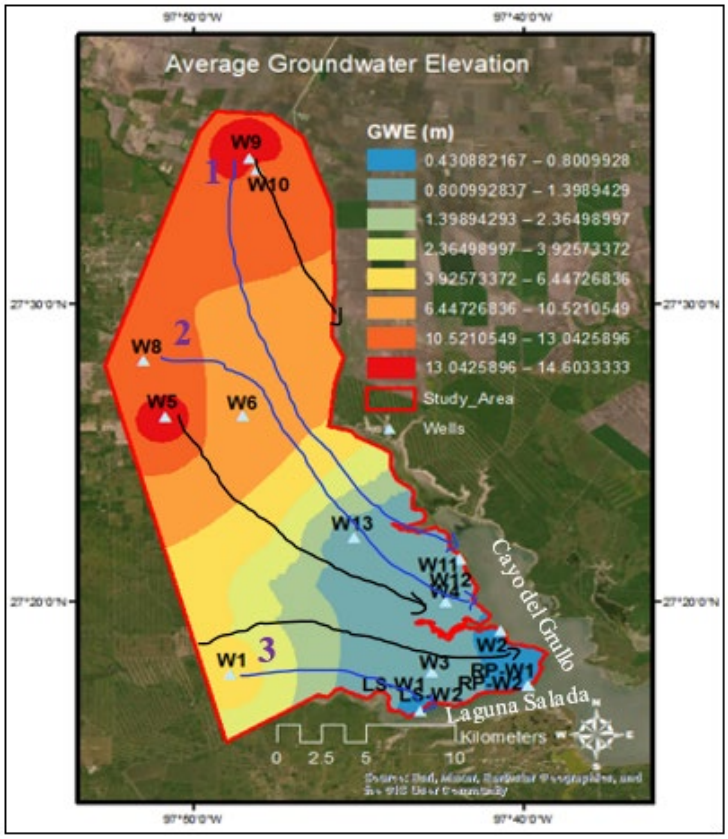

Figure 3. Flow paths derived from an average groundwater elevation map. Three paths are emphasized in blue and represent distinct regions throughout the study site.

Radiogenic Isotopes SGD Rate Estimates

Radium mass balance and SGD Rates

Samples for radium (radium-224 [^{224}Ra], radium-226 [^{226}Ra]) analysis were collected in three-20L jugs (approximately 45 to 60 L total volume) at each of the two sampling sites using a sump pump positioned ~0.2 m above the sediment-water interface. The radium was extracted by processing the samples through ~15g manganese dioxide, MnO_2, impregnated acrylic fibers two times at a flow rate <1 L·min^{-1} (Kim, Burnett et al. 2001, Dimova, Burnett et al. 2007). The Mn-fibers were then rinsed thoroughly with Ra-free water to eliminate any salts or particulates and then pressed to a water to fiber ration of 0.3-1g (i.e. 20-30g wet weight) (Sun and Torgersen 1998). The fibers were tested for ^{224}Ra (half-life: 3.6 days) on a Radium Delayed Coincidence Counter (RaDeCC). Activities of ^{224}Ra were measured within three days of collection given the short half-life (Moore 2006). After the short-lived isotope measurements, the fibers were flushed with nitrogen gas and sealed for >21 days to reach secular equilibrium before measuring the ^{226}Ra (half-life: 1,600 years) on a RAD-7 with measurements corrected to a calibration curve determined from 5 standards (Moore 1996).

Radium-226 based SGD estimates, representative of the portion of the bay where measurements were conducted (Charette, Buesseler et al. 2001), were determined using a radium mass balance approach. Radium apparent age (T_r) is an essential term in the radium mass, and although not direct measurements of bay residence times, they are an indicator of how fast water moves through the porous media (Swarzenski, Reich et al. 2007). Relative radium apparent ages of the surface water represent the relative time that has passed since Ra first entered a well-mixed estuary, and therefore has been separated from its radionuclide source (i.e., subsurface sediments). They were calculated using the activity ratio (AR) of the short-lived ^{224}Ra ($t_{½}$ = 3.66 days) to the longer-lived ^{226}Ra ($t_{½}$ = 1,600 yr) isotope, i.e., equation 4, following the steps described in numerous previous studies (Moore 2000, Dulaiova and Burnett 2008, Knee, Garcia-Solsona et al. 2011).

$$T_r = \frac{AR_{GW} - AR_{CO}}{AR_{CO} \times \lambda_{224}} \quad (4)$$

where AR_{GW} is the initial activity ratio of the discharging groundwater source, AR_{CO} is the measured activity ratio of the surface water at the station of interest, and λ_{224} is the decay constant (d^{-1}) for the short-lived ^{224}Ra isotope.

A mass balance was developed for each location to determine the excess ^{226}Ra (due to groundwater flux) in the bay. Briefly, this includes all sources of radium other than groundwater, including tidal exchange, riverine dissolved input (where applicable), desorption from riverine suspended sediments, and decay (i.e., ^{224}Ra). The mathematical expression and detailed explanation of terms are found in Moore (1996) and (Lopez, Murgulet et al. 2020). Expressed mathematically, excess ^{226}Ra ($^{226}Ra_{ex}$ [Bq·d^{-1}]) in the bay equals:

$$Ra_{ex} = \left[\frac{(Ra_{BB} - Ra_{Sea})V_{bay}}{T_r}\right] - [Ra_r Q_r] - [Ra_{des} Q_r] + [(1 - e^{\lambda T_r})V_{Bay}] \quad (5)$$

where Ra_{BB} is the average measured ^{226}Ra activity in the bay; Ra_{sea} is the average ^{226}Ra activity in the offshore water body (i.e., Laguna Madre in the case of Baffin Bay), which exchanges tidally with the bay of interest; Ra_r is the average ^{226}Ra activity from rivers and streams, Ra_{des} is the average ^{226}Ra activity from desorption experiments, Q_r is the average stream discharge, V_{bay} is the volume of the bay of interest; T_r is the residence time, or flushing rate, estimated from the apparent radium water ages (i.e., equation 4).

Endmembers for offshore or tidal influence were selected from previous projects (Spalt, Murgulet et al. 2019, Douglas, Murgulet et al. 2020, Lopez, Murgulet et al. 2020) or from the lowest activity sample in a time series, which acts as a background activity level, providing a conservative excess radium measurement, similar to Peterson, Burnett et al. (2008). Specific to this study, desorption laboratory experiments from sediment cores, conducted following the experimental setup by Sadat-Noori, Santos et al. (2016), collected at each location showed that the dissolved ^{226}Ra fluxes from bottom sediments alone ($\bar{x}$: 1.2 dpm·m^{-2}·d^{-1} and 1.9x10^{-4} dpm·m^{-2}·d^{-1}, respectively) were negligible. This agrees with other studies that excluded sediment desorption from the ^{226}Ra mass balance (Moore 2000, Beck, Rapaglia et al. 2007, Beck, Rapaglia et al. 2008, Sadat-Noori, Santos et al. 2016, Tait, Maher et al. 2017, Lopez, Murgulet et al. 2020). For radium input from riverine discharge, radium desorption experiments were conducted using riverbed sediment samples (i.e., 0 -10 cm) from the freshwater portion of bay tributaries. Bay water samples, of salinities 20 and 30, were filtered through Whatman GF/F filters to remove suspended solids and processed as described by Lopez, Murgulet et al. (2020) and references therein (Ward and Armstrong 1997, Gonneea, Morris et al. 2008). Riverine contributions of ^{226}Ra, , were determined by normalizing the total activity to the sediment mass, multiplied by the respective season tributaries sediment flux from USGS and Texas Water Development Board's (TWDB) modeled

freshwater inflows (TWDB 2019, TWDB 2019, TWDB 2019, USGS 2019, USGS 2019). The TWDB modelled inflows include the ephemeral creek discharges, surface runoff, and return flows to the creeks. The decay rate of ^{226}Ra was neglected, given that its half-life is much longer with respect to the bay mixing time.

The excess activity from the mass balance is assumed to be the result of SGD. Using the porewater endmember activity (Ra_{PW}) for ^{226}Ra at each location for the corresponding season, SGD is calculated from:

$$SGD_{Ra} = \frac{Ra_{ex}}{Ra_{PW}} \quad (6)$$

Douglas, Murgulet et al. (2020) and Lopez, Murgulet et al. (2020), found that SGD estimates using both porewater and groundwater endmembers were in close agreement, but seasonal fluctuations in porewater radium activities need to be accounted for. Porewater geochemical characteristics reflect mixing of terrestrial and marine (i.e., recirculated seawater) sources and any deep groundwater short-lived radium isotope would approach equilibrium with near surface sediments before entering surface water (Knee, Garcia-Solsona et al. 2011). Thus, they are likely the most representative endmember.

Radon mass balance and SGD Rates

All porewater and groundwater samples for ^{222}Rn analysis were collected in 250 mL gas-tight borosilicate bottles filled from the bottom and allowed to overflow for one volume before being sealed with no headspace. Measurements of ^{222}Rn were conducted with a Durridge RAD-7 following the WAT250 protocol (Durridge Company Inc. 2017) within 2 days of sample collection to prevent loss due to decay (half-life 3.8 days) and decay corrected to time of sampling. Surface water samples from Los Olmos Creek or offshore surface water were collected in 2L bottles and ^{222}Rn was measured using the Durridge RAD7 radon-in-air monitor with the soda bottle accessories and protocols (Lee and Kim 2006).

Stationary time series measurements of ^{222}Rn were used to construct a mass balance and inventory as described in detail by Burnett and Dulaiova (2003), Lambert and Burnett (2003), Smith and Robbins (2012), and references therein. The inventory of ^{222}Rn over time allows for an evaluation of losses/gains due to mixing with waters of different ^{222}Rn activities (i.e., depleted offshore waters), atmospheric evasion, and sediment inputs. Therefore, changes over time, if any, are used to determine ^{222}Rn fluxes (F_{total}) as shown in equation 4. Water fluxes ($cm \cdot d^{-1}$) were estimated by dividing ^{222}Rn fluxes by the ^{222}Rn activity of the advective groundwater fluids ($^{222}Rn_{gw}$) (Burnett and Dulaiova 2003), as shown below:

$$SGD = \frac{F_{total}}{^{222}Rn_{gw}} = \frac{[z(A_{Rn} - \lambda_{222}A_{Ra})] + F_o - F_i - F_{sed} + F_{atm} \pm F_{mix}}{^{222}Rn_{gw}} \quad (7)$$

where A_{Rn} is the activity of ^{222}Rn in the water column, $\lambda_{222}A_{Ra}$ is the flux of ^{222}Rn due to production from dissolved ^{226}Ra in the water column, z is the water column depth, F_o is the offshore flux (flood tide), F_i is the inshore/nearshore flux (ebb tide), F_{sed} is the sediment flux, F_{atm} is the losses due to atmospheric evasion, and F_{mix} is the losses due to mixing processes. Using the total flux (F_{total}) and the excess ^{222}Rn of the advective fluids ($^{222}Rn_{GW}$), which in this study is the activity of ^{222}Rn in groundwater, ^{222}Rn fluxes (F_{total}) are converted to SGD as in equation 3.

Although short term tidal fluctuations are insignificant in this area (no more than 12 cm observed for the duration of time series at all sites and seasons), the mass balance accounts for any change in water level throughout the monitoring period from hourly measurements at the RAD7 intake. Offshore endmember selection during the time series has proven difficult given sudden changes in wind direction, thus, changes in direction of flow and endmember activity. For that reason, the maximum absolute values of the observed negative fluxes during each time-series event

were used to correct ^{222}Rn fluxes for losses via mixing, after correction for atmospheric evasion. Given the persistent winds and the shallow nature of these systems, there are concerns that atmospheric evasion may not accurately be estimated by the ^{222}Rn mass-balance (Spalt, Murgulet et al. 2018, Lopez, Murgulet et al. 2020). To compensate for this, gas transfer velocities, were calculated using wind speeds for the day and the preceding two days of sampling (Rodellas, Stieglitz et al. 2021).

Corrections for in-situ production of ^{222}Rn were done using surface water ^{226}Ra at high and low tides during each sampling event. Sediment-supported ^{222}Rn was derived from laboratory equilibration experiments using site-specific sediment cores (ranging in length from 21 to 59 cm, $\bar{x}$ core length 38.6 cm) as outlined by Corbett, Burnett et al. (1998).

Groundwater Characteristics

Seasonal Change

To further analyze nutrient loading in Baffin Bay, continuous data was used to assess how concentrations varied throughout the year. Seasonal patterns can reveal periods susceptible to HABs and other detrimental consequences of a nutrient flux. To help visualize this, data collected throughout the study period was divided into four seasons and plotted in Excel to illustrate differences in nutrient concentrations with standard bar and line graphs. The 3-D Map function was also utilized to help visualize spatial characteristics in an accessible fashion. Data was interpolated in ArcGIS, and an IDW methodology was utilized due to the low density of data points and the small scale of the study area. The scale and colors of the maps were normalized to ensure ease of comparison.

For the stable isotope and some of the nutrient results and discussion sections, seasons were divided meteorologically with Spring referred to as March to May, Summer as June to August, Fall as September to November, and Winter as December to February. To simplify the results and discussion, wells were classified according to similar characteristics by K means clustering. W1, 2, 3, 5 and 10 were classified as group I, W4, 6, 8, 9 and 13 were classified as group II and W11 and 12 were classified as group III (Figure 4). The comparisons of concentrations and isotope compositions among samples/seasons/wet-dry periods/groups were conducted using the analysis of variance (ANOVA). When the p value was lower than 0.05, the result was significantly/statistically different; when the p value was higher than 0.05, the result was not different. The correlations between analytes were conducted using the Pearson Correlation method.

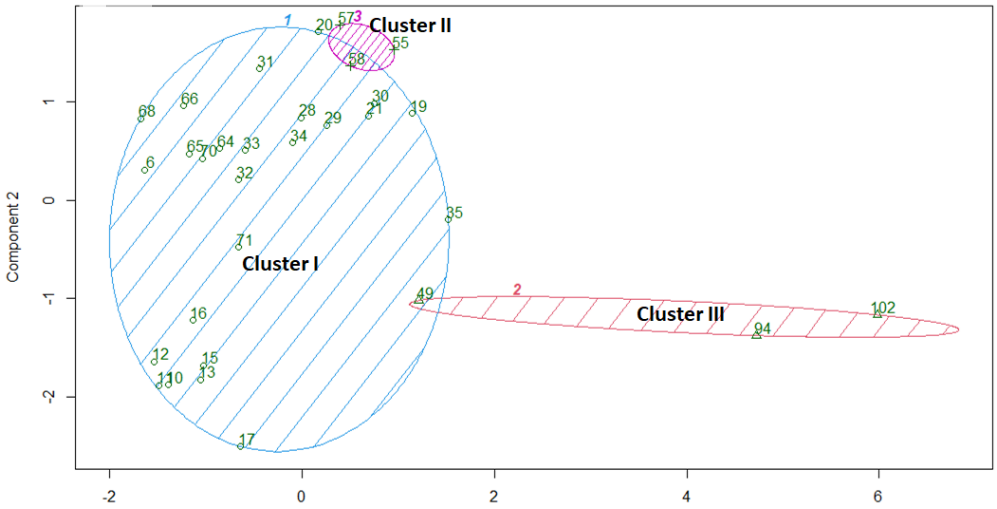

Figure 4. The K-means clusters of groundwater groups that takes into account NO_3^- and DON concentrations $\delta^{15}N\text{-}NO_3^-$, $\delta^{18}O\text{-}NO_3^-$, $\delta^{15}N\text{-}DON$, dissolved oxygen concentrations, and salinities. W1, 2, 3, 5 and 8 fall in cluster I, W4 and 6 fall in cluster II and W11 and 12 fall in cluster III. W9, 10 and 13 had too many missing data to apply the K-means clustering as the algorithm cannot deal with not available data. Strong linear correlations are found in $\delta^{15}N\text{-}NO_3^-$: $\delta^{18}O\text{-}NO_3^-$ trajectories when W10 is plotted with wells in cluster I and W9 and 13 are plotted with wells in cluster II (Figure 6b), suggesting W10 could fall within cluster I and W9 and 13 within cluster II. Another component the K-means algorithm cannot deal with is the soil texture feature.

Groundwater Recharge Estimates

Seasonal groundwater recharge rates were determined for wells based on continuous piezometer data collected in the middle of the study period, between April and July of 2021, using the following equation:

$$R(tj) = Sy^* (dh/dt)$$

This method of calculation is useful for estimating recharge rates for shallow, unconfined aquifers and assumes that a change in water table level is due to the arrival of recharge rainwater (Healy and Cook, 2002). In the equation, *Sy* represents specific yield, *dh* is the change in height in the water table, and *dt* is the length of time in which the change occurred. Specific yield values were derived from previously mentioned well-core data. Because there was a consistent layer of sandy material where the aquifer was expected, a Sy of 0.15 was used (Johnson, 1967).

To compare recharge across the wells, a singular abnormally heavy May rainfall was used to determine the change in water level pre- and post-event. On May 19th, 2021, around 3.5 inches of rain fell on the Baffin Bay region. Consequently, this period was chosen because each of the well's groundwater elevations showed a sharp, meaning that the water table's response could be compared at different locations within the same time frame. This provided an interesting perspective of how recharge rates varied by location.

Results

Subsurface Composition

In the Baffin Bay study area, the shallow substrate is highly heterogenous with soil profiles that vary with both depth and location (Figures 5 and 6). Relative to continuity of the subsurface profile, several layers are maintained throughout most of the study site. Almost every well has a

thin layer of vertisol, or clay-rich soil that tends to shrink and swell when in contact with water (USDA, 2021). Wells 5, 8, 9, and 10 are located further inland and therefore reside at a higher elevation above sea level than wells closer to the bay. Subsequently, the first three or four layers beneath these wells do not span across the study site. The first layer in the fence diagram that is continuous is about 12 feet below the surface at Wells 8, 9, and 10 towards the northern portion of the study site. This layer is comprised of clay with chalk, but also shows pockets of sand. Directly below this layer, a strip of clay runs parallel along the core transect, followed by a sandy clay layer. At the bottom of the diagram which represents the vertical extent of the drilling, a sand layer is present at most locations.

At the northern end of the diagram where well depth is greater, several discontinuous layers are evident. Just a few feet beneath the surface of Wells 9 and 10, a thin layer of sand overlays a clay-rich area that runs south about halfway across the study site. Then, there is a sandy clay layer that appears to be of similar length. Beneath Wells 5 and 8, a relatively thick sandy clay layer stretches northward, ending just shy of Wells 9 and 10. Finally, Well 1 data shows a thick sand layer extending about 20 feet below the surface. To note, the vertosols clay is not continuous and, when dry, it develops large crevices that act as a rock with a dense network of fractures that act as conduits for recharge immediately following rain events. Also, to note is that both the sandy-clayey soils and the thin clay-rich layer deeper in the subsurface are absent in the deep incised creek valleys and the human-made canals. Therefore, it is expected that these water bodies are in direct contact with the water table aquifer.

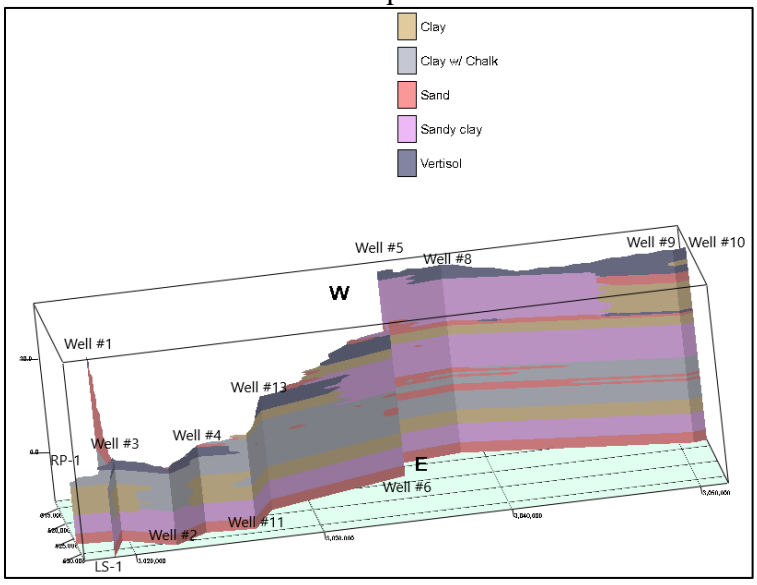

Figure 5. East perspective of the subsurface composition in the Baffin Bay study area (from Figure 1)

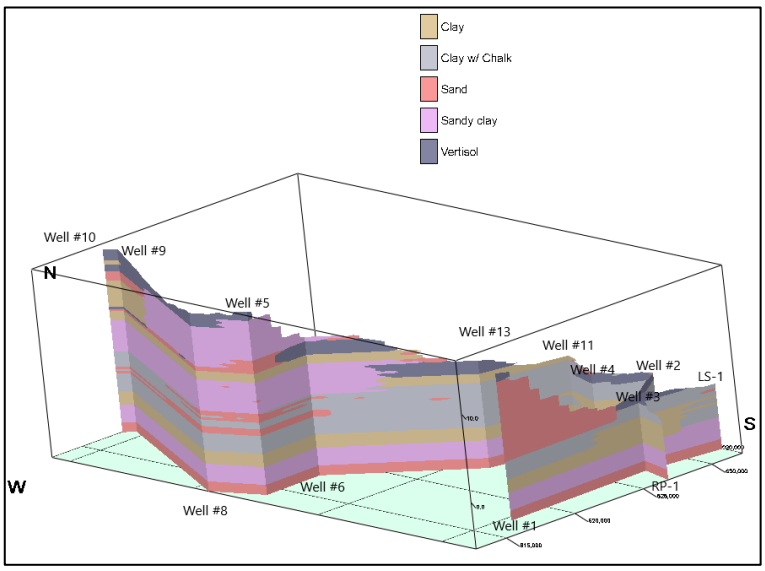

Figure 6. Southwest perspective of the subsurface

Groundwater Recharge

Groundwater levels range from about half a meter at Well 4 to above 15 meters above mean sea level at Well 5. (Figure 7). Visually, the largest changes appear to occur within Wells 4 and 6, with both undergoing rapid transitions to a higher groundwater elevation. This is confirmed in Figure 8a which shows that Well 4 rose 117 cm and Well 6 increased by 107 cm. The smallest shift after the rain event occurred at Well 9, which rose about 36 cm after the rain event. However, Well 10 was similar with a 37 cm increase. Wells 9 and 10 are located in very similar geographic proximity to each other, and much further inland, adjacent to a stream.

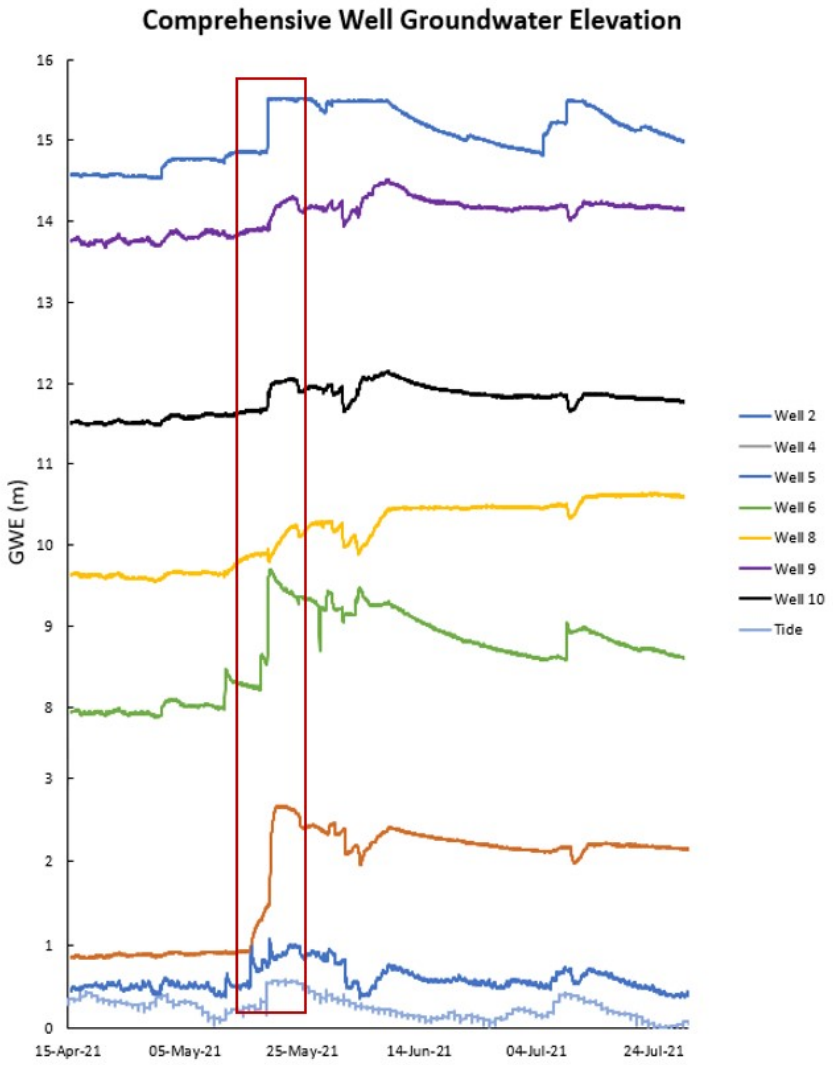

Figure 7. Continuous groundwater elevation data for multiple wells within the study site. A large 3.6-inch rain event is demarcated by the red boxed area, revealing where a rapid increase in water table elevation is seen for all the wells. Tidal movement during the study period is also plotted at the bottom of the graph to observe whether any movement of the low groundwater elevation wells was due to tides rather than recharge from precipitation. Well 2 was omitted from further analysis due to its apparent influence from daily tidal variation.

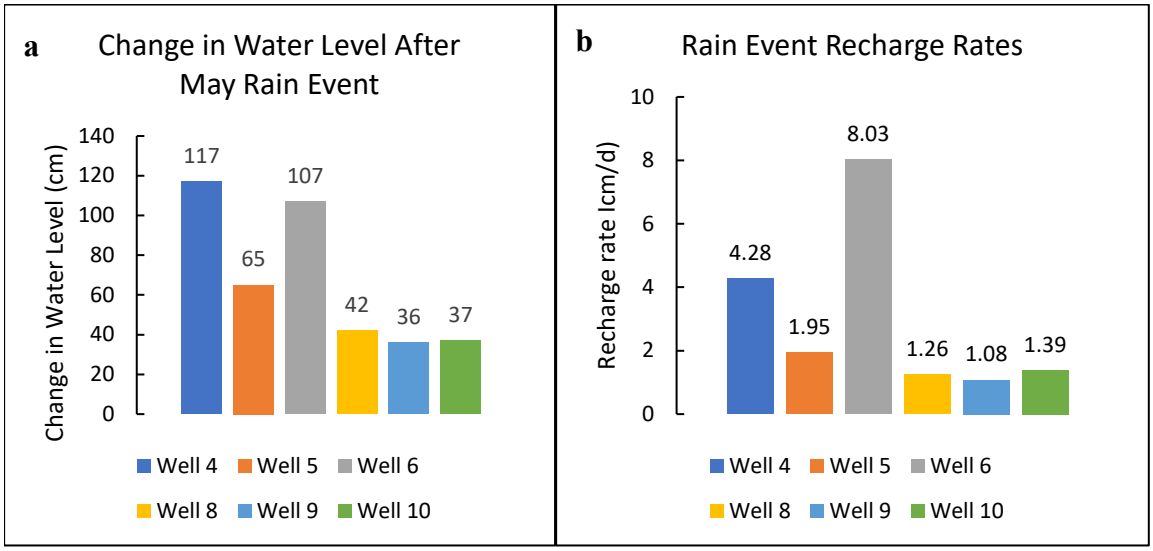

Figure 8. a. Change in water level (cm) directly following a significant (~3.6 in) rain event in May 2021. The rise in groundwater level was measured from the start of the rain event to the peak where water began to drop once again. **b.** The calculated recharge rates are based on the water table fluctuation method. The rate is based on an average specific yield for the typical soil type of the aquifer which was 0.15.

Aquifer recharge rates calculated for each well are illustrated in Figure 8b. According to the data, the fastest recharge rate occurred at Well 6, which increased at a rate of 8.03 cm/d until it reached its peak elevation post-rain event. Well 4 had the next highest rate at 4.28 cm/d, followed by Well 5 at 1.95 cm/d. After these locations, there was a drop off in rate values, and Wells 8, 9, and 10 all fell within 1.08 to 1.39 cm/d. The overall average for each of the wells in Figure 8b was about 3 cm/d. It is important to note that the calculated recharge rates are a result of infiltration from precipitation and losses due to discharge to surface water, even though calculations only take into account precipitation amounts and not rates at which groundwater leaves the system as SGD, for instance.

Nutrients

Inorganic and Organic Nitrogen concentrations

Temporal Inorganic Nitrogen Groundwater Concentrations

Inorganic nutrient concentrations varied dramatically by well type (Figure 9a, b). For inland wells, the dominant form of nitrogen was NO_3^-. Relative to seasonal distribution, the highest concentrations occurred in Summer 2021, with an average of 1257 µM. Winter 2020-21 had the lowest average concentrations at 722 µM. The groundwater bordering the Baffin Bay shoreline at LS and RP wells, on the other hand, showed a much different pattern, with values ranging from 22.2 µM in Summer 2021 to 36.6 µM in Summer 2022. Concentration patterns for NH_4^+ were inversely related. For this parameter, inland wells had a minute amount of NO_3^- with only Fall 2021 and Spring 2022 having observable levels. Conversely, groundwater at LS and RP had higher concentrations, ranging from 225 µM to 276 µM.

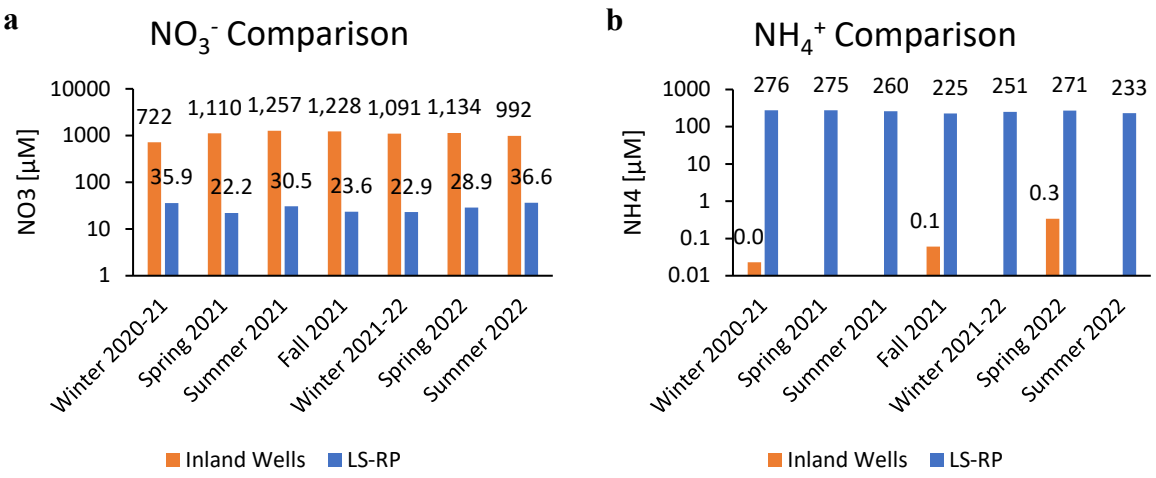

Figure 9. **a.** Seasonal NO_3^- concentrations throughout the study period. There is a striking difference between inland wells and LS-RP wells with inland regions displaying much higher values across the board. **b**. Seasonal NH_4^+ concentrations. Like NO_3^-, a strong contrast exists between inland and LS-RP wells, but in an opposite direction.

Due to the sharp divide in inorganic nutrient type, NO_3^- was further plotted for the inland wells, and NH_4^+ for the LS and RP wells. Temporal analysis illustrates how concentrations of each nutrient type varied across time. Figure 10a, b shows that for inland wells, NO_3^- values are relatively steady across time except for Wells 11 and 4. Well 11 saw a sharp increase in May 2021 before returning to a level more in line with other wells, although still very high (~2000 µM). Well 4, on the other hand, had a more erratic trajectory and ranged from 1220 µM to 7601 µM. Concentrations never reached the initial value from the beginning of the sampling period.

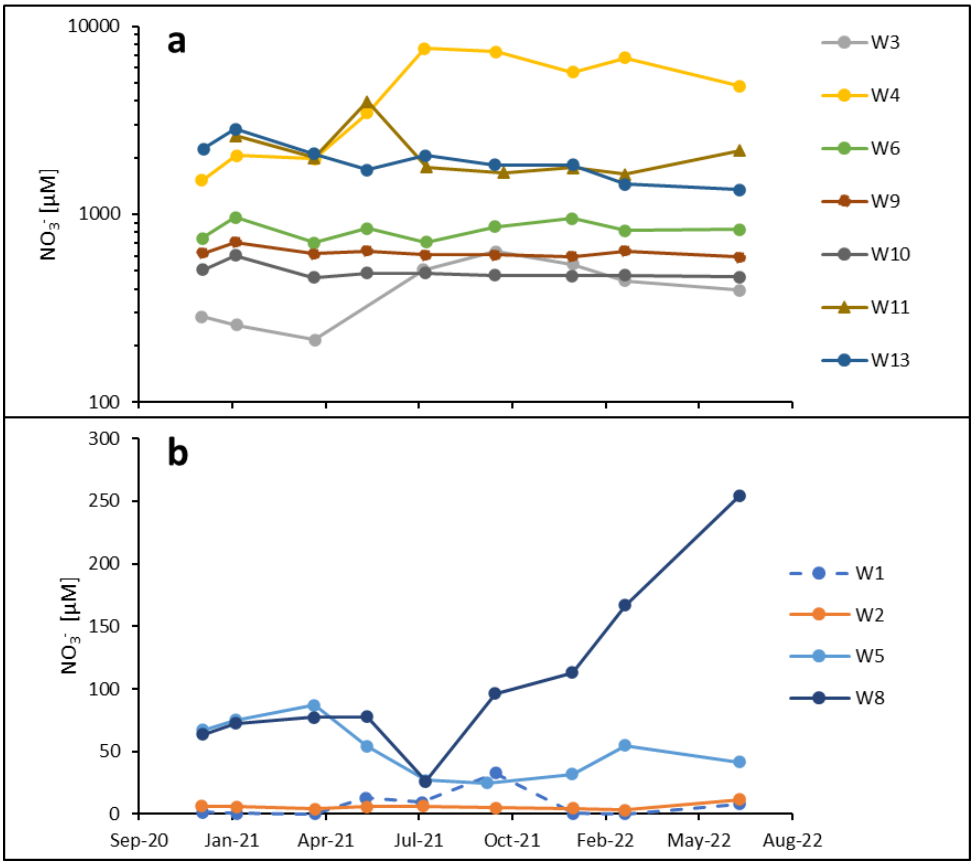

Figure 10. a) Temporal NO_3^- concentrations for inland Wells 3, 4, 6,9,10,11, and 13. **B)** Temporal NO_3^- concentrations for inland Wells 1, 2, 5, 8. Note that wells are plotted separately by their concentrations for better visualization. Well 4 exhibits noticeably higher concentrations, especially starting in July 2021, where it peaks at 7621 µM.

At the LS and RP, NH_4^+ dominates, specifically at LS-W1 (Figure 11), which had consistently NH_4^+ levels above 600 µM, while LS-W2, RP-W1, and RP-W2 were less than 100 µM. The highest concentration for LS-W1 was in May 2021 with a concentration of 1184 µM. LS-W2, the second location with the most abundant ammonium levels, peaked at about 76 µM in January 2021.

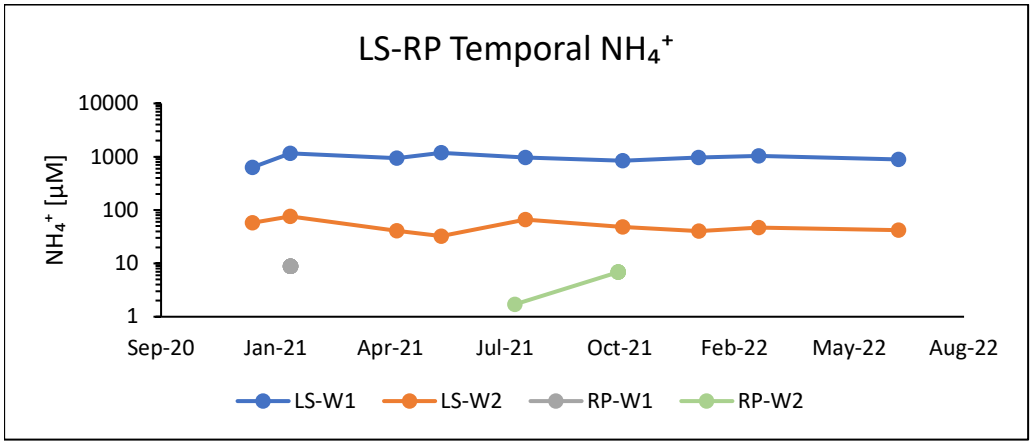

Figure 11. Temporal NH_4^+ data for LS and RP wells. LS-W1 consistently displays higher ammonium values, even relative to the LS-W2 counterpart.

Groundwater Inorganic Nitrogen Temporal and Spatial Variation

ArcGIS interpolation analysis shows both spatial and temporal seasonal variation in nutrient concentrations. Nitrate concentrations were consistently highest at the wells near or bordering Baffin Bay, specifically along the Cayo del Grullo (Wells 13, 11, 12, 4, and 1). Here, groundwater elevation is typically low due to proximity to the bay. Lower concentrations tend to be located further inland (Wells 8, 5, 10), as well as along the Laguna Salada (LS-W1, LS-W2, and W3) (Figures 12 and 13). Fall had the highest concentrations among the seasons, at around 5000-7000 µM (Figure 12) around Well 4.

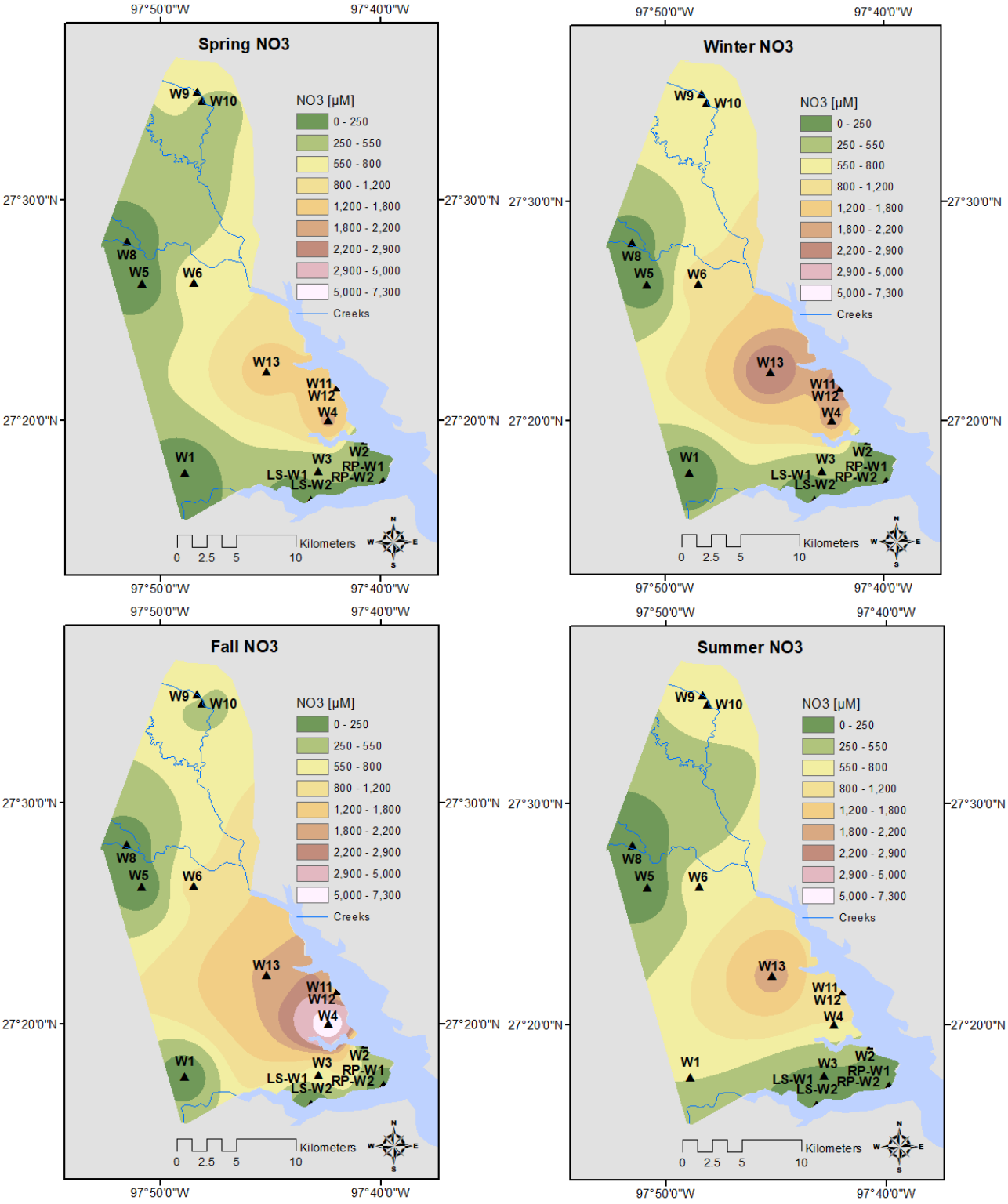

Figure 12. Seasonal nitrate concentrations within the study period. The highest values occur in Fall, reaching the 5000-7300 µM categorization.

As mentioned previously, nutrient concentrations at the LS and RP wells were consistently lower in NO_3^- (the green color scheme on the map). Besides differing values, the maps show relatively constant spatial distribution of higher and lower concentrations. Winter and Fall tend to be especially similar with the most prominent concentrations between 250-550 µM. Likewise, Spring and Summer concentrations resemble, but the predominant concentration range was higher, between 550-800 µM.

Ammonium interpolation maps also reveal some degree of variation, although not as noticeable as NO_3^- (Figure 14 and 15). By far, the most prominent range of values is 0-70 µM, which covers much of the north and central portions of the site every season. Winter, Spring, and Fall are very similar in both spatial distributions and concentration levels, with the maximum range

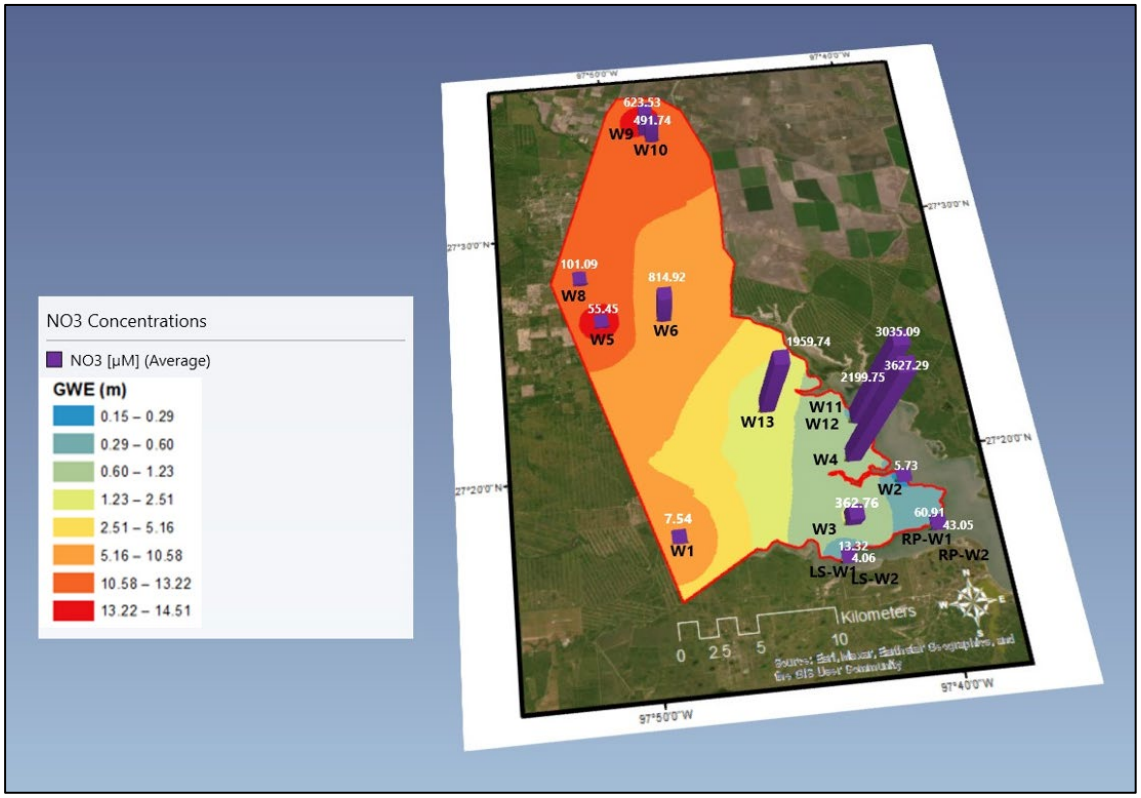

Figure 13. 3-D map illustrating how nitrate concentrations vary by location. These values are also overlayed on a groundwater elevation map. Most of the high values occur along the Cayo del Grullo in shallow groundwater elevation territory.

being around 250-360 µM. In Summer, the higher value areas spread more laterally to the west, with the 140-215 µM concentration reaching as far as Well 1. These figures reaffirm that areas around the LS and RP wells are dominated by NH_4^+ rather than NO_3^-. As clearly shown in Figure 15, this form of nitrogen is virtually absent within inland groundwater.

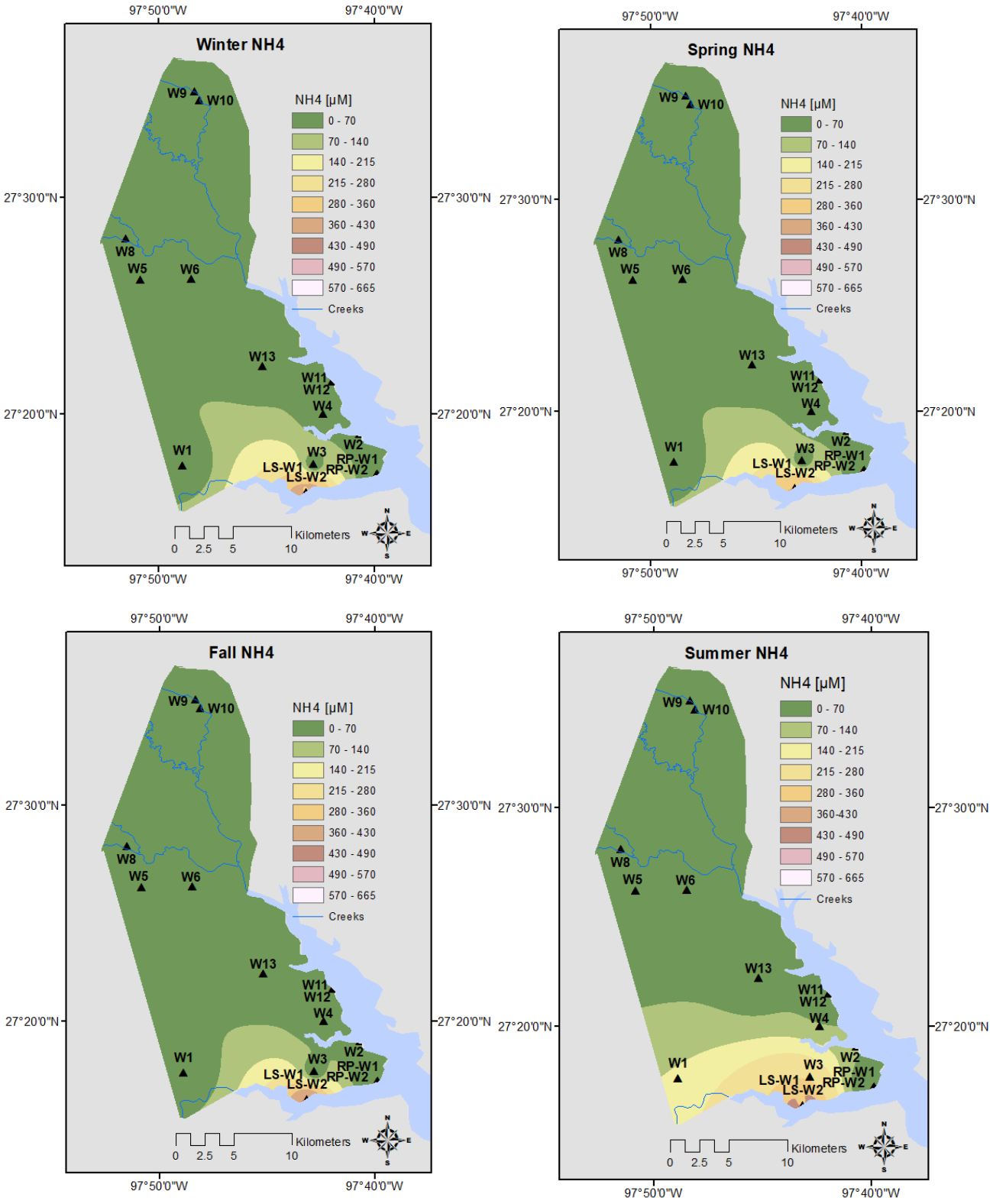

Figure 14. Seasonal NH_4^+ concentrations within the study period. The primary difference lies in Summer, where the higher value areas extend further to the west relative to other seasons.

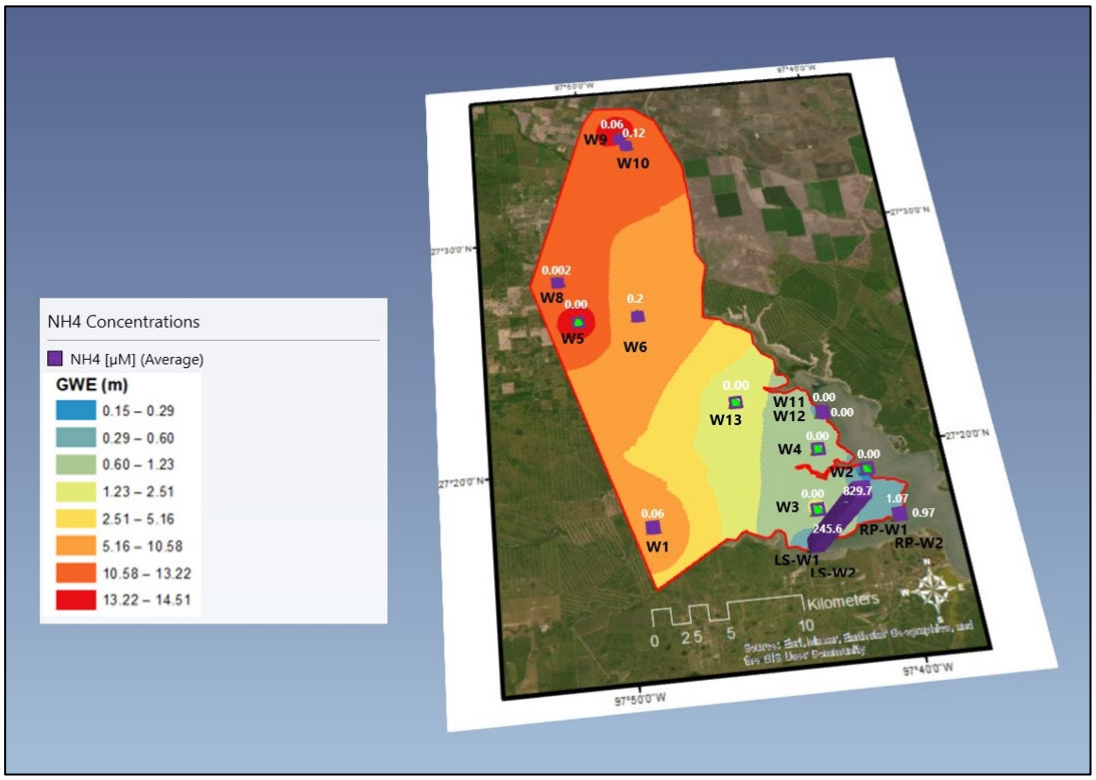

Figure 15. 3-D map illustrating how NH_4^+ concentrations vary by location. These values are also overlayed on a groundwater elevation map. Most of the high values occur along Laguna Salada in very shallow groundwater elevation wells.

Spatial and Temporal Variations of NH_4^+ and $\delta^{15}N$-NH_4^+

Porewater ($\bar{x}$: 324.6 ± 188.0 µM, n = 75) had higher NH_4^+ concentrations than surface water ($\bar{x}$: 1.3 ± 1.7 µM, n = 77) and groundwater ($\bar{x}$: below detection limit, n = 100) ($p < 0.05$) (Figure 16). P4 ($\bar{x}$: 188.5 ± 63.2 µM, n = 8) and P6 ($\bar{x}$: 139.5 ± 171.4 µM, n = 7) had lower NH_4^+ concentrations than the other porewaters ($p < 0.05$). Although not significant, porewater NH_4^+ was slightly higher in Summer 2021 ($\bar{x}$: 373.4 ± 165.9 µM, n = 19) than the other sampling events ($\bar{x}$: 308.0 ± 193.5 µM, n = 56) ($p = 0.2$).

Groundwater did not have $\delta^{15}N$-NH_4^+ values available as none of groundwater samples had NH_4^+ concentrations higher than the isotope method detection limit (i.e., 3 µM). Surface water ($\bar{x}$: 8.8 ± 6.9‰, n = 77) had higher $\delta^{15}N$-NH_4^+ values than porewater ($\bar{x}$: 4.1 ± 7.3‰, n = 65) ($p < 0.05$) (Figure 17). Surface water $\delta^{15}N$-NH_4^+ values did not display significant spatial ($p = 0.4$) or temporal ($p = 0.3$) variations. The porewater $\delta^{15}N$-NH_4^+ values were lower in summer 2021 ($\bar{x}$: -3.8 ± 7.4‰, n = 19) when compared to the other sampling events ($\bar{x}$: 7.4 ± 5.7‰, n = 46) ($p < 0.05$).

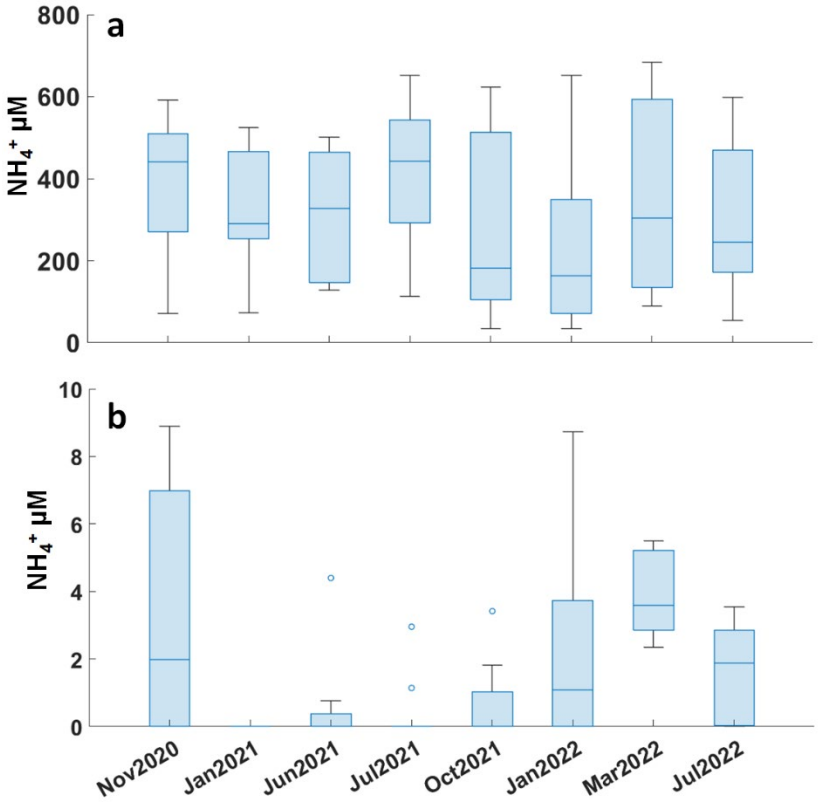

Figure 16. NH_4^+ concentrations of porewater (a) and surface water (b) over the sampling period. The NH_4^+ concentrations of groundwater were below the detection limit during the sampling period, thus were not plotted on the graph.

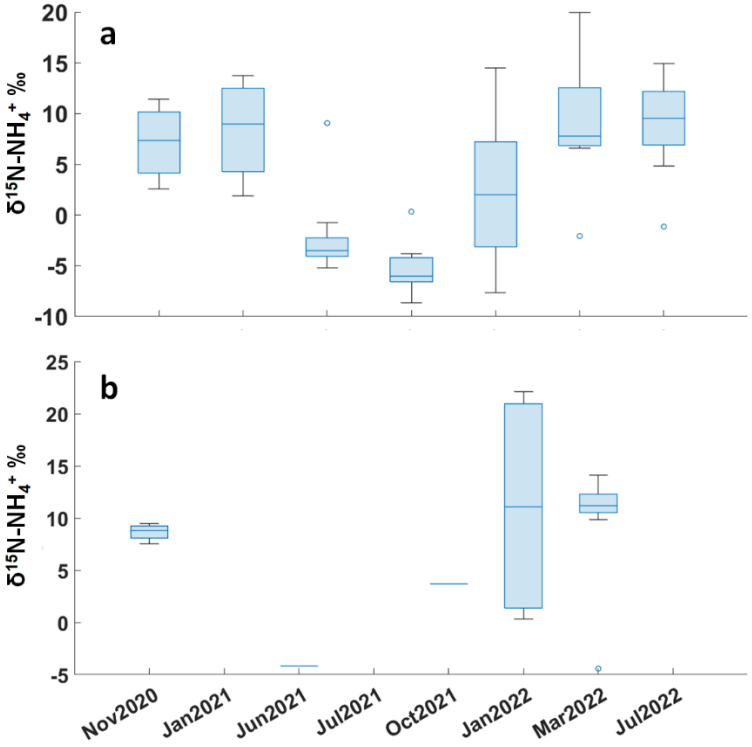

Figure 17. $\delta^{15}N\text{-}NH_4^+$ values of porewater (a) and surface water (b) over the sampling period. The NH_4^+ concentrations of groundwater did not meet the isotope analysis limit (3 μM) during the sampling period, thus the $\delta^{15}N\text{-}NH_4^+$ values were not available.

Spatial and Temporal Variations of NO_3^- and $\delta^{15}N\text{-}NO_3^-$

Groundwater ($\bar{x}$: 1064 ± 1555 μM, n = 100) had higher NO_3^- concentrations ($p < 0.05$) than surface water ($\bar{x}$: 1.4 ± 2.6 μM, n = 77) and porewater ($\bar{x}$: 0.5 ± 1.5 μM, n = 76) (Figure 18). Among groundwater groups, group I ($\bar{x}$: 187.8 ± 233.3 μM, n = 44) had the lowest concentration followed by group II ($\bar{x}$: 1611.8 ± 1927.2 μM, n = 45) and group III ($\bar{x}$: 2329.6 ± 944.7 μM, n = 11) had the highest concentration ($p < 0.05$). Significant temporal concentration variations were not observed in groundwater ($p = 1$) and porewater ($p = 0.1$). Higher surface water concentrations were found in July 2022 ($p < 0.05$).

As surface water and porewater did not have samples that exceed isotope method detection limit (3 μM), $\delta^{15}N\text{-}NO_3^-$ values were not available. The highest $\delta^{15}N\text{-}NO_3^-$ values occurred in the groundwater group II ($\bar{x}$: 25.2 ± 10.8‰, n = 40) followed by group I ($\bar{x}$: 20.9 ± 8.8‰, n = 34) while group III ($\bar{x}$: 7.5 ± 0.2‰, n = 10) had the lowest values ($p < 0.05$) (Figure 19a). Temporal isotopic variations were not observed in groundwater ($p = 1.0$). In a $\delta^{15}N\text{-}NO_3^-$ versus $\delta^{18}O\text{-}NO_3^-$ plot (Figure 19b), both groups I and II displayed strong linear correlations (group I: $R^2 = 0.9$, $p < 0.05$; group II: $R^2 = 0.7$, $p < 0.05$) with slopes of 0.9 and 0.2, respectively. Group III, on the other hand, had a poor linear correlation between $\delta^{15}N\text{-}NO_3^-$ and $\delta^{18}O\text{-}NO_3^-$ ($R^2 = 0.2$, $p = 0.6$). Most groundwater data were clustered in the isotopic range of wastewater and soil nitrate.

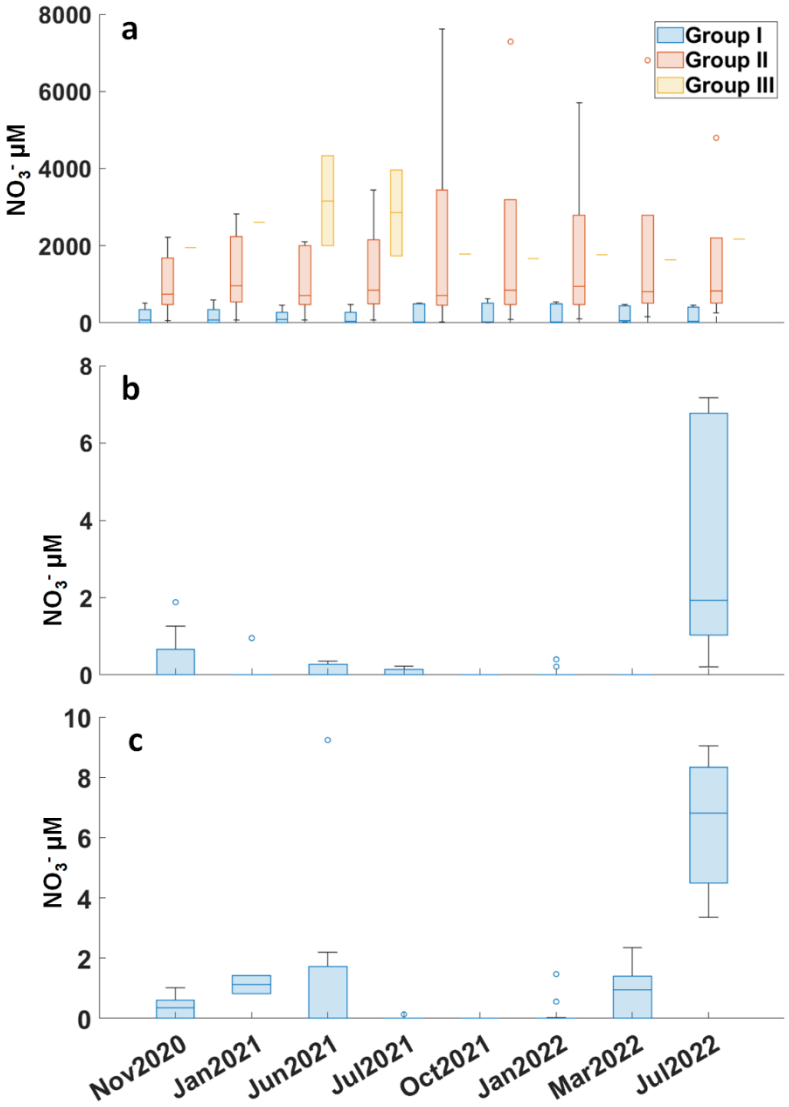

Figure 18. NO_3^- concentrations of groundwater (a), porewater (b), and surface water (c) over the sampling period.

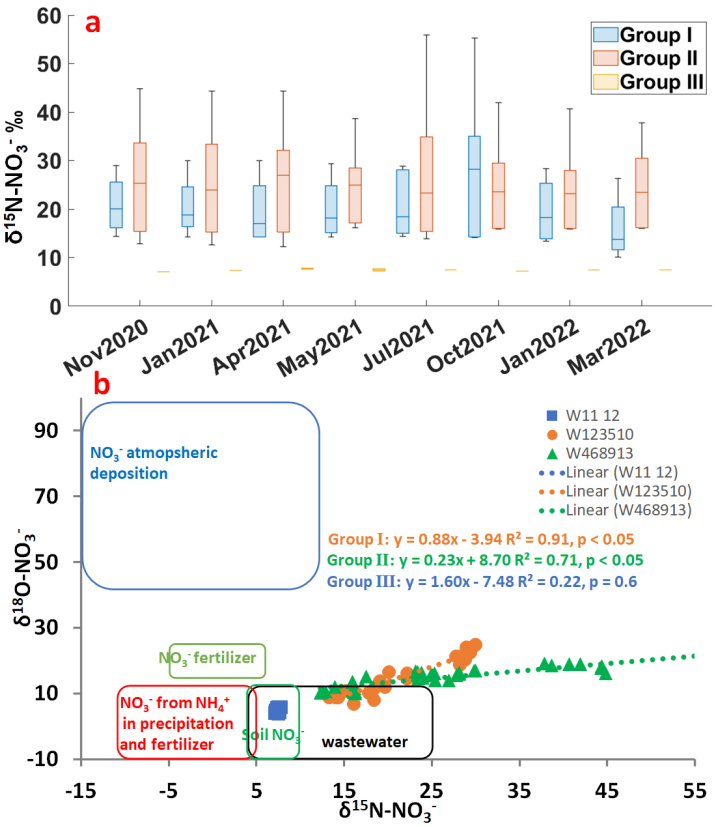

Figure 19. δ^{15}N-NO_3^- values of groundwater (a) over the sampling period and the δ^{15}N-NO_3^- to δ^{18}O-NO_3^- trajectories (b).

Spatial and Temporal Variations of DON and δ^{15}N-DON

Surface water had higher DON concentrations (x̄: 49.9 ± 11.4 µM, n = 77) than porewater (x̄: 21.5 ± 7.1 µM, n = 75) ($p < 0.05$) (Figure 20). Among porewaters, P4 (x̄: 22.4 ± 2.3 µM, n = 8) and P6 (x̄: 24.3 ± 7.3 µM, n = 7) had statistically higher DON concentration than P1, 2, 3 and 5 (x̄: 18.8 ± 6.2 µM, n = 24) ($p < 0.05$). Among groundwater groups, group I (x̄: 28.3 ± 26.3 µM, n = 44) had the lowest DON concentration followed by group II (x̄: 72.1 ± 110.7 µM, n = 45) and group III (x̄: 169.9 ± 139.1 µM, n = 12) had the highest concentration ($p < 0.05$). Groundwater ($p = 0.2$) DON concentrations did not vary significantly with time. Lower porewater DON concentrations were observed in Spring and Summer (x̄: 19.3 ± 7.2 µM, n = 38) and higher in Fall and Winter (x̄: 23.7 ± 6.4 µM, n = 37) ($p < 0.05$).

Surface water (x̄: 8.8 ± 2.3‰, n = 77) had lower δ^{15}N-DON values than porewater (x̄: 10.8 ± 3.6‰, n = 65) and groundwater (x̄: 18.1 ± 5.1‰, n = 38) ($p < 0.05$) (Figure 21). Among groundwater groups, both group I (x̄: 18.7 ± 4.1‰, n = 26) and II (x̄: 20.6 ± 4.4‰, n = 10) had higher δ^{15}N-DON values than group III (x̄: 8.1 ± 1.7‰, n = 2) ($p < 0.05$) and group I was not statistically different from group II ($p = 0.2$). Groundwater ($p = 0.1$) and porewater ($p = 0.3$) δ^{15}N-DON values did not display significant temporal variation.

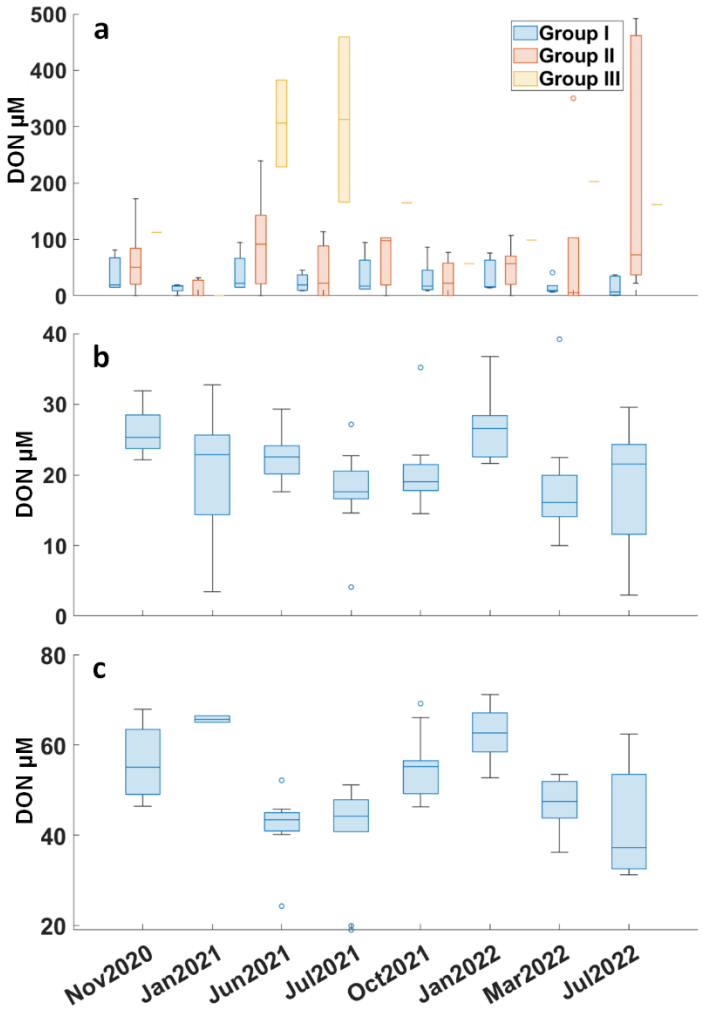

Figure 20. DON concentrations of groundwater (a), porewater (b), and surface water (c) over the sampling period.

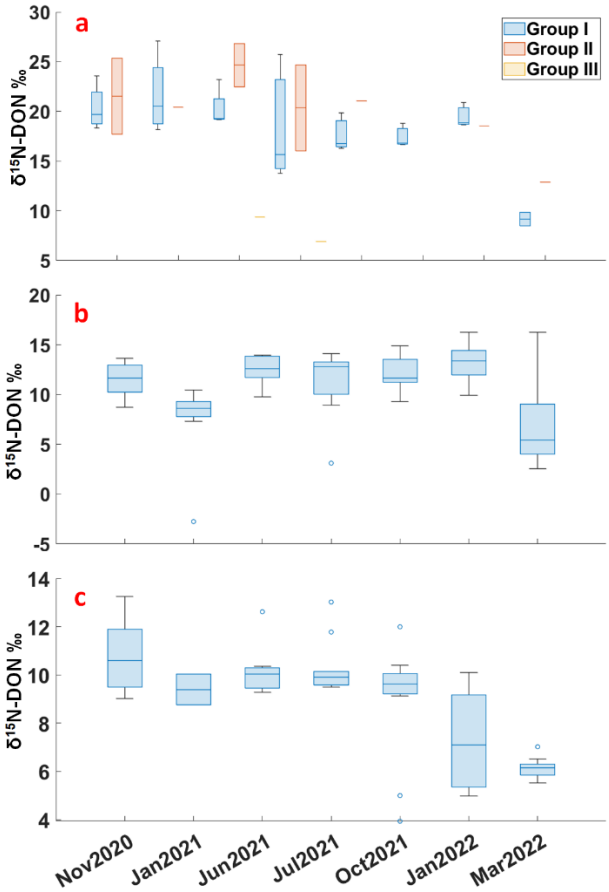

Figure 21. δ^{15}N-DON values of groundwater (a), porewater (b), and surface water (c) over the sampling period. The sensitivity test suggested if there was a 0.2‰ increase/decrease on the measured δ^{15}N-NO_3, which was the systematic error for the isotope analysis, the back calculated δ^{15}N-DON values would fluctuate over 10% when the DON concentration was less than 10% of the TDN. The DON concentrations of W10 and all the wells in group II and III were found to be only 9%, 4% and 8% of the TDN pool and their δ^{15}N-TDN values resembled their δ^{15}N-NO_3^- values. Thus, only representatives of these groundwater samples had δ^{15}N-DON values back calculated as references for further comparison.

NO_3^- source apportionments of groundwater

The results of NO_3^- mixing model indicated wastewater NH_4^+ (40 ± 28%) as the dominant NO_3^- source to wells in group I followed by fertilizer NO_3^- (33 ± 4%) (Figure 22). Wells in group II had fertilizer NO_3^- (52 ± 29%) as the dominant source followed by wastewater NH_4^+ (44 ± 29%). Wells in group III had manure (51 ± 35%) and wastewater (35 ± 34%) derived NH_4^+ as the primary contributors.

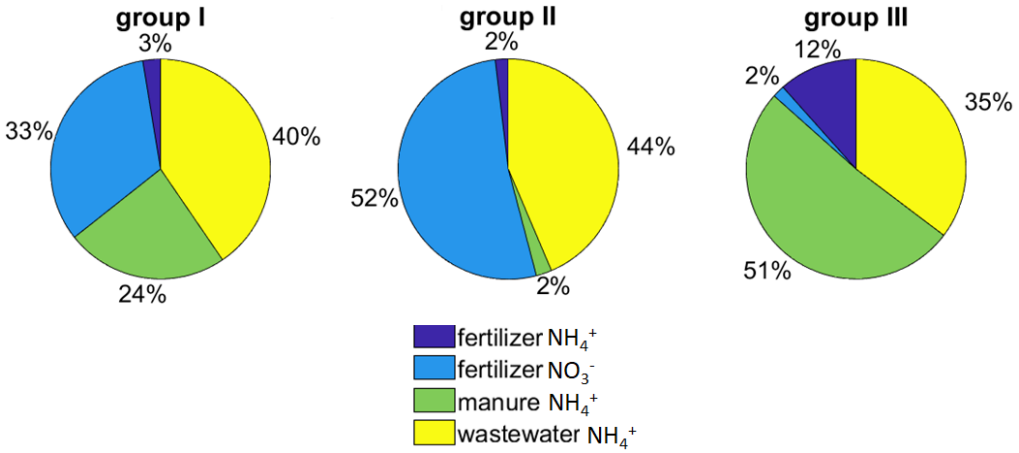

Figure 22. The NO_3^- source apportionments of groundwater.

Submarine Groundwater Discharge Estimates

Darcy Discharge Rate Estimates

Darcy's SGD estimates reveal differing hydrologic properties relative to geographic location. Flow Paths 1 and 2, which discharge towards the Cayo del Grullo section of Baffin Bay, have similar rates throughout the year. Although not much variable, the highest estimates occurred in Spring, with Flow Path 1 rate of about 4.5 cm/d and Flow Path 2 of 4.4 cm/d. Summer is typically the season with the lowest discharge rates, with Flow Path 1 discharge rate of 3.8 cm/s and Flow Path 2 of 3.8 cm/d. The average discharge rate for Flow Path 1 was 4.2 cm/d, and 4.0 cm/d for Flow Path 2.

Table 2: Estimated recharge rates for three primary flow paths that lead to Baffin Bay

Flow Path ID	Discharge (cm/d)			
	Winter	Spring	Fall	Summer
Flow Path 1	4.24	4.46	4.27	3.84
Flow Path 2	3.86	4.42	4.00	3.82
Flow Path 3	0.08	0.12	0.09	0.08

Flow Path 3, which discharges to the Laguna Salada, displayed lower discharge rates compared to the other routes. In this region, all seasonal estimates are around 0.1 cm/d. Overall, the combined seasonal averages for all three flow paths within the study site were 2.7 cm/d for Winter, 3 cm/d for Spring, 2.8 cm/d for Fall, and 2.6 cm/d for Summer, meaning that overall changes in hydraulic gradients do not have a large impact on the discharge rates to the bay.

Radon Activities and SGD

The average grab sample ^{222}Rn activities in the surface water was 120 $Bq \cdot m^{-3}$ (n=169). The highest readings were found near Poenish beach (Campbell) in the Cayo del Grullo branch of Baffin Bay. The lowest ^{222}Rn was found at Riviera Park (RP). For groundwater, the average grab sample ^{222}Rn was 3,128 $Bq \cdot m^{-3}$ with the highest readings (20,548 $Bq \cdot m^{-3}$) found at well 6 and lowest readings found at LS-W1 (61 $Bq \cdot m^{-3}$). The average porewater ^{222}Rn was 147 $Bq \cdot m^{-3}$ with the lowest readings found at LS-P1D, and the highest readings at PB-P2 (Figure 2). Radon,

measured continuously over spatial distances in the bay, was on average 81 $Bq \cdot m^{-3}$ and was used to determine submarine groundwater discharge (SGD) rates for the bay.

Continuous Radon SGD

SGD rates were determined using groundwater radon activities as the endmember. Radon is transported by both saline and fresh waters and does not have an affinity for being adsorbed onto sediments (Key, Guinasso Jr et al. 1979), this makes it well suited for capturing recirculation of water through the subsurface sediments. Given the recirculation component it would be expected that the radon SGD would be greater than the radium SGD as radium is best suited for capturing mostly the saline component of SGD (Murgulet, Lopez et al. 2022).

The average SGD was 39.1 $cm \cdot d^{-1}$. An increasing trend in SGD rates is observed following the significant rain events beginning in Spring 2021. A lag of a few months between the time the water table peaks until the time SGD is at its highest is expected. Indeed, the highest SGD rate was measured in January 2022 (95.7 $cm \cdot d^{-1}$) and the lowest in January of 2021 at 6.7 $cm \cdot d^{-1}$. Generally, late Fall (October) was higher for both years. As with Spring-Summer 2021, higher than norm rain occurred in Spring-Summer 2020, indicating that, much like the baseflow, SGD will increase in September-October (e.g., hydrologic year). The sharp decrease in SGD rate in July 2021 is attributed to ^{222}Rn degassing due to persistent winds and white capping. This in turn would enhance recirculation, leading to an increase in the radium-derived SGD as observed for July 2021 (Table 3, Figure 23).

Table 3. SGD rates in $cm \cdot d^{-1}$ as they have been normalized to the surface area of the bay. Table contains both radium and ^{222}Rn-based SGD rates based on either groundwater (GW) or pore water (Kim, Burnett et al.) end members.

SGD Type/End member	Events								
	1020	1220	0121	0421	0621	0721	1021	0122	0322
Ra GW	0.2	0.3	0.1	1.4	3.8	0.6	2.0	7.5	4.2
Ra PW	0.2	0.7	0.3	1.5	2.9	8.1	3.3	7.2	4.3
Rn Well	34.6	--	6.7	--	63.0	18.0	40.1	95.7	15.4

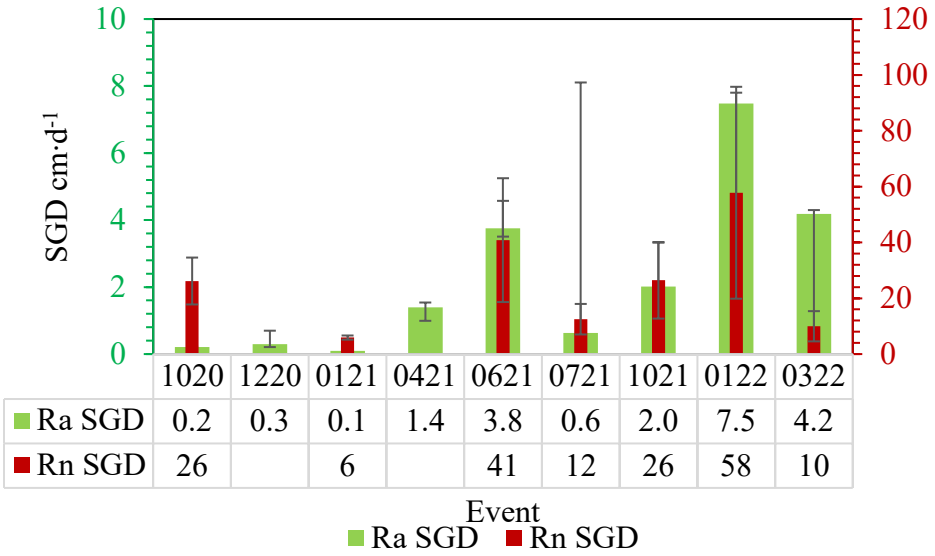

Figure 23. Graph shows radium and ^{222}Rn-based SGD using the project's wells as the groundwater endmember for SGD calculations, the top error bar represents the SGD calculated using the lowest groundwater activity and the lowest error bar was determined using the highest measured activity as the end member.

Radium Activities and SGD

Average surface water ^{224}Ra and ^{226}Ra in surface waters was 1,356 dpm·m^{-3} (n=169) and 2,377 dpm·m^{-3} (n=39), respectively. The highest and lowest activities of both isotopes were measured at Riviera Park in July and October 2021, respectively. Groundwater ^{224}Ra and ^{226}Ra activities were in average 17,847 (n=120) and 2,581 dpm·m^{-3} (n=65) with the highest readings at LS-W1 and the lowest at W3. Porewater ^{224}Ra and ^{226}Ra activities were in average 4,296 dpm·m^{-3} (n=92) and 2,430 dpm·m^{-3} (n=57), with the highest readings at station 1-P and the lowest at LS-P1D.

Radium SGD rates were calculated with pore water or groundwater as endmembers of the source. Using the groundwater radium activity as the endmember, the average SGD was 2.2 cm·d^{-1} and 3.2 cm·d^{-1} when pore water was the assumed source. Similar to the Rn-derived SGD, the highest rates from radium occurred stating with May 2021 following the beginning of the wet event while the lowest during the first three events (October '20, December '20, January '21).

Nutrient Fluxes

Nutrient fluxes were determined with two different nutrient sources, either the concentration of nutrients in groundwater or that of porewater. As well, the SGD rates used to calculate fluxes are also derived using the two different radon and radium activities of porewater and/or groundwater. Radium-derived SGD rates are believed to be mostly representative of extended recirculated seawater which includes a mix of surface water-porewater and nearshore groundwater, thus are used here to calculate nutrient fluxes reported herein.

Fluxes derived using groundwater nutrient concentrations are vastly different from those derived from porewater (Figure 24, Table 4). When using groundwater for SGD rates and average nutrient concentrations of groundwater and porewater as the endmembers, the maximum flux of NH_4^+ across all events was 18,790, average 9518, and minimum 2475,760 µM·m^{-2}·d^{-1}.

Table 4. Nutrient fluxes (µM·m^{-2}·d^{-1}) based on average of groundwater and pore water nutrients using radium based (groundwater end member) SGD rates by season and by nutrient.

Event	Type	DOC	TDN (- NH_4^+)	DON	NH_4^+	NO_3^-	NO_2^-	NOx
1020	Max	25832	105	75	738	22	8	30
	Avg.	17764	79	64	733	11	4	15
	Min	9697	56	54	728	1	1	0
1220	Max	20881	1921	121	1133	1743	57	2418
	Avg.	20881	1011	107	635	873	31	1217
	Min	20881	102	93	138	3	6	17
0121	Max	2928	737	19	272	710	8	718
	Avg.	2765	378	15	178	359	4	365
	Min	2601	19	11	85	8	0	13
0421	Max	14680	12319	1109	4661	11074	136	11209
	Avg.	14303	6252	647	2759	5537	68	5605
	Min	13925	186	185	857	0	1	0
0621	Max	--	36223	2457	11462	33432	334	33767
	Avg.	--	19659	1668	5731	17819	172	17991
	Min	--	3096	880	0	2205	11	2215
0721	Max	34983	4218	408	2375	3727	83	3811
	Avg.	26711	2166	260	1528	1864	42	1906
	Min	18439	113	112	680	1	0	1
1021	Max	140228	19081	576	5670	18258	247	18505
	Avg.	140228	9750	497	3440	9129	124	9253
	Min	140228	418	418	1210	0	0	0
0122	Max	346789	68801	3092	16010	65071	638	65709
	Avg.	346789	35420	2563	10353	32538	319	32857
	Min	346789	2038	2034	4696	4	0	4
0322	Max	184317	37337	2038	14656	35070	229	35299
	Avg.	159942	19115	1459	8841	17535	121	17655
	Min	135568	891	879	3025	0	12	12
All seasons	**Max**	96330	20082	1099	6331	18790	193	19052
	Avg.	91173	10426	809	3800	9518	98	9652
	Min	86016	769	518	1269	247	3	251

Fluxes of NOx reached a maximum of 19,052, average 9652, and a minimum of 251 $\mu M \cdot m^{-2} \cdot d^{-1}$. Fluxes of DOC were between 3 to 34 times higher than the TDN ($NOx+NH_4^+$). The lowest DOC fluxes occurred in January 2021 (average 2,765 $\mu M \cdot m^{-2} \cdot d^{-1}$) and the highest in November 2021 (average 346,789 $\mu M \cdot m^{-2} \cdot d^{-1}$). This higher fluxes in November, while are also a result of higher SGD rates, the two orders of magnitude difference is caused by larger DOC fluxes in the endmember source. Fluxes of DON were up to two orders of magnitude lower than DOC but follow a similar trend with the lowest magnitudes in January 2021 (15 $\mu M \cdot m^{-2} \cdot d^{-1}$) and the highest in November 2021 (2,563 $\mu M \cdot m^{-2} \cdot d^{-1}$).

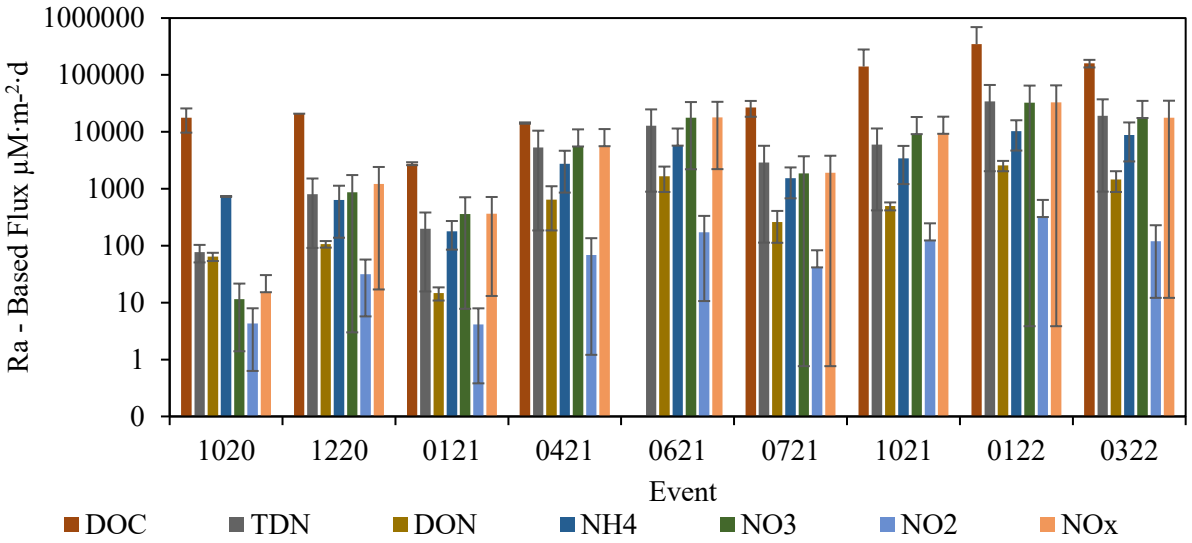

Figure 24. Average nutrient fluxes (in $\mu M \cdot m^{-2} \cdot d^{-1}$) from radium-derived SGD rates. Plotted concentrations are derived from the average groundwater and porewater nutrient concentrations. The nutrient fluxes from the high and low of the groundwater nutrient concentrations making the high and low error bars.

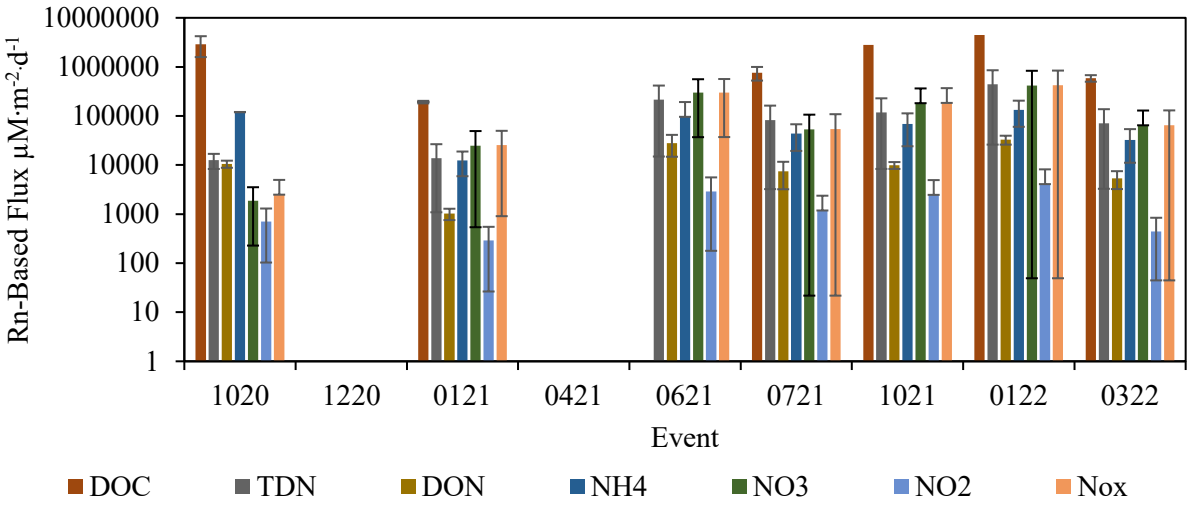

Figure 25. Average nutrient fluxes are estimated using the average groundwater-derived radium SGD rates from the groundwater and porewater. The lower and upper error bars were derived using the groundwater and porewater nutrient concentrations.

Radon-based nutrient fluxes represent different inputs than those from radium (Figures 24, 25). These distinctions come not only from the different reactive nature of the isotopes, but from spatial resolution of sampling. For example, the ^{222}Rn-based SGD is calculated using high resolution measurements throughout the bay, which means that it captures hot spots of SGD, while the radium SGD includes a small number of samples, given the intense labor associated with sampling and processing.

Discussion

Groundwater *Recharge and Nutrient Loading*

Estimating groundwater recharge rates from precipitation provides important information relative to nutrient infiltration susceptibility throughout the study site. A higher recharge rate implies that terrestrial nutrient sources may be able to penetrate the water table and ultimately reach Baffin Bay. Estimates show that areas near Wells 4 and 6 have the highest recharge rates following the May 2021 rain event. The idea that recharge may heighten nutrient infiltration seems especially plausible for Well 4. Here, some of the highest NO_3^- concentrations were found, including the highest concentration of any location or season of 7621 µM in July 2021. There is a high intensity of agricultural activity in the area, particularly cotton, a crop that received nitrogen fertilizer on about 86% of Texas acres in 2019. As the land use map in Figure 26 reveals, there are some cotton fields around the location. Furthermore, fertilizer application for cotton commonly occurs in the Spring and Summer (NASS, 2020). Even the high values seen in the Fall may be due to a lag time between application and the time it takes to infiltrate. Whatever the source of the nitrogen may be, the land around Well 4 does seem to be susceptible to nutrient infiltration.

Well 6, where the highest recharge rate was measured, also shows elevated nitrate levels, although not quite to the extent of Well 4. Both wells reside in similar agricultural territory. Out of all the wells in the study site, Well 6 sits on the higher end of the nitrate spectrum with average NO_3^- concentrations at ~800 µM, especially relative to the neighboring Well 5 and Well 6. The combination of a high recharge rate and elevated NO_3^- levels suggests that the location may be susceptible to nutrient infiltration, perhaps due to a localized change in vertical hydraulic conductivity. Still, there is quite a drop from the nitrate concentrations in Well 4. At first glance, one possible explanation for this involves the depth-to-water (dtw) at the two locations. A larger dtw could filter out nutrients as surface water percolates into the water table, and Well 4 is closer to Baffin Bay so consequently has a much lower groundwater elevation. However, the dtw difference at the two locations is very minimal. Therefore, the higher concentrations at Well 4 must be due to different factors such as the flow of groundwater.

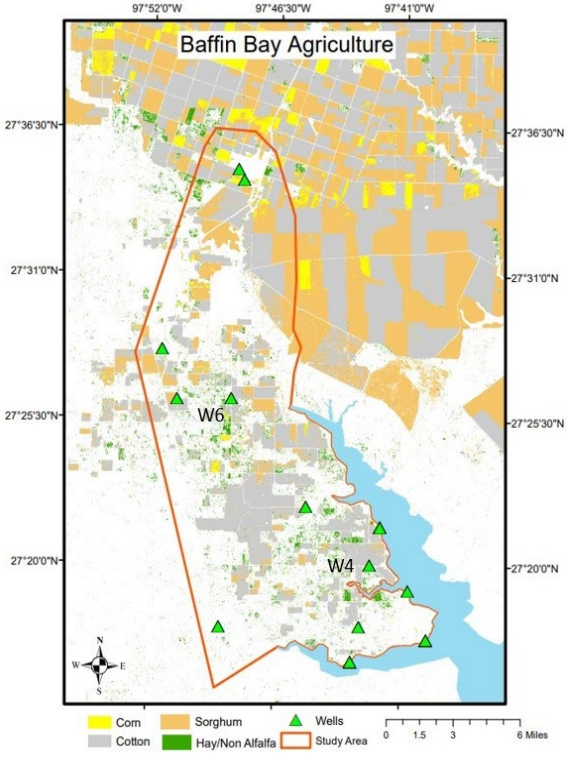

Figure 26. Land use map for the Baffin Bay region illustrating agricultural activity in the area.

Groundwater Discharge Rates and Nutrient Fluxes

Darcy calculations indicate that discharge rates along Flow Path 3 is distinct from both 1 and 2, even though the hydraulic gradients are similar (around 0.0004-0.0005). Flow Path 3 is the furthest south discharging into the Laguna Salada. A primary reason for this difference is the type of sediment in that region, which is of much lower permeability as revealed by well logs from a previous study. Flow Path 3 starts from the close proximity to Well 1 where the aquifer is made of

highly conductive material, but it transports water through less conductive, more clay rich material, near the Laguna Salada shoreline (Figs. 5, 6). Thus, this transition in sediment properties heavily contributes to the difference in water movement velocity.

The higher velocity calculated for Flow Paths 1 and 2 may have implications for nutrient transport towards the bay. With higher SGD rates, in nutrient-laden aquifers, it is expected that not only higher fluxes of nutrients to the bay will occur, but nutrient transformations also occur at lower rates. Thus, a higher presence of NOx compared to the flow path near Laguna Salada. Nutrient levels around the Cayo del Grullo were shown to be elevated relative to the Laguna Salada. Although estimated to have a higher discharge rate, (around 4 cm/d across the year). Slow movement of water allows accumulation of terrestrial-based nutrients in nearshore waters and within the subterranean estuary. Within the study site, it is important to note that a majority of the groundwater flow from inland wells is ultimately directed towards the Cayo Del Grullo. This, combined with the increased velocity, suggests that a higher volume of water and nutrients is arriving around this section of the bay.

In comparing the three methods, the radon-based method tends to yield the highest SGD estimates because it captures both the saline and fresh components of SGD. However, it is more sensitive to environmental conditions such as wind and white capping, which can cause degassing of radon and decrease the SGD estimate. The radium-based method yields lower SGD estimates because it captures mostly the saline component of SGD. However, it is less sensitive to wind and white capping, and these conditions can actually enhance recirculation and increase the radium-based SGD.

Darcy's law-based estimates provide a different perspective on SGD, revealing differences in hydrologic properties relative to geographic location. These estimates are less variable than the radon- and radium-based estimates, and they show that overall changes in hydraulic gradients do not have a large impact on the discharge rates to the bay.

Nutrient fluxes using the radium-derived SGD rates and the average nutrient concentration of porewater, and groundwater indicate that for seasonal averages NH_4^+ makes up the large majority of TDN in the early stages of monitoring, starting with 90% in October 2020 and decreasing to 23% in June 2021. On the other hand, NOx fluxes increased from 2% in October 2020 to 74% as soon as January 2021. Porewaters are much more enriched in NH_4^+ when compared to the further inland groundwater while the opposite is the case with NO_x, as discussed in the nutrient section of the report. Thus, the higher predominance of NOx is because of extremely high NOx concentrations in groundwater, which also increased with precipitation and aquifer recharge.

While NO_x transported from terrestrial sources to the bay is converted to NH_4^+ while transitioning from fresh oxic environments to saline to hypersaline anoxic environments, addition of NH_4^+ in bay porewaters likely occurs from organic matter mineralization and dissociative nitrate reduction to ammonia (DNRA) as evidenced by the isotopic changes measured in the $\delta^{15}N$. As expected, the result is an opposite behavior for NO_x fluxes, which are much higher when the groundwater concentrations are used as the endmember ($\overline{x}$: 11,361 $\mu M \cdot m^{-2} \cdot d^{-1}$, n=6) versus the porewater-derived fluxes ($\overline{x}$: 17 $\mu M \cdot m^{-2} \cdot d^{-1}$, n=6, respectively).

Fluxes of DON made up less than 10% of the TDN SGD-derived fluxes with very little fluctuations and lower generally due to magnitudes of SGD. However, some areas of the monitored aquifer had higher DON levels than surface water and porewater. On the other hand, DOC fluxes, not described in the results section, were between 2 to 80 times greater than TDN and one to two orders of magnitude higher than DON. An abundance of DOC has been linked with an additional source of CO_2 derived from photo-oxidation of autochthonous DOC processes from phytoplankton

(Raymond and Bauer 2001) or oxidation directly to CO_2 through bacterial respiration (Dutta, Kumar et al. 2021)). Excessive biomass has been suggested as the most likely source of DOC in other saline system. Organic carbon loading supply favors DNRA in estuarine sediments, particularly with increasing temperature and salinity, when DOC is used as an electron donor by heterotrophic microbes (fermentative DNRA) (Li, Qian et al. 2020).

NH_4^+ Processing and Transformation in Baffin Bay Watersheds

Porewater (324.6 ± 188.0 μM) had a larger NH_4^+ pool than groundwater (below detection limit) and surface water (1.3 ± 1.7 μM) ($p < 0.05$) (Figure 16). Previous work indicated the remineralization of organic nitrogen and dissimilatory nitrate reduction to ammonium (DNRA) were potential NH_4^+ sources in Baffin Bay sediment (Qiu, Felix et al. in prep). Porewater temperature was found to be positively-correlated with ln[NH_4^+] while negatively-correlated with δ^{15}N-NH_4^+ ($p < 0.05$) (Figure 27), indicating temperature-dependent remineralization. The higher temperature favors remineralization, which produces NH_4^+ enriched with ^{14}N (Segschneider and Bendtsen 2013, Sigman and Fripiat 2019). This current work suggested photo-ammonification might also produce NH_4^+ in the surface sediment, which could be further recirculated into deeper porewater. The rate of photo-ammonification could be the highest in summer due to longer sunlight duration and higher solar radiation (NSRDB 2020, NOAA 2020, 2021 and 2022, NSRDB 2021), which might be the reason for the observed slightly higher porewater NH_4^+ in summer 2021 (373.4 ± 165.9 μM) ($p = 0.2$) (Figure 16). In addition, photo-ammonification is subjected to kinetic fractionation, which generates depleted δ^{15}N-NH_4^+. The higher photo-ammonification rate in summer could produce more depleted δ^{15}N-NH_4^+ in the surface sediment. At the end of May, Baffin Bay received over 53 cm of precipitation, which created higher turbulence, presumably leading to higher recirculation rate at the sediment. The higher recirculation rate transferred more NH_4^+ with low δ^{15}N values into the deeper porewater, possibly resulting in the detected lower porewater δ^{15}N-NH_4^+ in summer 2021 (-3.8 ± 7.4‰) ($p < 0.05$) (Figure 17). A significant negative correlation between porewater NH_4^+ and DON concentrations ($p < 0.05$) was found (Figure 27), which was possibly due to these two NH_4^+ generation processes (i.e., remineralization and photo-ammonification). Both processes breakdown organic nitrogen and produce NH_4^+. However, the isotope fractionation of organic nitrogen remineralization was reported to be small (3 to 5‰) (Sigman and Fripiat 2019), which would lower porewater δ^{15}N-NH_4^+ values but not enough to reduce the δ^{15}N-NH_4^+ found in the remainder of the sampling period (7.4 ± 5.7‰) down to negative values like observed in the summer 2021 (-3.8 ± 7.4‰) (Figure 17). This further evidenced photo-ammonification as the likely cause of the slightly higher NH_4^+ concentration and negative δ^{15}N-NH_4^+ values detected in summer 2021, although the fractionation of photo-ammonification remains unconstrained.

The NH_4^+ emission flux at the water-sediment interface was assumed to be substantial because of the large concentration difference between porewater and surface water (1 to 3 orders of magnitude) (Figure 16). However, the typical long residence time in arid/semi-arid estuaries led to the extended processing and prolonged mixing in Baffin Bay, which let the phytoplankton-favored N form (i.e., NH_4^+) be preferentially and substantially utilized. The growth cycle of phytoplankton further made NH_4^+ either stored in the sediment as NH_4^+/PON/DON or recirculated back to the surface water as NH_4^+/DON. DON is relatively stable in the redox environment and might be difficult to be depleted by phytoplankton in the bay as NH_4^+ was consistently supplied by the emission at the water-sediment interface. This N cycle left DON to be the only N form accumulating in the bay. Whereas DON was found to be bioavailable to certain harmful phytoplankton species (Muhlstein and Villareal 2007), rendering Baffin Bay subjected to

intermittent harmful algae blooms and hypoxia even when the DIN concentrations were low, which threatened the ecosystem and biodiversity of the bay.

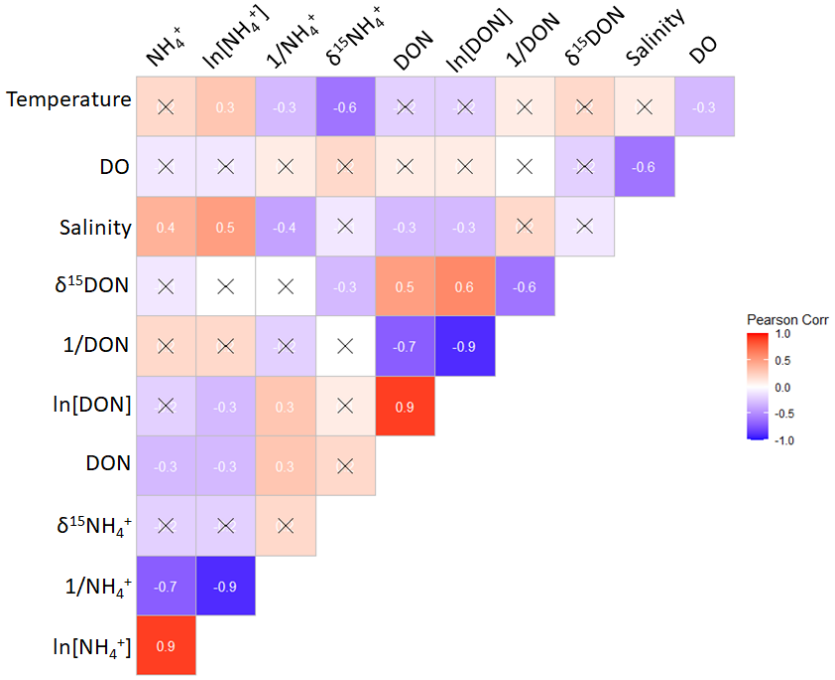

Figure 27. The correlation heatmaps of Baffin Bay porewater. When the p value is less than 0.05, the correlation is believed to be significant. When it is not significant, the correlation value is marked with the black cross.

NO_3^- Processing and Transformation in Baffin Bay Watersheds

Groundwater had varied NO_3^- concentrations (from below detection limit to 7293.3 μM) (Figure 18), suggesting NO_3^- or NH_4^+ contamination. Although groundwater NH_4^+ concentrations were below detection limit over the sampling period, agriculture/septic derived NH_4^+ could be nitrified to NO_3^- before/after reaching the water table and therefore be the actual source of the higher levels of NO_3^-. During nitrification, one of the three NO_3^- oxygen atoms is acquired from oxygen gas and the other two are from water. As a result, the nitrified $\delta^{18}O\text{-}NO_3^-$ would be equal to $\delta^{18}O\text{-}O_2/3 + 2*\delta^{18}O\text{-}H_2O/3$, assuming there is no oxygen exchange causing fractionation (Xuan, Tang et al. 2020). The $\delta^{18}O$ of O_2 was reported as ~23.5‰ (Luz and Barkan 2011) and the average groundwater $\delta^{18}O\text{-}H_2O$ was measured to be -3.9 ± 0.6‰, meaning groundwater $\delta^{18}O\text{-}NO_3^-$ should be ~5.2‰ if nitrification was the dominant process in the system. In group III, the $\delta^{18}O\text{-}NO_3^-$ values (4.6 ± 0.8‰) were close to the suggested $\delta^{18}O\text{-}NO_3^-$ produced by nitrification (i.e., 5.2‰), implicating nitrification as the main process. However, group I (13.9 ± 5.8‰) and II (14.5 ± 3.0‰) had higher $\delta^{18}O\text{-}NO_3^-$ and displayed significant linear $\delta^{18}O\text{-}NO_3^-$ to $\delta^{15}N\text{-}NO_3^-$ trajectories, indicating denitrification might be the primary process that influenced the nitrogen and oxygen isotope compositions of NO_3^- in the system (Figure 19). Denitrification converts NO_3^- to NO_2^- /N_2O/N_2 and causes parallel enrichment on the residual $\delta^{15}N\text{-}NO_3^-$ and $\delta^{18}O\text{-}NO_3^-$ (Kendall, Elliott et al. 2007, Granger and Wankel 2016). Group I had a linear $\delta^{18}O\text{-}NO_3^-$ to $\delta^{15}N\text{-}NO_3^-$ trajectory with a slope of 0.9, which was close to the reported denitrification slope (~1) (Kendall, Elliott et al. 2007, Granger and Wankel 2016). Group II, on the other hand, had a lower slope (0.2), which could be the result of aerobic denitrification (Granger 2006). Certain denitrifying bacteria were found to be able to reduce NO_3^- in aerobic conditions (Song, Zhang et al. 2021). Unlike in low DO

level conditions (e.g., group I: 1.3 ± 1.4 mg/L) where respiratory nitrate reductase (NAR) reduces NO_3^- and poses approximately equal fractionation on residual nitrogen and oxygen isotope compositions, the higher DO condition (e.g., group II: 3.3 ± 2.1 mg/L) could repress NAR but activate periplasmic nitrate reductase (Knapp, Sigman et al.) that reduces NO_3^- in aerobic conditions and causes a higher nitrogen fractionation than oxygen (Figure 28) (Granger, Sigman et al. 2008). In this case, when $\delta^{18}O\text{-}NO_3^-$ was plotted against $\delta^{15}N\text{-}NO_3^-$, a linear trajectory leaning toward the $\delta^{15}N\text{-}NO_3^-$ axis (i.e., slopes lower than 1) would be observed, which was likely what happened in group II. In anaerobic denitrification, organic carbon (OC) and NO_3^-/ NO_2^- serve as the electron donor and acceptor, respectively (Chung, Amin et al. 2014). When the DO concentration increases, O_2 would work as the electron acceptor and repress NAR. However, it was reported when the amount of electron donors (i.e., OC) was disproportionally higher than electron acceptors (i.e., O_2) in aerobic environments, NO_3^-/NO_2^- could work as electron acceptors as well and aerobic denitrification through NAP would occur (Marchant, Ahmerkamp et al. 2017). Although OC was not measured in this study, the relative amount of electron donor and acceptor in the system could possibly explain why the similar DO concentration in group II and III favored different processes (Figure 28).

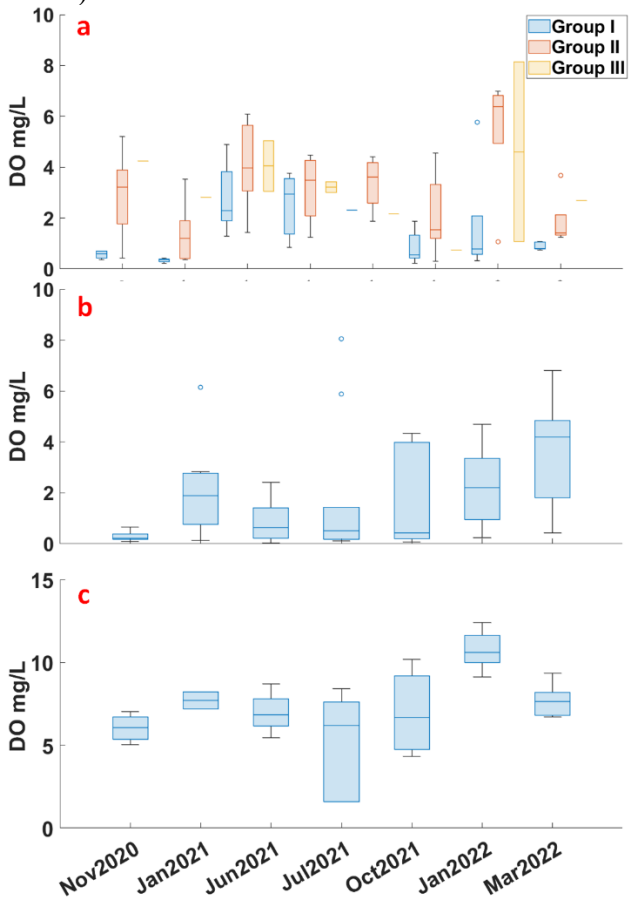

Figure 28. DO concentrations of groundwater (a), porewater (b), and surface water (c) over the sampling period.

As for groundwater NO_3^- sources, the NO_3^- dual mixing model results indicated wastewater (40 ± 28%) and manure (24 ± 18%) derived NH_4^+ and fertilizer derived NO_3^- (33 ± 4%) to be the primary NO_3^-sources in group I (Figure 22). However the $\delta^{15}N$ values of wastewater NH_4^+ (4.4 ±

4.6‰), manure (7.4 ± 3.8‰) NH_4^+, and fertilizer NO_3^- (0 ± 3‰) are much lower than the measured $\delta^{15}N\text{-}NO_3^-$ of group I (20.9 ± 8.8‰) (Figure 19) (Nikolenko, Jurado et al. 2018). This was a result of the detected denitrification as discussed above that could raise the residual $\delta^{15}N\text{-}NO_3^-$ values by 5-25‰ (Granger and Wankel 2016). The $\delta^{18}O$ values of fertilizer NO_3^- (17-25‰) is higher than the measured group I $\delta^{18}O\text{-}NO_3^-$ (13.9 ± 5.8‰) (Nikolenko, Jurado et al. 2018). While by mixing with the nitrification products of wastewater and manure, which had $\delta^{18}O$ values of ~5.2‰ as discussed above, fertilizer NO_3^- along with wastewater and manure derived NH_4^+ could together contribute to the observed NO_3^- in group I. Septic and manure NO_3^- was not identified as potential sources as septic effluent and manure samples mainly contain NH_4^+ and DON (Widory, Kloppmann et al. 2004, Lusk, Toor et al. 2017).

In group II, the mixing model results indicated wastewater derived NH_4^+ (44 ± 29%) and fertilizer derived NO_3^- (52 ± 29%) were dominant contributors (Figure 22). Group II had similar $\delta^{15}N\text{-}NO_3^-$ (25.2 ± 10.2‰) and $\delta^{18}O\text{-}NO_3^-$ (14.5 ± 3‰) values as group I (Figure 19). Both groups had strong linear correlation of $\delta^{18}O\text{-}NO_3^-$ to $\delta^{15}N\text{-}NO_3^-$ ($p < 0.05$) while group II generated a lower slope (i.e., 0.2), indicating denitrification was significant at both groups while if there was an increase of 1‰ in $\delta^{18}O\text{-}NO_3^-$, $\delta^{15}N\text{-}NO_3^-$ would increase by 5‰ in group II (Figure 19). This indicated manure NH_4^+, which had relatively higher $\delta^{15}N$ values (7.4 ± 3.8‰) and was identified as a primary source in group I, might be a less important source in group II. Group III had the lowest groundwater $\delta^{15}N\text{-}NO_3^-$ (7.5 ± 0.2‰) ($p < 0.05$) and a significant nitrification process was indicated by the $\delta^{18}O\text{-}NO_3^-$ values (4.6 ± 0.8‰) (Figure 19), indicating fertilizer NH_4^+ ($\delta^{15}N$: -7.4 to 5.1‰), manure NH_4^+ ($\delta^{15}N$: 7.4 ± 3.8‰) and/or septic NH_4^+ ($\delta^{15}N$ 4.4 ± 4.6‰) were potential contaminants (Nikolenko, Jurado et al. 2018). However, the $\delta^{15}N$ value ranges of fertilizer NH_4^+ ($\delta^{15}N$: -7.4 to 5.1‰) was lower than the measured $\delta^{15}N\text{-}NO_3^-$ values in group III (7.5 ± 0.2‰), making manure NH_4^+ and/or septic NH_4^+ to be the important NO_3^- sources, which was consistent with the mixing model results that manure (51.3 ± 35.4‰) and septic (35.3 ± 34.8‰) derived NH_4^+ were the primary sources in group III (Figure 22). The mixing model results were also consistent with the agriculture dominated land use (i.e., cultivated crop and pasture/hay) of the region that had onsite septic tanks as the most common wastewater treatment facilities (Figure 2).

Porewater (0.5 ± 1.5 μM) and surface water (1.4 ± 2.6 μM) had low NO_3^- concentrations. Porewater did not display temporal variations (porewater $p = 0.1$) and higher surface water concentrations were found in July 2022 (Figure 18).

DON Processing and Transformation in Baffin Bay Watersheds

The DON concentration in groundwater along Baffin Bay watershed varied from below detection limit to 491.8 μM (Figure 20), presumably indicating a DON contamination from varying sources in the watershed. The dominant land use along the watersheds is agriculture and there are 794 septic tanks within the coastal zone of two Baffin Bay sub-watersheds (Figure 2) (Texas A&M AgriLife Extension OSSF 2020, USGS 2022), indicating both agriculture and septic source could contaminate the water table. However, the texture of the top soil layer as found in the sediment cores from the wells in group I is clay loam (Figures 5, 6), which is difficult for the agriculture source to infiltrate from the ground surface. Additionally, urea, which is the DON applied in fertilizers, was reported to have low concentrations in the Baffin Bay surface water (Murgulet Unpublished work). Septic tanks, however, are buried structures, meaning the migration of septic effluent downward to the water table is not impeded by low permeability soils, and thus contamination of the nearby groundwater is imminent particularly. This may suggest that groundwater in this area associated with group I may not be as vulnerable to surface infiltration of nutrients give the lower permeability top soils, leaving septic systems as the likely prominent

inputs. Although this speculation warrants further investigation, the high δ^{15}N-DON of group I (18.7 ± 4.1‰) (Figure 21) is also reflective of septic DON isotope signatures (+22.3 ± 7.9‰) (Qiu, Felix et al. in prep). However, given the mostly horizontal direction of groundwater flow, it was also possible that agricultural sources percolating to groundwater in areas with higher permeability soils may travel to these locations along flow paths towards the coast. Agriculture sources have lower nitrogen isotope signatures (fertilizer: -0.6 ± 0.3‰; manure: +3.9 ± 0.2‰) compared with the δ^{15}N-DON of group I (18.7 ± 4.1‰), which may indicate fractionation that made the residual DON enriched in ^{15}N. This theory should also be accompanied by higher groundwater δ^{15}N-DON in the warmer season when higher rates of volatilization and degree of fractionation occur. Nevertheless, significant seasonal variation of δ^{15}N-DON was not observed in group I. Thus, septic or a mixture of septic and manure were more likely to be the DON sources in group I. As for group II and group III, except for W6, their top layer soil textures are less compact (Figures 5, 6), which are potentially subjected to the infiltration of both agriculture and septic sources. Wells of group II all had high δ^{15}N-DON values like group I (Figure 21), which were likely to be affected by septic sources or agricultural sources that have undergone processing. Wells in group III had the lowest groundwater δ^{15}N-DON (8.1 ± 1.7‰), which was higher than the reported nitrogen isotope signature of agriculture source (manure: +3.9 ± 0.2‰) but lower than septic DON isotope signature (+22.3 ± 7.9‰) (Campbell 2018, Qiu, Felix et al. in prep). This indicated it might be a combined contamination of agriculture and septic sources or just agriculture sources that experienced volatilization, which made the δ^{15}N-DON that reached group III higher than the original agriculture source signatures (Ti, Ma et al. 2021).

Porewater is a sink of particle organic nitrogen (PON) from the water column. The reported δ^{15}N-PON in the study area was 3.9 ± 1.4‰ (Wetz unpublished work). The reported fractionation of PON breakdown to DON and subsequent DON remineralization could increase the residual δ^{15}N-DON by 5‰ (Sigman and Fripiat 2019) and could contribute to the observed average porewater δ^{15}N-DON (10.8 ± 3.6‰) (Figure 21). Porewater δ^{15}N-DON values were also under the influence of two other DON processing. 1) Mixture with groundwater DON. As discussed above, a part of the water tables along Baffin Bay watersheds possessed high DON concentrations and δ^{15}N-DON values (e.g., group I: 18.7 ± 4.1‰; II: 20.6 ± 4.4‰). The interaction between groundwater and porewater may lead to groundwater DON diffusion to porewater and affect porewater δ^{15}N-DON. 2) Photo-ammonification of DON. Photo-ammonification in the photic zone sediment discriminated ^{14}N and increased the residual δ^{15}N-DON, which could be recirculated into deeper sediment. Baffin Bay is a shallow estuary. The average water depth was 1.8 ± 0.6 m during the sampling period. In shallow estuaries, the majority of sediment surface falls within the photic zone (Hardison, Anderson et al. 2011). Photo-ammonification of DON was observed in Baffin Bay porewater samples that were subjected to photo-simulation (TON 2022), suggesting DON in the surface layer of Baffin Bay sediment could be converted to NH_4^+, which might be recirculated into deeper sediment. The photo-ammonification theory was also consistent with the observed DON seasonal variation. Spring and summer had longer sunlight duration and higher solar than Winter and Fall in southern Texas (NSRDB 2020, NOAA 2020, 2021 and 2022, NSRDB 2021), which presumably led to a higher rate of photo-ammonification at the top-layer sediment in Spring and summer compared with Winter and Fall, resulting in the lower porewater DON concentrations in Spring and Summer (19.3 ± 7.2 μM) than Winter and Fall (23.7 ± 6.4 μM) ($p < 0.05$) (Figure 20).

Conclusion

The comprehensive study on SGD and nutrient sources and fluxes in Baffin Bay, Texas, provides valuable insights into the complex dynamics of water and nutrient transport in coastal environments. The findings underscore the importance of SGD as a significant pathway for nutrient delivery to coastal waters, with potential implications for water quality and ecosystem health.

The study reveals that SGD rates and nutrient fluxes are subject to seasonal variations and are influenced by environmental conditions. This understanding is crucial for predicting and managing the impacts of SGD on coastal water quality, particularly in the context of nutrient pollution. The study also highlights the importance of differentiating between nutrient sources, as the nutrient fluxes derived from groundwater and porewater showed significant differences.

The detailed analysis of nitrogen species in groundwater, porewater, and surface water provides a nuanced understanding of nutrient dynamics in the study area. The dominance of nitrate in groundwater, ammonium in porewater, and DON in surface water points to distinct biogeochemical processes in these different compartments. This knowledge can inform targeted strategies for nutrient management and pollution control.

The study's findings have significant implications for public policy and regulatory frameworks. Understanding the role of SGD in nutrient transport can inform the development of effective strategies for managing nutrient pollution in coastal waters. This could include measures to control nutrient inputs at the source, such as improved management of agricultural practices or wastewater treatment, as well as strategies to mitigate the impacts of nutrient pollution, such as restoration of coastal ecosystems that can absorb and process excess nutrients.

In conclusion, this study underscores the importance of a holistic understanding of coastal hydrological and nutrient dynamics in managing water quality and ecosystem health. It provides a strong scientific basis for informed decision-making by the public and regulatory agencies, contributing to the sustainable management of our precious coastal resources.

References

Aluwihare, L. I., et al. (2005). "Two Chemically Distinct Pools of Organic Nitrogen Accumulate in the Ocean." Science **308**(5724): 1007-1010.

Beck, A. J., et al. (2007). "Radium mass-balance in Jamaica Bay, NY: Evidence for a substantial flux of submarine groundwater." Marine Chemistry **106**(3-4): 419-441.

Beck, A. J., et al. (2008). "Submarine groundwater discharge to Great South Bay, NY, estimated using Ra isotopes." Marine Chemistry **109**(3-4): 279-291.

Bighash, P. and D. Murgulet (2015). "Application of factor analysis and electrical resistivity to understand groundwater contributions to coastal embayments in semi-arid and hypersaline coastal settings." Science of The Total Environment **532**: 688-701.

Brock, D. (2001). "Uncertainties in Individual Estuary N-Loading Assessments." Nitrogen Loading in Coastal Water Bodies: An Atmospheric Perspective: 171-185.

Burnett, W. C. and H. Dulaiova (2003). "Estimating the dynamics of groundwater input into the coastal zone via continuous radon-222 measurements." Journal of environmental radioactivity **69**(1-2): 21-35.

Campbell, J. (2018). Investigating the isotopic composition of reactive nitrogen in a South Texas estuary (Baffin Bay). Corpus Christi, Texas, Texas A&M University-Corpus Christi.

Chaillou, G., et al. (2014). "Total alkalinity and dissolved inorganic carbon production in groundwaters discharging through a sandy beach." Procedia Earth and Planetary Science **10**: 88-99.

Charette, M. A., et al. (2001). "Utility of radium isotopes for evaluating the input and transport of groundwater-derived nitrogen to a Cape Cod estuary." Limnology and Oceanography **46**(2): 465-470.

Chung, J., et al. (2014). "Autotrophic denitrification of nitrate and nitrite using thiosulfate as an electron donor." Water Research **58**: 169-178.

Conley, D. J., et al. (2009). "Controlling Eutrophication: Nitrogen and Phosphorus." Science **323**(5917): 1014-1015.

Corbett, D. R., et al. (1998). "A multiple approach to the determination of radon fluxes from sediments." Journal of Radioanalytical and Nuclear Chemistry **236**(1-2): 247-252.

Dimova, N., et al. (2007). "Automated measurement of 224Ra and 226Ra in water." Applied radiation and isotopes **65**(4): 428-434.

Douglas, A. R., et al. (2020). "Submarine groundwater discharge in an anthropogenically disturbed, semi-arid estuary." Journal of Hydrology **580**: 124369.

Dulaiova, H. and W. C. Burnett (2008). "Evaluation of the flushing rates of Apalachicola Bay, Florida via natural geochemical tracers." Marine Chemistry **109**(3-4): 395-408.

Durridge Company Inc. (2017). RAD7 Radon Detector User Manual. Billerica, MA, USA. **Revision 7.4.5**.

Dutta, M. K., et al. (2021). "Carbon biogeochemistry of two contrasting tropical estuarine ecosystems during premonsoon." Estuaries and Coasts **44**: 1916-1930.

Felix, J., et al. (2013). "Characterizing the isotopic composition of atmospheric ammonia emission sources using passive samplers and a combined oxidation-bacterial denitrifier approach." Rapid Communications in Mass Spectrometry **27**(20): 2239-2246.

Fowler, D., et al. (2013). "The global nitrogen cycle in the twenty-first century." Phil. Trans. R. Soc. B **368**(1621): 20130164.

Giblin, A. E. and A. G. Gaines (1990). "Nitrogen inputs to a marine embayment: the importance of groundwater." Biogeochemistry **10**(3): 309-328.

Giblin, A. E., et al. (2010). "The Effects of Salinity on Nitrogen Losses from an Oligohaline Estuarine Sediment." Estuaries and Coasts **33**(5): 1054-1068.

Gonneea, M. E., et al. (2008). "New perspectives on radium behavior within a subterranean estuary." Marine Chemistry **109**(3-4): 250-267.

Granger, J. (2006). Coupled nitrogen and oxygen isotope fractionation of nitrate imparted during its assimilation and dissimilatory reduction by unicellular plankton.

Granger, J. and D. M. Sigman (2009). "Removal of nitrite with sulfamic acid for nitrate N and O isotope analysis with the denitrifier method." Rapid Communications in Mass Spectrometry **23**(23): 3753-3762.

Granger, J., et al. (2008). "Nitrogen and oxygen isotope fractionation during dissimilatory nitrate reduction by denitrifying bacteria." Limnology and Oceanography **53**(6): 2533-2545.

Granger, J. and S. D. Wankel (2016). "Isotopic overprinting of nitrification on denitrification as a ubiquitous and unifying feature of environmental nitrogen cycling." Proceedings of the National Academy of Sciences **113**(42): E6391-E6400.

Hadas, O., et al. (2009). "Seasonally varying nitrogen isotope biogeochemistry of particulate organic matter in Lake Kinneret, Israel." Limnology and Oceanography **54**(1): 75-85.

Hardison, A. K., et al. (2011). "Carbon and nitrogen dynamics in shallow photic systems: Interactions between macroalgae, microalgae, and bacteria." Limnology and Oceanography **56**(4): 1489-1503.

He, S., et al. (2022). "Identification and apportionment of shallow groundwater nitrate pollution in Weining Plain, northwest China, using hydrochemical indices, nitrate stable isotopes, and the new Bayesian stable isotope mixing model (MixSIAR)." Environmental Pollution **298**: 118852.

Holmes, R. M., et al. (1999). "A simple and precise method for measuring ammonium and marine and freshwater ecosystems." Canadian Journal of Fisheries and Aquatic Sciences **56**(10): 1801-1808.

Holmes, R. M., et al. (1998). "Measuring 15N–NH4+ in marine, estuarine and fresh waters: An adaptation of the ammonia diffusion method for samples with low ammonium concentrations." Marine Chemistry **60**(3): 235-243.

Holmes, R. M., et al. (2000). "Nitrogen biogeochemistry in the oligohaline zone of a New England estuary." Ecology **81**(2): 416-432.

Hu, C., et al. (2006). "Hurricanes, submarine groundwater discharge, and Florida's red tides." Geophysical Research Letters **33**(11).

Jolly, I. D., et al. (2008). "A review of groundwater-surface water interactions in arid/semi-arid wetlands and the consequences of salinity for wetland ecology." Ecohydrology **1**(1): 43-58.

Kendall, C., et al. (2007). Tracing Anthropogenic Inputs of Nitrogen to Ecosystems. Stable Isotopes in Ecology and Environmental Science**:** 375-449.

Key, R., et al. (1979). "Emanation of radon-222 from marine sediments." Marine Chemistry **7**(3): 221-250.

Kim, G., et al. (2001). "Measurement of Ra-224 and Ra-226 activities in natural waters using a radon-in-air monitor." Environmental science & technology **35**(23): 4680-4683.

Knapp, A. N., et al. (2005). "N isotopic composition of dissolved organic nitrogen and nitrate at the Bermuda Atlantic Time-series Study site." Global Biogeochemical Cycles **19**(1).

Knapp, A. N., et al. (2011). "Interbasin isotopic correspondence between upper-ocean bulk DON and subsurface nitrate and its implications for marine nitrogen cycling." Global Biogeochemical Cycles **25**(4).

Knee, K. L., et al. (2011). "Using radium isotopes to characterize water ages and coastal mixing rates: A sensitivity analysis." Limnology and Oceanography: Methods **9**(9): 380-395.

Krest, J. M., et al. (2000). "Marsh nutrient export supplied by groundwater discharge: Evidence from radium measurements." Global Biogeochemical Cycles **14**(1): 167-176.

Kroeger, K. D., et al. (2007). "Submarine groundwater discharge to Tampa Bay: Nutrient fluxes and biogeochemistry of the coastal aquifer." Marine Chemistry **104**(1): 85-97.

Lambert, M. J. and W. C. Burnett (2003). "Submarine groundwater discharge estimates at a Florida coastal site based on continuous radon measurements." Biogeochemistry **66**(1-2): 55-73.

Lee, J.-M. and G. Kim (2006). "A simple and rapid method for analyzing radon in coastal and ground waters using a radon-in-air monitor." Journal of environmental radioactivity **89**(3): 219-228.

Li, C., et al. (2019). "Identification of sources and transformations of nitrate in the Xijiang River using nitrate isotopes and Bayesian model." Science of The Total Environment **646**: 801-810.

Li, X., et al. (2020). "Soil organic carbon controls dissimilatory nitrate reduction to ammonium along a freshwater-oligohaline gradient of Min River Estuary, Southeast China." Marine Pollution Bulletin **160**: 111696.

Liu, S., et al. (2018). "Using dual isotopes and a Bayesian isotope mixing model to evaluate sources of nitrate of Tai Lake, China." Environmental Science and Pollution Research **25**(32): 32631-32639.

Lopez, C. V., et al. (2020). "Radioactive and stable isotope measurements reveal saline submarine groundwater discharge in a semiarid estuary." Journal of Hydrology **590**: 125395.

Lusk, M. G., et al. (2017). "A review of the fate and transport of nitrogen, phosphorus, pathogens, and trace organic chemicals in septic systems." Critical Reviews in Environmental Science and Technology **47**(7): 455-541.

Luz, B. and E. Barkan (2011). "The isotopic composition of atmospheric oxygen." Global Biogeochemical Cycles **25**(3).

Marchant, H. K., et al. (2017). "Denitrifying community in coastal sediments performs aerobic and anaerobic respiration simultaneously." Isme j **11**(8): 1799-1812.

Matson, E. A. (1993). "Nutrient flux through soils and aquifers to the coastal zone of Guam (Mariana Islands)." Limnology and Oceanography **38**(2): 361-371.

Moore, W. (1996). Large groundwater inputs to coastal waters revealed by 226Ra enrichments.--p. 612-614, En: Nature (London)(United Kingdom).--Vol. 380, no. 6575 (1996).

Moore, W. S. (1996). "Large groundwater inputs to coastal waters revealed by Ra-226 enrichments." Nature **380**(6575): 612-614.

Moore, W. S. (2000). "Ages of continental shelf waters determined from 223Ra and 224Ra." Journal of Geophysical Research: Oceans **105**(C9): 22117-22122.

Moore, W. S. (2000). "Determining coastal mixing rates using radium isotopes." Continental Shelf Research **20**(15): 1993-2007.

Moore, W. S. (2006). "Radium isotopes as tracers of submarine groundwater discharge in Sicily." Continental Shelf Research **26**(7): 852-861.

Moore, W. S. (2010). "The effect of submarine groundwater discharge on the ocean." Annual review of marine science **2**: 59-88.

Muhlstein, H. I. and T. A. Villareal (2007). "Organic and inorganic nutrient effects on growth rate–irradiance relationships in the Texas brown-tide alga Aureoumbra lagunensis (Pelagophyceae)1." Journal of Phycology **43**(6): 1223-1226.

Murgulet, D. (Unpublished work).

Murgulet, D., et al. (2022). "Radioactive and stable isotopes reveal variations in nearshore submarine groundwater discharge composition and magnitude across low inflow northwestern Gulf of Mexico estuaries." Science of The Total Environment **823**: 153814.

Nikolenko, O., et al. (2018). "Isotopic composition of nitrogen species in groundwater under agricultural areas: A review." Science of The Total Environment **621**: 1415-1432.

NOAA (2020, 2021 and 2022). NOAA Solar Calculator.

NSRDB (2020). National Solar Radiation Database.

NSRDB (2021). National Solar Radiation Database.

Paerl, H. W. (1997). "Coastal eutrophication and harmful algal blooms: Importance of atmospheric deposition and groundwater as “new” nitrogen and other nutrient sources." Limnology and oceanography **42**(5part2): 1154-1165.

Peterson, R. N., et al. (2008). "Radon and radium isotope assessment of submarine groundwater discharge in the Yellow River delta, China." Journal of Geophysical Research **113**(C9).

Prokopenko, M., et al. (2011). "Denitrification in anoxic sediments supported by biological nitrate transport." Geochimica et Cosmochimica Acta **75**(22): 7180-7199.

Qiu, Y., et al. (in prep). "Isotopic compositions of organic and inorganic nitrogen reveal processing and source dynamics at septic influenced and undeveloped estuary sites ".

Raymond, P. A. and J. E. Bauer (2001). "Use of 14C and 13C natural abundances for evaluating riverine, estuarine, and coastal DOC and POC sources and cycling: a review and synthesis." Organic Geochemistry **32**(4): 469-485.

RCRA SOP (2009). Protocol for Groundwater/Surface Water Interface Sampling Using a Pore Water Sampler. Standard Operating Procedure Change Record. B. Beneski and E. Bonenfant, Department of Environmental Protection Bureau of Remediation and Waste Management RCRA Program.

Robinson, C. E., et al. (2018). "Groundwater dynamics in subterranean estuaries of coastal unconfined aquifers: Controls on submarine groundwater discharge and chemical inputs to the ocean." Advances in Water Resources **115**: 315-331.

Rodellas, V., et al. (2021). "Conceptual uncertainties in groundwater and porewater fluxes estimated by radon and radium mass balances." Limnology and Oceanography.

Sadat-Noori, M., et al. (2016). "Fresh meteoric versus recirculated saline groundwater nutrient inputs into a subtropical estuary." Science of The Total Environment **566**: 1440-1453.

Santos, I. R., et al. (2012). "The “salt wedge pump”: Convection-driven pore-water exchange as a source of dissolved organic and inorganic carbon and nitrogen to an estuary." Limnology and Oceanography **57**(5): 1415-1426.

Schlarbaum, T., et al. (2010). "Turnover of combined dissolved organic nitrogen and ammonium in the Elbe estuary/NW Europe: results of nitrogen isotope investigations." Marine Chemistry **119**(1-4): 91-107.

Schulz, H. D., et al. (1994). "Early diagenetic processes, fluxes, and reaction rates in sediments of the South Atlantic." Geochimica et Cosmochimica Acta **58**(9): 2041-2060.

Segschneider, J. and J. Bendtsen (2013). "Temperature-dependent remineralization in a warming ocean increases surface pCO2 through changes in marine ecosystem composition." Global Biogeochemical Cycles **27**(4): 1214-1225.

Sigman, D. M., et al. (2001). "A Bacterial Method for the Nitrogen Isotopic Analysis of Nitrate in Seawater and Freshwater." Analytical Chemistry **73**(17): 4145-4153.

Sigman, D. M. and F. Fripiat (2019). Nitrogen Isotopes in the Ocean☆. Encyclopedia of Ocean Sciences (Third Edition). J. K. Cochran, H. J. Bokuniewicz and P. L. Yager. Oxford, Academic Press**:** 263-278.

Sipler, R. E. and D. A. Bronk (2015). Chapter 4 - Dynamics of Dissolved Organic Nitrogen. Biogeochemistry of Marine Dissolved Organic Matter (Second Edition). D. A. Hansell and C. A. Carlson. Boston, Academic Press**:** 127-232.

Smith, C. G. and L. L. Robbins (2012). Surface-Water Radon-222 Distribution along the Western-Central Florida Shelf, U.S. Geological Survey**:** 26.

Song, T., et al. (2021). "A review of research progress of heterotrophic nitrification and aerobic denitrification microorganisms (HNADMs)." Science of The Total Environment **801**: 149319.

Spalt, N., et al. (2019). "Spatial variation and availability of nutrients at an oyster reef in relation to submarine groundwater discharge." Science of The Total Environment: 136283.

Spalt, N., et al. (2018). "Relating estuarine geology to groundwater discharge at an oyster reef in Copano Bay, TX." Journal of Hydrology **564**: 785-801.

Sun, Y. and T. Torgersen (1998). "The effects of water content and Mn-fiber surface conditions on 224Ra measurement by 220Rn emanation." Marine Chemistry **62**(3): 299-306.

Swarzenski, P. W., et al. (2007). "Ra and Rn isotopes as natural tracers of submarine groundwater discharge in Tampa Bay, Florida." Marine Chemistry **104**(1): 69-84.

Tait, D. R., et al. (2017). "Radium-derived porewater exchange and dissolved N and P fluxes in mangroves." Geochimica et Cosmochimica Acta **200**: 295-309.

TCEQ (2012). Surface Water Quality Monitoring Procedures, Volume 1: Physical and Chemical Monitoring Methods. Austin, TX.

Texas A&M AgriLife Extension OSSF (2020). Coastal Zone Act Reauthorization Amendments (CZARA) - On-Site Sewage Facilities (OSSFs) Coastal Inventory and Chocolate Bayou OSSF

Inspections, Contract # 582-20-10160 funded by Environ. Prot. Agency Clean Water Act Sect. 319(h) funds through Texas Comm. Environ. Qual. (TCEQ).

Ti, C., et al. (2021). "Changes of δ15N values during the volatilization process after applying urea on soil." Environmental Pollution **270**: 116204.

TON, Q. (2022). Seasonal Ammonium Bethinic Flux and Photo-ammonification of Dissolved Organic Nitrogen in Baffin Bay - Texas, Texas A&M University-Corpus Christi

Tsikas, D. (2007). "Analysis of nitrite and nitrate in biological fluids by assays based on the Griess reaction: Appraisal of the Griess reaction in the l-arginine/nitric oxide area of research." Journal of Chromatography B **851**(1-2): 51-70.

Tsunogai, U., et al. (2008). "Sensitive determinations of stable nitrogen isotopic composition of organic nitrogen through chemical conversion into N2O." Rapid Communications in Mass Spectrometry **22**(3): 345-354.

TWDB (2019). Hydrology for the Laguna Madre Estuary Watershed. C. f. W. S. Studies.

TWDB (2019). Hydrology for the Nueces Bay Estuary Watershed. C. f. W. S. Studies.

TWDB (2019). Hydrology of the Lamar Peninsula. C. f. W. S. Studies.

USGS (2019). USGS 08211520 Oso Ck at Corpus Christi, TX. U. T. W. S. C. W.-D. Inquiries, National Water Information System: Web Interface.

USGS (2019). USGS 08212400 Los Olmos Ck nr Falfurrias, TX. U. T. W. S. Center, National Water Information System: Web Interface.

USGS (2022). USA NLCD Land Cover.

Ward, G. H. and N. E. Armstrong (1997). Current Status and Historical Trends of Ambient Water, Sediment, Fish and Shellfish Tissue Quality in the Corpus Christi Bay National Estuary Program Study Area: Summary Report, Natural Resources Center, TAMU-CC.

Wetz, M. (unpublished work).

Widory, D., et al. (2004). "Nitrate in groundwater: an isotopic multi-tracer approach." Journal of Contaminant Hydrology **72**(1): 165-188.

WSDE (2017). "Nitrogen from Atmospheric Deposition." from ecy.wa.gov/programs/eap/Nitrogen/nitrogenAtmosphere.html.

Xuan, Y., et al. (2020). "Mechanisms of nitrate accumulation in highly urbanized rivers: Evidence from multi-isotopes in the Pearl River Delta, China." Journal of Hydrology **587**: 124924.

Xue, D., et al. (2009). "Present limitations and future prospects of stable isotope methods for nitrate source identification in surface- and groundwater." Water Research **43**(5): 1159-1170.

Zhang, L., et al. (2007). "Sensitive Measurement of NH4+ 15N/14N (δ15NH4+) at Natural Abundance Levels in Fresh and Saltwaters." Analytical Chemistry **79**(14): 5297-5303.

Task 3:

Quantifying Benthic Fluxes of Inorganic and Organic Nutrients

Prepared by:

Hussain Abdulla, Ph.D.

Joseph Felix, Ph.D.

Quan Ton

Summary

This study quantified the sediment porewater flux of ammonium (NH_4^+) and photo-ammonification from benthic dissolved organic nitrogen (DON) as well as investigated changes in porewater DOM chemical structures of Baffin Bay - Texas during different irradiation time periods using the state of art Orbitrap Fusion Tribrid Mass Spectrometer. Baffin Bay (BB) is a semi-arid inverse estuary ecosystem that has experienced prolonged and intense brown tide blooms (*Aureoumbra lagunensis* species) since the 1990s, and several occurrences of hypoxia conditions that caused seagrass die-off and several occasions of large fish kill over the past decades. Porewater samples were collected from six stations in the bay during six seasons (October 2020, February 2021, June 2021, October 2021, February 2022, and May 2022) for depth profile analysis. The bay showed a large spatial variability of NH_4^+ benthic flux, with BB1 having the lowest average NH_4^+ flux at 56 ± 27 $\mu mol.m^{-2}.day^{-1}$ and BB3 had the highest average flux at 347 ± 211 $\mu mol.m^{-2}.day^{-1}$. The seasonal NH_4^+ average benthic flux to the entire bay water column was 124 – 244 $\mu mol.m^{-2}.day^{-1}$ and served as a significant source of inorganic nutrients to support the primary production. In addition, the photo-ammonification rate of benthic DON (after it entered the water column) ranged from 0.038-0.361 $\mu mol.L^{-1}.hour^{-1}$ and served as an additional source of inorganic nutrients to primary production. Chromophoric dissolved organic matter (CDOM) absorbed sunlight radiation then degraded to lower molecular weight CDOM and released ammonia, deaminated peptides, free amino acids, and organic acids. Peptides and deaminated peptides with chromophoric amino acids such as tryptophan, tyrosine, proline, phenylalanine, and histidine degraded with solar irradiation. It was suggested that rings and conjugated double bonds were responsible for absorbing sunlight radiation and degrading CDOM structures. This study shed light on internal N cycling and transformations in Baffin Bay and the need to consider these processes in any future attempt to remediate and lower the brown tide events in the bay.

1. Background

Since the early 1990s, the Baffin Bay (BB) ecosystem has experienced prolonged and intense brown tide blooms (*Aureoumbra lagunensis* species) and several occurrences of hypoxia conditions that caused seagrass die-off and several occasions of large fish kill over the past decades (Wetz et al., 2017). Nutrient patchiness is the second most influential factor (after temperature) in site seasonal variability of net primary production (Caffrey, 2014). This guides a consensus that nitrogen (N) loading is a primary factor in eutrophication and hypoxia. Despite this recognized connection between excess N loading and ecosystem decline, the internal N cycling and transformations in coastal areas are still not well characterized. Dissolved inorganic nitrogen (DIN) plays an important role in controlling the primary production rate (PPR) and the food web in marine systems. PPR in estuaries and coastal area ecosystems could range seasonally and spatially. For example, in the Bristol Channel estuary, UK (a highly turbid estuary), the daily PPR ranged from 18 - 450 $mgC.m^{-2}.day^{-1}$ (Joint and Pomroy 1981). In Baffin Bay, TX, the daily PPR ranged from 1-132 $mgC.m^{-2}.day^{-1}$ (Blanchard and Montagna 1995). Caffrey et al. (2014) measured an annual PPR from 825 g C m^{-2} $year^{-1}$ in Weeks Bay to 401 $g.C\ m^{-2}.year^{-1}$ for Apalachicola Bay and 377 $g\ C.m^{-2}.year^{-1}$ in Grand Bay in three different estuaries in the northern Gulf of Mexico. They found a correlation between the nitrogen loading and annual PPR in these three bays.

Ammonium is the form of DIN that is most easily consumed by microorganisms via a process called "assimilation". As the detritus particulate organic nitrogen (PON) of microbes (and other organisms) decomposes to dissolved organic nitrogen (DON) in the surrounding seawater, a host of micro-organisms consume PON and DON, converting some of the nitrogen back to ammonium via remineralization. The reduced form of nitrogen, ammonium (NH_4^+), is easier for most microbes to assimilate than oxidized nitrogen compounds such as nitrate (Francis et al., 2007). Ammonium (NH_4^+) sources contributing to estuaries vary from rivers, groundwater, fixed atmospheric nitrogen, and sediment benthic fluxes. Nitrogen can enter estuaries as terrestrial runoff from forests, agricultural lands, or urban areas. Nitrogen can also come from atmospheric deposition such as emissions of nitrogen oxides from automobiles and industrial sources and ammonia emissions from nitrogen fixation. Another source of nitrogen includes sewage treatment plants and industrial facilities (Castro et al., 2003). In addition, sediment benthic flux also contributes nitrogen to estuaries as an internal circulation source (Nixon, 1981; Rizzo, 1990). The release of nutrients from resuspended porewater and sediment particles has been implicated in the stimulation of heterotrophic microplankton in estuarine waters (Wainright, 1987). Ammonium concentrations in sediment porewaters were reported to be high in anoxic conditions from 1-5 $mmol.L^{-1}$ in the Santa Barbara Basin (Abdulla et al., 2018) and 0.35-3.85 $mmol.L^{-1}$ in Laguna Madre estuary (Morin et al., 1999). Therefore, its contribution to the water column via benthic flux would need to be considered as a major source.

However, not all DON can undergo complete remineralization and release NH_4^+ in anoxic conditions. Some DON leaves behind a peptide skeleton and becomes bio-refractory for microbes to digest. DON, such as humic substances, was believed to make a negligible contribution to eutrophication (Kieber et al., 1989) until it was discovered to be photochemically reactive (Bushaw et al., 1996). Photo-ammonification of DON has been recognized in many studies to be a significant source of bioavailable nitrogen (Morell and Corredor, 2001; Xie et al., 2012), and its essential contribution to biomass production and eutrophication (Rain-Franco et al., 2014; Vahatalo and Jarvinen, 2007). Photo-ammonification was shown to contribute up to 50–178% of the NH_4^+ needed for phytoplankton in primary production (Rain-Franco et al., 2014). Many studies have been conducted to investigate the relationship between photo-ammonification rate and other

ecosystem factors like pH (Zhang and Anastasio, 2003), salinity (Funkey et al., 2015), or temperature (Xie et al., 2012). Mechanism simulation was hypothesized (Davies and Truscott 2001), but the information on reaction pathways was not clarified. There also have been some conflicting results in the photo-ammonification of DON in natural water. Despite all of these studies, no assessment (to the best of our knowledge) of photo-ammonification of benthic DON flux that diffused to the water column has been conducted. Little is known about benthic DON flux and its transformation in marine waters. Thus, the efflux of DON and ammonia represents a major pathway for organic nitrogen to escape from being preserved in the long geological carbon cycle and then stimulate further primary productions resulting in an extended hypoxia event. The benthic DON can be further remineralized to produce NH_4^+ and/or diffused to surface water photic zone where it can be exposed to sunlight and undergo photochemical degradation to produce NH_4^+, low molecular weight acids, and free amino acids, which can support primary production and microbial respiration that possibly support the primary production at the surface water.

In Baffin Bay, as the freshwater runoff is very low in the bay, this led to speculation that the agricultural runoff is responsible for the nutrient pulses that initiate and sustain the brown tide bloom. However, this speculation overlooks the role of benthic fluxes in delivering dissolved organic nitrogen (DON) and nutrients to the bay. The current estimated dissolved organic matter (DOC) benthic flux from coastal sediments is almost equivalent to the riverine DOC flux to the open ocean. Relative to riverine DOM, benthic porewater has a much higher DON. A recent study showed that the depth profile of porewater NH_4^+ strongly correlated with DON concentration (R^2 =0.96) (Abdulla et al., 2018). Many studies showed NH_4^+ concentrations can buildup up to ~ 7 mM within the first 1-2 meters of the sediment profiles (Abdulla et al., 2014). The fate of DON in sediment porewaters after entering the water column remains mysterious and needs investigating. One of the possible transformations of sediment DON in the water column is photo-oxidation by sunlight which leads us to our research, the photo-ammonification of DON in sediment porewaters.

In this study, we 1) quantified the seasonal benthic sediment flux of ammonium (NH_4^+) and 2) Track the fate of the benthic nutrients and DON in the bay water column using both N-isotope signatures (NH_4^+ and DON) as well as investigated changes in porewater DON chemical structures during different irradiation time periods using the state of art Orbitrap Fusion Tribrid Mass Spectrometer.

2. Methods

2.1 Sampling

Surface water and porewater samples were collected at Baffin Bay at six different locations Figure 1 (BB1, BB2, BB3, BB4, BB5, BB6) during six different seasons: October 2020 (Oct 31st, 2020), February 2021 (February 4th, 2021), June 2021 (June 12th, 2021), October 2021 (October 6th, 2021), February 2022 (February 8th, 2022), and May 2022 (May 26th, 2022). Before the sample collection, all the glassware was cleaned with tergazyme and soaked in 5% HCl for 12 hours followed by cleaning with deionized (DI) and Milli-Q ultrapure grade water, respectively. After cleaning, glassware was oven-dried and combusted at 450^{o}C for 12 hrs. The same cleaning process was applied to the plasticware excluding the combustion. In the field, polycarbonate bottles, cores and core caps were rinsed several times with bay water before collecting the samples. A total of 72 surface water samples (two 1L bottles per station per season) were collected and stored in pre-cleaned polycarbonate bottles and then filtered through 0.22 µm (cellulose acetate filter, Corning®). Two sediment cores (~35cm, polycarbonate core liner) were collected at each station and were stored in an icebox and transported back to the lab where samples were kept in the

refrigerator until further analysis (within 2 days maximum). Field parameters such as salinity were measured using Fisher Scientific Optical Refractometer and pH were measured using Horiba LAQUA twin pH meter Model: S010.

The first core was used for porewater sampling with Rhizone samplers (0.12µm pore size

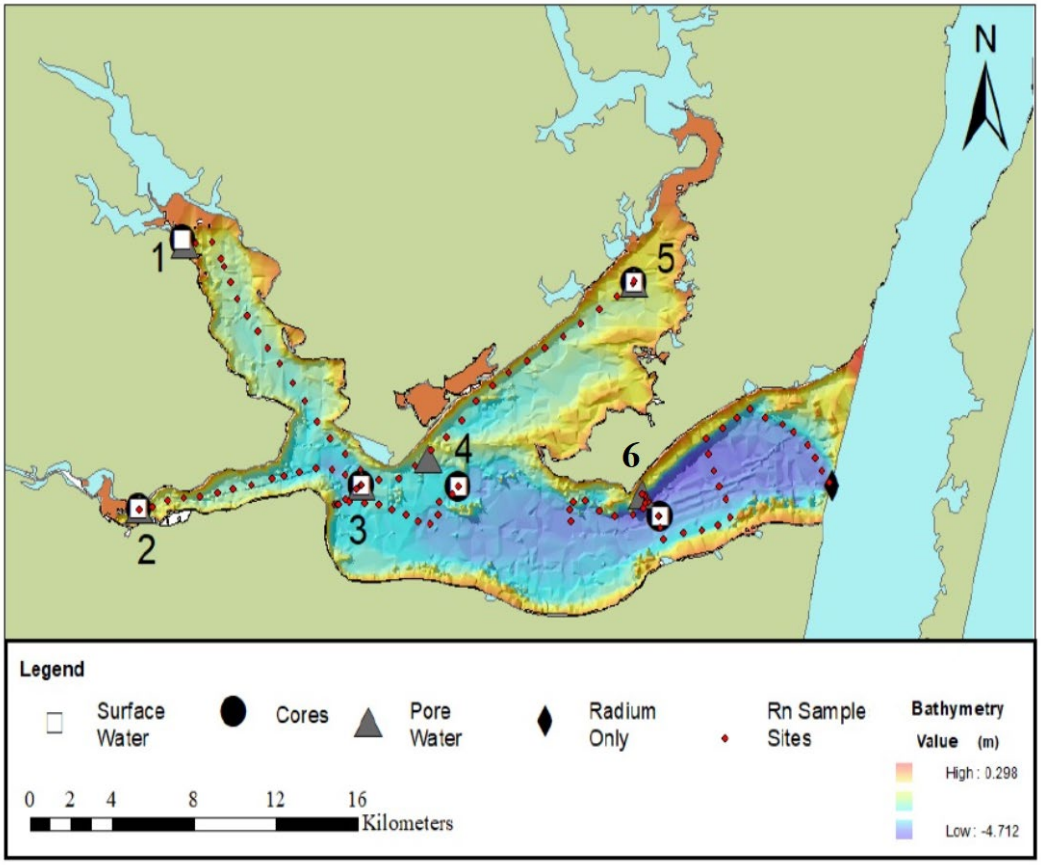

Figure 1. *Sample site locations in Baffin Bay*

membrane) at every 2 centimeters depth. The porewaters were subsampled for NH_4^+, dissolved organic nitrogen (DON), dissolved organic carbon (DOC), NO_3^- concertation and mass spectrometer analysis. The second core was used for solar irradiation experiments and porosity analysis. Sediment was sectioned every 2-cm depth. Subsample sediments were taken for porosity analysis. The remaining sediments were centrifuged at 9,600 rpm for 15 min, filtered, collected and combined in 500 ml combusted glass bottles. The porewater samples were purged with pure nitrogen gas in a basic environment (add concentrated NaOH to pH ~ 12) to remove almost all the initial ammonium in porewaters prior to the irradiation experiment. Purged porewaters were expected to have less than 5µM of ammonium. The samples were then acidified to bring them back to their original pH value using concentrated hydrochloric acid.

2.2.Ammonium (NH_4^+) concentration measurements

Ammonium (NH_4^+) concentrations were determined using the Ortho-phthaldialdehyde (OPA) method (Holmes et al., 1999) and measurements were conducted with the fluorescence detector in High-Performance Liquid Chromatography (HPLC) Ultimate 3000 model. OPA working solution (WS) is made up of 200mL borate buffer + 1mL sodium sulfite + 10mL OPA as

the ratio is Borate: Na_2SO_3: OPA = 200:1:10. Borate buffer solution: 8g of sodium tetraborate in 200 mL H_2O makes up 200 mL of borate buffer for the WS. Sodium sulfite solution: 0.08g of Na_2SO_3 in 10 mL of H_2O makes up 10 mL of sodium sulfite solution, then take only 1 mL for the WS. OPA fluorescence solution: 0.4g of OPA in 10 mL of ethanol makes up 10 mL of OPA fluorescence solution for the WS. The WS will be stored in the dark for at least 1 day prior to the reaction with samples. For the determination of ammonium (NH_4^+) concentration, 0.25 mL of a sample is mixed with 1 mL of the WS and then incubated in the dark for at least 2 hours prior to the detection by HPLC - fluorescence detector. The NH_4^+ concentration must be measured between 2-8 hours of incubation time. Ammonium chloride (NH_4Cl) solutions were used as the calibration standard from 0.1 – 400 μM.

2.3.Sediment porosity

Porosity was measured by weighing and then drying 166cm^3 saturated sediment core cylinders in an oven at 105° C. After constant weight measurements, sections were weighed for dry mass. Porosity was then derived using the relationship between bulk density and particle density (Avnimelech et al., 2001).

$$\phi = 1 - \frac{\rho_b}{\rho_g} \text{ ---------- (1)}$$

where ϕ is porosity, ρ_b is the bulk density, and ρ_g is the particle density assuming a constant and conventionally agreed upon value of 2.65g/cm3 (Klute, 1986).

2.4.Benthic ammonium flux

The diffusive flux of ammonia was calculated using Fick's First Law

$$F^i = -\phi D_s^i \frac{dC^i}{dz} \text{ ---------- (2)}$$

where F^i is the diffusive flux of pore water solute *i*, ϕ is sediment porosity, D_s^i is the whole sediment diffusion coefficient of solute *i*, and dC^i/dz is the concentration gradient of solute *i* at sediment depth. Porosity at various depth intervals was calculated using an exponential function that would fit the porosity data from the same sediment cores as described by Komada et al. (2016). D_s^i was calculated from the modified Weissberg relation, $D_s^i = D_0^i / \{1-\ln(\phi^2)\}$ (Boudreau, 1997), where D_0^i is the free seawater diffusion coefficient of ammonium. The ammonia D_0^i ($m^2\ s^{-1}$) constants were used according to Schulz (2006). We assumed steady-state conditions and molecular diffusion is the primary factor controlling ammonium concentrations down the profile.

2.5.Solar Simulator experiments

For this study, a solar simulator (Model: Atlas SUNTEST CPS+) was used to irradiate the sample for a different time interval (up to 72 hrs) and the samples were further analyzed accordingly. with its irradiation wavelength set at 300-400 nm which transfers the following heat fluxes (kJ/m^2): 702 in 3 hours, 2808 in 12 hours, 5616 in 24 hours, and 16848 in 72 hours. Most photochemical reactions that mineralize dissolved organic carbon at the surface water occur within these wavelengths (Mopper and Kieber 2000; Vähätalo et al., 2000; Minor et al., 2007). The solar simulator lamps were kept on for the entire experimental period during the irradiation of the samples. Five subsamples (60-65mL each) in five quartz flasks underwent irradiation at 3, 12, 24, and 72 hours along with a dark control. A dark control was aluminum wrapped and exposed to irradiation for 72 hours to monitor the heat effect. The irradiated waters were then preserved for the following experiments: ammonium concentration, UV-Vis measurement, and structural elucidation by Mass Spectrometry.

2.6.Ammonium isotope analysis

Porewater NH_4^+ and photo-produced NH_4^+ were oxidized to NO_2^- before isotope analysis so it could be measured by the denitrifier bacteria method at the University of California, Davis Stable Isotope Facility. International $\delta^{15}N\text{-}NH_4^+$ standards USGS25 and USGS26 were prepared, oxidized, and analyzed in the same manner as the samples for data normalization and to test the efficiency of the coupled method oxidation and denitrifier method. Additional internationally recognized standards (USGS32, USGS34, USGS35, IAEA-N3) were measured during sample analysis to provide known $\delta^{15}N\text{-}NO_3^-$ references for data correction. The average standard deviation for $\delta^{15}N\text{-}NO_3^-$ reference materials was 0.2‰. Propagated standard deviation for the NH_4^+ and NO_3^- isotope standards was 0.9‰. Nitrate and NO_2^- were not detected in original pore water samples and due to observations in previous experiments and literature, any photochemical NO_3^- and NO_2^- production is assumed to be minimal relative to ammonium production thus not significantly affecting the reported $\delta^{15}N\text{-}NH_4^+$.

The NH_4^+ nitrogen isotopic composition ($\delta^{15}N\text{-}NH_4^+$) was denoted by the following equation and was reported in permil (‰):

$$\delta_{sample}\,(‰) = (R_{sample}/R_{standard} - 1) * 1000 \qquad (3)$$

where R is the ratio of $^{15}N/^{14}N$ and the $R_{standard}$ is atmospheric nitrogen with an accepted value of 0‰.

2.7.UV-Vis absorption measurement

Chromophoric dissolved organic matter (CDOM) samples were analyzed using a Cary 60 UV-Vis Spectrophotometer (*Agilent*) with the absorption spectra of 200-800 nm, 1 cm wide quartz cuvette, and Milli-Q water as a blank. All the sample spectra were baseline and blank corrected. Instrument absorption of samples was converted to the absorption coefficient, *a*, using the following equations (Helms et al., 2008):

$$a = 2.303A/l \text{ ---------- (4)}$$

- $a \equiv$ Absorption coefficient (m^{-1})
- $A \equiv$ Absorbance over a path length
- $l \equiv$ Path length of the cuvette (m)

The spectral slope (S) was calculated by fitting absorption data to the following exponential equation (Helms et al., 2008):

$$a_\lambda = a_{\lambda ref}\, e^{-S(\lambda - \lambda ref)} \text{ ----------(5)}$$

- $a \equiv$ absorption coefficient (m^{-1})
- $\lambda \equiv$ wavelength (nm)
- $\lambda_{ref} \equiv$ reference wavelength (nm)
- $S \equiv$ spectral slope (nm^{-1})

$$\ln(a_\lambda) = \ln(a_{\lambda ref}) - S(\lambda - \lambda_{ref}) \text{ ----------(6)}$$

The spectral function for the 200-800 nm ($S_{200-800}$) interval was determined by plotting the respective values in equation (4). The spectral slope for the interval of 275 – 295 ($S_{275\text{-}295\ nm}$) and 350-400 ($S_{350\text{-}400\ nm}$) was calculated by fitting the best linear regression log-transformed absorption coefficient (*a*) spectra using equation (5). The ranges, 275–295 nm and 350–400 nm, were chosen because the first derivative of natural-log spectra indicated that the greatest variations in S from a variety of samples (marsh, riverine, estuarine, coastal, and open ocean) occurred within the narrow bands of 275–295 nm and 350–400 nm (Helms et al., 2008). The slope ratio (S_R) was calculated as the ratio of $S_{275\text{-}295}$ to $S_{350\text{-}400}$. This methodology avoids the use of spectral data near

the detection limit of the instruments and focuses on absorbance values that shift significantly during estuarine transit and photochemical alteration of CDOM (Helms et al., 2008).

2.8. DOM Chemical Characterization & Structural Elucidation by Mass Spectrometry

Samples were prepared for mass spectral analysis using PPL solid phase extraction cartridges (Agilent, Bond Elut PPL, 200 mg resin, 3 mL volume (Dittmar et al., 2008). A liquate of 10 mL of filtered porewater samples was acidified using trace metal grade hydrochloric acid (HCl) to pH 2. The samples were extracted using 200 mg, 3mL Bond elute-PPL cartridges. Blank Milli-q water was extracted as a sample. Final DOM extracts were eluted using 6 mL HPLC Optima grade methanol and collected in pre-combusted glass vials. Final SPE-DOM extracts were dried using a Centrivap benchtop concentrator and diluted to 1 mL Milli-q water. The samples were analyzed with both UPLC-OT-FTMS (positive mode) and IC-OT-FTMS (negative mode) according to (Bergmann 2021).

DOM extracted samples were analyzed for positive mode detection analysis by Vanquish Ultra Pressure Liquid Chromatography – Orbitrap Fusion Tribrid Mass Spectrometer (UPLC-OT-FT-MS). The analytes were separated on the 1.7 μm ACQUITY UPLC BEH C_{18} reversed-phase column by Waters (130 Å, 1.7 μm, 2.1 mm × 150 mm) and guided to a heated electrospray (H-ESI) and the Orbitrap Fusion Tribrid Mass Spectrometer. The injection volume of each sample was 20 μL. The Eluent A, Milli-Q with 0.1 % (*v*/v) formic acid, and eluent B, acetonitrile with 0.1 % (v/v) formic acid, were mixed with curve 5 to a flow rate of 0.200 mL/min. The total run lasted 31 min with 7 min re-equilibration and the following gradient: 0-2 min hold at 5 % B, ramp to 65 % B for 18 min, then ramp to 100 % B for 1 min and hold at 100 % B for 3 min. The H-ESI setting was 3500V for the positive spray voltage with ion transfer tube temperature at 300 °C and vaporization temperate at 225 °C. The three gases on the H-ESI were 35 for sheath gas, 7 for aux gas, and 0 for sweep gas. The OT-FT-MS was set at 500,000 (FWHM at m/z 200) resolution and mass range 80-800 m/z with RF lens at 40%. Two MS^2 were scanned with the Ion Trap following the full scan via two filters, Dynamic Exclusion (n = 1 for 30s) and Intensity Threshold (min = 5000, max = 1.0e20). Both MS^2 scans were isolated via the Quadrupole with a mass bandpass of 0.7 m/z, but one fragmentation scan was generated using collision-induced dissociation (CID) with assisted energy collision, and the other fragmentation scan was generated with higher-energy collisional dissociation (HCD) with stepped energy collision. Both MS^2 scans had an automatic gain control (AGC) set at 1.0e4 and a maximum injection time of 50 msec.

For negative mode analysis, extracted DOM samples were run on Thermo Scientific Dionex ICS-5000^+ – Orbitrap Fusion Tribrid Mass Spectrometer (IC-OT-FT-MS). The analytes were run in 1-dimension with a Dionex IonPac AS11-HC 4 μm column by Thermo Scientific (2000 Å, 4 μm x 2 mm x 250 mm), a Dionex IonPac AG11-HC 4 μm guard column by Thermo Scientific (13 μm, 2mm x 50 mm), and Dionex AERS 500e Anion Electrolytically Regenerated Suppressor for External Water Mode (2 mm). To enhance the deprotonation of DOM compounds for negative detection, a solution consisting of 1L acetonitrile, 30 mL Milli-Q, and 3 mL ammonium hydroxide was flowing with the sample at 0.2 mL/min to the H-ESI ion source after exiting the conductivity detector via a t-shaped connection. The total analysis run was 20 min with 1 min re-equilibration, 0.4 mL/min flow, 40 μL injection volume, and the following gradient: started with initial 0.1 mM KOH, increased to 4 mM KOH 0.1-5.0 min, ramped to 60 mM KOH 5.0-11.0 min, held at 60 mM KOH from 11.0-16.0 min, and decreased to 1 mM KOH 16.-16.1 min. The temperature in the DC compartment was set at 35.0 °C. The H-ESI was set at 3100V for the negative spray voltage with ion transfer tube temperature at 350 °C and vaporization temperate

at 300 °C. The three gases on the H-ESI were 50 for sheath gas, 20 for aux gas, and 2 for sweep gas. The Orbitrap was run at 500,000 (FWHM at m/z 200) resolution and mass range 85-700 m/z with an RF lens at 40 % to focus on low m/z compounds for the full scan analysis. Following the full scan, two MS^2 were scanned with the Ion Trap via two filters, Dynamic Exclusion (n = 3 for 60s) and Intensity Threshold (min = 1000, max = 1.0×10^{20}). Both MS^2 scans were isolated with the Quadrupole (0.7 m/z), but one fragmentation scan was generated through CID with assisted energy collision, and the other fragmentation scan was generated through HCD with stepped energy collision. MS^2 scan with CID had an automatic gain control (AGC) set at 3.0e4 and a maximum injection time of 50 msec, and the MS^2 scan with HCD had an AGC of 1.0e4 and a maximum injection time of 50 msec.

Compound Discoverer software 3.2 (Thermo Fisher) was used to identify the DOM compounds. All chromatography spectra' retention times (RT) were aligned using an adaptive curve with a maximum shift of 0.2 min and 5 ppm mass tolerance. To identify a compound, the following conservative criteria were met: 1) a signal-to-noise (S/N) above 3, 2) a minimum of 5 mass scans per chromatographic peak, 3) a minimum peak intensity of 50,000, and 4) at least one isotope peak (M + 1) was detected. We have used the ratio of the M + 1 to parent peaks to confirm the number of carbon atoms. We also used the M + 2 peak ratios to confirm the presence of the S atom in the compound. *De novo* structural elucidation was performed on the MS^2 fragments, and these structures were putatively annotated using *in silico* fragmentation prediction software (Mass Frontier). Deaminated peptides and peptides were identified through a combination of the following 5 multi-confidant points: 1) high mass accuracy of OT-FTMS, 2) identification and matching of isotopic patterns (at least M+1 isotopes) to confirm ionized charge and the estimated number of carbon atoms, 3) cross-referencing with in-house deaminated peptide database, 4) matching retention times between different samples, 5) structure confirmation through MS^2 fragmentation by both CID and HCD techniques and verification using *in silico* fragmentation prediction software with a FiSH score of 70% or higher.

3. RESULTS

3.1. Salinity and precipitation of Baffin Bay during six sampling seasons

The first two seasons, Oct_20 and Feb_21, indicated the hypersaline condition in Baffin Bay with an average salinity of 45.1±1.8 and 48.5±1.9, respectively (Figure 2). According to NOAA (ref. 65), the precipitation in the region was low before sampling dates in Oct_20 (<6 inches) and Feb_21 (<4 inches) (Figure 3). The average salinity dropped significantly to 16 ± 8.3 in Jun_21. There was heavy precipitation in the region that occurred in May_21 (17.89 inches), which was expected to bring in freshwater and flush the semi-closed water system resulting in a drop in salinity recorded in the next sampling season, Jun_21. After that, the average salinity of the bay gradually increased to 17.9±2.2, 22.9±1.5 and 33.0±1.0 in Oct_21, Feb 22 and May_22, respectively. The low rainfall during this period (after Jun_21) could be responsible for the increase in salinity of the bay along with the high evaporation rate in the region. The average pH of the Baffin Bay surface water ranged from 7.92 to 8.50 with the highest (more alkaline) in Jun_21. The water temperature ranged from 11.93 ºC to 29.38 ºC, with the highest in Jun_21 (summer) and the lowest in Feb_22 (winter). The surface water dissolved oxygen (DO) ranged from 7.11 mg/L to 10.61 mg/L with the highest in Feb_22 and lowest in May_22.

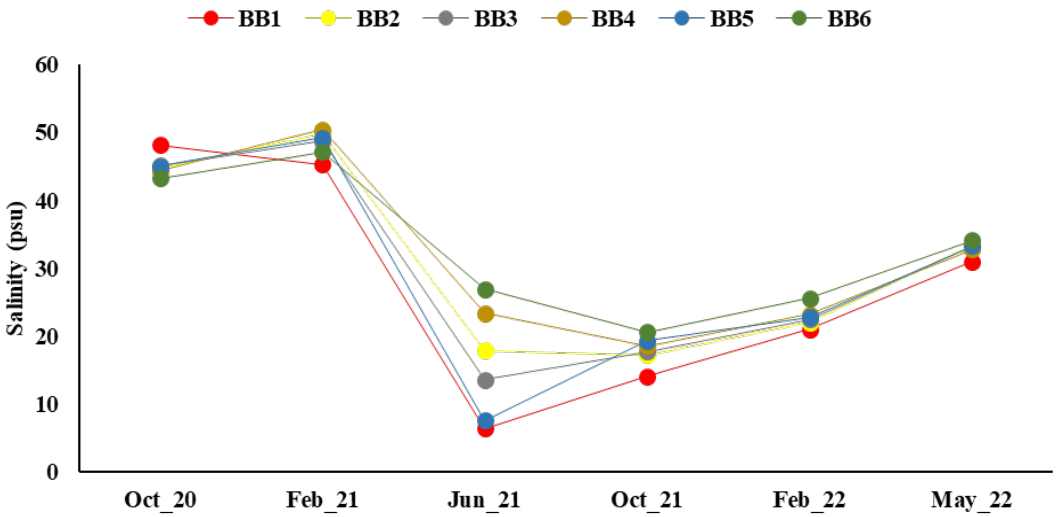

Figure 2. *Salinity of six sampling sites throughout six seasons.*

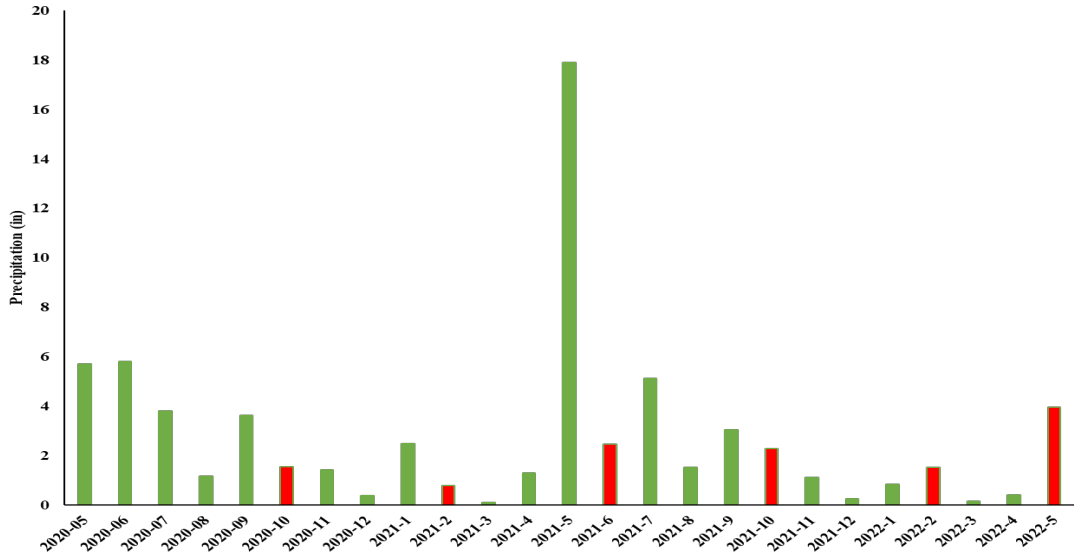

Figure 3. *Precipitation (inches) in Baffin Bay during six sampling seasons (NOAA, Station Kingsville 6.5 SSE, TX US). Precipitation includes rain, melted snow, etc. "Red" columns*

3.2.<u>Ammonium (NH_4^+) in the surface water and sediment porewater</u>

Ammonium concentrations of surface waters ranged from 11 µmol-N.L^{-1} to below the detection limit (0.1 µmol-N.L^{-1}) in all six stations during six seasons (*Figure 4*). Oct_20 had the highest average [NH_4^+] on surface water with 6 ± 3 µmol-N.L^{-1} while May_22 showed that [NH_4^+] was below the detection limit for all the six stations. Porewater ammonium (NH_4^+) concentrations were measured for six stations during six seasons (*Figure 5*). Note that BB1-October 2020 was missing due to the loss of the sample core. NH_4^+ concentration ranged from 32 to 2,181µmol-N.L^{-1}. Geographically, the highest average porewater [NH_4^+] was 935 ± 637 µmol-N.L^{-1} at BB6 (near

the Laguna Madre) followed by BB3 (center of the Bay) and BB2 (Laguna Salada) with 861 ± 482 and 618 ± 342 µmol-N.L^{-1}, respectively. On the other hand, BB5 reported the lowest average [NH_4^+] of 381 ± 128 µmol-N.L^{-1}. The spatial average [NH_4^+] showed significant differences between each station with chi-squared = 424, *p* value = 2×10^{-89}. Seasonally, the highest average porewater [NH_4^+] was 844 ± 534 µmol-N.L^{-1} in February_2022 followed by February_2021, October_2020 and May_2022 with 684 ± 531, 660 ± 594 and 634 ± 169 µmol-N.L^{-1}, respectively. The lower average [NH_4^+] was in October_2021 and June_2021 with 482 ± 158 and 434 ± 249 µmol-N.L^{-1}, respectively. The seasonal average [NH_4^+] showed significant differences between each season with chi-squared = 176, *p-value* = 3×10^{-36}.

Ammonium concentrations in six stations were seasonally compared (Figure 6). Significant differences were evaluated using paired t-test on a confidence level of 95%. BB1 and BB2 reported a slight increase in ammonium concentrations over time (insignificant, $p > 0.05$). The NH_4^+ porewater showed a drastic increase in February 2022 (significant, $p < 0.05$). BB3 was consistent during six seasons (insignificant, $p > 0.05$) except February 2022 with a dramatic increase in NH_4^+ concentrations (significant, $p < 0.05$). BB4 recorded the highest in May 2022 (significant, $p < 0.05$). BB5 and BB6 showed significant changes during the seasons ($p < 0.05$). In both stations, porewater [NH_4^+] dropped after the rainfall in May_21 and then gradually increased back. BB5 peaked in February 2022 and while BB6 lost all its ammonium after the rainfall in May_21 then gradually accumulated it back. Overall, February 2022 reported the highest porewater [NH_4^+] in Baffin Bay, especially at BB2 and BB3 (significant, $p < 0.05$), while BB6 had the most considerable seasonal variation of porewater NH_4^+ concentration (significant for every season, $p < 0.05$). At BB6, the first two seasons had a median above 1,800 µmol-N.L^{-1}. However, the concertation dropped to 67 µmol-N.L^{-1} in Jun_21 sampling season. We observed a decrease in water salinity at the BB6 site (from above 40 in the first two seasons to a salinity of 26 in Jun_21) resulting from the heavy rainfall in May_21. The other stations, BB1, BB2, BB4 and BB5 showed no significant changes after rainfall in May_21 ($p > 0.05$).

Comparing the ammonium concentrations between six stations geographically (Figures 5 and 6) showed that BB3 and BB6 peaked in the first two seasons, October 2020 and February 2021 (significant, $p < 0.05$). After the rainfall in May_21, the porewater [NH_4^+] at BB3 stayed the same (646±260 µmol-N.L^{-1}) (insignificant, $p > 0.05$) while it dropped dramatically to 71±11 µmol-N.L^{-1} at BB6 (significant, $p < 0.05$). BB3 still showed the highest [NH_4^+] in June 2021, October 2021, and February 2022 until May 2022 (significant, $p < 0.05$) when BB6 and BB4 had higher [NH_4^+]. In six seasons, BB1 and BB5 showed the lowest [NH_4^+] (significant, $p < 0.05$). In conclusion, porewater [NH_4^+] varied from season to station and tended to increase with sediment depth.

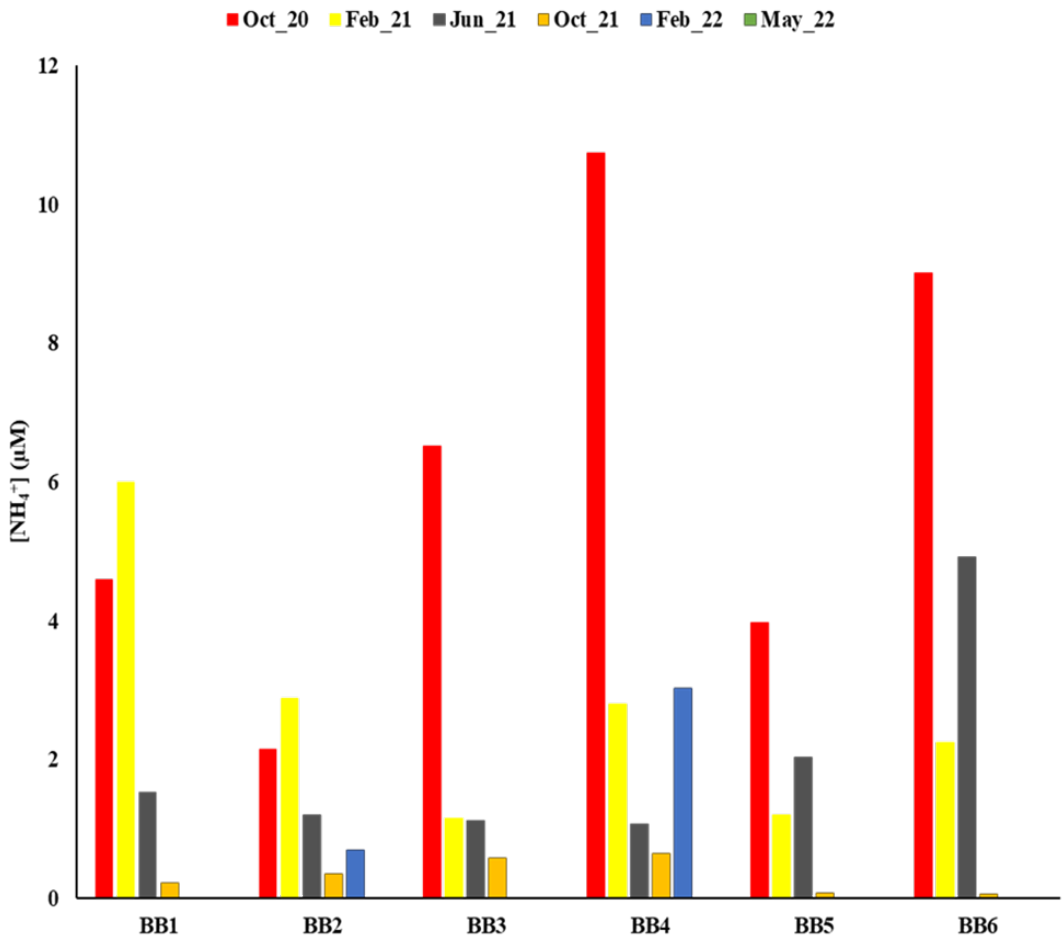

Figure 4. *Ammonium concentration on surface water. February 2022 and May 2022 reported non-detectable concentration (below detection limit).*

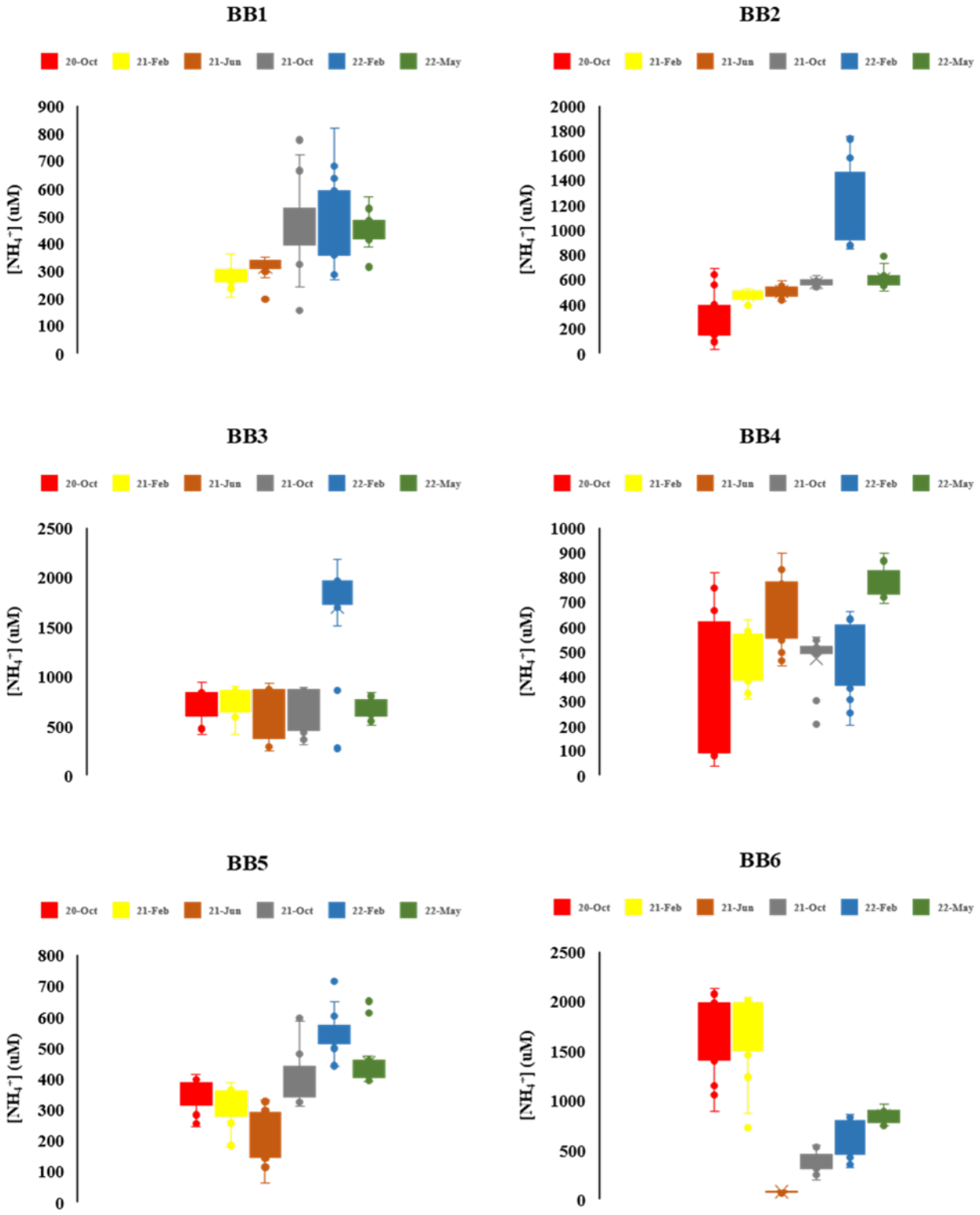

Figure 5. *Seasonal ammonium (NH_4^+) profile of Baffin Bay porewater in six stations.*

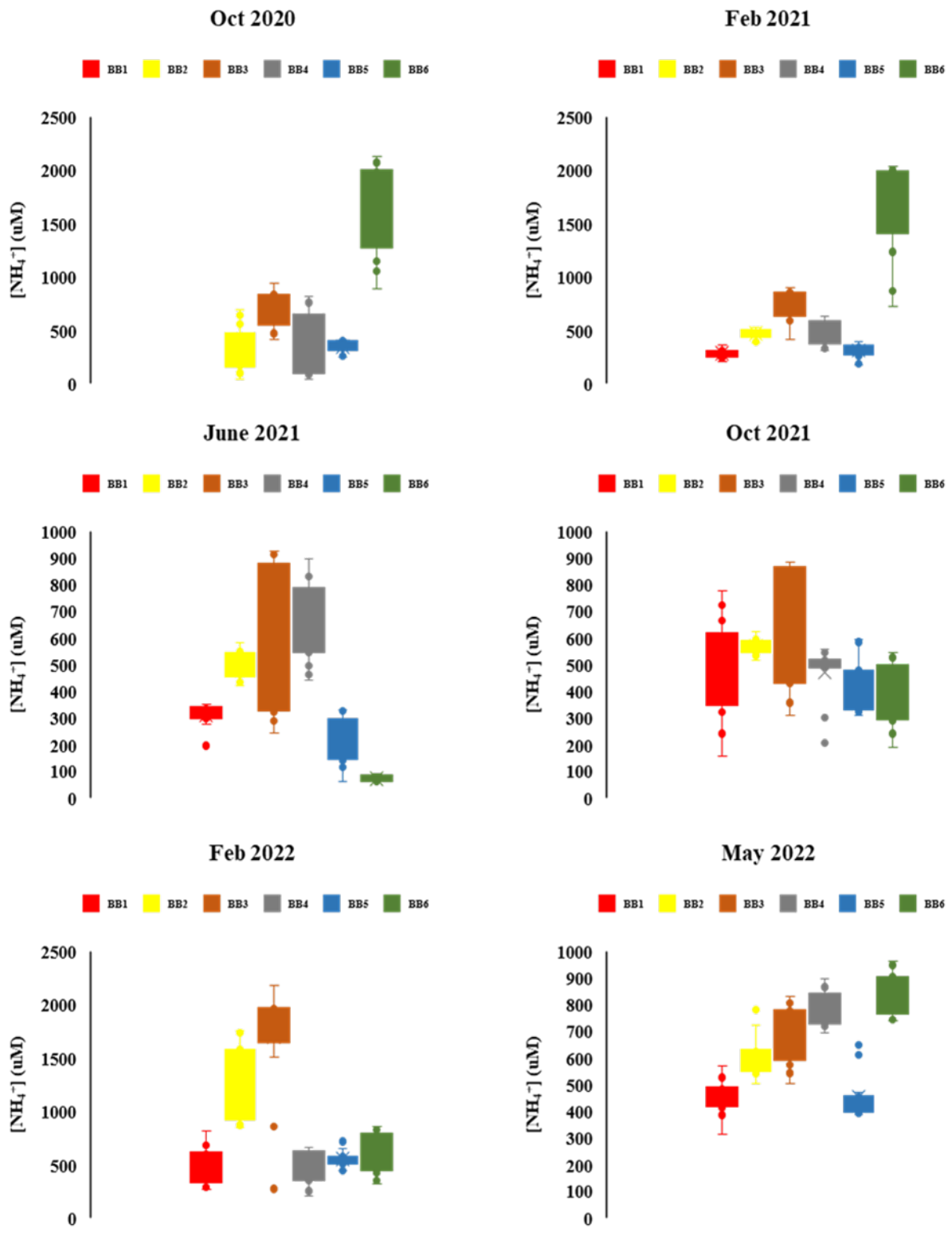

Figure 6. *Geographical ammonium (NH_4^+) profile of Baffin Bay porewater in six stations during six sampling seasons.*

3.3. Ammonium benthic flux to the water column

In general, the NH_4^+ porewater profiles showed an increase along with sediment depth (Figure 7). Applying Fick's first law of diffusion, we estimated the ammonium benthic flux to the water column (*Table 1*). Spatially, BB1 had the lowest average NH_4^+ flux at 56 ± 27 μmol.m^{-2}.day^{-1}. BB3 porewater diffused with the highest average flux at 347 ± 211 μmol.m^{-2}.day^{-1}, followed by BB6, BB4, BB2, BB5 with fluxes of 215 ± 196, 191 ± 111, 108 ± 115, and 102 ± 50 μmol.m^{-2}.day^{-1}, respectively. The spatial average NH_4^+ fluxes showed significant differences between each station with chi-squared = 325, p value = 4×10^{-68}. Seasonally, May_22 had the lowest average NH_4^+ flux at 124 ± 79 μmol.m^{-2}.day^{-1}. Feb_22 porewater diffused with the highest average flux at 244 ± 254 μmol.m^{-2}.day^{-1}, followed by Jun_21, Feb_21, Oct_20, Oct_21 with fluxes of 187 ± 181, 187 ± 156, 161 ± 189, and 133 ± 87 μmol.m^{-2}.day^{-1}, respectively. The seasonal average NH_4^+ fluxes showed significant differences between each season with chi-squared = 56, p value = 7×10^{-11}. The diffusive flux was a function of sediment porosity (Φ), diffusion coefficient (D_s), and instantaneous change of concentrations over depth (dC/dz). The lowest porosity was at BB1 with an average of 0.35, while BB2 and BB6 were 0.55, BB5 was 0.60, and BB3 and BB4 were 0.70.

Ammonium fluxes in six stations were seasonally compared (Figure 8). BB1 showed significant differences in ammonium fluxes with the highest flux in Oct_21 at 87 μmol.m^{-2}.day^{-1} and the lowest flux in May_22 at 29 μmol.m^{-2}.day^{-1} (chi-squared = 117, p value = 8×10^{-14}). BB2 and BB3 ammonium flux showed a drastic increase in Feb_22 with 332 and 723 μmol.m^{-2}.day^{-1}, respectively (chi squared = 610 & 644, significant $p = 1\times10^{-129}$ & 7×10^{-137}, respectively). BB4 and BB5 ammonium fluxes showed significant differences during six seasons with chi-squared = 325 & 124, significant $p = 4\times10^{-68}$ & 3×10^{-25}, respectively. BB6 showed a dramatic decrease in ammonium flux after the rainfall in May_21 then gradually increased back (chi-squared = 896, significant $p = 1\times10^{-191}$. Overall, Feb_22 reported the highest ammonium fluxes in sediment porewaters of Baffin Bay at BB2 and BB3 and Oct_20 and Feb_21 had the highest fluxes at BB6.

Comparing the ammonium fluxes between six stations geographically (Figure 9), BB3 and BB4 with the highest porosity of 0.7 showed the highest fluxes in Jun_21, Oct_21, Feb_22, and May_22. BB1 with the lowest porosity of 0.35 showed the lowest fluxes in Feb_21, Feb_22, and May_22. BB2 & BB6 and BB5 had similar porosity of 0.6 and 0.55 so its fluxes were significantly dependent on the change of ammonium concentrations over depth. In conclusion, porewater NH_4^+ fluxes were significantly dependent on the sediment porosity and changes in the ammonium depth profile.

Table 1. *Benthic fluxes (μmol. m^{-2}.day^{-1}) of Baffin Bay in six seasons.*

	Oct_20	Feb_21	Jun_21	Oct_21	Feb_22	May_22	Spatial Mean	St. Dev.
BB1		31	79	87	54	29	56	27
BB2	60	51	48	30	332	128	108	115
BB3	177	284	464	188	723	246	347	211
BB4	36	218	349	264	112	166	191	111
BB5	50	103	163	158	87	48	102	50
BB6	484	436	18	69	159	125	215	196

Seasonal Mean	161	187	187	133	244	124
St. Dev.	189	156	181	87	254	79

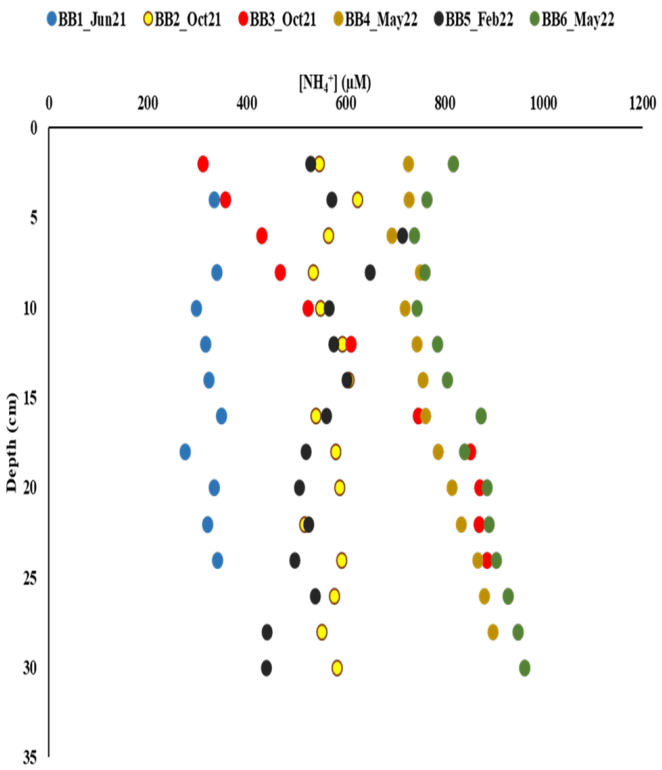

Figure 7. *Ammonium depth profile of pore water. Data points were from BB1_June21, BB2_October21, BB3_October 21, BB4_May22, BB5_February 22, and BB6_May22*

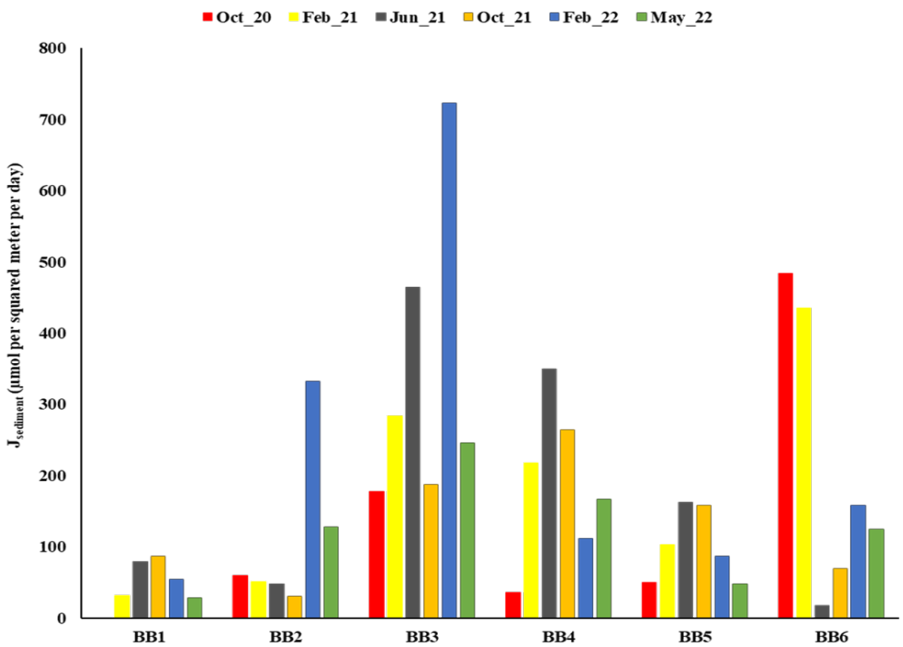

Figure 8. *Benthic ammonium fluxes (µmol.m^{-2}.day^{-1}) of sediment porewater to the water column at six stations during six sampling seasons.*

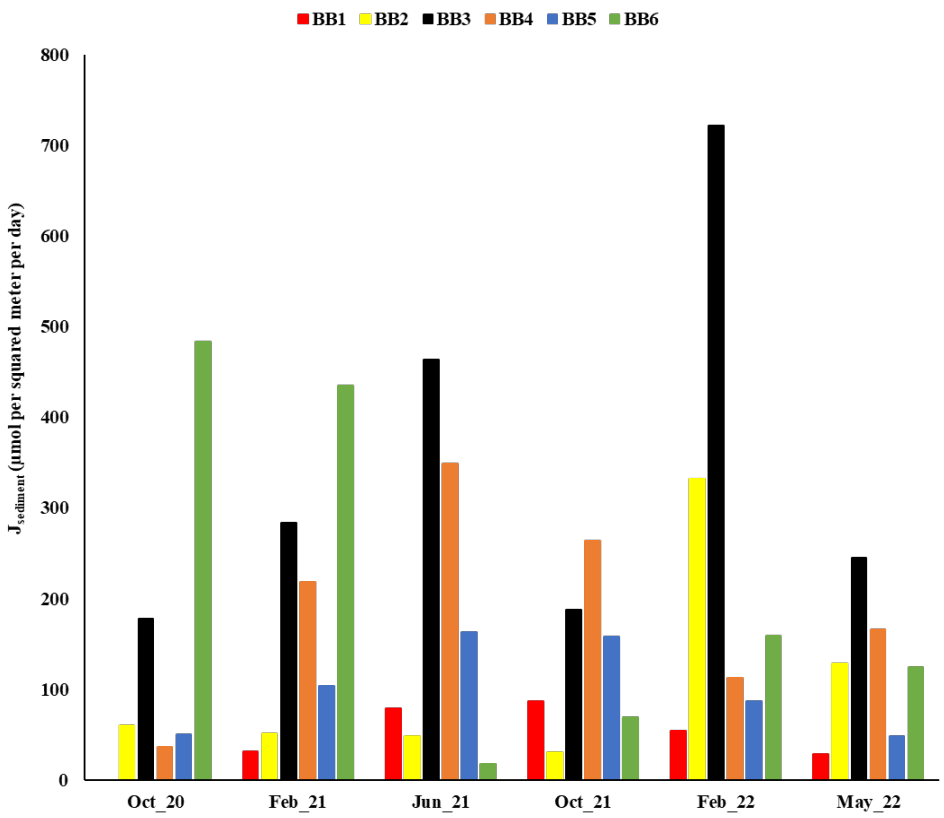

Figure 9. *Benthic ammonium fluxes (µmol.m^{-2}.day^{-1}) of sediment porewater to the water column during six sampling seasons.*

3.4.Ammonium (NH_4^+) photo-production from porewater DON

Ammonium concentrations were measured at each irradiation time point: 0 (the initial after ammonia purging), 3, 12, 24, and 72 hours along with a dark control. Ammonium concentrations were measured for six stations during five seasons. Note that seasons October 2020 (BB1 only) and June 2021 were missing due to the loss of sample cores. All the irradiation experiments showed an increase in the NH_4^+ concentration with irradiation time (*Figure 10*). To estimate the rate of photo-production of ammonium, the slope of the linear regression line between irradiation time (x-axis) and ammonium concentration (y-axis) was calculated (*Table 2*). On average, [NH_4^+] photo-production rate was the highest at BB1 at 0.19 ± 0.08 µmol.L^{-1}.hour^{-1} followed by BB2, BB4, BB3, BB6, and BB5 at 0.17 ± 0.09, 0.17 ± 0.10, 0.16 ± 0.14, 0.13 ± 0.04, 0.11 ± 0.08 µmol.L^{-1}.hour^{-1}, respectively. Seasonally, February 2022 produced the highest average rate of ammonium photo-production at 0.23 ±0.08 µmol.L^{-1}.hour^{-1} followed by October 2021, May 2022 at 0.21 ± 0.08 and 0.18 ± 0.02 µmol.L^{-1}.hour^{-1}, respectively. Feb_21 and Oct_20, produced a rate at 0.08 ± 0.04 and 0.05 ± 0.03 µmol.L^{-1}.hour^{-1}, respectively. Note that [NH_4^+] was the highest at 72 hours and was slightly higher in dark control samples than the initial 0-hour in all the experiments. However, [NH_4^+] in dark control was lower than the 3-hour irradiation time point which could indicate a slight production due to other factors like thermal changes.

Table 2. *Ammonium photo-production rates in µmol.L^{-1}.hr^{-1}.*

	Oct_20	**Feb_21**	**Oct_21**	**Feb_22**	**May_22**	**Mean**	**St. Dev.**
BB1		0.10	0.27	0.24	0.16	0.19	0.08
BB2	0.03	0.13	0.22	0.25	0.20	0.17	0.09
BB3	0.04	0.04	0.23	0.36	0.15	0.16	0.14
BB4	0.05	0.09	0.31	0.21	0.19	0.17	0.10
BB5	0.03	0.03	0.17	0.11	0.19	0.11	0.08
BB6	0.10	0.12	0.08	0.19	0.16	0.13	0.04
Mean	0.05	0.08	0.21	0.23	0.18		
St. Dev	0.03	0.04	0.08	0.08	0.02		

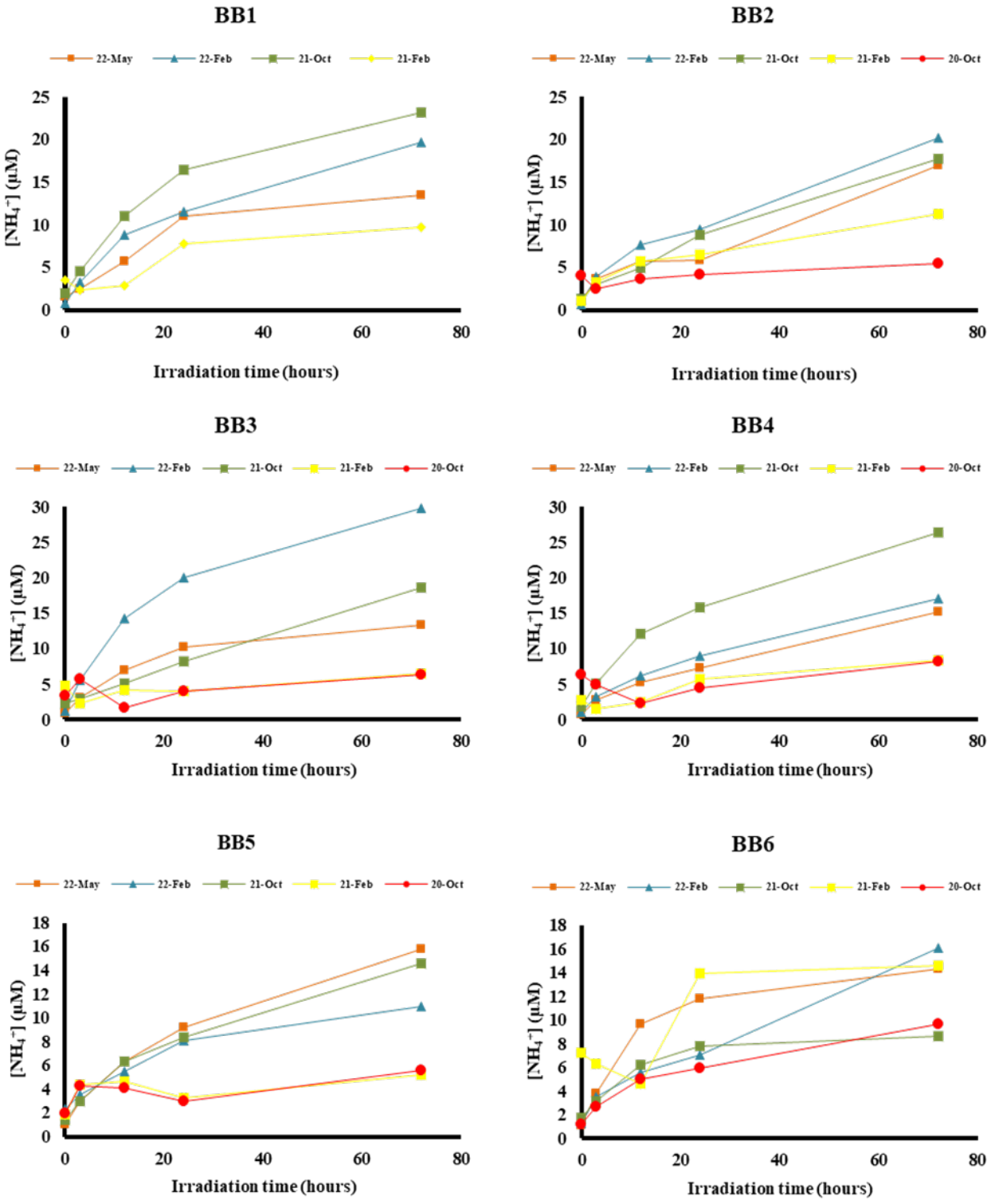

***Figure 10**. Ammonium photo-production at each irradiation increment of six stations during five sampling seasons.*

3.5.Isotopic composition of photo-produced ammonium

The $\delta^{15}N$ values of NH_4^+ produced in photochemical experiments ranged from 3.1 to 23.3‰ with an average of 11.3 ± 5.9‰ (Table 3). The photochemical production of the NH_4^+ is a kinetic process that favors the lighter ^{14}N isotope in the NH_4^+ product. However, with time, the product $\delta^{15}N$ value will increase as the reactant pool $\delta^{15}N$ also increases. While this trend is not clearly observed in each individual experiment, if the experiments are taken as a whole, the average $\delta^{15}N$-NH_4^+ of the 24-hour product is lower than the average value of the 72-hour product as would be expected in a continuing kinetic reaction (Figure 11).

Table 3. Photo-irradiation experiment isotope and concentration data. *All NH_4^+ in the original porewater sample was removed before the photochemical experiments

	Original porewater NH_4^+ (µM)	Original porewater $\delta^{15}N$-NH_4^+ (‰)	*24 hr $\delta^{15}N$-NH_4^+ (‰)	*24 hr NH_4^+ (µM)	*72 hr $\delta^{15}N$-NH_4^+ (‰)	*72 hr NH_4^+ (µM)
BB1 Oct21	414.9	12.7	15.6	15.4	15.3	22.2
BB2 Oct21	507.3	14.4	4.6	9.0	22.1	18.2
BB3 Oct21	586.2	13.8	5.2	8.0	4.2	18.4
BB4 Oct21	418.5	23.3	15.1	15.7	6.6	25.9
BB5 Oct21	331.1	20.5	14.3	8.8	5.1	15.1
BB6 Oct21	456.0	12.1	18.9	8.1	11.6	9.7
BB1 May22	370.7	13.5	4.0	12.1	5.6	10.6
BB2 May22	539.5	16.8	7.9	6.1	21.7	12.4
BB3 May22	1155.7	11.1	14.2	8.4	3.1	7.9
BB4 May22	443.6	8.0	8.7	5.8	23.3	11.6
BB5 May22	470.7	10.5	15.9	6.8	6.1	11.7
BB6 May22	538.7	8.8	6.2	12.2	21.6	9.5
BB1 Feb22	414.2	10.2	17.8	10.3	18.9	17.6
BB2 Feb22	640.2	9.8	11.6	8.7	7.5	19.0
BB3 Feb22	671.9	11.8	6.3	19.9	11.4	29.3
BB4 Feb22	663.7	9.4	19.7	8.5	7.8	17.3
BB5 Feb22	413.3	10.2	3.4	7.8	9.5	11.6
BB6 Feb22	785.6	10.3	6.4	6.8	6.7	15.6
Overall average	545.7 ± 151.4	12.6 ± 0.8	10.9 ±6.7	9.9 ±4.8	11.6±4.5	15.8 ± 5.9

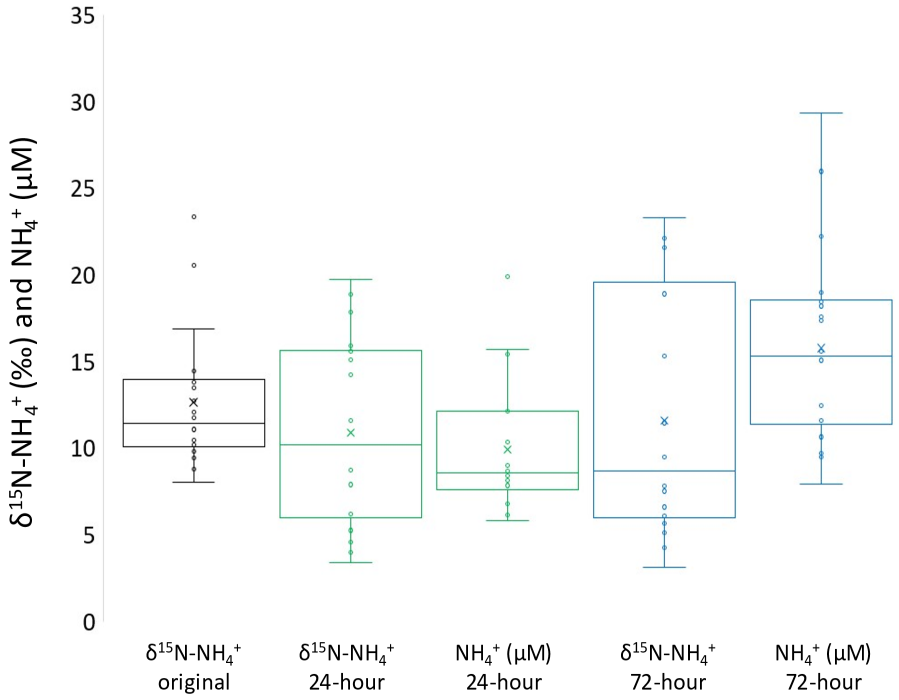

Figure 11. *Box and whisker plots of the overall data from the photochemical experiments. The line that separates the upper and lower quartile is the median, the "x" represents the average, and the whiskers represent the minimum and maximum.*

3.6.<u>*UV-Vis absorbance measurements during the irradiation experiment*</u>

Absorption coefficient spectra were measured for six stations during five seasons during the irradiation experiments (Figure 12). Absorption coefficients decreased with irradiation time increments at 250-400nm while staying constantly close to zero at 400-800nm. The absorption was the lowest at 72 hours. Note that the dark control samples showed the same or slightly different absorption as the 0-hour samples. The absorption coefficients were natural-logged to calculate the spectral slopes, $S_{275\text{-}295}$ and $S_{350\text{-}400}$. The spectral slopes appeared to be negative, which meant a decrease in absorption along with irradiation increments. Data showed that $S_{275\text{-}295}$ became more negative over time while $S_{350\text{-}400}$ became less negative over time. The slope Ratio (S_R) was calculated by dividing $S_{350\text{-}400}$ by $S_{275\text{-}295}$. In general, S_R increased along with irradiation time increments and peaked at 72 hours. S_R stayed consistent from 0-hour until 12-hour then abruptly increased at 24-hour and peaked at 72-hour (Figure 13). Note that dark control S_R was the closest to the 0-hour and even the same in some cases. When we reported the spectral slopes as positive values, the slope ratio became $S_R = -(S_{350\text{-}400})/-(S_{275\text{-}295})$. Hence, S_R and $S_{275\text{-}295}$ became positively correlated, while S_R and $S_{350\text{-}400}$ were negatively correlated. In conclusion, S_R and $S_{275\text{-}295}$ increased with irradiation increments, while $S_{350\text{-}400}$ decreased with irradiation increments.

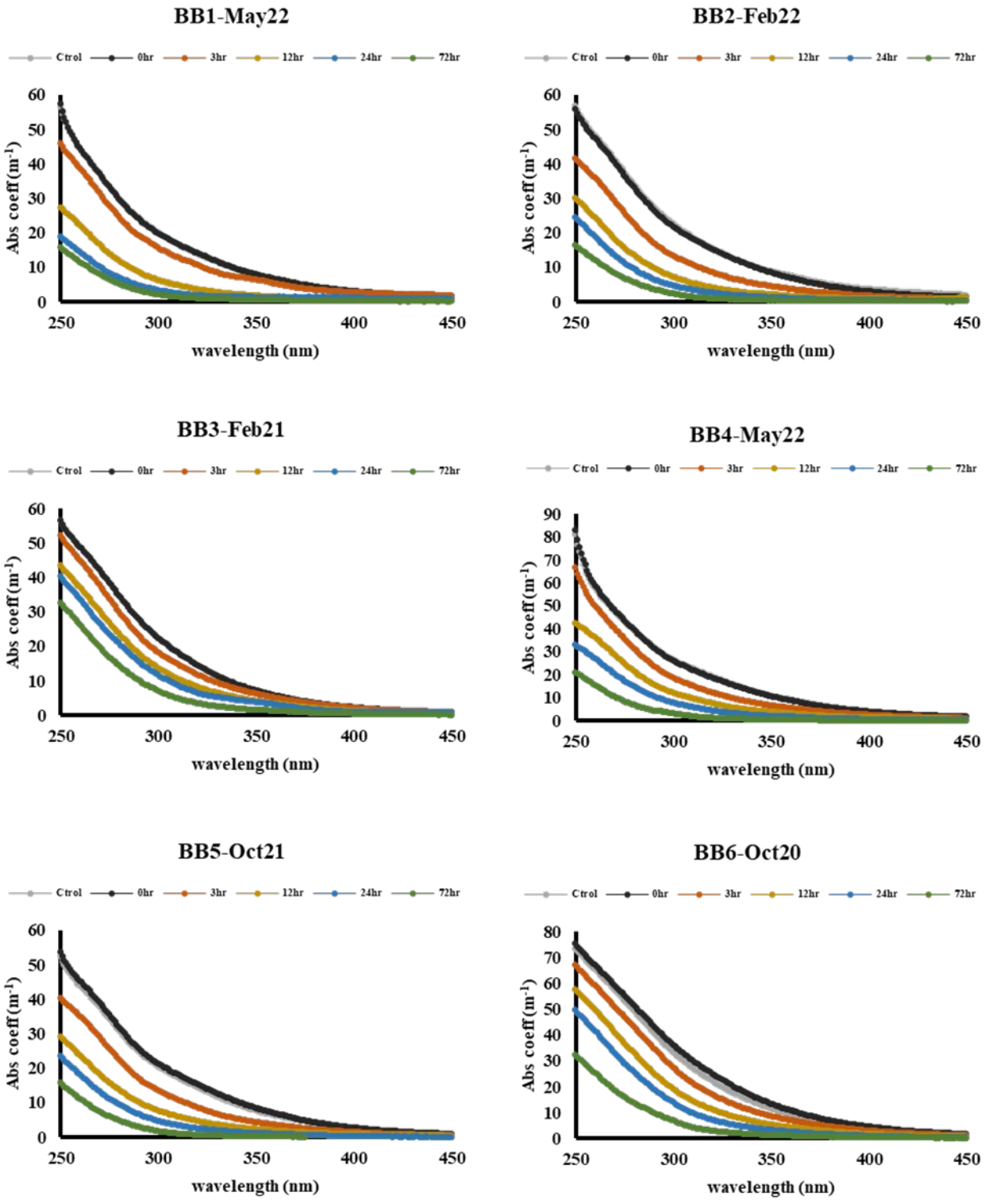

Figure 12. *Absorption coefficient (m^{-1}) spectra of CDOM in porewaters with irradiation time increments.*

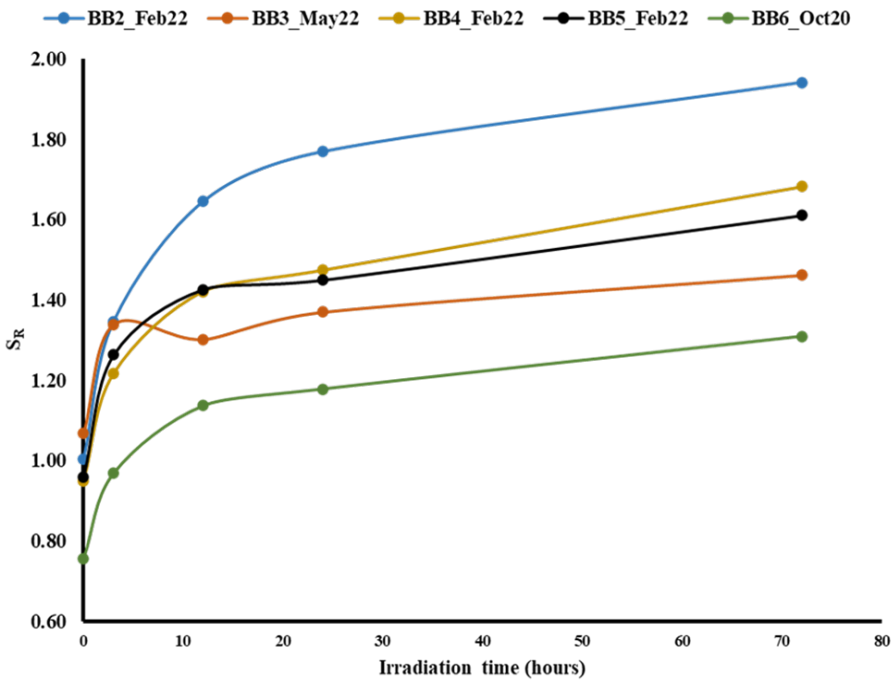

Figure 13. *Slope Ratio (S_R) during irradiation time increments.*

3.7. Photochemical & Seasonal Changes in DOM Chemical Characterization by Mass Spectrometry

3.7.1. Molecular composition

We analyzed the mass spectrometry data of the irradiation samples from three seasons: October 2020, February 2021, and October 2021. In IC-MS/MS negative mode, 2360 compounds were detected while 2464 were detected in LC-MS/MS positive mode, and the combined total was 4824. In those 4824 compounds, we were able to assign a unique molecular formula to 3815

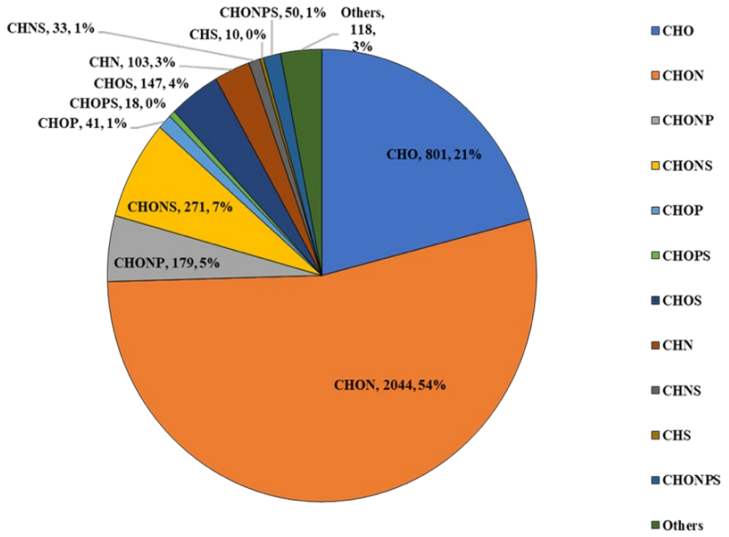

Figure 14. *Classification of 3815 detected compounds with molecular formula assigned.*

compounds. Out of 3815 compounds, CHONs were the most dominant, with 204 4 compounds (54%) followed by CHOs 801 (21%) (Figure 14). With respect to heteroatom composition, nitrogen, phosphorus, and sulfur-containing compounds contributed 70.2%, 7.5 %, and 1.4 %, respectively, to our DOM pool in irradiated DOM porewater.

3.7.2. Peptides and Deaminated Peptides

After combining both negative and positive detection modes, we structurally elucidated 97 compounds to be peptides and 581 compounds to be deaminated peptides based on our generated databases (678 total). Van Krevelen diagram (Figure 15) showed the distribution of the detected peptides and deaminated peptides by plotting the oxygen/carbon (O/C) ratio versus the hydrogen/carbon ratio (H/C). Peptides had a range of O/C from 0.2-0.64 and H/C from 1.2-2. Deaminated peptides had a range of O/C from 0.2-1 and H/C from 0.93-2. The deaminated peptides appeared to be more oxygenated than the peptides. Both shared the same H/C ratio.

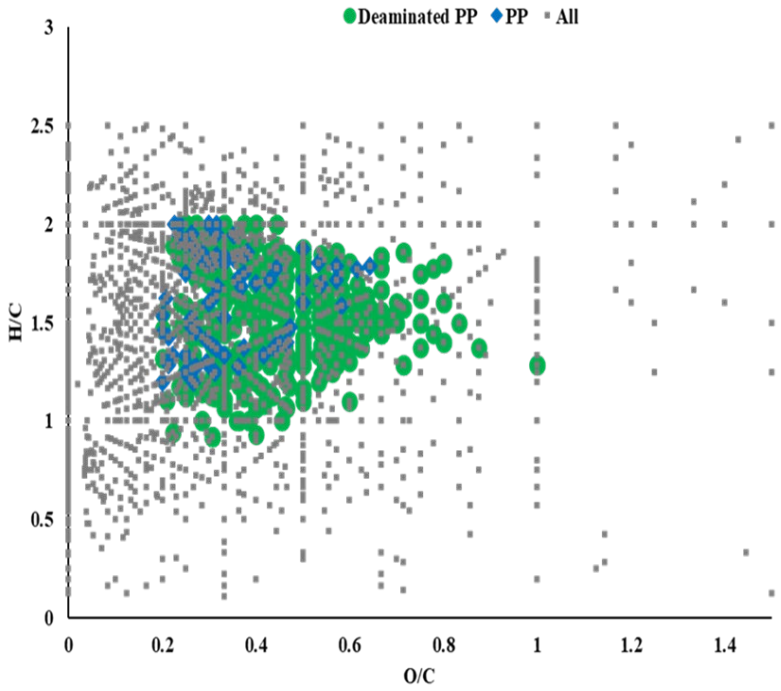

Figure 15. *Van Krevelen diagram of assigned formulas of the pore water DOM. "x" axis represents oxygen/carbon ratio while "y" axis represents hydrogen/carbon ratio. "Grey" dots were all compounds with molecular formulas assigned. "Green" circles were confirmed to be deaminated peptides (581) while "Blue" squares were to be peptides (97).*

3.7.3. Volcano analysis

Three volcano plots were generated to compare detected compounds between three seasons: Oct_20, Feb_21, and Oct_21 (Figure 16a-c). Compounds were significant to the right-hand region when their "Log2 Fold Change (right side/ left side)" (x-axis) were greater than 1, which meant right-side compounds were more intense at least twice than left-side compounds, and p-values were less than 0.05 (95% confidence level). Volcano plots indicated 224 significant compounds for Oct_20 vs. 262 significant compounds for Feb_21, 246 significant compounds for

Oct_21 vs. 107 significant compounds for Oct_20, and 158 significant compounds for Oct_21 vs. 51 significant compounds for Feb_21. Uniquely, 105 compounds were significant to only Oct_20, 50 compounds were significant to only Feb_21, and 61 compounds were significant to only Oct_21. Out of those 105 significant compounds of Oct_20, 36.5% were classified to be CHO, 36.5% CHON; in 50 significant compounds of Feb_21, 33.3% were classified to be CHO, 30.7% CHON; in 61 significant compounds of Oct_21, 22.4% were classified to be CHO, 51.7% CHON (Figure 17). The 4171 insignificant compounds were present in all three seasons.

Based on our generated database, we were able to structurally elucidate 4 peptides and 10 deaminated peptides that were significant to Oct_20, 2 peptides and 9 deaminated peptides significant to Feb_21, and 2 deaminated peptides (0 peptides) significant to Oct_21. The 595 insignificant peptides and deaminated peptides were present in all three seasons.

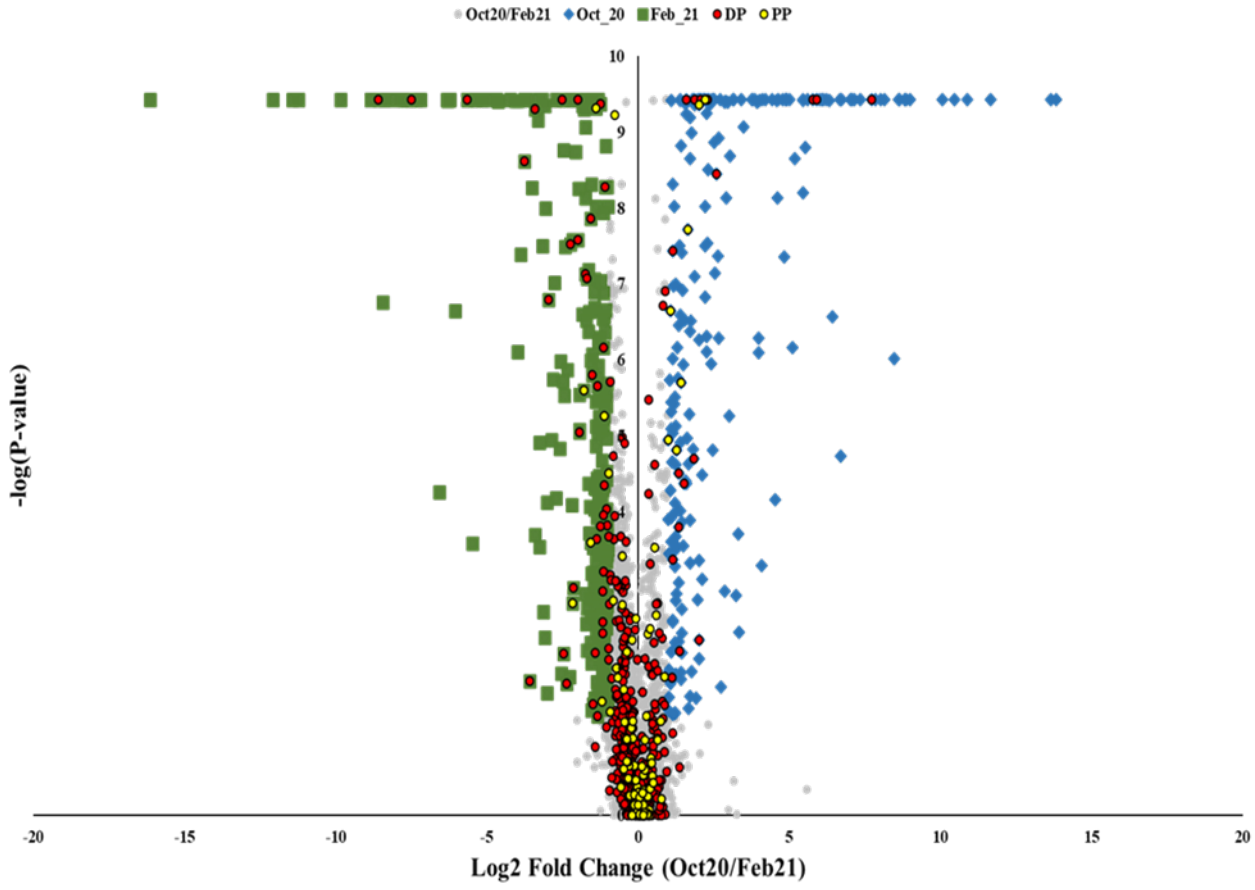

Figure 16a. *Volcano plot of Oct_20 (right half) and Feb_21 (left half) detected compounds. "Blue" squares (224) represent significant compounds for Oct_20 and "Green" squares (262) represent significant compounds for Feb_21. "Grey" circles represent insignificant compounds that appeared equivalently in both seasons. "Yellow" circles are deaminated peptides and "Red" circles are peptides.*

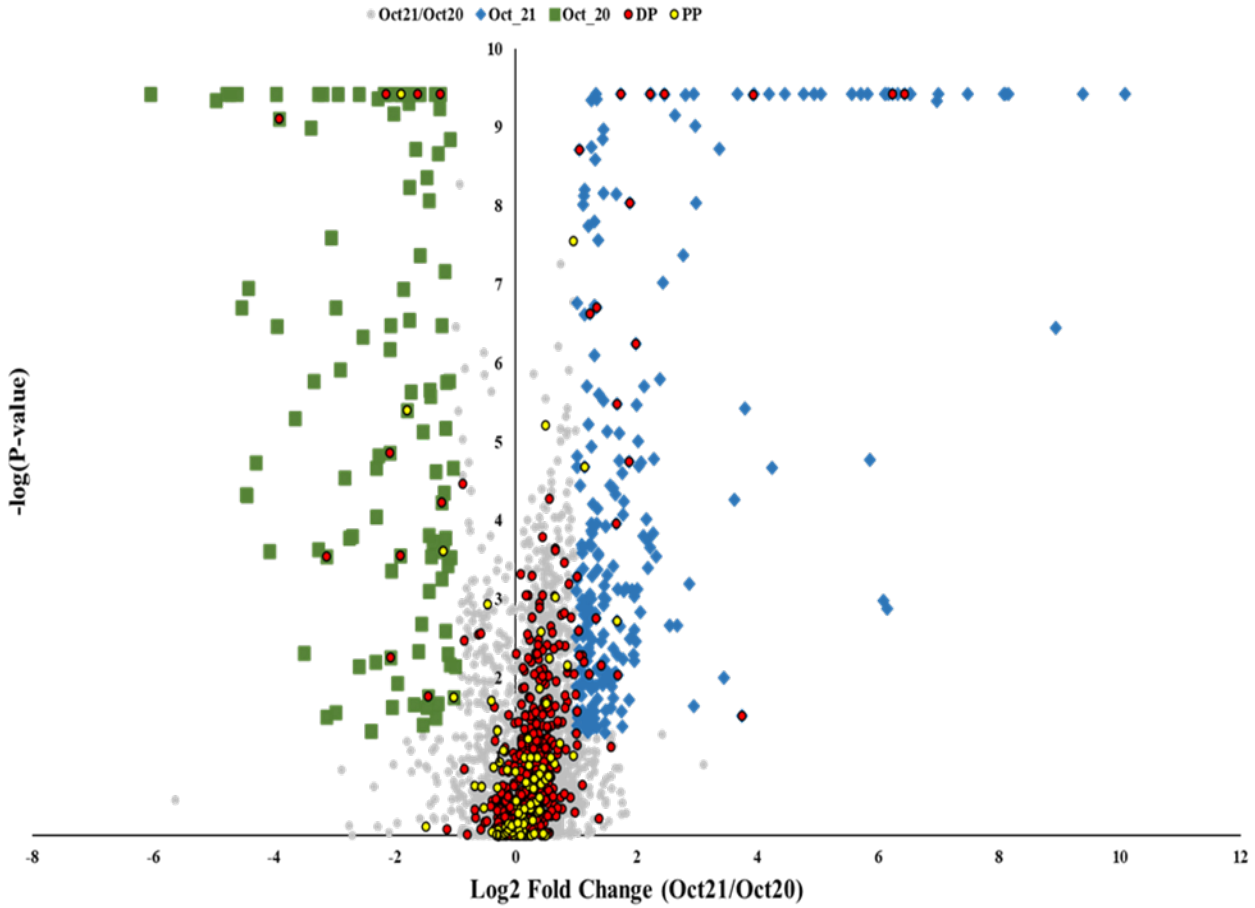

Figure 16b. *Volcano plot of Oct_21 (right half) and Oct_20 (left half) detected compounds. "Blue" squares (246) represent significant compounds for Oct_21 and "Green" squares (107) represent significant compounds for Oct_20. "Grey" circles represent insignificant compounds that appeared equivalently in both seasons. "Yellow" circles are deaminated peptides and "Red" circles are peptides.*

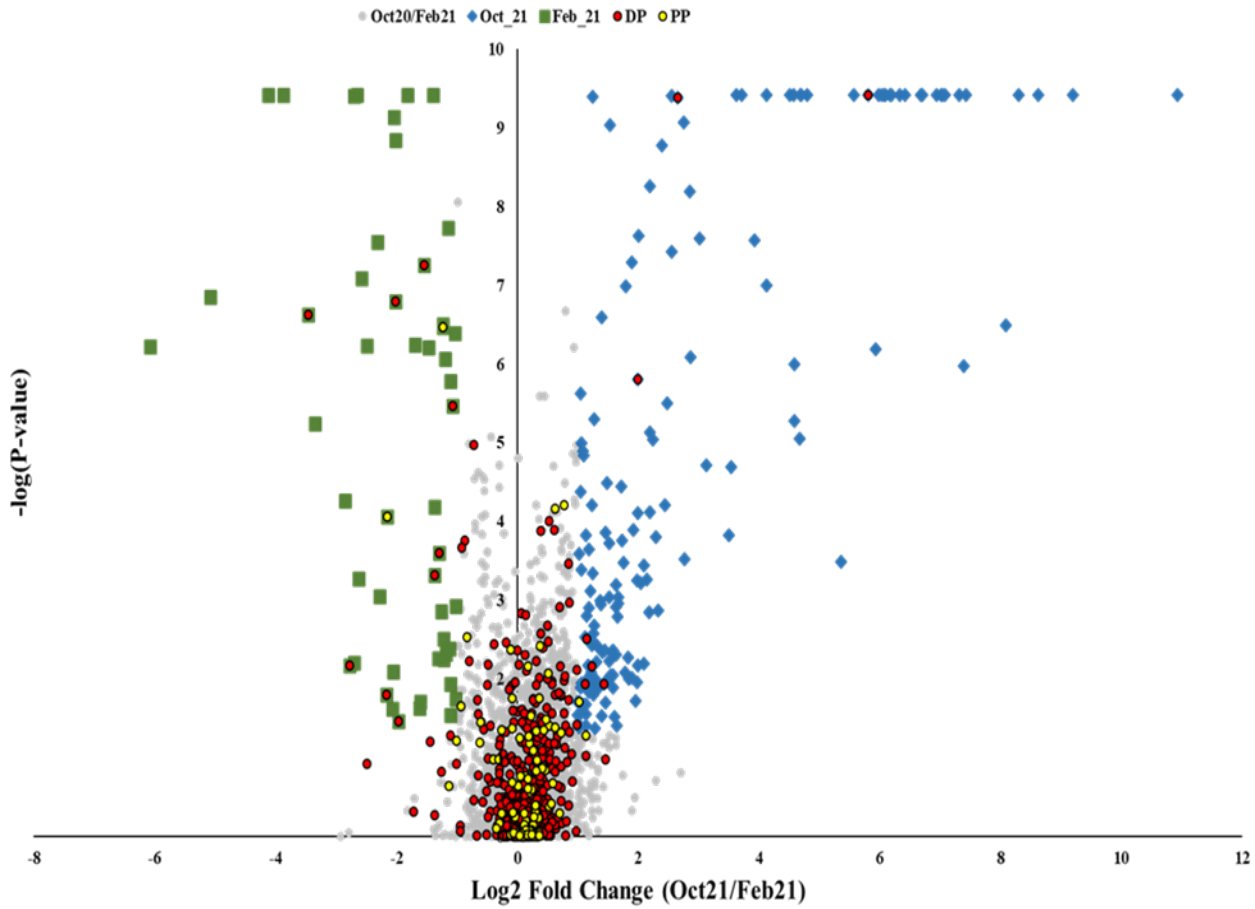

Figure 16c. *Volcano plot of Oct_21 (right half) and Feb_21 (left half) detected compounds. "Blue" squares (158) represent significant compounds for Oct_21 and "Green" squares (51) represent significant compounds for Feb_21. "Grey" circles represent insignificant compounds that appeared equivalently in both seasons. "Yellow" circles are deaminated peptides and "Red" circles are peptides.*

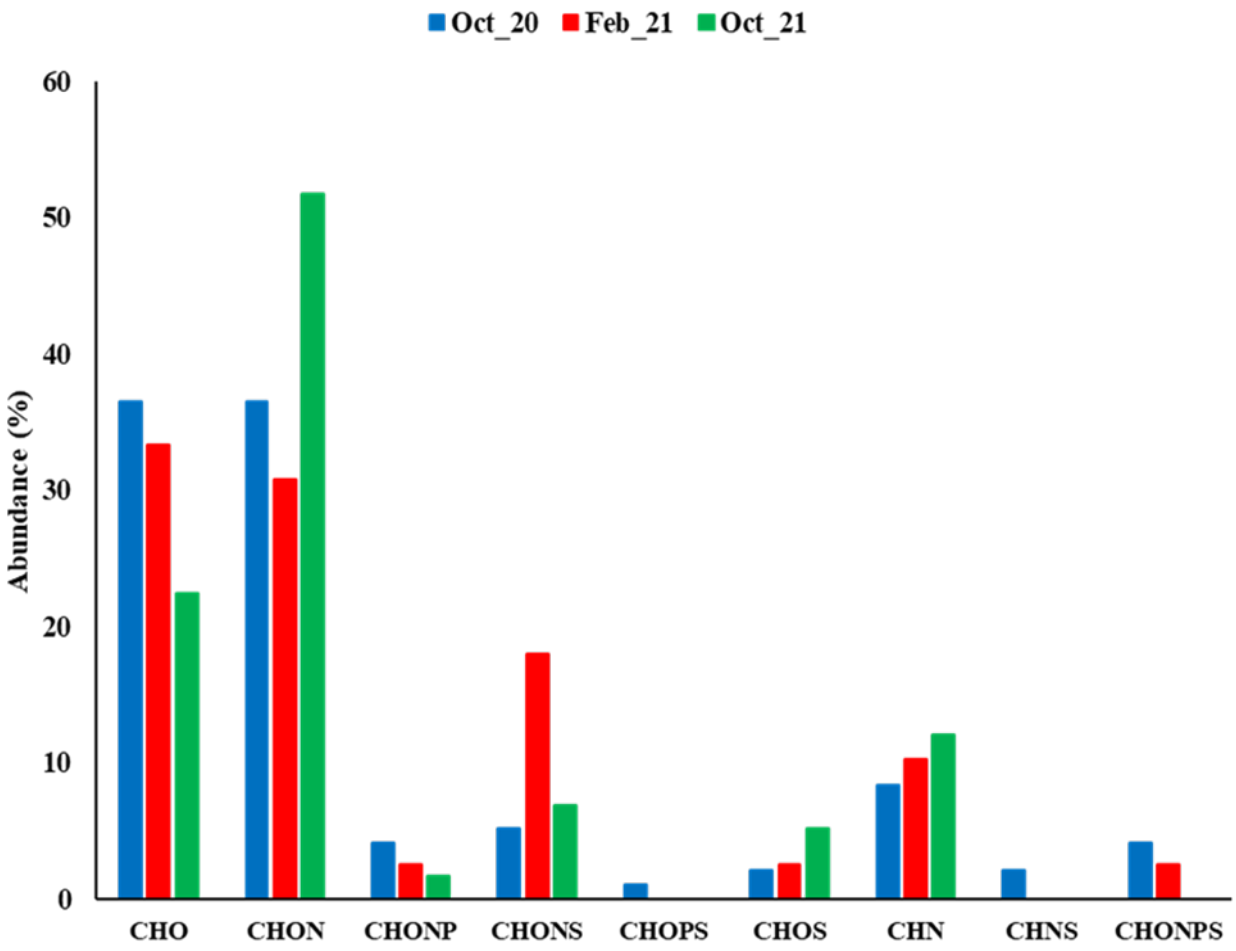

Figure 17. *Classification of significant compounds in each season.*

4. DISCUSSION

4.1. Factors controlling the ammonium benthic flux to the water column in Baffin Bay

The diffusive fluxes were significantly dependent on the sediment porosity and changes in the ammonium depth profile. The lowest porosity was at BB1 with an average of 0.35, which resulted in BB1 having the lowest diffusion rate for porewaters NH_4^+ to the water column. These spatial porosity differences in Baffin Bay are due to the spatial variation of sedimentation type in the bay. The type of Baffin Bay's sediment ranged from sandy spits and serpulid reefs, clayey-silt, muddy sand to black mud (Figure 18). BB1 is located on the upper bay that is characterized by sandier facies sediment, which has low porosity. On the other hand, stations BB3 and BB4, which has the highest porosity of 0.7, are in the center of the bay and characterized by black mud sedimentation (Simms et al., 2010; Lopez et al., 2020). Based on sedimentation type, sampling stations were categorized into two groups: 1) Branched stations (BB1, BB2, BB5) where the sediments are coated grains and 2) Center stations (BB3, BB4, BB6) where the sediments are

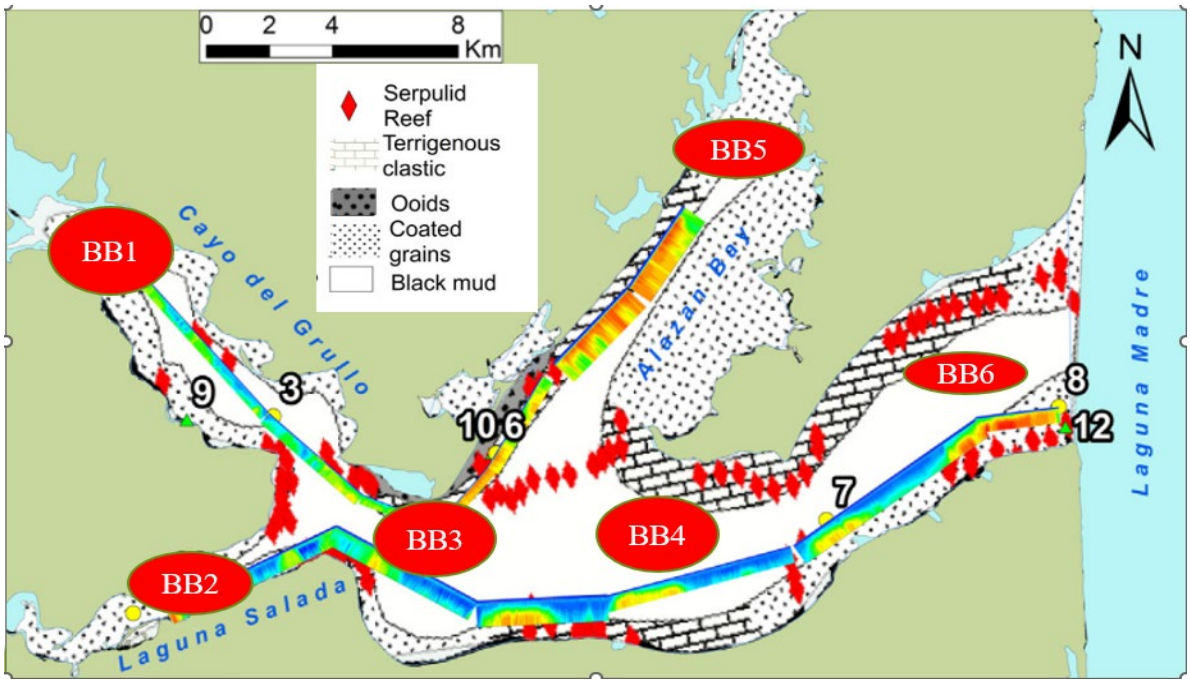

Figure 18. *Sedimentation type of Baffin Bay (Lopez et al., 2020).*

black mud. Center stations have higher porosity than branched stations due to differences in sedimentation type.

The other significant factor responsible for the benthic flux difference between stations was the instantaneous change of concentrations along the depth profile. The steeper the slope and the higher the $[NH_4^+]$ diffused to the water column, the higher the flux. In branched stations, BB1 and BB5 had low porewater $[NH_4^+]$ with an average of 411 & 381 $\mu mol.L^{-1}$, respectively and low $[NH_4^+]$/depth with an average of 29 and 21 $\mu mol.L^{-1}.cm^{-1}$, respectively. Therefore, BB5 and BB1 had the lowest fluxes with 102 and 53 $\mu mol.m^{-2}.day^{-1}$, respectively. BB2 also had low fluxes of 108 $\mu mol.m^{-2}.day^{-1}$ due to low porosity and low $[NH_4^+]$/depth of 31 $\mu mol.L^{-1}.cm^{-1}$. In center stations, BB3 had the highest fluxes of 347 $\mu mol.m^{-2}.day^{-1}$ due to its highest porosity and high average $[NH_4^+]$/depth of 59 $\mu mol.L^{-1}.cm^{-1}$, especially in Feb_22. BB6 had high fluxes of 215

μmol.m^{-2}.day^{-1} due to its high average [NH_4^+]/depth of 57 μmol.L^{-1}.cm^{-1}, even though its porosity was not significantly high (0.55). Similarly, BB4 had higher fluxes of 191 μmol.m^{-2}.day^{-1} due to its highest porosity of 0.7 even though its average [NH_4^+]/depth was only 31 μmol.L^{-1}.cm^{-1}. Seasonally, BB6 had its fluxes drop dramatically in Jun_21 after the rainfall in May_21 due to the drop in [NH_4^+] (significant $p < 0.05$) (Figure 9). The dramatic drop in [NH_4^+] at BB6 in Jun_21 after the heavy rainfall in May_21 was due to freshwaters being brought in to flush the bay ecosystem leading to a decrease in salinity from above 40 to 16 ± 8 and porewater [NH_4^+]. The dramatic drop in porewater [NH_4^+] was also predicted to have been impacted by an internal force such as submarine groundwater discharge (SGD). On the other hand, it was previously reported at Baffin Bay that there was a decline in chlorophyll abundance (*A. lagunensis*) as salinity decreased after heavy rainfall in the Spring of 2015 (Cira & Wetz 2019). We anticipated that precipitation of rainfall or melted ice would bring in freshwaters and flush away all the residuals in Baffin Bay, such as nutrients, phytoplankton, or other autotrophs. Lowering the primary production in the bay will lead to lower organic matter sedimentation rates and affect the early diagnosis rate and decrease the ammonia microbial production in the sediment. Also, BB6 was the southernmost and furthest away from the three input branches: Alazan Bay on the north (BB5), Cayo del Grullo (BB1) and Laguna Salada (BB2); therefore, it received the least nutrient inputs and the most freshwaters. In conclusion, the rainfall in May_21 was expected to lower salinity and porewater [NH_4^+] and remove the algal blooms at BB6.

From a seasonal perspective, Baffin Bay had two-fold changes in the seasonal benthic fluxes. The lowest was 124 ± 79 μmol.m^{-2}.day^{-1} in May_22, and the highest was 244 ± 254 μmol.m^{-2}.day^{-1} in Feb_22. Feb_22 with the highest average [NH_4^+]/depth of 65 μmol.L^{-1}.cm^{-1} accounted for the highest flux and could indicate a large organic matter sedimentation rate from detritus phytoplankton or other photoautotrophs on surface water to the sediment after Oct_21. In a study of algal blooms in Baffin Bay, Cira and Wetz 2019 showed that the chlorophyll population (*A. lagunensis*) peaked in the summer months and declined in the winter months. Hence, primary productivity was predicted to be high from October 2021 to February 2022 and might account for the large biomass accumulation in the sediment.

In 1990, Baffin Bay was reported to have a primary production rate (PPR) at ~1-132mg C.m^{-2}.day^{-1} or 83 – 110 μmolC.m^{-2}.day^{-1} (Blanchard and Montagna 1995). Assuming the Redfield ratio 106C: 16N, it was converted to 12.5 – 16.6 μmolN.m^{-2}.day^{-1} . Based on this PPR, the benthic flux of ammonia could supply 992 – 1470 % of the N nutrient needed to sustain this level of PPR. Other studies had reported higher benthic fluxes on other Gulf of Mexico estuaries than our measured fluxes. For example, West Florida estuaries – nearshore Gulf of Mexico NH_4^+ flux was 430-3360 μmolN.m^{-2}.day^{-1} (Dixon et al., 2014), Galveston Bay NH_4^+ flux was 240 - 350 μmolN.m^{-2}.day^{-1} (Warnken et al., 2000), and Apalachicola Bay – northeastern Gulf of Mexico flux was approaching 3000 μmolN.m^{-2}.day^{-1} (Mortazavi et al., 2000). In the other estuarian systems, Great Bay estuary – New Hampshire had NH_4^+ flux at 1400 μmolN.m^{-2}.day^{-1} (Percuoco et al., 2015), Curonian lagoon – Lithuania was at 210 – 2950 μmolN.m^{-2}.day^{-1} (Zilius et al., 2012), and the ammonium flux in the Baltic Sea, a semi-enclosed shelf sea, was −40.5 and 1370.1 μmolN.m^{-2}.day^{-1} (Lengier et al., 2021). We attributed the lower average benthic flux in Baffin Bay relative to other estuary ecosystems to two factors: 1) The wide spatial sedimentation types in the bay. As some parts were characterized by black mud (center of the bay), in other regions, the sediment had sandy sediment 2) The bay ecosystem was under abnormal conditions during our sampling seasons (results of the heavy rainfall in May_21), as reflected in relatively low salinity values (salinity ranges from 10s- 20s) in most of the seasons than the average salinity of the bay (~45) and

occasionally reach up to 70 in hypersaline condition (Wetz et al., 2017). Seasonal changes in ammonia benthic fluxes are also observed in other studies. For example, Dixon et al., 2014 showed a decrease in fluxes from 2007 – 2009 in Tampa Bay, Sarasota Bay, and Sarasota offshore but an increase in Charlotte Harbor. The NH_4^+ flux was reported to be low in cold-weather months but high when temperatures rose in the summer (Mortazavi et al., 2000; Warnken et al., 2000; Zilius et al., 2012; Percuoco et al., 2015).

To estimate the N loading from NH_4^+ benthic flux for the entire Baffin Bay, the benthic ammonium fluxes in μmol. $m^{-2}.day^{-1}$ were multiplied by 60% of the Baffin Bay area for center stations (0.6*219 km^2) and 40% of the Baffin Bay area for branched stations (0.4*219 km^2) (Figure 19). On average, benthic [NH_4^+] flux was the highest in Feb_22 with 9556 ± 11219 $mol.day^{-1}$ followed by Feb_21, Jun_21, Oct_20, and Oct_21 at 7746 ± 7236, 7480 ± 8276, 6750 ± 8510, and 5142 ± 4009 $mol.day^{-1}$, respectively. May_22 produced the lowest flux at 4916 ± 3750 $mol.day^{-1}$. In comparison with other potential N-loading sources to the Baffin Bay, we extrapolated the N loading of atmospheric deposition (in upper Laguna Madre) and the agricultural runoff, urban nonpoint sources to the region measured by Castro et al. (2003) to estimate the N-loading to the entire bay from these two sources. Based on these calculations, the atmospheric deposition delivered 857 $mol\text{-}N.day^{-1}$ from the upper Laguna Madre to the entire Baffin Bay, while the agricultural runoff estimated the N-loading to the entire bay to be 3000 $mol.day^{-1}$. This indicated that our benthic flux delivered N loading in a 2-3 higher order of magnitude than the atmospheric deposition and agricultural runoff.

Benthic ammonium flux served as a significant source of inorganic nutrients that contributed to the water column along with other nutrient sources to feed photoautotrophs such as phytoplankton. Baffin Bay is a unique closed system of marine ecosystems with little input of terrestrial nutrients; therefore, primary production on the surface water is exclusively dependent on ammonium benthic flux and other nonpoint sources (e.g., atmospheric deposition and agricultural runoff). However, ammonium concentrations in surface waters of Baffin Bay are significantly low (< 5 μM) which suggests that the consumption of surface water is highly demanded. Estimating these fluxes is crucial as it serves as another ammonium source to the water column in the bay ecosystem. Phytoplankton and other autotrophs require ammonium and other nutrients in an oxic environment to photosynthesize on the surface water. However, excessive nutrients can also cause eutrophication leading to hypoxia which kills fish and marine animals and is accounted for the experience with harmful brown tide bloom, which had been existing and will last for decades in Baffin Bay.

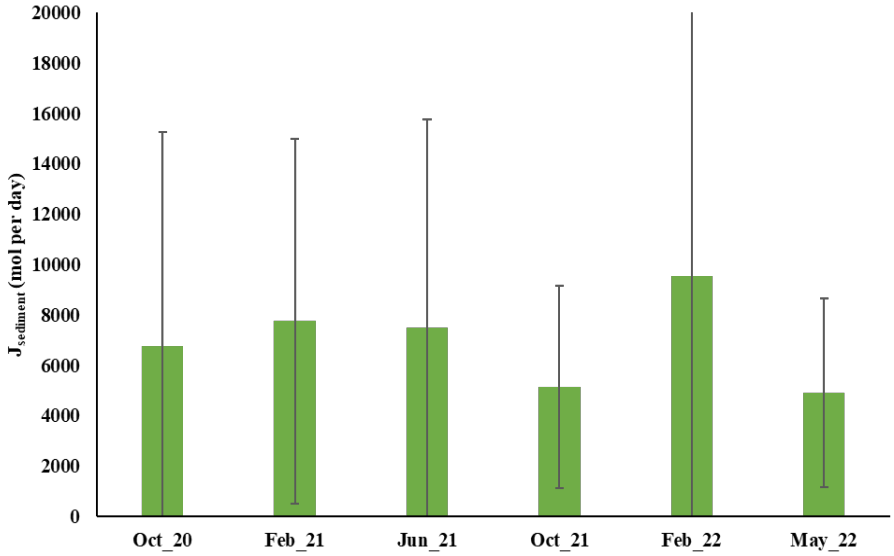

Figure 19. *Average benthic ammonium fluxes (mol per day) of Baffin Bay.*

4.2. Photo-ammonification rate from benthic DON

The rate of ammonium photo-production was shown to be positively correlated to the ammonium concentration in porewater. BB5 had the lowest [NH_4^+] in porewater (381 µmol.L^{-1}) and the lowest [NH_4^+] rate (0.11 µmol.L^{-1}.$hour^{-1}$). At BB2 and BB3, Feb_22 had the highest [NH_4^+] in sediment porewater (Figure 4) and the highest [NH_4^+] rate (Figure 20). At BB1, the three seasons of Oct_21, Feb_22, and May_22 showed higher porewater [NH_4^+] as well as [NH_4^+] photo-production rates than Feb_21. In summary, the photo-ammonification rate of Baffin Bay sediment porewater ranged from 0.038-0.361 µmol.L^{-1}.$hour^{-1}$. Other studies have shown similar rate; for example, photo-ammonification rate ranged from 0.23-0.36 µmol.L^{-1}.$hour^{-1}$ for different river water samples (Bushaw et al., 1996) or much lower rate at 0.015 µmol.L^{-1}.$hour^{-1}$ (river water samples, (Morell & Corredor, 2001), 0.006 µmol.L^{-1}.$hour^{-1}$ for Baltic Sea porewater, (Vahatalo and Zepp, 2005). On the other hand, the photo-ammonification rate of surface water in Baffin Bay was reported to range from 0.034 – 0.086 µmol.L^{-1}.$hour^{-1}$ (Shrestha, 2022), or up to 0.032 µmol $L^{-1}h^{-1}$ in the coastal lagoon of Hog Island Bay (Buffam and McGlathery, 2003). We concluded that photo-ammonification of anoxic sediment porewater was 12 - 320 % higher than of oxic surface water in Baffin Bay. Exposure to natural sunlight leading to the natural degradation of CDOM in surface water might account for the lower photo-ammonification rate on surface water. Photo-ammonification rates have also been reported to be different with seasonal changes and rainfall (Yang et al., 2021) or sample type. For example, humic substances (soil samples) had a high photo-ammonification rate of 0.34 µmol $L^{-1}h^{-1}$ (Li et al., 2020).

Dissolved organic nitrogen (DON) was expected to degrade and release ammonium. [DON] and [NH_4^+] were shown to be positively correlated with each other (unpublished data; Abdulla et al., 2018). As [NH_4^+] was excessive in sediment porewater, DON was expected to be enriched. After DON diffused upwards and entered the water column, it became exposed to sunlight and started to degrade to release inorganic nutrients that feed autotrophs. Photo-ammonification by UV-Vis radiation, along with ammonium benthic flux from sediment, enriched

the nutrient level in surface water and served as a food web for microbes and phytoplankton or other plants to grow. This significant source of bioavailable N may contribute to brown tide bloom and hypoxia conditions in Baffin Bay.

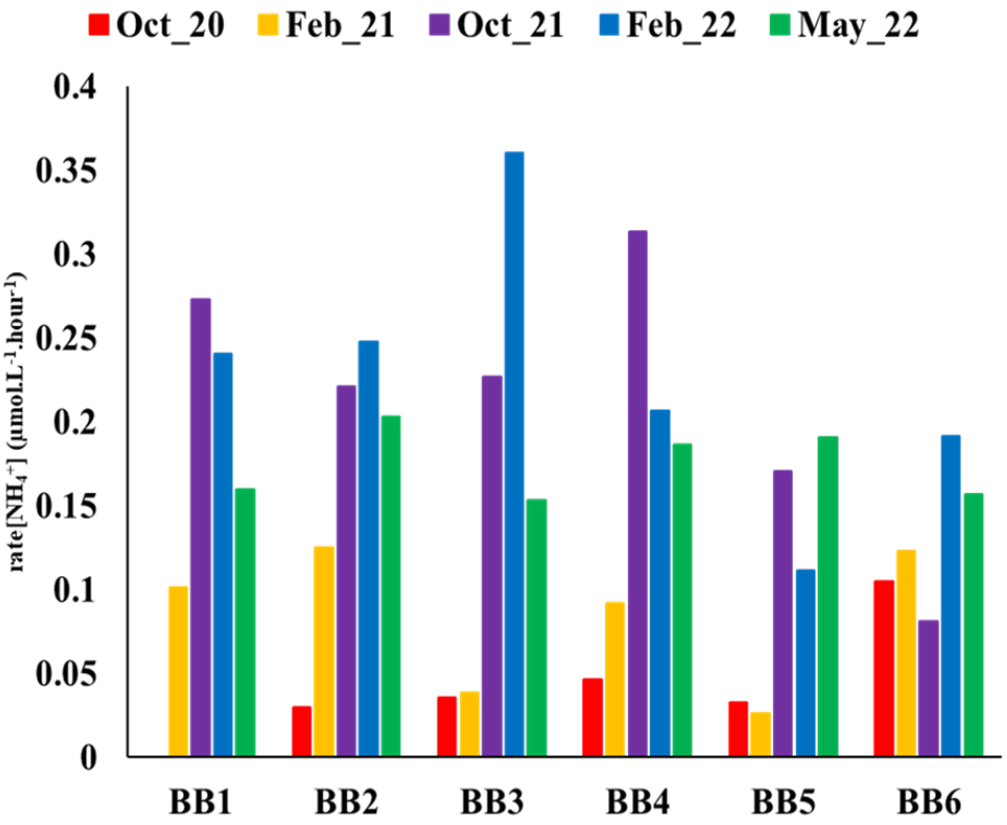

Figure 20. *Rate of photo-ammonification (mole NH_4^+ per liter per hour) from porewaters at six stations of Baffin Bay during five sampling seasons.*

4.2.Nitrogen isotope fractionation during ammonia photo production

The fractionation modeled by plotting overall ln[NH_4^+] vs. $\delta^{15}N$ is minimal (~1.5 ‰) for the 24- and 72-hour time points and the overall original porewater $\delta^{15}N$-NH_4^+ is not distinguishable from the overall photoproduced $\delta^{15}N$-NH_4^+ (ANOVA; $p = 0.34$). These results would suggest the photochemically produced NH_4^+ from porewater DOM may not be able to be distinguished from the porewater $\delta^{15}N$-NH_4^+ when observing the dynamics of the entire estuary. However, the difference may be more distinguishable in different regions of the estuary or, in this case, on a sampling site basis. The logical pattern of increasing NH_4^+ concentration and isotopic concentration associated with an ideal kinetic reaction is more apparent when looking at site 1, 2 and 6 averages together. When plotting the average ln(24-hour) and ln(72-hour) concentrations vs. $\delta^{15}N$-NH_4^+ at these sites, a strong relationship is seen indicating a kinetic photochemical reaction with a fractionation factor of ~8.8 ‰ ($p = 0.02$) (Figure 21) which falls in line with predicted photo-ammonification fractionation estimates of 3 to 10‰ (Thibodeau et al., 2017). This

magnitude of fractionation could cause a significant difference between the $\delta^{15}N$ of NH_4^+ originating in pore water and photoproduced NH_4^+ thus helping to confirm the source of NH_4^+ in the estuary's surface water. This straightforward relationship breaks down at sites 3, 4 and 5 and becomes an insignificant ($p > 0.5$) but opposite trend. This could be due to the photodegradation of NH_4^+ occurring or product NH_4^+ being reincorporated in the production of new DOM as the photochemical experiments progress. The likelihood of these types of reactions may be directly tied to the complex nature of the DON pool in the porewater which will vary greatly across sampling sites and sampling periods. The $\delta^{15}N$ of the individual compounds that are more susceptible to photo-ammonification could have wide variations in $\delta^{15}N$ values that differ from the bulk $\delta^{15}N$-DON. This would mean varying reactants not only from site to site and season to season but also throughout the individual experiments. This would cause variations in the $\delta^{15}N$ value which would be difficult to differentiate without characterizing the isotopic composition of thousands of individual compounds. It is possible that as DON pool compositions become more complex, the straightforward photochemical production of NH_4^+ is masked by the variations in individual DON isotopic compositions and competing reactions. This isotopic approach in task 3 set out to determine if porewater NH_4^+ could be differentiated from that of photochemical produced NH_4^+. Preliminary results suggest the difference could be significant on a site-by-site basis and may be applied more readily across entire water bodies with less complex DON assemblages.

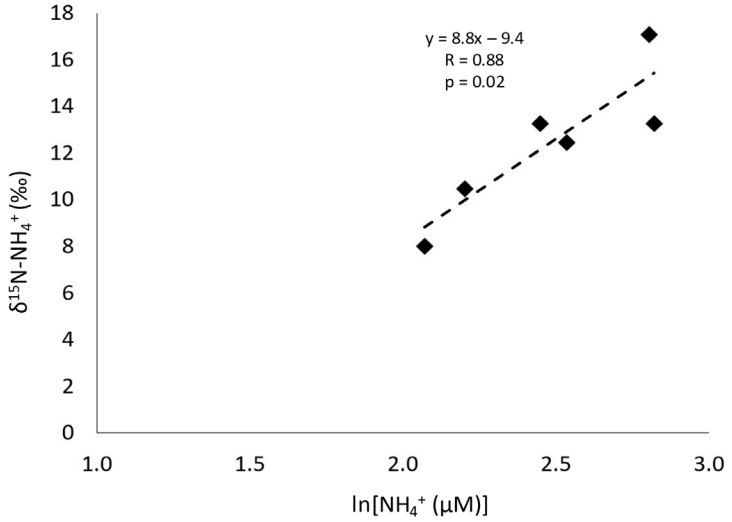

Figure 21. Average of natural log of ammonium concentrations vs average of $\delta^{15}N$-NH_4^+ values for photochemical experiment for site 1, 2 and 6 samples. The significant relationship ($p = 0.02$) and slope indicates a fractionation factor of 8.8 associated with photochemical production of ammonium.

4.3.Photo-degradation of CDOM and photo-ammonification

The chromophoric DOM (CDOM) absorbed visible and UVA and B radiation (300-400nm). The absorption coefficient at 300 nm (a_{300}) decreasing along irradiation increments indicated a degradation in the chromophoric portion of marine DOM. The absorption of electromagnetic frequency by CDOM degraded its organic structure and led to the photo-transformation of organic matter in the surface water (Del Vecchio and Blough 2002). Previous studies also suggested that photobleaching was a major factor that destroyed chromophores associated with higher molecular weight CDOM causing a breakdown to low molecular weight

CDOM (Moran and Zepp, 1997; Helms et al., 2008; Mesfioui et al., 2015). In addition, Helms et al., 2008 also proved that $S_{275–295}$ and S_R were inversely related to the molecular weight of the CDOM. Our calculated data indicated that $S_{275–295}$ and S_R were positively correlated to each other when both increased with irradiation time increments (Pearson slope $p<0.05$), while $S_{350-400}$ and S_R were negatively correlated to each other when $S_{350-400}$ decreased with irradiation increments ($p<0.05$). It also showed a negative correlation between a_{300} and S_R (Pearson $R^2 > 0.80$, $p < 0.05$). Degraded CDOM (due to decreasing a_{300}) lowered its molecular weight (due to increasing S_R) and reduced its ability to absorb UV-Vis radiation, and further affected depolymerization and adsorption of DOM while high-molecular-weight DOM exhibited more benefit to bind cadmium than low-molecular-weight DOM (Li et al., 2019). We concluded that the degradation of chromophores associated with high-molecular-weight CDOM during photobleaching transformed a significant portion of the CDOM from the high-molecular-weight pool to the low-molecular-weight pool.

The decreasing a_{300} and increasing $[NH_4^+]$ along with irradiation time showed a strong negative correlation between each other (Pearson $R^2 > 0.72$, slope p-value < 0.05). Also, we estimated the correlation between the photo-production rate of ammonium and a_{300} at 0-hour in each season of Baffin Bay and found that Oct_20 and Feb_22 showed a significant positive correlation (Pearson $R^2 > 0.68$, slope p-value < 0.05). BB3 and BB5 also showed a significant positive correlation throughout the five seasons (Pearson $R^2 > 0.85$, slope p-value < 0.05). This resulted in the capability of DOM to photo-produce ammonium with a high absorption coefficient. In conclusion, a strong negative correlation between NH_4^+ photo-production and CDOM a_{300} indicated the photo-degradation of CDOM and photo-ammonification due to photobleaching.

4.4. Amino acids make up the detected peptides and deaminated peptides

To determine the structural composition of microbial peptides and deaminated peptides, we analyzed the relative abundances of individual amino acids used to build the peptide bond. The microbial proteins' pool indicated high abundances of glycine (~14%), alanine, lysine, proline, serine, glutamine and valine (>7%). On the other hand, glutamic acid, methionine, tryptophan, and arginine contributed to low abundances (Figure 22). Alanine was also found to be rich in microbial soil with more than 10% relative abundance along with glutamic acid (>10%) while methionine and cysteine typically were the lowest abundance amino acids (Moe, 2013). Tyrosine, glutamine, and asparagine were highly abundant in anoxic sediment porewaters of Santa Barbara Basin while tryptophan, histidine and methionine showed very low abundances (Abdulla, 2018). The amino acid composition of these peptides and deaminated peptides may account for their incomplete hydrolysis to free amino acids and oxoacids, therefore making them refractorily accumulated in sediment.

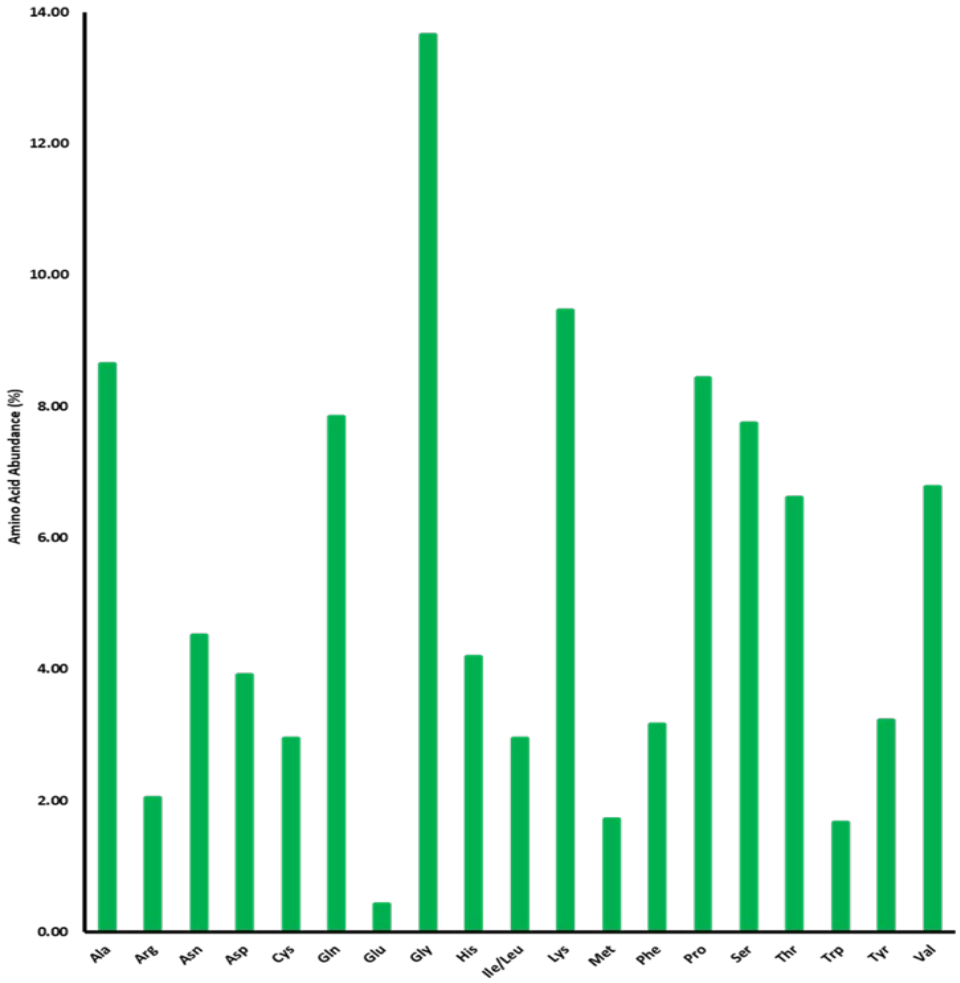

Figure 22. *Relative abundance of individual amino acids in peptides and deaminated peptides detected in Baffin Bay porewaters.*

4.5. Irradiation effects on molecular composition and chemical structures

In 4824 detected compounds, 2500 showed significant changes in concentration (95% confidence level of linear regression slope ≠ 0), in which 1106 compounds only increased with irradiation time, 1052 only decreased with irradiation time, and 342 showed both increasing and decreasing concentration. In 1394 pre-irradiation compounds, those with decreasing concentrations over irradiation time, CHON made up 50%, followed by CHO, CHONS, and CHONP with 25%, 8%, and 7%, respectively. Nitrogen-containing compounds accounted for 52%, followed by sulfur-containing compounds and phosphorus-containing compounds with 12% and 7%, respectively. In 1448 post-irradiation compounds, those with increasing concentrations over irradiation time, CHON made up 50%, followed by CHO, CHONS, and CHONP with 26%, 8%, and 6%, respectively. Nitrogen-containing compounds accounted for 56%, followed by sulfur-containing compounds and phosphorus-containing compounds with 12% and 7%, respectively. The similar composition did not give us any clue about the role of UV-Vis radiation on these

organic matters. Therefore, structural elucidation by mass spectrometry would open a brighter view of these structures.

Of 1394 pre-irradiation compounds detected, 164 were confirmed to be peptides or deaminated peptides and 245 peptides or deaminated peptides were confirmed from 1448 post-irradiation compounds. The amino acid components of these peptides and deaminated peptides were examined for composition analysis (Figure 23). Tryptophan, tyrosine, and cystine-containing peptides/deaminated peptides degraded over irradiation time increments while valine, threonine, and serine-containing compounds concentrated over time. From a structural point of view, the degrading peptides/deaminated peptides contained 81 ring structures and 31 conjugated double-bond structures. From an amino-acid-with-ring-structure point of view, compounds with proline contributed 38%, histidine 22%, tyrosine 18%, phenylalanine 16%, tryptophan 16%, and cystine 2%. Note that the sum of contribution percentage exceeded 100% due to multiple appearances of an amino acid within one peptide/deaminated peptide structure.

Chromophoric amino acids presented in proteins were tryptophan (Trp), tyrosine (Tyr), phenylalanine (Phe), histidine (His), cysteine (Cys) and cystine, according to Davis & Truscott 2001. These chromophoric amino acids absorbed radiation with wavelength > 230 nm while all other major amino acids did not absorb significantly in this region. Peptide bond exhibited a weak absorption at 210-220nm; therefore, chromophoric amino acids were responsible for absorbing UVA-Vis radiation. The photo-oxidation of dissolved organic matter could happen in a direct or indirect way. In conclusion, the molecular composition of CDOM did not account for the photo-transformation of DON; hence molecular structures were elucidated to provide a brighter view of these refractory peptides and deaminated peptides. More studies need to be conducted to have a

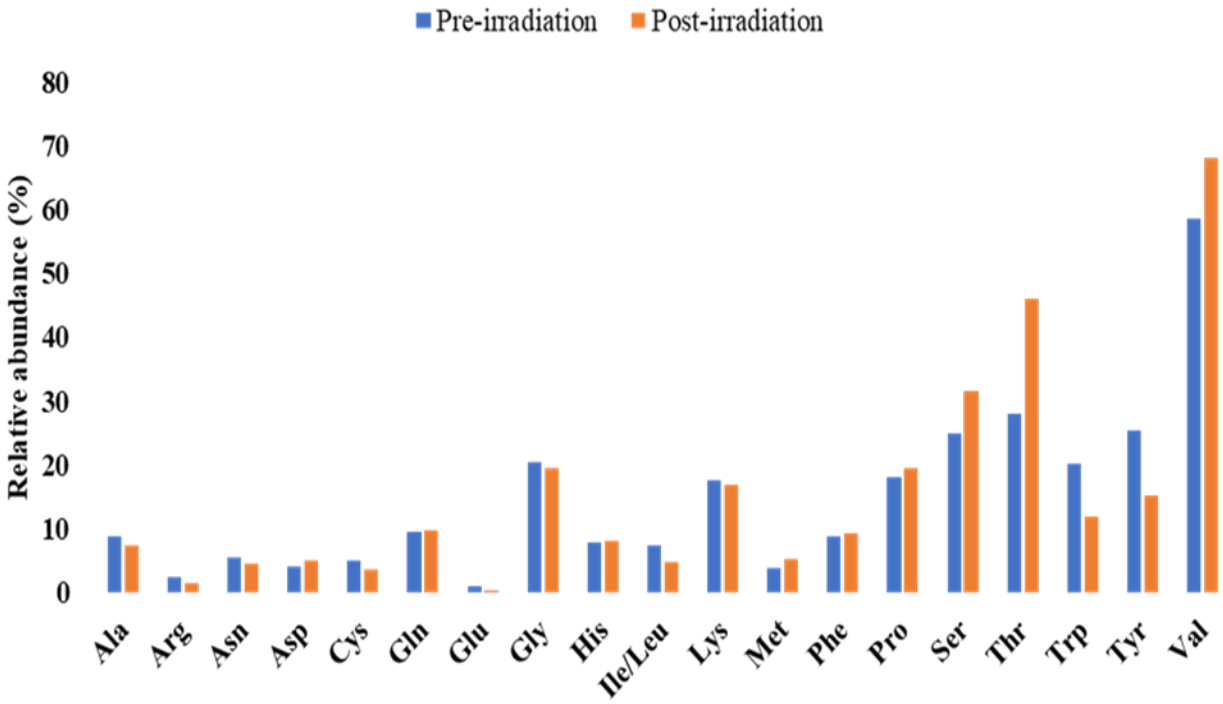

Figure 23. *Relative abundances of amino acids that made up pre-irradiation and post-irradiation peptides and deaminated peptides.*

better understanding of the transformation pathways of peptides/ deaminated peptides to free amino acids and organic acids.

5. CONCLUSION

The study suggested ammonium benthic fluxes served as a major source of inorganic nutrients that contributed to the Baffin Bay water column along with other nutrient sources to feed photoautotrophs such as phytoplankton. In addition to the benthic flux, photo-ammonification of porewater DON was a significant source of ammonium to the water column. In the water column, chromophoric DOM absorbed sunlight radiation then degraded to lower molecular weight CDOM and released ammonia, deaminated peptides, free amino acids, and organic acids. CDOM with aromatic rings or conjugated double bonds was responsible for absorbing sunlight and shielding biota from harmful UV radiation. Peptides and deaminated peptides with chromophoric amino acids such as tryptophan, tyrosine, proline, phenylalanine, histidine, and cystine degraded along with irradiation time increments. Therefore, more studies need to be conducted to have a deeper understanding of the mechanisms that transformed CDOM from a high molecular weight to a low molecular weight pool. The in-lab solar irradiation study suggested that photo-ammonification of pure porewaters served as a significant source of ammonium, and CDOM was responsible for the photo-transformation of DON in pore waters. In the next chapter of the study, surface water samples will be structurally elucidated to compare the effect of sunlight radiation with simulated solar radiation and quantify the portion of porewater CDOM that was photo-reactive in surface water.

The Baffin Bay showed significant differences in spatial and seasonal benthic fluxes of ammonia to surface water. This was possibly due to the spatial sedimentation type and seasonal change in rainfall precipitations and primary production rates. This study highlights the role of the internal circulation of nutrients as a significant source to the bay, which needs to be taken into account when an attempt to provide a plan for any remediation and reduce the occurrence of brown tides and other harmful algal blooms events in the bay.

References

Abdulla, H.A., Burdige, D.J. and Komada, T., 2018. Accumulation of deaminated peptides in anoxic sediments of Santa Barbara Basin. *Geochimica et Cosmochimica Acta*., 223, pp.245-258.

Avnimelech, Y., Ritvo, G., Meijer, L.E. and Kochba, M., 2001. Water content, organic carbon and dry bulk density in flooded sediments. *Aquacultural Engineering*, *25*(1), pp.25-33.

Bergmann, D., 2021. *Comprehensive Approach for Dissolved Organic Matter Chemical Characterization Using Orbitrap Fusion Tribrid Mass Spectrometer Coupled with Ion and Liquid Chromatography Techniques* (Master Thesis, Texas A&M University-Corpus Christi).

Blanchard G.F., Montagna P.A., 1995. Assessment of a brown tide impact on microalgal benthic communities in Baffin-bay (texas) in 1990 using a primary production simulation-model. *Oceanologica Acta*., 18(3), 371-377.

Boudreau, B.P., 1997. *Diagenetic models and their implementation* (Vol. 505). Berlin: Springer.

Bushaw, K.L., Zepp, R.G., Tarr, M.A., Schulz-Jander, D., Bourbonniere, R.A., Hodson, R.E., Miller, W.L., Bronk, D.A., Moran, M.a.J.N., 1996. Photochemical release of biologically available nitrogen from aquatic dissolved organic matter. *Nature 381,* 6581, 404–407.

Buffam, I. and McGlathery, K.J., 2003. Effect of ultraviolet light on dissolved nitrogen transformations in coastal lagoon water. *Limnology and Oceanography*, *48*(2), pp.723-734.

Caffrey, J.M., Murrell, M.C., Amacker, K.S., Harper, J.W., Phipps, S. and Woodrey, M.S., 2014. Seasonal and inter-annual patterns in primary production, respiration, and net ecosystem metabolism in three estuaries in the northeast Gulf of Mexico. *Estuaries and Coasts*, *37*, pp.222-241.

Castro, M.S., Driscoll, C.T., Jordan, T.E., Reay, W.G., & Boynton W.R., 2003. Sources of Nitrogen to Estuaries in the United States. *Estuaries*, 26 (3), p. 803–814.

Cira, E.K., Wetz, M.S., 2019. Spatial-temporal distribution of Aureoumbra lagunensis ("brown tide") in Baffin Bay, Texas. *Harmful Algae*, 89, 101669.

Davies, M.J., Truscott, R.J.W., 2001. Photo-oxidation of proteins and its role in cataractogenesis. *Journal of Photochemistry and Photobiology B: Biology,* 63, 114–125.

Del Vecchio and Blough, 2002. Chromophoric DOM in the coastal environment. *In Biogeochemisty of marine dissolved organic matter*.

Dixon, L.K., Murphy, P.J., Becker, N.M., Charnigaa, C.M., 2014. The potential role of benthic nutrient flux in support of Karenia blooms in west Florida (USA) estuaries and the nearshore Gulf of Mexico. *Harmful algae*, 38, 30-39.

Dittmar, T., Koch, B., Hertkorn, N. and Kattner, G., 2008. A simple and efficient method for the solid-phase extraction of dissolved organic matter (SPE-DOM) from seawater. *Limnology and Oceanography: Methods*, *6*(6), pp.230-235.

Felix, J. D., Elliott, E.M., Gish, T.J., McConnell, L.L. and Shaw, S.L., 2013. Characterizing the isotopic composition of atmospheric ammonia emission sources using passive samplers and a combined oxidation-bacterial denitrifier approach. *Rapid Communications in Mass Spectrometry*, *27*(20), pp.2239-2246.

Francis, C.A., Beman, J.M. and Kuypers, M.M., 2007. New processes and players in the nitrogen cycle: the microbial ecology of anaerobic and archaeal ammonia oxidation. *The ISME journal*, 1(1), pp.19-27.

Funkey, C.P., Latour, R.J., Bronk, D.A., 2015. Abiotic effects on effluent dissolved organic nitrogen along an estuarine transect. *Water Environ. Res*. 87 (3), 258–265.

Holmes, R. M., A. Aminot, R. Kérouel, B. A. Hooker, and B. J. Peterson, 1999. A simple and precise method for measuring ammonium in marine and freshwater ecosystems. *Can. J. Fish. Aquat. Sci*., 56(10), 1801–1808.

Helms, J. R., A. Stubbins, J. D. Ritchie, E. C. Minor, D. J. Kieber, and K. Mopper, 2008. Absorption spectral slopes and slope ratios as indicators of molecular weight, source, and photobleaching of chromophoric dissolved organic matter. *Limnology and Oceonography,* 53(3), 955-969.

Joint, I.R., Pomroy, A.J., 1981. Primary Production in a Turbid Estuary. *Estuarine, Coastaland & Shelf Science*. 13, 303-316.

Kieber, D.J., Mcdaniel, J., Mopper, K., 1989. Photochemical source of biological substrates in sea water: implications for carbon cycling. *Nature 341* (6243), 637–639.

Klute, A., 1986. Water retention: laboratory methods. *Methods of soil analysis: part 1 physical and mineralogical methods*, *5*, pp.635-662.

Komada, T., Burdige, D.J., Li, H.L., Magen, C., Chanton, J.P. and Cada, A.K., 2016. Organic matter cycling across the sulfate-methane transition zone of the Santa Barbara Basin, California Borderland. *Geochimica et Cosmochimica Acta*, *176*, pp.259-278.

Li, S., Hou, X., Shi, Y. *et al.,* 2020. Rapid photodegradation of terrestrial soil dissolved organic matter (DOM) with abundant humic-like substances under simulated ultraviolet radiation. *Environ Monit Assess* 192, 103.

Lopez, C.V., Murgulet, D. and Santos, I.R., 2020. Radioactive and stable isotope measurements reveal saline submarine groundwater discharge in a semiarid estuary. *Journal of Hydrology*, 590, p.125395.

Lengier, M., Szymczycha, B., Brodecka-Goluch, A., Kłostowska, Ż. and Kuliński, K., 2021. Benthic diffusive fluxes of organic and inorganic carbon, ammonium and phosphates from deep water sediments of the Baltic Sea. Oceanologia, 63(3), pp.370-384.

Mesfioui, R., Abdulla, H.A. and Hatcher, P.G., 2015. Photochemical alterations of natural and anthropogenic dissolved organic nitrogen in the York River. *Environmental science & technology*, *49*(1), pp.159-167.

Minor, E.C., Dalzell, B.J., Stubbins, A. and Mopper, K., 2007. Evaluating the photoalteration of estuarine dissolved organic matter using direct temperature-resolved mass spectrometry and UV-visible spectroscopy. *Aquatic Sciences*, *69*, pp.440-455.

Moran, A., Zepp, R.G., 1997. Role of photoreactions in the formation of biologically labile compounds from dissolved organic matter. *Limnol Ocermogr*. 42(6), 1307-1316.

Morin, J., Morse, J.W., 1999. Ammonium release from resuspended sediments in the Laguna Madre estuary. *Marine Chemistry*, 65(1-2), pp. 97-110.

Mortazavi, B., Iversonl, R.L., Huang, W., Lewis, F.G., Caffrey, J.M., 2000. Nitrogen budget of Apalachicola Bay, a bar-built estuary in the northeastern Gulf of Mexico. *Mar. Eco. Prog. Ser.*, 195, 1-14.

Morell, J.M., Corredor, J.E., 2001. Photomineralization of fluorescent dissolved organic matter in the Orinoco River plume: estimation of ammonium release. *J. Geophys. Res*. 106 (C8), 16807–16813.

Moe, L.A., 2013. Amino acids in the rhizosphere: From plants to microbes. *American Journal of Botany*, 100, 1692-1705.

Mopper, K. and Kieber, D.J., 2000. Marine photochemistry and its impact on carbon cycling. *The effects of UV radiation in the marine environment*, *10*, pp.101-129.

Nixon, S.W., 1981. Remineralization and Nutrient Cycling in Coastal Marine Ecosystems. In: Neilson, B.J., Cronin, L.E. (eds) Estuaries and Nutrients. Contemporary Issues in Science and Society. Humana Press.

NOAA, Station Data Inventory, Access & History. *NOAA*. https://www.ncdc.noaa.gov/cdoweb/datasets/GHCND/stations/GHCND:US1TXKL0002/detail.

Percuoco, V.P., Kalnejais, L.H., & Officer, L.V., 2015. Nutrient release from the sediments of the Great Bay Estuary, N.H. USA. *Estuarine*, Coastal and Shelf Science, 161, 76-87.

Rain-Franco, A., Munoz, C., Fernandez, C., 2014. Ammonium production off Central Chile (36 degrees S) by photodegradation of phytoplankton-derived and marine dissolved organic matter. *PLoS One* 9 (6), 13.

Rizzo, M., 1990. Nutrient exchanges between the water column and a subtidal benthic microalgal community. *Estuaries,* 13 (3), 219-226.

Schulz, H.D., 2006. Quantification of early diagenesis: dissolved constituents in pore water and signals in the solid phase. *Marine geochemistry,* 73-124. Springer, Berlin, Heidelberg.

Shrestha, S., 2022. Investigating the photochemical transformation of Dissolved Organic Nitrogen at the Molecular level in Baffin Bay, Texas, USA. *PhD dissertation – Texas A&M University – Corpus Christi*.

Sigman, D.M., Casciotti, K.L., Andreani, M., Barford, C., Galanter, M.B.J.K. and Böhlke, J.K., 2001. A bacterial method for the nitrogen isotopic analysis of nitrate in seawater and freshwater. *Analytical chemistry*, *73*(17), pp.4145-4153.

Thibodeau, B., Bauch, D. and Voss, M., 2017. Nitrogen dynamic in Eurasian coastal Arctic ecosystem: Insight from nitrogen isotope. *Global Biogeochemical Cycles*, *31*(5), pp.836-849.

Vahatalo, A., Salonen, K., Munster, U., Jarvinen, M., Wetzel, R., 2003. Photochemical transformation of allochthonous organic matter provides bioavailable nutrients in a humic lake. *Archiv Fur Hydrobiologie,* 156 (3), 287–314.

Vahatalo, A.V., Zepp, R.G., 2005. Photochemical Mineralization of Dissolved Organic Nitrogen to Ammonium in the Baltic Sea. *Environ. Sci. Technol*., 39, 6985-6992.

Vahatalo, A.V., Jarvinen, M., 2007. Photochemically produced bioavailable nitrogen from biologically recalcitrant dissolved organic matter stimulates production of a nitrogen-limited microbial food web in the Baltic Sea. *Limnol. Oceanogr*., 52 (1), 132–143.

Wetz, M.S., Cira, E.K., Sterba-Boatwright, B., Montagna, P.A., Palmer, T.A. and Hayes, K.C., 2017. Exceptionally high organic nitrogen concentrations in a semi-arid South Texas estuary susceptible to brown tide blooms. *Estuarine, Coastal, and Shelf Science*, 188, pp.27-37.

Wainright, S.C., 1987. Stimulation of heterotrophic microplankton production by resuspended marine sediments. *Science*, 238 (4834), pp. 1710-1712.

Warnken, K.W., Gill, G.A., Santschi, P.H., & Griffin, L.L, 2000. Benthic exchange of nutrients in Galveston Bay, Texas. *Estuaries*, 23(5), 647-661.

Xie, H., Belanger, S., Song, G., Benner, R., Taalba, A., Blais, M., Tremblay, J., Babin, M., 2012. Photoproduction of ammonium in the southeastern Beaufort Sea and its biogeo-chemical implications. *Biogeosciences* 9 (8), 3047–3061.

Yang, Y. et al.,, 2021. Photo-ammonification in surface water samples: Mechanism and influencing factors. *Science of The Total Environment*, 759, 143547.

Zhang, Q., Anastasio, C., 2003. Conversion of fogwater and aerosol organic nitrogen to ammonium, nitrate, and NO_x during exposure to simulated sunlight and ozone. Environ. *Sci. Technol.* 37 (16), 3522–3530.

Zhang, L., Altabet, M.A., Wu, T. and Hadas, O., 2007. Sensitive measurement of NH4+ 15N/14N (δ15NH4+) at natural abundance levels in fresh and saltwaters. *Analytical Chemistry*, *79*(14), pp.5297-5303.

Zilius, M., Daunys, D., Petkuviene, J., & Bartoli, M., 2012. Sediment-water oxygen, ammonium and soluble reactive phosphorus fluxes in a turbid freshwater estuary (Curonian lagoon, Lithuania): evidence of benthic microalgal activity. *J. Limnol*., 71(2), 309-319.

Task 4:

Modelling Freshwater Inflow, Nutrient and Sediment Loads

Prepared by:

Mohamed Ahmed, Ramadan Abdelrehim, Ahmed Omar, Mohamed Mousa, Muhamed Elshalkany, Meghan Bygate

1. Summary:

The Soil and Water Assessment Tool (SWAT) model was developed to quantify water, sediment, and nutrient yields in the Baffin Bay watershed during the period from 2001 to 2020. Statistical metrics such as the P-factor, R-factor, coefficient of determination (R^2), and Nash–Sutcliffe (NS) were used as indicators for the goodness of fit between the observed and the model-simulated streamflow data. Results indicated that the (1) SWAT model performed reasonably well in simulating streamflow in the Baffin Bay watershed (P-factor: 0.22 to 0.75, R-factor: 0.13 to 1.28, R^2: 0 to 0.78, and NS: -0.11 to 0.28), (2) model performance was primarily influenced by field data availability, the placement of calibration gauges, and the basin's hydrological and topographical characteristics, (3) watershed's average annual precipitation, surface runoff, actual evapotranspiration, and total recharge were estimated at 686 mm, 165 mm, 481 mm, and 37 mm, respectively, (4) watershed's average annual sediment and nitrate (in surface runoff) loadings were estimated at 3000 kg/ha, and 0.9 kg/ha, respectively, and (5) spatial variations in water yield were found to be primarily influenced by rainfall, evapotranspiration, land cover/land use (LCLU) and soils, whereas sediment and nutrient loading were mainly controlled by changes in LCLU and soil types.

2. Introduction:

Estuaries, as dynamic ecosystems characterized by significant environmental variations, frequently possess an exceptionally high ecological and human values relative to their size (Pendleton, 2010; Barbier et al., 2011). Low-inflow estuaries, typically located in subtropical regions, exhibit distinct characteristics such as limited freshwater input for extended durations, restricted connectivity to the ocean, and shallow depths (Largier, 2010). Baffin Bay, located along the southern coast of Texas (Figure 1), is one of these systems. Due to the lack of a direct connection to the Gulf of Mexico (GOM) and minimal initial freshwater input, Baffin Bay frequently experiences hypersaline conditions (Wetz et al., 2017). During prolonged dry periods, Baffin Bay has experienced harmful occurrences of brown tides (e.g., Buskey et al., 2001; Cotner et al., 2004; Cira and Wetz, 2019). These events have had detrimental effects on both the ecosystem and the related ecosystem services (Buskey and Hyatt, 1995; Street et al., 1997).

While Baffin Bay typically experiences low inflow, occasional high inflow events can introduce elevated nutrient and sediment loads from land, leading to rapid shifts in salinity (Cira et al., 2021; Beecraft and Wetz, 2022). However, due to the absence of an oceanic connection, these nutrients may be retained in the bay for extended periods, increasing its susceptibility to eutrophication. The implementation of an effective nutrient management plan within the Baffin Bay watershed can significantly reduce the occurrence of brown tide blooms. The most recent bloom events have been characterized by widespread geographic distribution, prolonged duration, increased presence of toxic species, greater impacts on fisheries, and higher associated costs compared to historical events (Anderson, 1989; Smayda, 1990; Hallegraeff, 1993; Anderson et al., 2002; Glibert et al., 2005; Heisler et al., 2008). A comprehensive understanding of the spatial and temporal variations in water, nutrients, and sediment loads is essential for effectively controlling and managing contaminants in Baffin Bay. By thoroughly studying these variations, appropriate strategies can be developed to control and mitigate the degradation of water quality in the system.

Relying solely on monitoring activities is inadequate for comprehensively capturing the complex spatial and temporal variability in water, nutrients, and sediment loads associated with natural and human-induced processes within the Baffin Bay watershed (Mirchi et al., 2010; Dagnew et al., 2019). Hydrological models, however, have proven to be crucial in characterizing complex watersheds and understanding the intricate relationships between natural and human activities and ecosystems, while also exploring the consequences of human actions on watershed systems (Ghaith and Li, 2020; Kmoch et al., 2022).

The Soil and Water Assessment Tool (SWAT) is a physically based, semi-distributed hydrological model that operates in a continuous time step (Arnold et al., 1998; Tuppad et al., 2011; Akoko et al., 2021). Widely recognized as a leading hydrological model, the SWAT model has been extensively utilized to address various hydrologic and environmental concerns (Gassman et al., 2007; Pisinaras et al., 2010; Aloui et al., 2023). In this research, the SWAT model is implemented to quantify water, nutrients, and sediment loads in the Baffin Bay watershed (Figure 1). The selection of SWAT was based on its open-access availability, compatibility with geographic information system (GIS) software, adaptability in spatial and temporal dimensions, and integration of optimization algorithms (Ghaith and Li, 2020; Lin and Zhang, 2021).

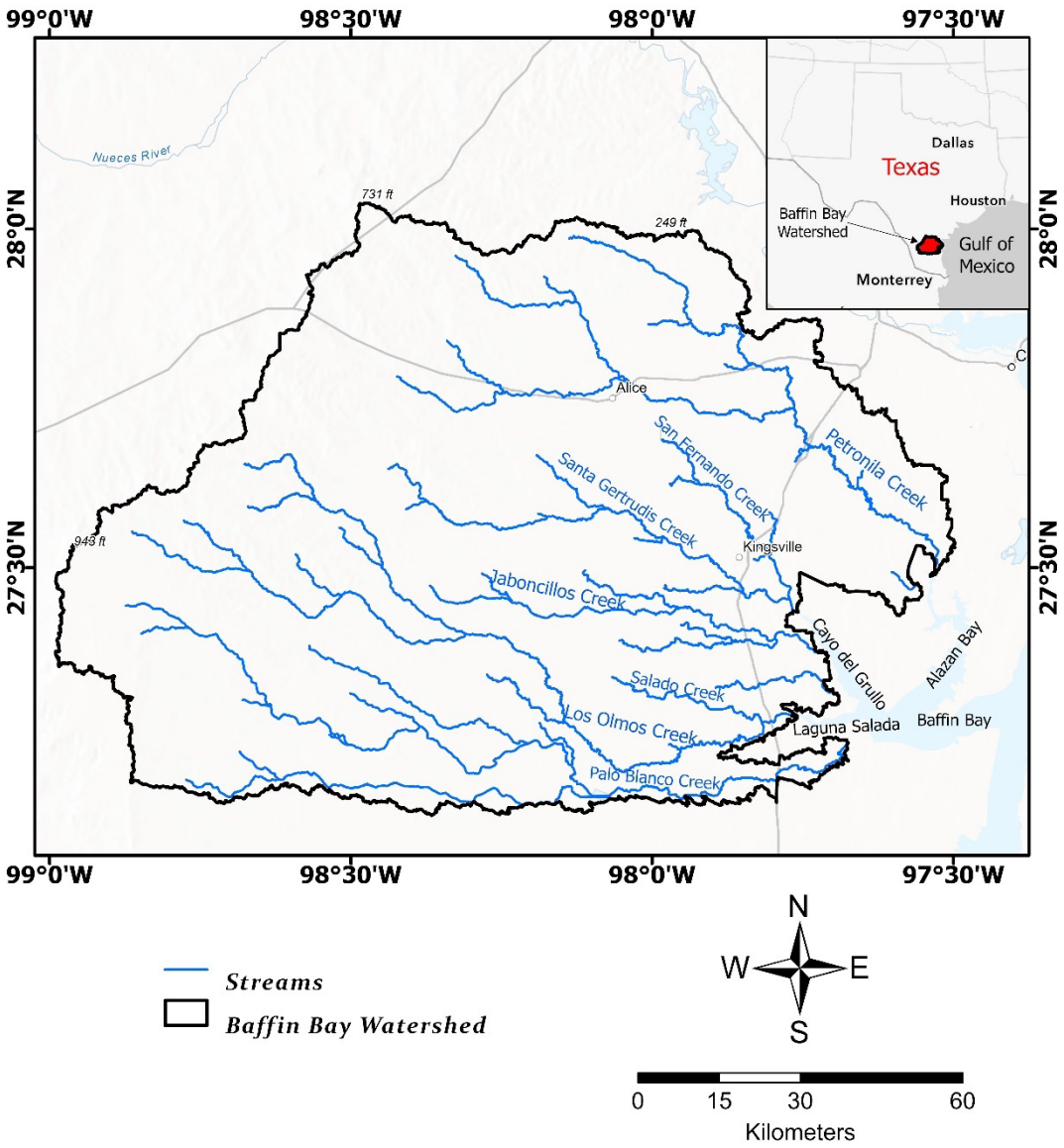

Figure 1. Spatial distribution of the Baffin Bay watershed.

3. Materials and Methods:

3.1. Study Area:

Baffin Bay (area: 219 km^2) is located approximately 80 km south of Corpus Christi, Texas, United States (Figure 1). In addition to its aesthetic appeal, Baffin Bay is recognized for its thriving commercial and fishing industry, accounting for some of the highest fishery production in the state of Texas (Ayers et al., 2021). Baffin Bay is characterized by its narrow dimensions and receives intermittent inflows from small streams that discharge into one of three bay branches: Alazan Bay to the North, Cayo del Grullo in the central part, and Laguna Salada to the south (Figure 1). The largest of these branches, Alazan, is primarily fed by Petronila Creek, the Cayo del Grullo is fed

by San Fernando Creek, and the smallest subsidiary bay, Laguna Salada, is fed by Los Olmos Creek (Ayers et al., 2021). Together, these branches comprise the Baffin Bay watershed (area: 10047 km^2). With a slow circulation rate, the bay eventually drains into the Laguna Madre (Figure 1).

Evidences suggest an ongoing eutrophication process in Baffin Bay, as indicated by elevated and increasing nutrient or chlorophyll concentrations observed during the past three to four decades (Wetz et al., 2017; Bugica et al., 2020). Recent tracer investigations have also identified a significant presence of nutrients in Baffin Bay originating from human activities (Beecraft and Wetz, 2022). For example, nitrogen inputs in Baffin Bay are mainly sourced from fertilizers and atmospheric deposition, while phosphorus inputs are primarily derived from fertilizer application (Rebich et al., 2011). Additionally, organic nitrogen is believed to be originate from crop residue during runoff events (Ockerman and Petri, 2001). During periods of significant rainfall or hurricanes, large freshwater inputs reduce the Baffin Bay's salinity levels, increase water levels, and deepen tidal inlets in the bay (TPWD).

3.2. SWAT Data:

The input data required for the SWAT model encompass various datasets, including topographical, climatic, soil, and land cover/land use (LCLU) data (Lam et al., 2012; Uniyal et al., 2023). In addition to these, calibration and validation of the model involve utilizing streamflow datasets (Santhi et al., 2001; Lam et al., 2012; Woznicki and Nejadhashemi, 2013). Table 1 lists SWAT input data and their sources.

Table 1. SWAT input data and their sources.

Input Data	**Sources**
Topography	Light Detection and Ranging (LiDAR) digital elevation model (DEM)
Soil	Soil Survey Geographic (SSURGO) and State Soil Geographic (STATSGO)
Land cover/land use (LCLU)	National Land Cover Dataset (NLCD)
Rainfall	Global Precipitation Measurement Mission (GPM)
Temperature	National Oceanic and Atmospheric Administration (NOAA)
Solar radiation, wind speed, and relative humidity	Simulated within the SWAT model
Streamflow	United States Geological Survey (USGS) and Texas Water Development Board (TWDB)
Nutrients	Texas Commission on Environmental Quality (TCEQ)

3.2.1. Topographical Data:

In this study, a digital elevation model (DEM) derived from a 1 m resolution Light Detection and Ranging (LiDAR) dataset was employed (Figure 2). The DEM was utilized for slope calculation,

stream extraction, and watershed delineation (USGS, 2020). Considering the relatively lower topographical variations in the Baffin Bay watershed (Figures 2 and 3), the DEM was resampled to 7 m using the nearest neighbor technique (Tan et al., 2015; Shen and Tan, 2020). This adjustment was made to improve computational efficiency and accelerate the simulation process.

The Baffin Bay watershed exhibits a maximum elevation of 288 m above sea level and a minimum elevation of approximately 1 m below mean sea level (Figure 2). The elevation gradually decreases from the western region towards the eastern direction, aligning with proximity to the GOM. The average elevation of the watershed is estimated to be 98 m. The slope of the watershed varies between 0° and 46°, with a gradual decrease towards the east, adjacent to the GOM (Figure 3). On average, the slope is less than 1°, indicating the predominantly flat nature of the watershed.

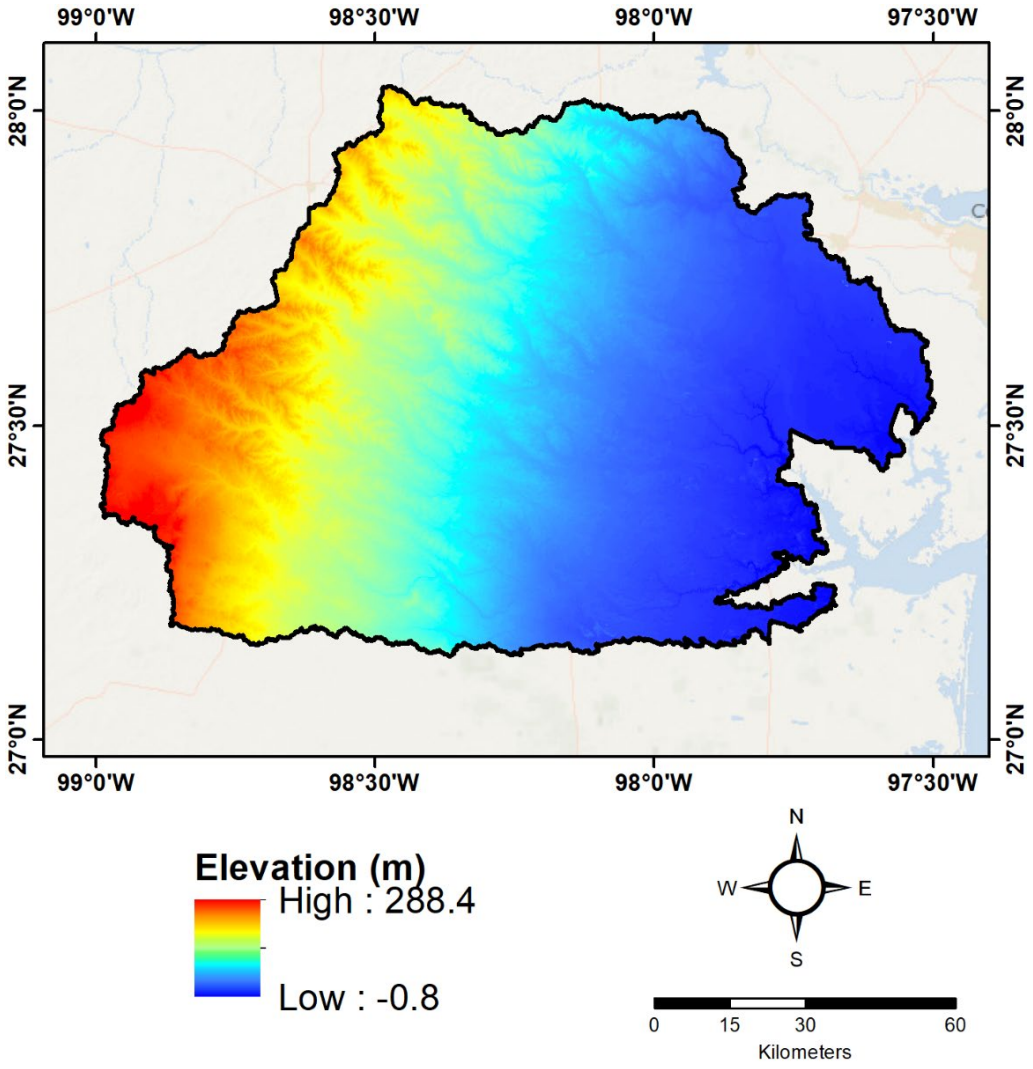

Figure 2. Elevation map of the Baffin Bay watershed.

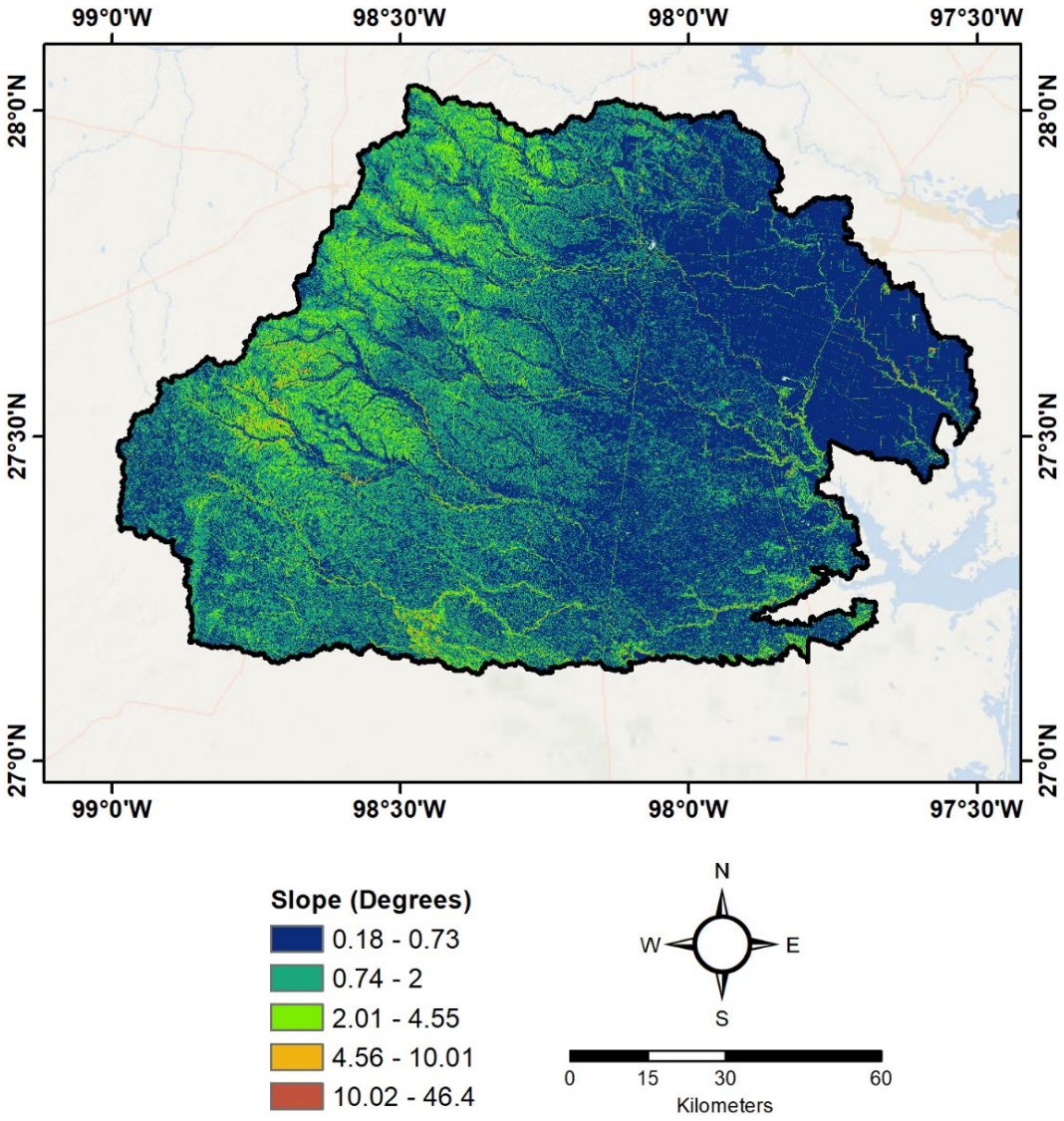

Figure 3. Slope map of the Baffin Bay watershed.

3.2.2. Soil Data:

Soil data over the Baffin Bay watershed was acquired from the Soil Survey Geographic (SSURGO) database (USDA-NRCS) and the State Soil Geographic (STATSGO) database (USDA-NRCS). We compared SWAT simulations using both sources within the Baffin Bay watershed and discovered that they exhibit significant similarities. The SSURGO database provides more detailed mapping information, but for the sake of ensuring robust and rapid model simulations, we have chosen to utilize the STATSGO database (Figure 4). Baffin Bay watershed is mainly covered by loamy and clay soils. The Victoria, Randado, Delmita, and Opelika soil series account for approximately 23%, 19%, 14%, and 13% of the Baffin Bay watershed, respectively (Table 2).

Table 2. Major soil types in the Baffin Bay watershed.

Soil Key	Soil series	Description	% area of the watershed
TX383, TX590, TX381	Victoria	Fine, smectitic, hyperthermic sodic haplusterts.	23.0
TX455	Randado	Loamy, mixed, active, hyperthermic, shallow petrocalcic paleustalfs.	19.2
TX131, TX363, TX365	Delmita	Fine-loamy, mixed, active, hyperthermic petrocalcic paleustalfs.	13.8
TX381, TX379	Opelika	Fine-loamy, mixed, active, hyperthermic mollic albaqualfs.	12.6
TX394	Palobia	Fine-loamy, mixed, active, hyperthermic typic natrustalfs.	7.5
TX234, TX005	Aguilare	Fine, smectitic, mesic vertic natrargids.	7.0
TX409, TX283, TX399, TX383	Lattas	Fine, smectitic, hyperthermic typic haplusterts.	6.7
TX204	Goliad	Fine, smectitic, hyperthermic petrocalcic paleustolls.	3.3
TX489	Runge	Fine-loamy, mixed, superactive, hyperthermic typic argiustolls.	3.2
TX409	Pernitas	Fine-loamy, mixed, superactive, hyperthermic typic argiustolls.	1.6
TX131, TX366, TX180, TX395, TX502	Falfurri	Mixed, hyperthermic typic ustipsamments.	0.9
TX365, TX106	Comitas	Loamy, mixed, active, hyperthermic arenic aridic paleustalfs.	0.9
TX366	Nueces	Loamy, mixed, active, hyperthermic arenic paleustalfs.	0.3

3.2.3. Land Cover/Land Use (LCLU) Data:

A 30-m resolution LCLU dataset over the Baffin Bay watershed were obtained from the 2011 National Land Cover Dataset (NLCD) database (Homer, C.H. et al., 2012) (Figure 5). The LCLU data reveals spatial variability. The distribution is as follows: range and grasslands for grazing cover approximately 50% of the area, agricultural lands cover 22%, hay and pasture areas cover 18%, urban areas cover 5%, wetlands cover 3%, and forest areas cover 2% (Figure 5; Table 3).

Table 3. Land use/Land cover units over the Baffin Bay watershed.

LCLU Code	LCLU Type	% area of the watershed
RNGB/RNGE	Rangeland - Barren/Sparsely Vegetated/Herbaceous	49.9
AGRR	Agricultural Row Crops	21.8
HAY	Hay/Pasture	18.3
UIDU/URHD/URLD/URMD	Urban Land	5.0
WETF/WETN	Wetland Forested and Non-Forested	2.9

FRSD/FRSE/FRST	Forest land	1.6
SWRN	Shrubland - Western	0.5
WATR	Open Water	0.1

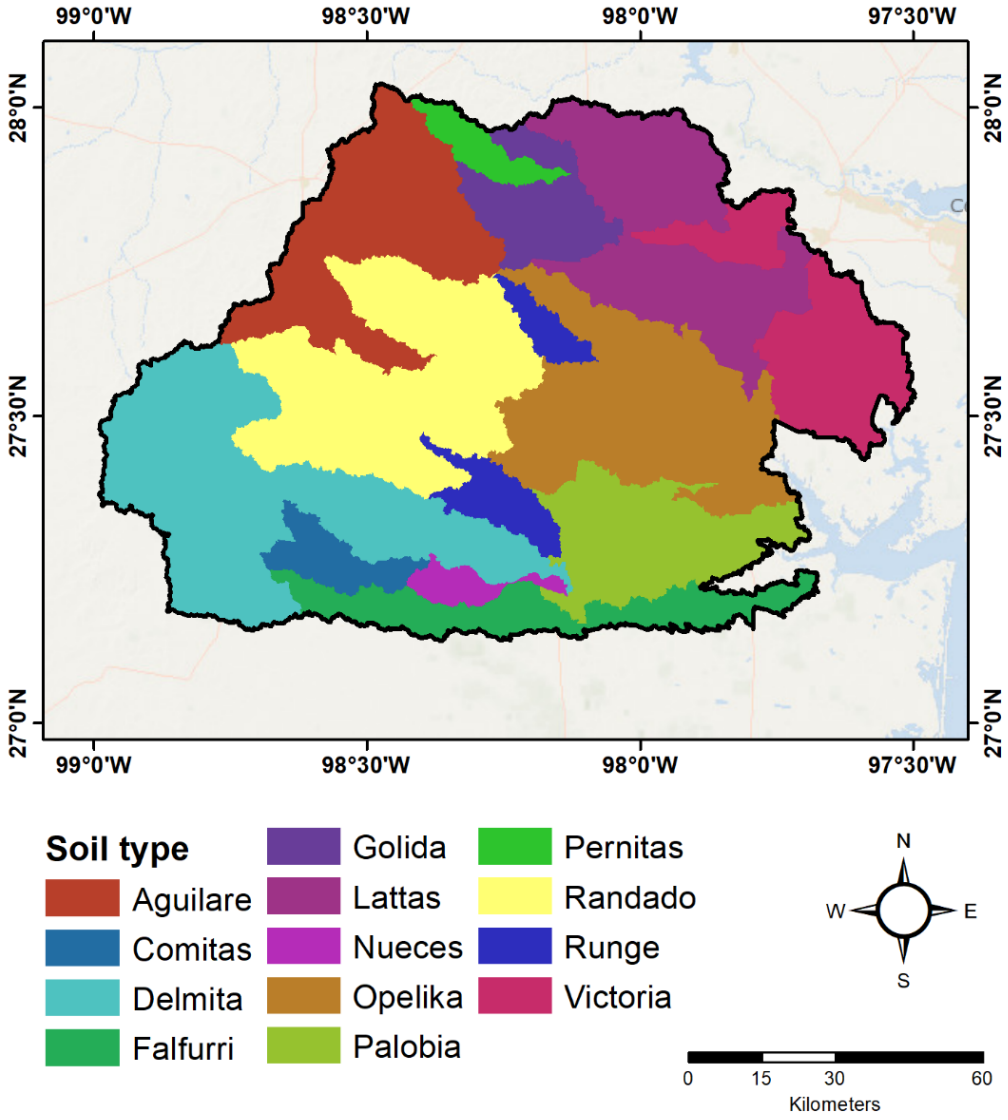

Figure 4. Soil map of the Baffin Bay watershed.

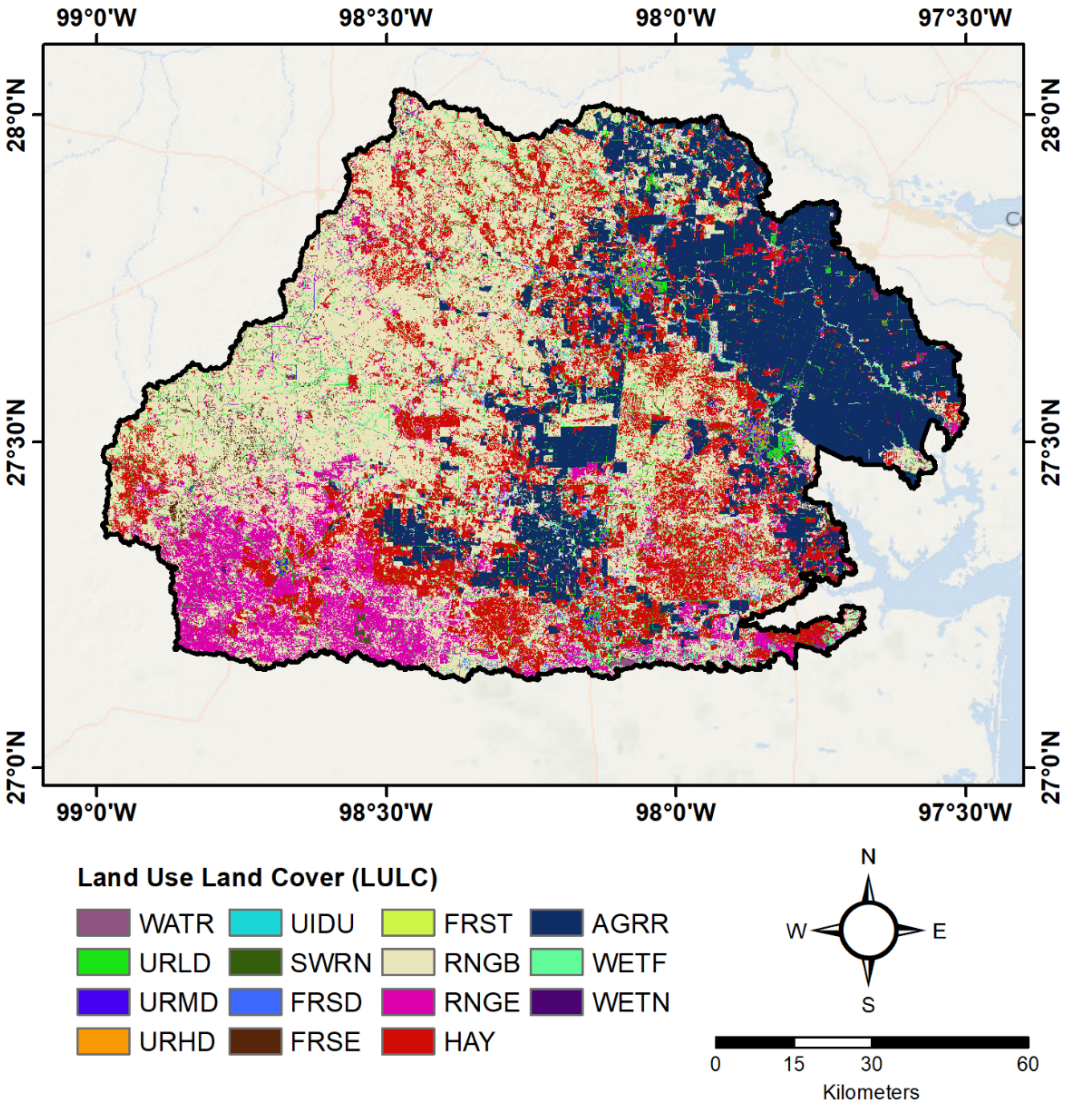

Figure 5. Land cover/land use map of the Baffin Bay watershed.

3.2.4. Climate Data:

The SWAT model requires several input climatic parameters (Grusson et al., 2017). These include rainfall, maximum and minimum temperatures, solar radiation, wind speed, and relative humidity. The spatial distribution of the climatic stations is shown in Figure 6. Given the limited number of the rainfall gauges and their observational gaps with the Baffin Bay watershed, the rainfall data was extracted from the Global Precipitation Measurement Mission (GPM) (Huffman. et al., 2014). Specifically, we employed the Integrated Multi-satellite Retrievals for GPM (IMERG) product, which offers half-hourly precipitation products on grid scale of 0.1° (Huffman et al., 2019). IMERG merges and interpolates satellite precipitation data with estimates from rain gauges to generate high-resolution products with enhanced spatial and temporal resolutions (Hou et al., 2014; Shen and Xiong, 2016). A total of 116 IMERG rainfall stations were used in this study (Figure 6). Maximum and minimum temperature data were collected from 18 stations operated

and maintained by the National Oceanic and Atmospheric Administration (NOAA). As for other climatic variables, such as solar radiation, wind speed, and relative humidity, they were simulated within the SWAT model. Previous studies have demonstrated the accuracy of these simulations in areas with similar climatic and geological settings (Nyeko, 2015; Donmez et al., 2020).

Baffin Bay is characterized by a sub-humid, semi-arid, subtropical climate (Ayers et al., 2021; Cira et al., 2021; Beecraft and Wetz, 2022). The region experiences high temperatures with average summer highs of 33.3 °C and winter lows of 8.3 °C. Rainfall is relatively low with yearly average of 680 mm, and humidity levels are high, averaging around 88%. Evaporation rates in the region are significantly high (Ayers et al., 2021; Cira et al., 2021). Appendix 1 and Appendix 2 provide descriptive statistics for daily temperature and rainfall data, respectively.

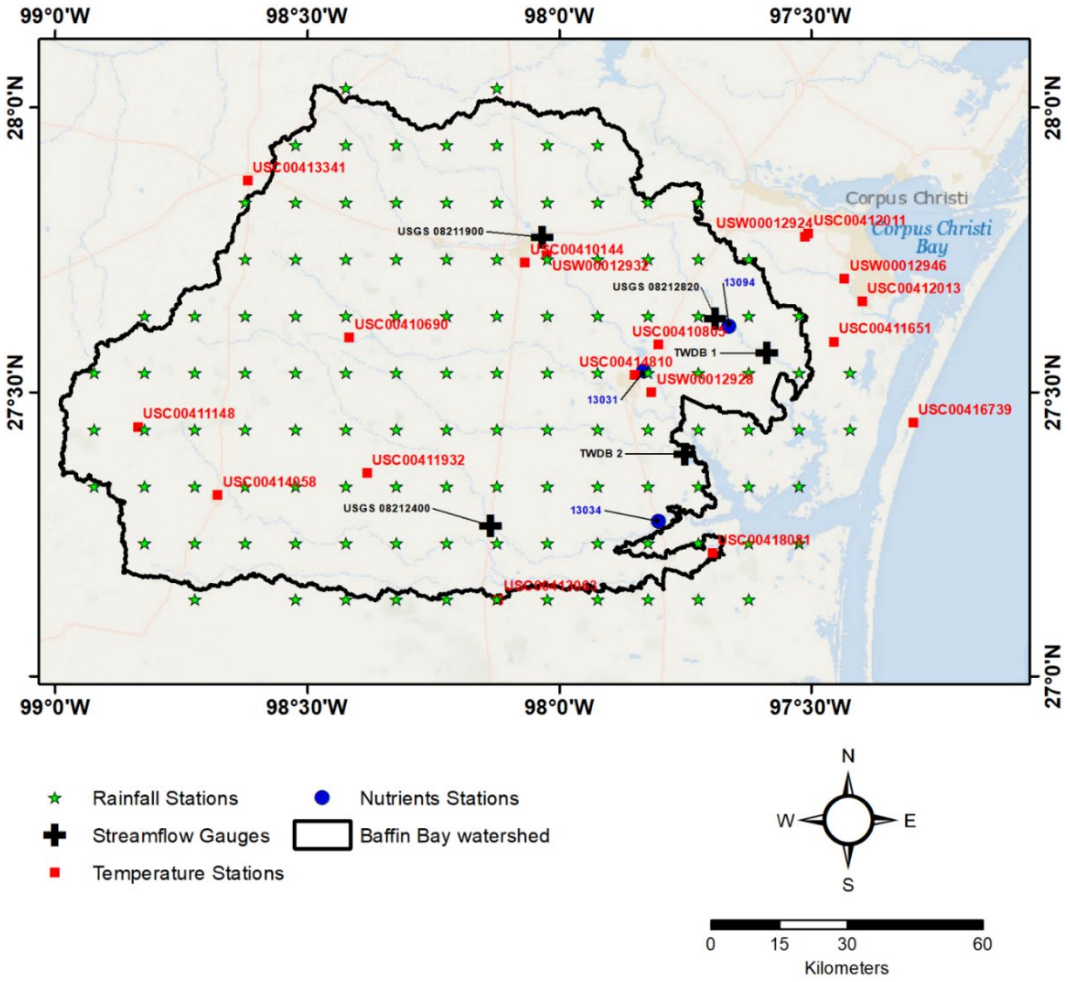

Figure 6. Map showing locations of the rainfall, temperature, streamflow, and nutrient stations.

3.2.5. Streamflow Data:

The calibration and validation of the SWAT model outputs involved the use of daily streamflow data extracted from three United States Geological Survey (USGS) gauges: USGS 08211900, USGS 08212400, and USGS 08212820 (Figure 6). The raw data were initially converted to

monthly averages in cubic meters per second (m^3/s) and then formatted to ensure compatibility with the SWATCUP model platform.

In addition to the USGS gauges, modeled data from two Texas Water Development Board (TWDB) locations were also used in SWAT calibration and validation (Figure 6). The TWDB data comprises five key components: gauged flow, modeled flow, diverted flow, return flow, and freshwater inflow (TWDB coastal hydrology website). The gauged flow data corresponds to the flow measurements obtained from the USGS flow gauges. The return flow component was employed as a point source within the watershed, while the modeled flow output was used for calibrating our SWAT-derived streamflow outputs. The freshwater inflow is calculated by adding the gauged, modeled, and return flows then subtracting the diverted flow (TWDB coastal hydrology website).

Statistics for streamflow data from USGS and TWDB are shown in Table 4. The USGS 08212820 gauge has 209 missing data. Examination of Table 4 indicated typical characteristics of an arid watershed, with approximately 75% of the recorded streamflow falling below 0.49 m^3/s. Notably, within the USGS 08211900 gauge record, stream low rates exceeded 4 m^3/s in only 5 out of 216 monthly measurements. Similarly, for both the USGS 08212820 and USGS 08212400 gauge records, there were only 4 measurements where streamflow rates surpassing 1 m^3/s. These observations highlight the arid to semi-arid nature of the Baffin Bay watershed, characterized by infrequent occurrence of extreme rainfall events associated with storms or hurricanes (Cira et al., 2021; Beecraft and Wetz, 2022).

Table 4. Streamflow data (m^3/s) statistics by station.

Station ID	**USGS 08211900**	**USGS 08212400**	**USGS 08212820**	**TWDB 1**	**TWDB 1**
Number of data points	216	216	31	240	202
Temporal coverage	1/1/2001 - 12/1/2018	1/1/2001 - 12/1/2018	6/1/2018 - 12/1/2020	1/1/2001 - 12/1/2020	1/1/2001 - 12/1/2020
Missing data as a percentage of the temporal record (%)	10	10	87	0	16
Mean	0.49	0.08	0.77	1.74	0.88
Standard Error	0.13	0.03	0.36	0.17	0.12
Median	0.04	0.00	0.04	0.87	0.23
Mode	0.04	0.00	-	-	0.01
Standard Deviation	1.89	0.40	2.03	2.68	1.70
Sample Variance	3.57	0.16	4.10	7.20	2.90
Kurtosis	47.47	58.53	12.08	38.54	23.12
Skewness	6.56	7.27	3.53	5.11	4.25

Range	16.72	3.88	9.03	27.44	13.72
Minimum	0.00	0.00	0.01	0.09	0.00
Maximum	16.72	3.88	9.04	27.53	13.72
Sum	106.84	16.69	23.96	416.55	176.83

3.2.6. Nutrient Data:

Nutrient data were primarily collected from groundwater and surface water sources within Baffin Bay watershed. Three nutrient stations (13031, 13452, and 13094; Figure 6) extracted from the Texas Commission on Environmental Quality (TCEQ), were utilized in this study. Surface Water Quality Monitoring (SWQM) program were used to extract the nutrient data utilized in this study (https://www.tceq.texas.gov/waterquality/monitoring). The collected data at these stations represents the total nitrate concentration (expressed in mg/L as N). All stations' records have significant gaps (Table 5).

To estimate the constituent loads of nitrogen, the LOADEST software was employed (Runkel et al., 2004). The rating curve regression-based technique (Stenback et al., 2011) that relates streamflow rate measurements to corresponding nutrient concentrations was utilized. Daily streamflow data, in conjunction with the rating curve, were used to obtain the estimated nitrogen loads at each location.

The availability of nutrient data during the modeling period (2001-2020) was highly limited. Furthermore, when data was available, it was irregularly concentrated on specific months while lacking information for other months. As a result of the scarcity of nutrient data, with up to 92% missing data as shown in Table 5, and the exceptionally low flow rate in the Baffin Bay watershed, the outputs generated from LOADEST were considered insignificant. Consequently, the decision was made to refrain from calibrating the nutrient outputs derived from SWAT.

Table 5. Nutrient data statistics by station.

Station ID	**13031**	**13034**	**13094**
Number of measurements	19	17	19
Temporal coverage	2002-2020	2018-2020	2002-2020
Missing data as a percentage of the temporal record (%)	92	93	92
Mean	2.08	3.07	0.59
Standard Error	0.41	1.93	0.25
Median	1.57	0.025	0.30
Mode	N/A	0.025	0.025
Standard Deviation	1.78	7.96	1.10
Sample Variance	3.18	63.41	1.20
Kurtosis	1.69	7.84	13.35

Skewness	1.32	2.85	3.50
Range	6.80	29.18	4.78
Minimum	0.027	0.025	0.025
Maximum	6.83	29.2	4.8
Sum	39.44	52.12	11.19

3.3. SWAT Model:

3.3.1. Overview:

The SWAT model functions on a daily time scale and is designed to assess the impacts of land use and management practices on water, sediment, and agricultural chemical yields at the watershed scale (Arnold et al., 2012). SWAT employs a process-based approach and is computationally efficient, enabling continuous simulations over extended time periods (Gassman et al., 2007; Neitsch et al., 2011). SWAT has been extensively used to quantify spatial and temporal variations in water, sediment, and nutrient loads for several watersheds across the globe (Lam et al., 2012; Woznicki and Nejadhashemi, 2013; Zhu and Li, 2014; Abbaspour et al., 2015; Verma et al., 2015; Her et al., 2017; Uniyal et al., 2023; Aloui et al., 2023).

Within the SWAT framework, the watershed is divided into several subbasins. These subbasins were subsequently subdivided into hydrologic response units (HRUs), characterized by their homogeneity in terms of land use, management practices, topography, and soil attributes (Li et al., 1977; Arnold et al., 2012; Her et al., 2015).

The simulation of watershed hydrology in SWAT is divided into two distinct phases (Arnold et al., 2012) (Figure 7). The land phase regulates the quantification of water, sediment, nutrient, and pesticide loads that enter the primary channel within each subbasin. On the other hand, the in-stream or routing phase encompasses the movement of water, sediments, and other constituents through the interconnected channel network of the watershed, eventually reaching the outlet (Arnold et al., 2012). The governing equations of the watershed hydrological components are presented thoroughly in the theoretical documentation of SWAT (Neitsch et al., 2011).

The SWAT-simulated runoff, sediments, and agricultural chemical yields from all subbasin and HRUs are aggregated to the main reach of the subbasin and routed through the channel network to the outlet(s) of the main catchment (Bieger et al., 2015). The hydrologic cycle as simulated by SWAT is based on the water balance equation:

$$SW_t = SW_0 + \sum_{i=1}^{t}\left(R_{day} - Q_{surf} - E_a - W_{seep} - Q_{gw}\right) \quad (1)$$

where SW_t is the final soil water content, SW_0 is the initial soil water content on day i, t is the time, R_{day} is the amount of precipitation on day i, Q_{surf} is the amount of surface runoff on day i, E_a is the amount of evapotranspiration on day i, W_{seep} is the amount of water entering the vadose zone from the soil profile on day i, and Q_{gw} is the amount of return flow on day i.

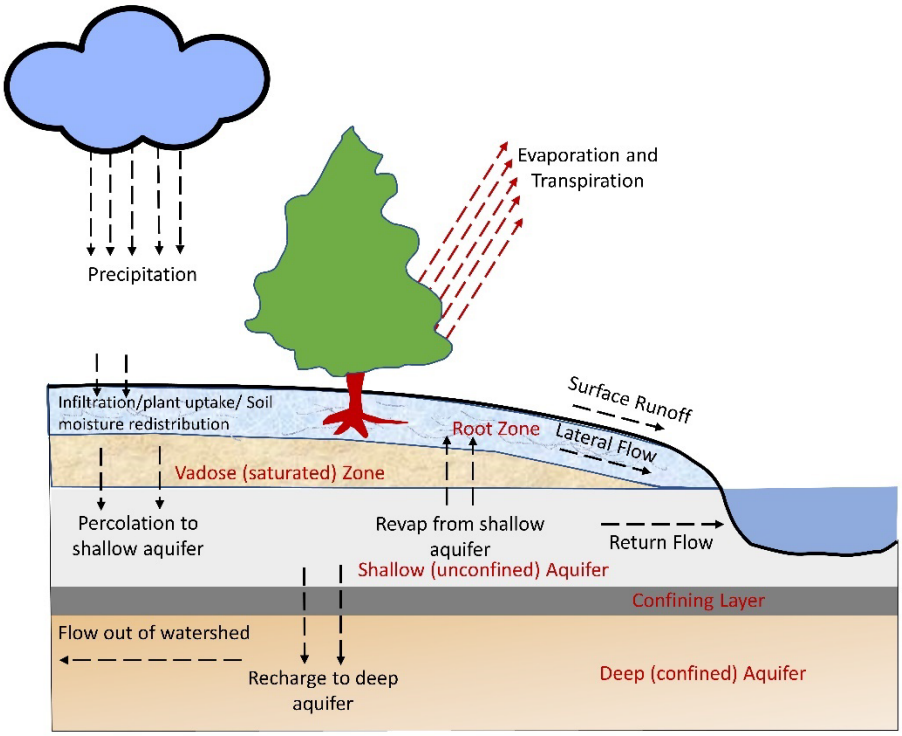

Figure 7. Watershed hydrology within the SWAT model (modified from ArcSWAT (ver. 2012.10_6.24).

As precipitation descends, it may be intercepted and held in the vegetation canopy or fall to the soil surface. Water on the soil surface will infiltrate into the soil profile or flow overland as runoff. Runoff moves relatively quickly toward a stream channel and contributes to short-term stream response. Infiltrated water may be held in the soil and later evapotranspired or it may slowly make its way to the surface-water system via underground paths. Water routed through channels to the main watershed outlets is generated from direct surface runoff, lateral soil flow, baseflow from groundwater storage, and tile flow (Shao et al., 2019). These flow components contribute to the catchment water yield that is defined as the net water volume leaving the HRU and entering a reach at the subbasin level into the main channel, as follows:

$$WYLD = Q_{surf} + Q_{lat} + Q_{gw} + Q_{tile} - T_{loss} \quad (2)$$

where $WYLD$ is the water yield, Q_{surf}, Q_{lat}, and Q_{gw} are the surface runoff, soil lateral flow, and return flow from the shallow aquifer to the main channel, respectively, Q_{tile} is the tile flow, and T_{loss} represents the losses from the tributary in the HRU via transmission through the riverbed.

SWAT provides three methods to simulate daily potential evapotranspiration (PET) at the HRU scale, namely the Penman-Monteith (Monteith, 1965), the Priestley-Taylor (Priestley and Taylor, 1972) , and the Hargreaves methods (Hargreaves et al., 1985). Between the three approaches, the Penman-Monteith equation is considered the most suited to estimate PET, as it explicitly separates the effects of climate and land cover properties on each of the evapotranspiration components

(Sarrazin et al., 2018; Ollivier et al., 2021). This method is represented as follows (Neitsch et al., 2011):

$$\lambda E = \frac{\Delta .(H_{net}-G)+\rho_{air} .c_p .[e_z^o-e_z]/r_a}{\Delta+\gamma .(1+r_c/r_a)} \quad (3)$$

where λE is the latent heat flux density, λ is the latent heat of vaporization, E is the depth rate evaporation, Δ is the slope of the saturation vapor pressure-temperature curve (de/dT), H_{net} is the net radiation, G is the heat flux density to the ground, ρ_{air} is the air density, c_p is the specific heat at constant pressure, e^o_z is the saturation vapor pressure of air at height z, e_z is the water vapor pressure of air at height z, γ is the psychometric constant, r_c is the plant canopy resistance, and r_a is the diffusion resistance of the air layer.

The soil surface runoff is estimated from precipitation using the modified Soil Conservation Service Curve Number (SCS-CN) approach. The SCS-CN approach simulates cumulative surface runoff based on cumulative precipitation and soil retention properties for daily time step (Bacopoulos et al., 2017; Campbell et al., 2018; Tan et al., 2020). Surface runoff is estimated with the SCS-CN procedure as follows (Thomas et al., 2021):

$$Q_{surf} = \frac{(R-I_a)^2}{(R-I_a)+S} \quad (4)$$

where Q_{surf} is the accumulated runoff, R is the total precipitation, I_a is the initial water abstraction prior to runoff due to surface storage interception and infiltration (generally approximated as 0.2S, but can vary with the soil type), and S is the soil moisture retention parameter.

The soil retention parameter (S) varies temporally with the changes in moisture content, and spatially in function of the soil type, land use, and management practices. It can also be assumed to vary with the accumulated plant evapotranspiration. The retention parameter is expressed as a function of the daily curve number (CN) of the antecedent moisture condition-II (AMC-II) for a given land use/cover and hydrological soil group as follows (Thomas et al., 2021):

$$S = \frac{25{,}400}{CN} - 254 \quad (5)$$

Water transmission losses can occur through the side and bottom of the river channels and enter the bank storage or the deep aquifer. Transmission losses are estimated as follows (Holvoet et al., 2008):

$$T_{loss} = K_{ch} . L_{ch} . P_{ch} . TT \quad (6)$$

where T_{loss} represents the channel transmission losses, K_{ch} is the effective hydraulic conductivity of the channel alluvium, L_{ch} is the channel length, P_{ch} is the wetted perimeter in the channel, and TT is the flow travel time.

In the original SWAT, sediment yield is estimated with the MUSLE method which can be depicted in the following general form (Williams, 1995):

$$sed = 11.8\left(Q * q_{peak} * Area_{hru}\right)^{0.56} . K_{USLE} . C_{USLE} . P_{USLE} . LS_{USLE} . CFRG \quad (7)$$

where *sed* is the soil loss; *Q* is the volume of surface runoff; q_{peak} is the peak flow rate; $Area_{hru}$ is the area of an HRU; and K_{USLE}, C_{USLE}, P_{USLE} and LS_{USLE} are the soil erodibility, crop management, conservation practice, and topography factors, respectively. *CFRG* is the coarse fragment factor. Additional details about sediment estimation module can be found in (Shi and Huang, 2021).

In SWAT model, the organic nitrogen (N) and phosphorus (P) and the nitrate and soluble P that are transported in the surface runoff are calculated as:

$$ER_i = 0.78\left(conc_{sed,surq}\right)^{-0.2468} \quad (8)$$

$$ORG_i = 0.001 * \frac{sed}{Area_{hru}} * Con_i * ER_i \quad (9)$$

$$NO_{3,surf} = \beta_{NO3} * conc_{NO3,mobile} * Q \quad (10)$$

$$P_{surf} = \frac{P_{solution} * Q}{\rho_b * H_0 * k_d} \quad (11)$$

where ER_i is defined as the enrichment ratio of organic nutrient *i* (N or P) (dimensionless); ORG_i is the loss of organic nutrient *i*; Con_i is the concentration of original soil nutrient *i*; $conc_{sed,surq}$ is the concentration of sediment in the runoff; P_{surf} and $NO_{3,surf}$ are the soluble phosphorus and nitrate migrated into the runoff, respectively; $P_{solution}$ and $conc_{NO3,mobile}$ are the concentration of phosphorus and nitrate, respectively, in the mobile water of the top soil of 10 mm; β_{NO3} and k_d are the nitrate percolation and phosphorus soil partitioning coefficient, respectively; ρ_b is the dry soil bulk density; and H_0 is the depth of the surface soil layer (Williams and Hann, 1978; Neitsch et al., 2011).

3.3.2. Model Setup:

In this study, the ArcSWAT version 2012.10_6.24 was employed within the ArcGIS platform. Figure 8 provides a visual representation of the inputs, outputs, and processes involved in the SWAT model simulations. The automatic watershed delineation feature was used to define streams and generate the stream network. The outlets were automatically designated and subsequently edited, employing a threshold of 2.5 km. Additional outlets were added near the gauges used for the latter calibration/validation purposes. For the Baffin Bay watershed, the resulting number of subbasins estimated at 78 (Figure 9). The following step is the HRU definition. This step delineates homogeneous areas within each subbasin based on land use, soil, topographical, and other relevant characteristics. A total of 349 HRUs were delineated within the Baffin Bay watershed (Figure 9). By accurately defining HRUs, ArcSWAT enables a more realistic representation of hydrological processes at a fine spatial resolution, contributing to a comprehensive understanding of water, nutrients, and sediments dynamics within the watershed. The step of writing SWAT input tables is a crucial stage in the modeling process, where various input tables are prepared to provide necessary information for simulating hydrological processes.

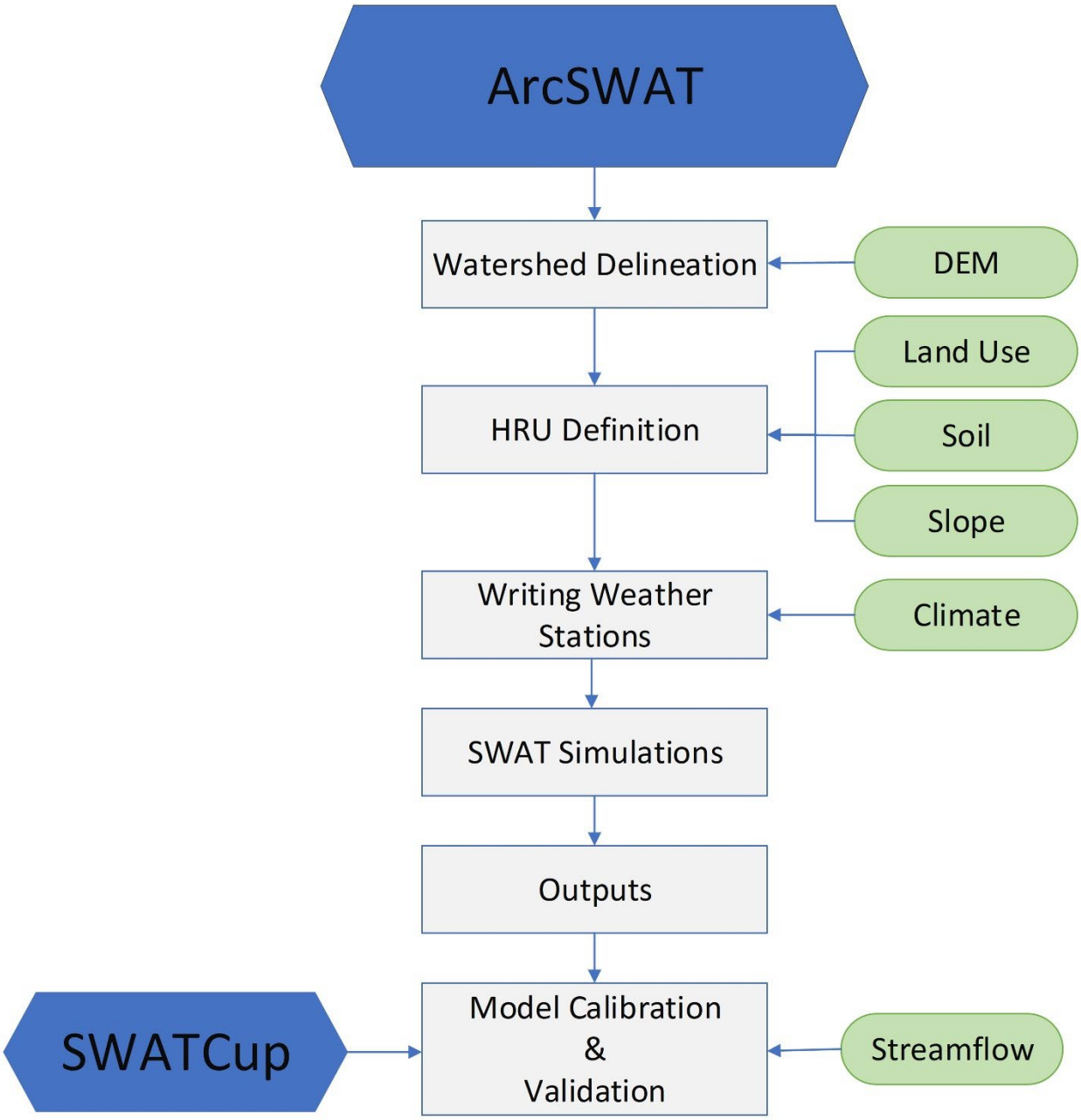

Figure 8. A flow diagram shows platforms (blue), inputs (green), and processes (gray) involved in the SWAT model simulations.

These include land use, soil, management, weather, and channel tables. The land use table defines land cover types and proportions, the soil table describes soil properties, the management table includes land management practices, the weather table contains daily climate data, and the channel table defines channel network characteristics within the watershed. In the process of running SWAT simulations, important configuration parameters such as start and end dates, time steps, and warm-up periods are defined. For this study, the SWAT simulations were performed on a monthly time step from 1998 to 2020, with a warm-up period of three years.

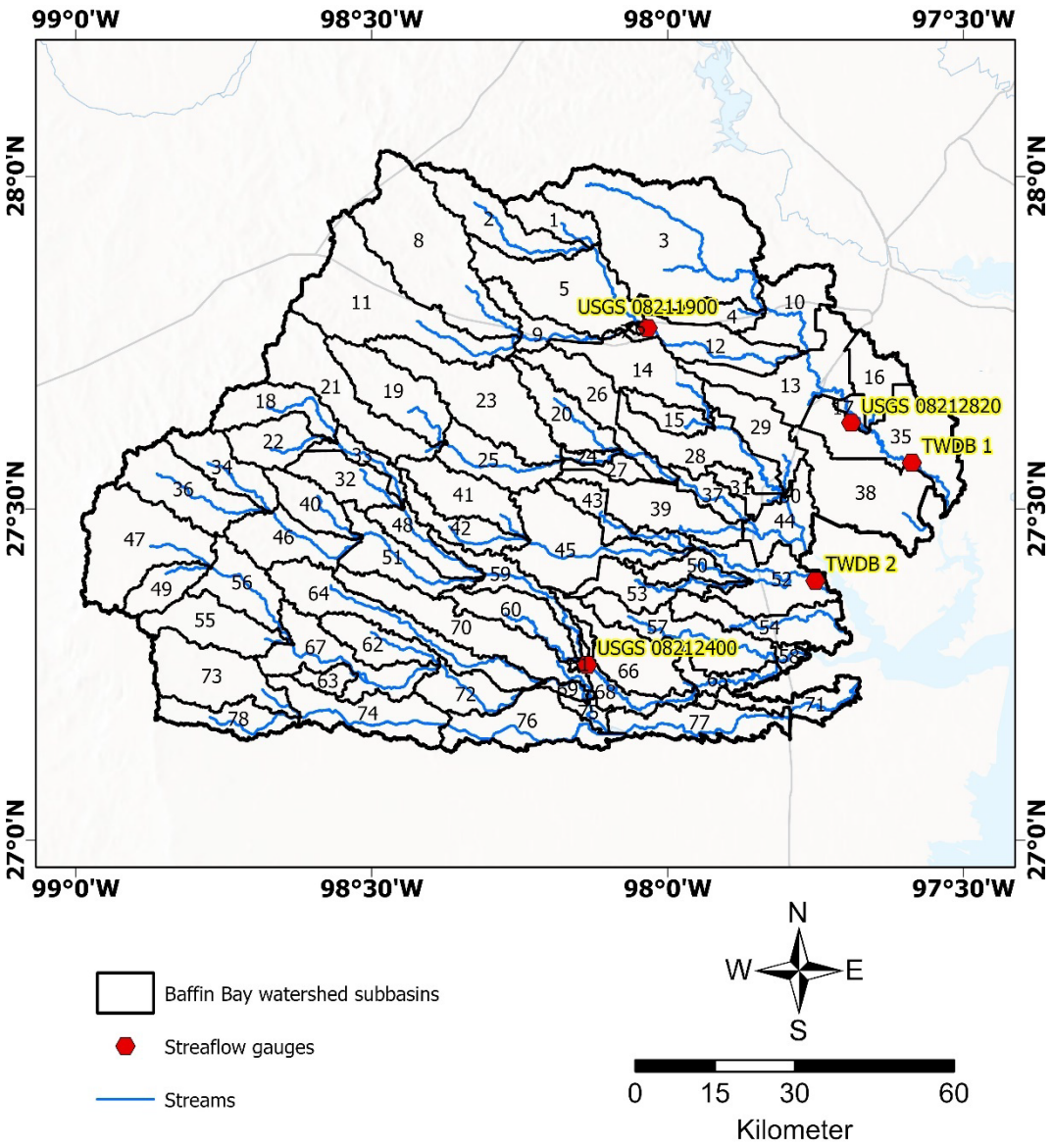

Figure 9. Major subbasins and streams within the Baffin Bay watershed.

3.3.3. Model Calibration and Validation:

The calibration of the SWAT model outputs was conducted using SWAT Calibration and Uncertainty Analysis Program (SWATCUP) software (Abbaspour, 2022). SWATCUP is a widely used tool specifically designed for calibrating and validating SWAT models (Abbaspour et al., 2007; Arnold et al., 2012; Ha et al., 2017; Mengistu et al., 2019). It employs various optimization algorithms to adjust and tune the model parameters and find the best fit between simulated and observed data. The calibration process aims to improve the model's accuracy and reliability in replicating real-world conditions of the watersheds. The SWAT-derived streamflow data were calibrated and validated against streamflow gauges (Table 6).

The SWAT-CUP utilized an auto-calibration technique and the SPE algorithms to discover a parameter set and corresponding values that effectively simulate streamflow. The SPE algorithm

employs two metrics, namely the P-factor and R-factor, to assess the accuracy of capturing observations within the simulated 95 percent prediction uncertainty (95 PPU) band. This band is calculated at the 2.5% and 97.5% levels (Aibaidula et al., 2023). The P-factor represents the percentage of observed data captured by the 95 PPU envelope, ranging from 0 to 1, where 1 signifies a perfect fit. Similarly, the R-factor indicates the width of the 95 PPU band relative to the standard deviation of the observed data, with a range from 0 to infinity. An R-factor of 0 and a P-factor of 1 correspond to a situation where the simulation perfectly matches the observed data (Arnold et al., 2012; Nepal and Parajuli, 2022; Aibaidula et al., 2023).

During the calibration and validation process, the streamflow data were divided in a manner that ensured representation of the entire dataset in both stages. The calibration and validation datasets were selected in blocks, but randomly to ensure an accurate representation of the temporal patterns in the streamflow datasets. Approximately 10 to 12 years of streamflow data were utilized for the calibration process, while an additional 8 to 10 years of data were reserved for model validation (Figure 10). This approach ensures that the calibrated SWAT model is adequately tested against independent data to assess its performance and reliability in predicting streamflow under different conditions (Arsenault et al., 2018; Shen et al., 2022).

During both the calibration and validation periods, various statistical metrics, in addition to P-factor and R-factor, were employed to assess the agreement between the observed and simulated stream flow. These metrics include coefficient of determination (R^2) and Nash–Sutcliffe efficiency (NS) (Arnold et al., 2012; Kouchi et al., 2017; Aibaidula et al., 2023). These metrics provide quantitative measures of the model's performance, capturing aspects such as the magnitude, timing, and variability of the simulated streamflow compared to the observed data (Arnold et al., 2012).

4. Results:

4.1. Streamflow Calibration and Validation:

In order to optimize the objective function in SWATCUP, the calibration process involved adjusting six parameters related to streamflow (Table 6). These parameters include the soil conservation service (SCS) curve number (CN2), available water capacity of the soil layer (SOL_AWC), soil evaporation compensation factor (ESCO), threshold depth of water in the shallow aquifer required for return flow to occur (GWQMN), groundwater re-evaporation coefficient (GW_REVAP), and threshold depth of water in the shallow aquifer for re-evaporation to occur (REVAPMN). These parameters were adjusted for the subbasins that contribute to the stations being considered. For instance, Station USGS 08211900 was associated with subbasins 1, 2, 5, 6, 7, 8, 9, and 11; USGS 08212820 was linked to subbasins 1, 2, 3, 4, 5, 6, 7, 8, 9, 10, 11, 12, and 13; USGS 08212400 was connected to subbasins 18, 22, 32, 33, 34, 36, 40, 46, 48, 51, 59, 60, and 61; TWDB 1 was linked to subbasins 1, 2, 3, 4, 5, 6, 7, 8, 9, 10, 11, 12, 13, 16, 17, and 35; and TWDB 2 was associated with subbasins 41, 42, 43, 45, 50, 52, and 53 (Figure 9). The streamflow-related parameters along with their maximum, minimum, optimal fitted values, and the fitting mechanisms (e.g., replacement, multiplication) are listed in Table 6.

Table 6. SWAT parameters used in streamflow calibration and validation process.

Station ID	Subbasins	Parameter	Fitted Value*	Minimum Value	Maximum Value
USGS 08211900	1, 2, 5, 6, 7, 8, 9, 11	CN2	R (0.33)	0.11	0.35
		SOL_AWC	R (0.16)	-0.03	0.44
		ESCO	V (0.12)	0.05	0.17
		GWQMN	V (3235.90)	2500.00	3600.00
		GW_REVAP	V (0.12)	0.10	0.17
		REVAPMN	V (95.61)	90.00	385.00
USGS 08212820	1, 2, 3, 4, 5, 6, 7, 8, 9, 10, 11, 12, 13	CN2	R (0.14)	-0.20	0.20
		SOL_AWC	R (-0.26)	-0.50	0.50
		ESCO	V (0.13)	0.00	0.20
		GWQMN	V (3698.80)	2500.00	3700.00
		GW_REVAP	V (0.12)	0.07	0.15
		REVAPMN	V (36.30)	0.00	300.00
USGS 08212400	18, 22, 32, 33, 34, 36, 40, 46, 48, 51, 59, 60, 61	CN2	R (-0.18)	-0.54	0.20
		SOL_AWC	R (0.55)	0.40	0.70
		ESCO	V (0.12)	0.00	0.20
		GWQMN	V (4778.50)	4500.00	5000.00
		GW_REVAP	V (0.16)	0.15	0.20
		REVAPMN	V (304.04)	51.00	375.00
TWDB 1	1, 2, 3, 4, 5, 6, 7, 8, 9, 10, 11, 12, 13, 16, 17, 35	CN2	R (-0.01)	-0.09	0.19
		SOL_AWC	R (-0.62)	-0.80	0.13
		ESCO	V (0.04)	0.00	0.20
		GWQMN	V (4887.50)	4500.00	5000.00
		GW_REVAP	V (0.18)	0.14	0.18
		REVAPMN	V (80.89)	15.00	360.00
TWDB 2	41, 42, 43, 45, 50, 52, 53	CN2	R (0.24)	-0.06	0.28
		SOL_AWC	R (-0.28)	-0.80	0.10
		ESCO	V (0.09)	0.00	0.20
		GWQMN	V (4393.00)	4000.00	4600.00
		GW_REVAP	V (0.19)	0.16	0.19
		REVAPMN	V (207.78)	155.00	519.00

**R means multiplication by 1+ given value; V means replacement of parameter value by the given value.*

Table 7 displays the performance metrics of the SWAT model for each streamflow gauge, while Figure 10 illustrates the relationship between the simulated and observed streamflow data at each gauge. The SWAT model performed reasonably well in capturing the streamflow events, especially when it comes to flow timing and frequency. However, the model consistently underestimates the streamflow values, particularly during the relatively high streamflow events, indicating a tendency towards lower predicted flow compared to the observed values.

The P-factor, which represents the accuracy of capturing observations within the simulated 95 PPU band, ranges from 0.22 to 0.74 for the calibration phase and 0.31 to 0.75 for the validate phase. Out of the five gauges, USGS 08212820 and USGS 08212400 have a P-factor greater than 0.6 for both calibration and validation phases. The remaining three gauges exhibit relatively lower P-factor values.

The R-factor, which indicates the width of the 95 PPU band relative to the standard deviation of the observed data, is lower than 1.3 for all stations during both calibration and validation phases. This suggests that the model's simulations closely align with the observed data, as the width of the uncertainty band is relatively small compared to the variability in the observations.

The R^2 values, which measure how well the SWAT model's simulated streamflow data fits the observed streamflow data, are lower than 0.8 for all stations during both calibration and validation phases. This indicates that a reasonable proportion of the observed streamflow variability is captured by the model's simulations. However, USGS 08212400 has an R^2 value of 0 during the calibration phase.

The NS values, which assess the relative agreement between the model's simulated streamflow values and the observed streamflow values, are all lower than 0.75 for all gauges during both calibration and validation phases. This suggests that the model did a fair job in capturing the full temporal variability in the observed streamflow data. It is worth mentioning that USGS 08212400 has an NS value of -0.05 during the calibration phase, while Station TWDB 1 has an NS value of -0.11 during the validation phase.

Table 7. Performance metrics of the SWAT model for both the calibration and validation phases of the stream flow data.

Station	Calibration				Validation			
	P-factor	**R-factor**	**R^2**	**NS**	**P-factor**	**R-factor**	**R^2**	**NS**
USGS 08211900	0.22	0.13	0.23	0.15	0.31	0.21	0.19	0.15
USGS 08212400	0.63	1.28	0	-0.05	0.66	0.63	0.32	0.28
USGS 08212820	0.74	0.3	0.5	0.27	0.75	1.06	0.78	0.72
TWDB 1	0.55	0.39	0.29	0.23	0.31	0.25	0.33	-0.11
TWDB 2	0.55	0.27	0.36	0.23	0.38	0.32	0.4	0.21

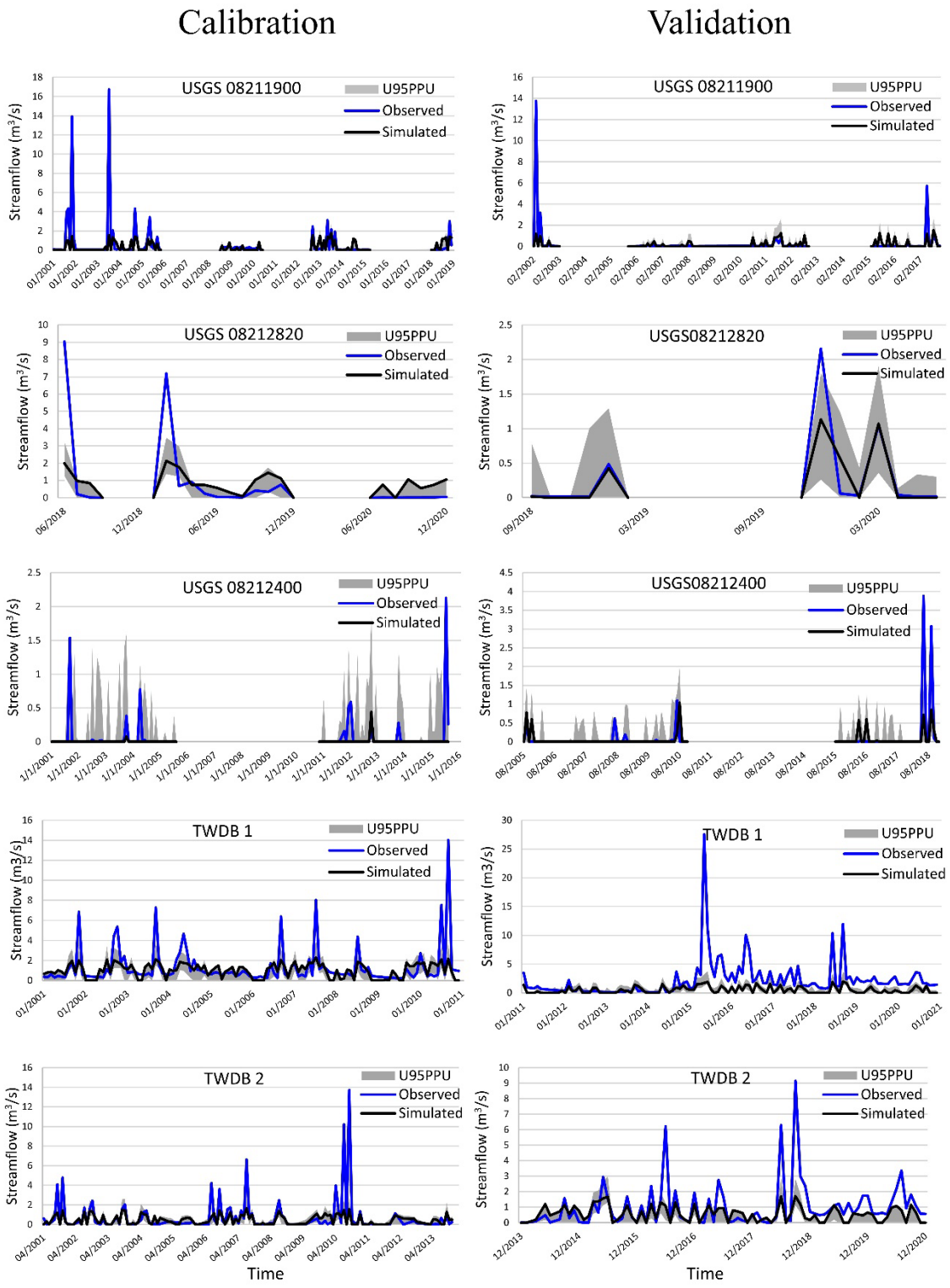

Figure 10. Observed and simulated monthly streamflow data during calibration (left column) and validation (right column) periods for stations USGS 08211900, USGS 08212820, USGS 08212400, TWDB 1, and TWDB 2.

4.2. Spatial and Temporal Variability in Water, Nutrient, and Sediment Yields:

During the investigated period (2001-2020), the Baffin Bay watershed received an average annual precipitation of 686 mm. Of this amount, 165 mm was partitioned as runoff (24% of rainfall), 481 mm as actual evapotranspiration (70% of rainfall), and 37 mm as total recharge (5% of rainfall). The average annual total water yield (Eq. 2) was estimated as 176 mm (26% of rainfall) (Figure 11a). The total sediment yield was estimated at 3000 kg/ha. The nitrate loading to stream in surface runoff is estimated at 0.9 kg/ha, whereas the organic nitrogen and phosphorus were estimated at 5 Kg/Ha and 0.6 kg/ha, respectively (Figure 11b).

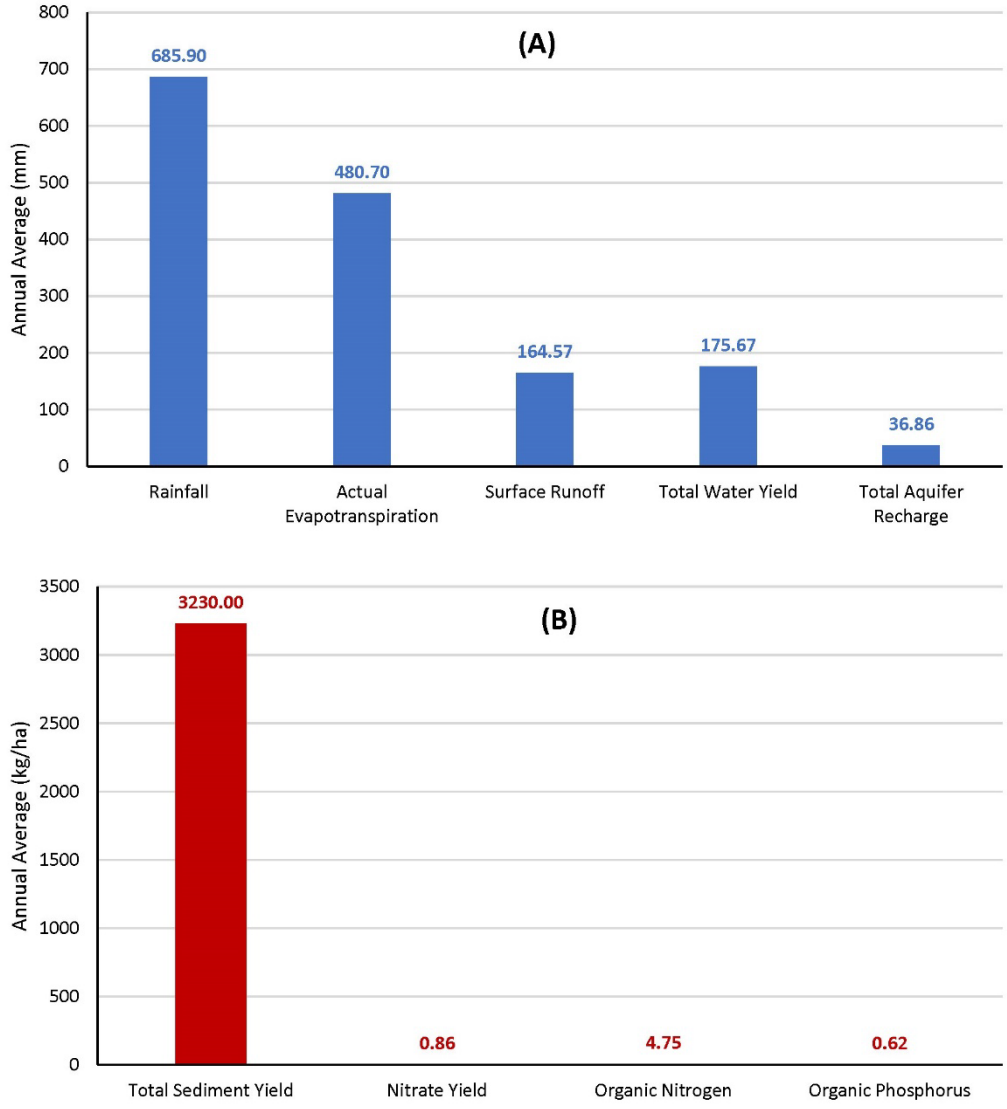

Figure 11. SWAT-derived average annual (a) rainfall, runoff, actual evapotranspiration, recharge, and water yield, (b) sediment, nitrate, organic nitrogen, and organic phosphorus yields over the Baffin Bay watershed.

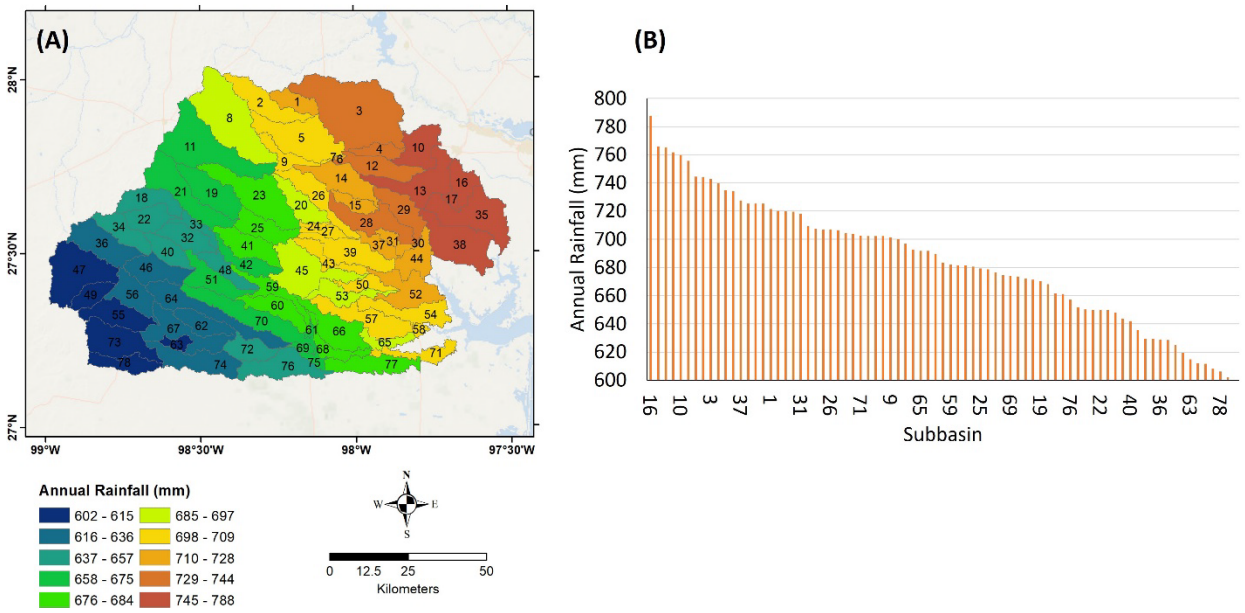

Figure 12. (a) Spatial distribution of average annual rainfall for each subbasin within the Baffin Bay watershed. (b) average annual rainfall by subbasin in a in descending order.

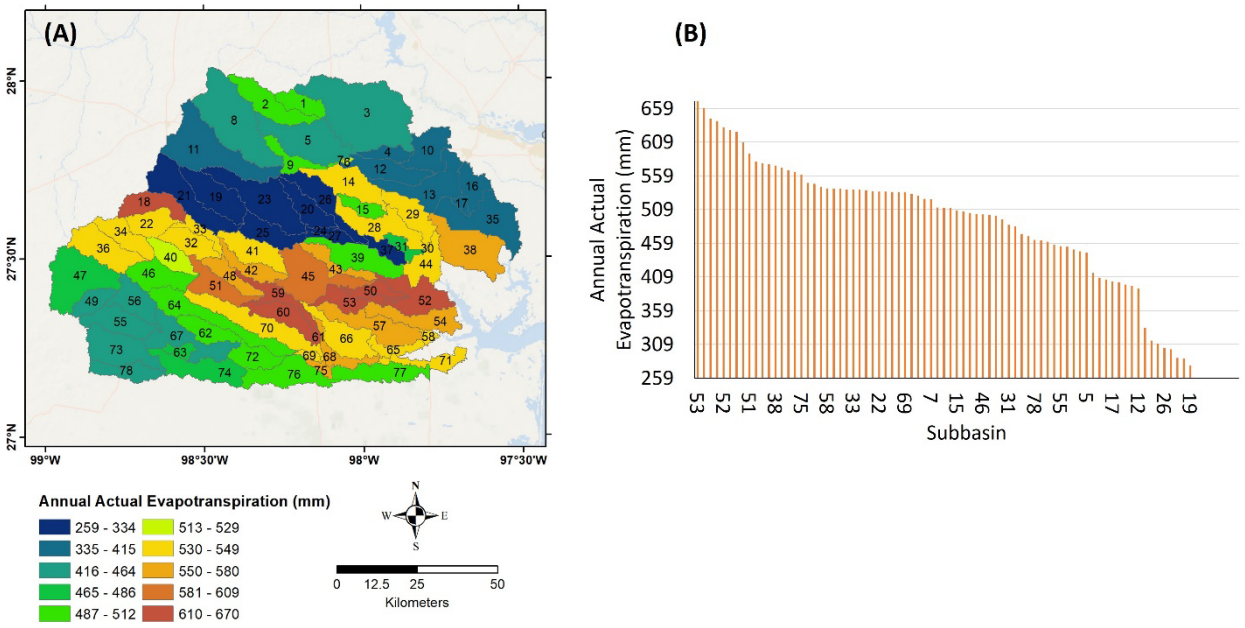

Figure 13. (a) Spatial distribution of SWAT-derived average annual actual evapotranspiration for each subbasin within the Baffin Bay watershed. (b) average annual actual evapotranspiration by subbasin in a in descending order.

SWAT-derived average annual water, sediment, and nutrient yields show spatial variability (Figures 12 to 17). Rainfall increases from the southwestern portions of the watershed towards the northeastern portions (Figure 12a). Subbasins 47, 73, and 78 receive the minimum annual rainfall of 605 mm, while subbasins 16, 17, and 35 receive the maximum amount of annual rainfall of 772 mm (Figure 12 b).

Actual evapotranspiration has a slightly different pattern (Figure 13a). Generally, northern subbasins exhibit relatively lower actual evapotranspiration compared to the southern subbasins. Subbasins 19, 21, and 23 have the minimum annual evapotranspiration of 274 mm, whereas subbasins 18, 53, and 61 have the maximum evapotranspiration of 657 mm (Figure 13b).

In contrast to actual evapotranspiration, Figure 14a shows that runoff exhibits opposite spatial patterns. Northern subbasins have relatively higher runoff values compared to the southern subbasins. For example, subbasins 18, 53, and 61 experience the minimum runoff values of 10.5 mm, while subbasins 21, 23, 26 receive the maximum values of 398 mm (Figure 14b). The spatial variability of total water yield is similar to that of runoff (Figure 15a). Subbasins 18, 53, and 61 receive the minimum total water yield (13 mm), whereas subbasins 21, 23, 26 receive the maximum values (399 mm) (Figure 15b).

Figure 16a shows that subbasins located upstream in the watershed have higher sediment yield values compared to those located downstream. Downstream subbasins (e.g., 51, 53, and 61) witness the minimum sediment values of 100 kg/ha, while upstream subbasins (e.g., 7, 21, and 25) experience the maximum values of 17,700 kg/ha (Figure 16b).

Subbasins located in the northern portions of the watershed receive higher amounts of nitrate compared to those located anywhere else (Figure 17a). For example, subbasins 49, 55, and 73 receive the minimum nitrate value of 0 kg N/ha, while subbasins 20, 26, and 37 receive the maximum values of 4.3 kg N/ha (Figure 17b).

Temporal variabilities in the monthly water yield derived from the SWAT model were observed, as shown in Figure 18. The basin's average rainfall, runoff, actual evapotranspiration, and water yield estimates exhibit a synchronized pattern, where peaks and troughs align in time. In the year 2011, the Baffin Bay watershed experienced the lowest values for rainfall, runoff, actual evapotranspiration, and water yield. Conversely, the year 2015 represents the period with the highest values for these variables (Figure 18). During the simulated period from 2001 to 2020, there were minimal declining trends observed in the rainfall, runoff, actual evapotranspiration, recharge, and water yield estimates. Trends of -5.3 mm/year, -0.8 mm/year, -3.1 mm/year, and -3.4 mm/year were identified for rainfall, actual evapotranspiration, runoff, and water yield, respectively (Figure 18).

Temporal variability of sediment and nutrient yields, as shown in Figure 19, is evident in the SWAT-derived data. The highest average sediment yield for the basin was recorded in 2010, while the lowest occurred in 2008. There was a slight downward trend of -0.08 ton/ha/yr in sediment yield. Nitrate levels reached their peak in 2004 and were at their lowest in 2012. A minor upward trend of 0.01 kg/ha/yr was observed for nitrate. Annual trends in organic nitrogen and organic phosphorus were estimated at -0.18 kg/ha/yr and -0.02 kg/ha/yr, respectively (Figure 19).

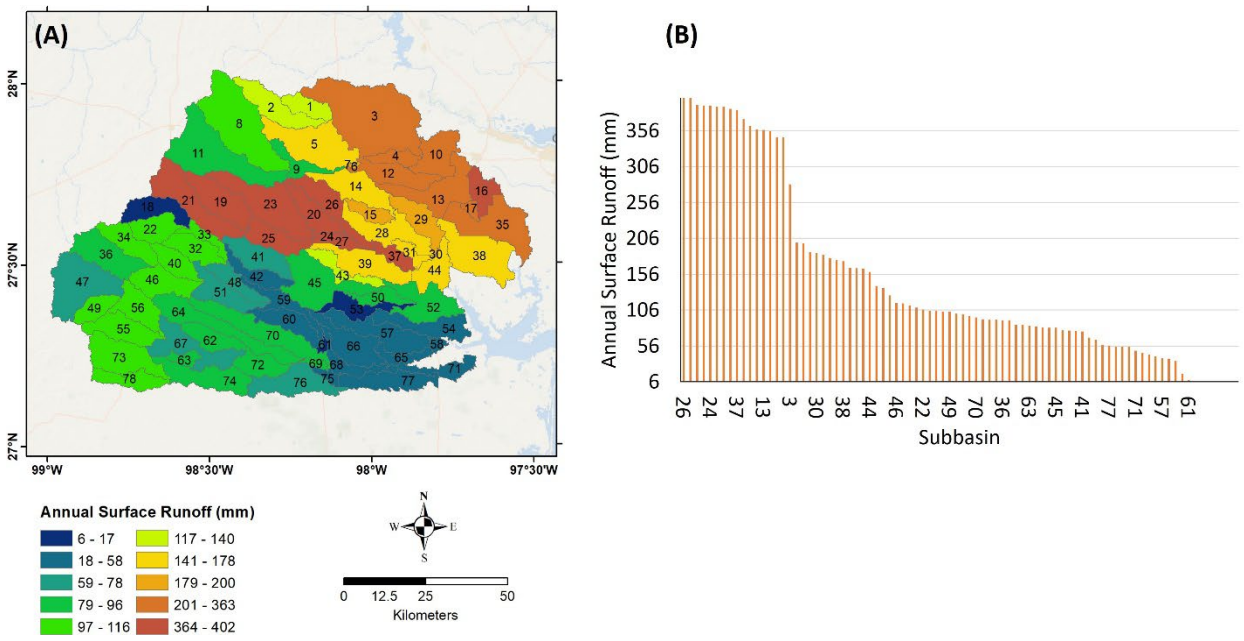

Figure 14. (a) Spatial distribution of SWAT-derived average annual surface runoff for each subbasin within the Baffin Bay watershed. (b) average annual surface runoff by subbasin in a in descending order.

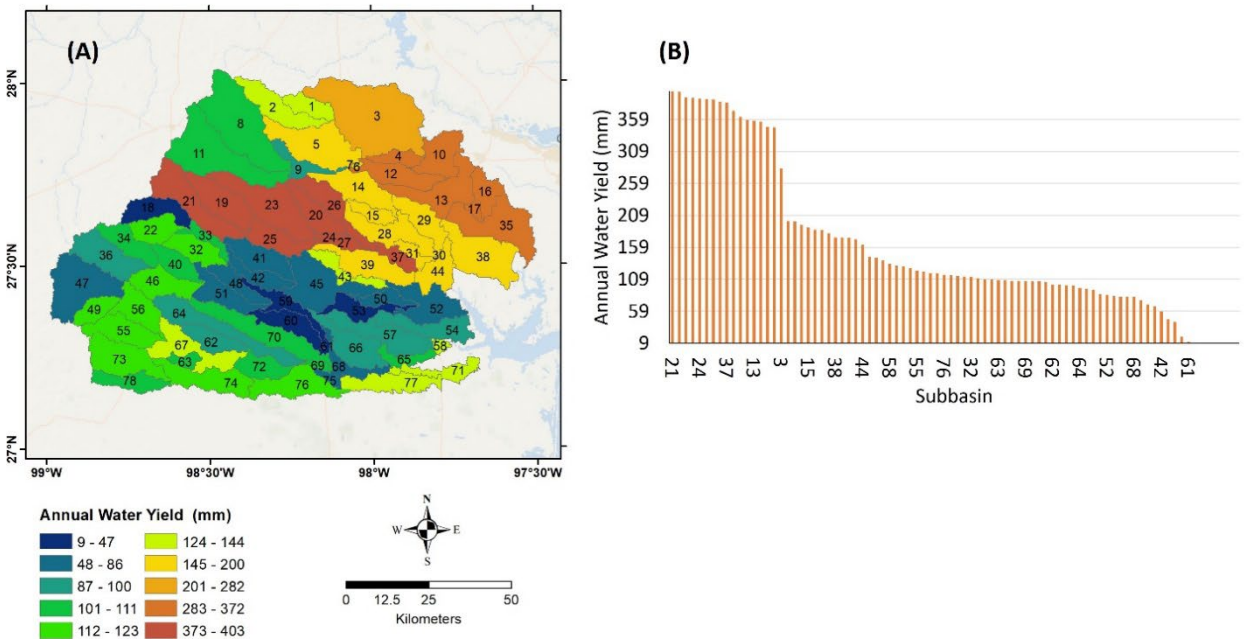

Figure 15. (a) Spatial distribution of SWAT-derived average annual total water yield for each subbasin within the Baffin Bay watershed. (b) average annual total water yield by subbasin in a in descending order.

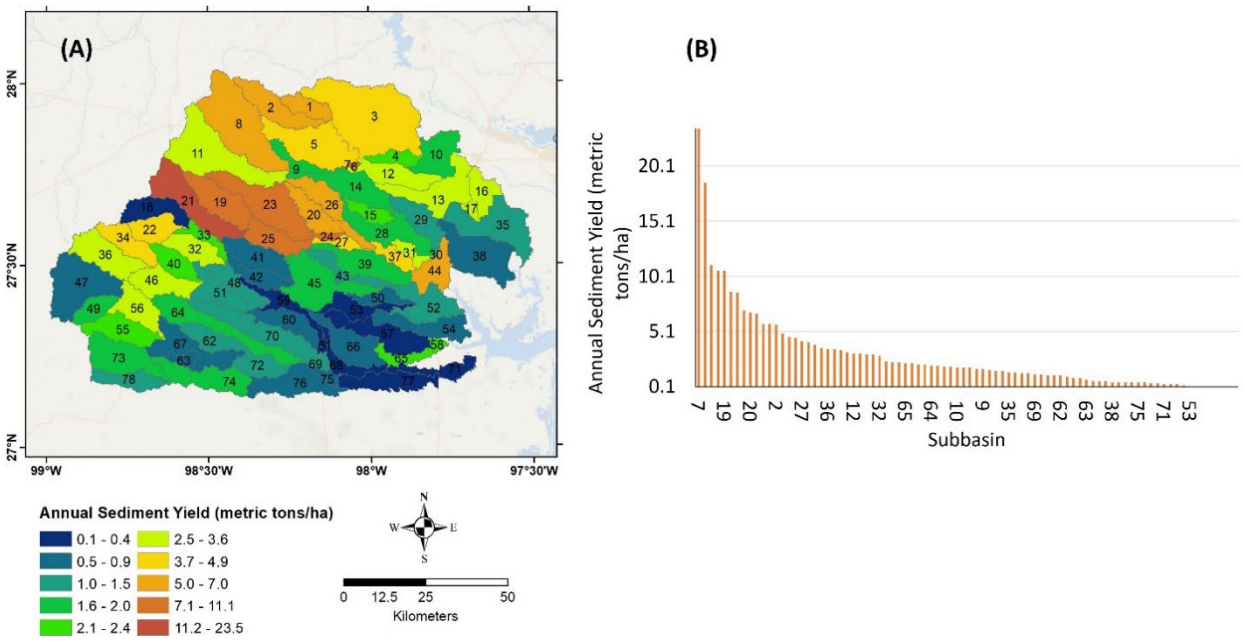

Figure 16. (a) Spatial distribution of SWAT-derived average annual sediment yield for each subbasin within the Baffin Bay watershed. (b) average annual sediment yield by subbasin in a in descending order.

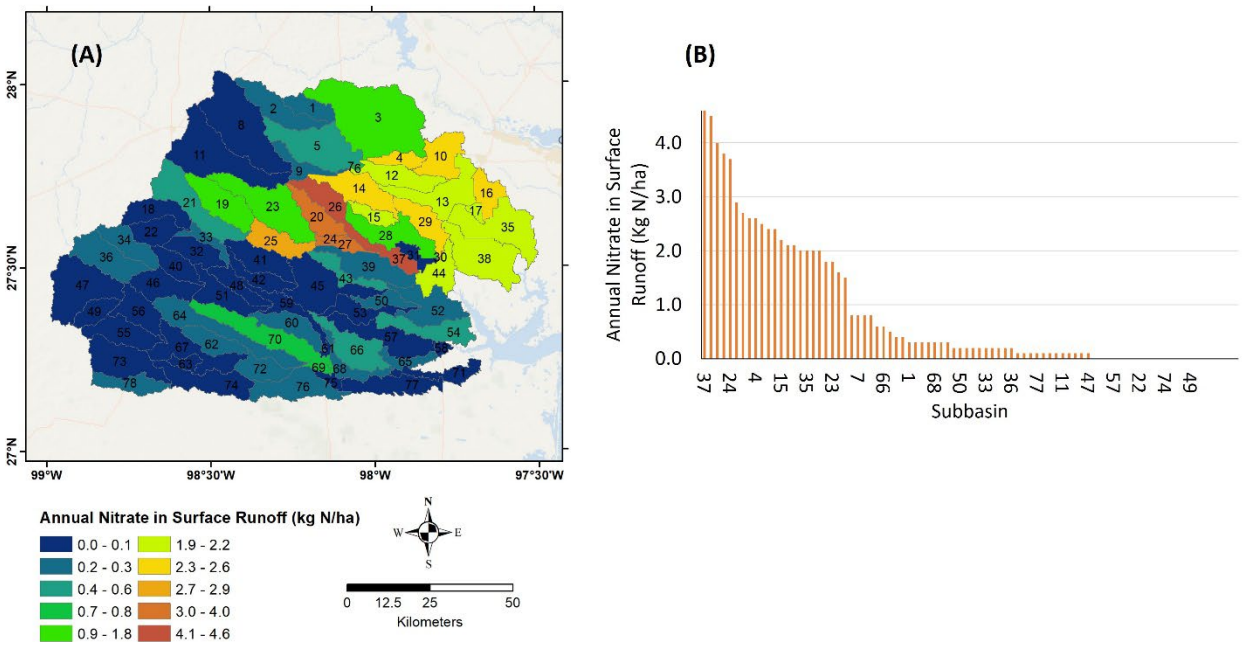

Figure 17. (a) Spatial distribution of SWAT-derived average annual nitrate in surface runoff for each subbasin within the Baffin Bay watershed. (b) average annual nitrate in surface runoff by subbasin in a in descending order.

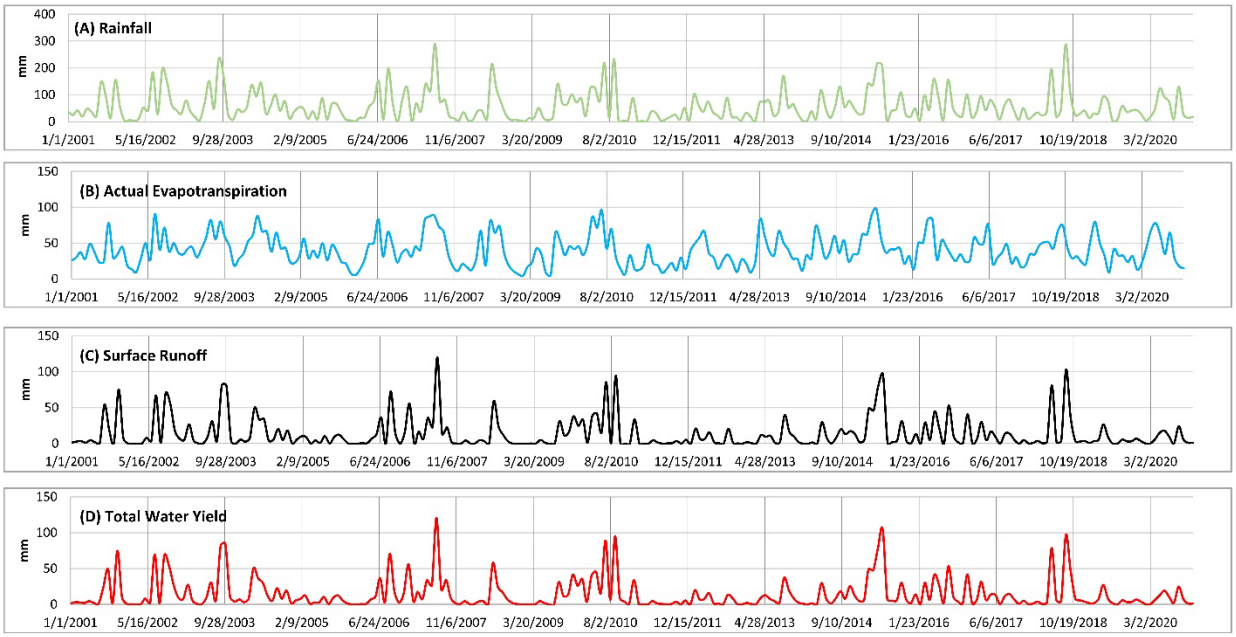

Figure 18. Temporal variations in the SWAT-derived average monthly (a) rainfall, (b) actual evapotranspiration, (c) surface runoff, and (d) total water yield over the Baffin Bay watershed.

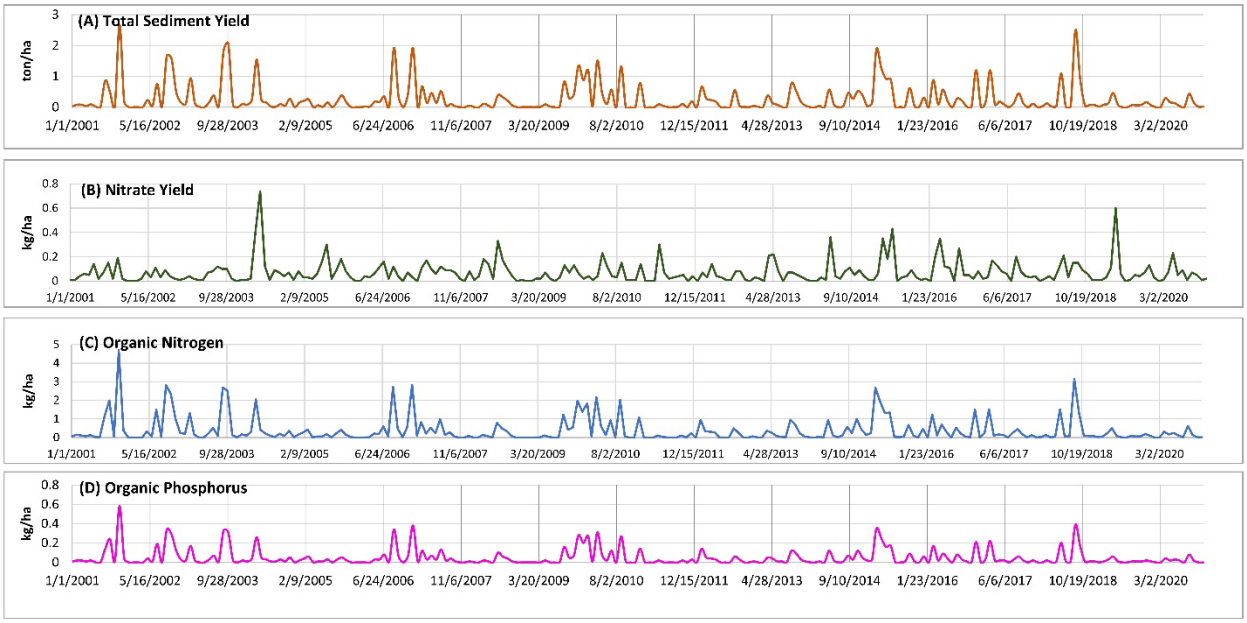

Figure 19. Temporal variations in the SWAT-derived average monthly (a) sediment yield, (b) nitrate yield, (c) organic nitrogen, and (d) organic phosphorus over the Baffin Bay watershed.

5. Discussion:

5.1. Performance of the SWAT Model:

The performance of the SWAT model in the Baffin Bay watershed is controlled by several factors. These include limitations in input data availability, inappropriate location of the calibration gauges, and the hydrological and topographical characteristics of the Baffin Bay watershed.

One of the challenges is the sparse climate data in the Baffin Bay watershed area. There is a lack of sufficient rainfall and temperature gauges, and important data such as wind speed, relative humidity, and solar radiation are not available. Over the entire Baffin Bay watershed (area: 10,047 km^2), only 12 temperature stations are available. These stations have gaps up to 86% of the observed records. The SWAT model relies on robust and extensive input data to accurately simulate hydrological processes, and the lack of data can lead to uncertainties and inaccuracies during model calibration and validation, resulting in relatively low performance (Donmez et al., 2020).

Furthermore, none of the streamflow gauges are located downstream at the intersection of the streams with the Baffin Bay (Figure 6). The upstream location of the stations presents challenges for the model since streamflow at upstream locations is influenced by different factors compared to downstream locations (Noh et al., 2018). The SWAT model may not effectively account for these local characteristics, leading to discrepancies between the simulated and observed streamflow.

The Baffin Bay watershed is situated in an arid climate zone, characterized by limited water availability, low precipitation, and high evapotranspiration rates. The SWAT model's ability to accurately represent hydrological processes such as infiltration, runoff, and groundwater flow becomes challenging in arid basins due to scarce water resources (Nyeko, 2015). Moreover, the unique hydrological processes observed in the Baffin Bay watershed, such as flash floods and intermittent streamflow, may not be adequately captured by the SWAT model since they were most likely missed in input data (e.g., rainfall), further impacting its performance (Wetz et al., 2017).

Lastly, a significant portion of the Baffin Bay watershed consists of relatively flat areas (86% of the basin with slope $\leq 3°$). In the SWAT model, flat basins often struggle to accurately represent slow and diffuse flow as the model assumes a more dominant role of channel flow rather than overland flow. This can lead to underestimation of surface runoff and poor representation of flow pathways (Donmez et al., 2020). Additionally, the absence of pronounced elevation changes in flat basins limits the model's ability to capture the spatial variability of hydrological processes (Donmez et al., 2020).

5.2. Factors Controlling Water, Nutrient, and Sediment Yields:

The Baffin Bay watershed is a typical arid to semi-arid basin that is characterized by limited rainfall rates and infrequent occurrence of extreme rainfall events associated with storms or hurricanes. The SWAT results indicated that runoff tends to increase in subbasins characterized by relatively higher rainfall rates and/or lower evapotranspiration rates (e.g., 3, 4, 10, 12, 13, 16, 17, 19, 20, 21, 23, 24, 25, and 26; Figures 12a, 13a, and 14a). Conversely, subbasins with higher evapotranspiration rates tend to exhibit decreased runoff (e.g., 18, 41, 42 50, 52, 53, 57, 58, 59, and 60; Figures 13a, and 14a). This relationship highlights the influence of evapotranspiration on the amount of water that ultimately contributes to runoff (Nyeko, 2015). The subbasins with lower evapotranspiration experience less water loss through evaporation and plant transpiration, allowing a larger portion of rainfall to contribute to runoff. On the other hand, subbasins with higher evapotranspiration rates exhibit greater water loss, reducing the amount of water available for runoff.

The SWAT-derived runoff rates are influenced by the LCLU patterns. In the Baffin Bay watershed, agricultural lands and urban areas (e.g., subbasins 3, 4, 10, 12, 13, 14, 17, 26, 29, 35, 38, 44, 45, 60, and 70), which make approximately 27% of the LCLU, are predominantly concentrated in the northeastern and central parts of the watershed. These regions witnessed the highest runoff rates, with average annual values ranging from 141 to 402 mm (Figures 5 and 14a). Conversely, the range and hay areas (e.g., subbasins 8, 9, 11, 18, 41, 42, 50, 52, 53, 54, 57, 58, 59, 60, 61, 71, and 77), which contribute about 68% of the LCLU, exhibit lower annual surface runoff rates, ranging from 6 to 96 mm (Figures 5 and 14a).

The soil types also affect the runoff rates. The Victoria, Opelika, Aguiral, and Lattas soil types, which cover approximately 49% of the soil, are primarily composed of fine and fine loamy materials (Table 2). These soils are predominantly found in various subbasins across the watershed, including subbasins 3, 4, 10, 12, 13, 16, 17, 19, 20, 21, 23, 24, 25, 26, 27, 28, 29, 35, 37, and 44 (Figures 4 and 14a). These regions exhibit the highest runoff levels, with an average annual range spanning from 141 to 402 mm. Conversely, subbasins such as 18, 41, 42, 50, 52, 53, 54, 55, 56, 57, 58, 59, 60, 61, 71, 72, 73, and 77 predominantly contain soil types such as Delmita, Palobia, Comitas, and Falfurri, characterized by mixed loamy to fine loamy materials, covering 23% of the soil (Figures 4 and 14a). The subbasins with these soil types experience the lowest levels of runoff, ranging from 6 to 96 mm annually (Figure 14a).

The LCLU significantly controls sediments and nutrient yields in the Baffin Bay watershed. Subbasins within the Baffin Bay watershed that engage in agricultural activities tend to experience higher sediment and nutrient yield compared to those with limited or no such activities (e.g., 3, 4, 10, 12, 13, 16, 19, 20, 21, 23, 24, 25, 26, 27, and 29; Figures 5, 16a, and 17a). The presence of agricultural practices, such as crop cultivation and livestock farming, can contribute to elevated levels of sediment and nutrient runoff (Pionke et al., 2000; Smith et al., 2007)). Agricultural activities involve various soil management practices such as plowing, tilling, and irrigation, which can disturb the soil structure and make it more susceptible to erosion. Rainfall and runoff can transport eroded soil particles, resulting in increased sediment yield (Srinivasan et al., 1993; Zhang, 2016). Along with sediment, agricultural activities often involve the application of

fertilizers and manure to enhance crop growth (Donmez et al., 2020). These fertilizers contain essential nutrients like nitrogen, phosphorus, and potassium. However, when applied in excessive amounts or under improper timing or conditions, these nutrients can be carried away by runoff and contribute to nutrient yield (Donmez et al., 2020).

The sediment yield within the watershed also influenced by the soil types. Subbasins including 1, 2, 3, 5, 8, 19, 20, 21, 22, 23, 24, 25, 26, 34, 36, 40, and 46 (Figures 4 and 16a) exhibited the highest sediment yields, ranging from 3.7 to 23.5 tons per hectare. These subbasins are predominantly covered by Randado, Delmita, Opelika, Aguilare, and Runge soil types, which account for approximately 55% of the watershed area. These soil types are characterized by fine loamy materials. On the other hand, subbasins such as 18, 53, 57, 59, 61, 68, 71, and 77 (Figures 4 and 16a) witnessed the lowest sediment yields, contributing less than 0.4 tons per hectare annually. These subbasins are primarily characterized by Victoria, Palobia, Falfurri, and Comitas soil types, which cover around 32% of the watershed area. These soil types are composed of various materials, including fine, loamy, mixed, active, hyperthermic with varied textures materials.

Soil types also influenced the nutrient yields. Subbasins 4, 10, 12, 13, 14, 15, 16, 17, 120, 24, 26, 27, 37, 65, 38, and 44 (Figures 4 and 17a) exhibited the highest nitrate loads, ranging from 2 to 4.6 kg per hectare. These subbasins are predominantly covered by Victoria, Opelika, and Lattas soil types, which account for approximately 42% of the watershed area. These soil types are characterized by fine loamy and smectitic materials. Conversely, subbasins such as 8, 11, 18, 22, 53, 57, 59, 61, 68, 71, and 77 (Figures 4 and 17a) displayed the lowest nitrate loads, less than 0.1 kg per hectare annually. These subbasins are primarily characterized by Delmita, Palobia, Aguilare, and Falfurri soil types, which cover around 29% of the watershed area. These soil types are composed of various materials, including fine loamy and mixed materials.

It is worth mentioning that the magnitude of sediment and nutrient yield in sub-basins with agricultural activities depends on several factors such as the intensity of farming practices, soil management techniques, type and timing of fertilizer application, and the presence of erosion control measures. Understanding the spatial patterns of nitrate and sediment loads can inform management strategies aimed at reducing pollution and preserving water quality within the watershed. Implementing erosion control measures such as contour plowing, terracing, and buffer strips can help mitigate erosion and reduce sediment and nutrient yield within the Baffin Bay watershed. Subbasins that witness higher sediment and nutrient yields (e.g., Figures 16a and 17a) might be used as a start point.

During the simulated period, there were no significant trends in rainfall rates over the Baffin Bay watershed. However, changes in climate patterns, including increased precipitation or extreme weather events, can impact water, nutrient, and sediment yields in the Baffin Bay watershed. Sustainable land management practices are essential for mitigating the effects of climate change on nutrient and sediment yields. Subbasins that witness higher rainfall and water yields (e.g., Figures 12a and 15a) might be used as a start point.

6. Conclusions and Recommendations:

6.1. Conclusions

The SWAT model was developed specifically for quantifying water, sediment, and nutrient yields in the Baffin Bay watershed. To create the SWAT model, a comprehensive dataset was utilized, including various inputs such as a DEM obtained through LiDAR technology, soil data from sources like SSURGO and SATSGO, land cover/land use data from the NLCD, precipitation data from the GPM project, air maximum and minimum temperatures from NOAA, relative humidity, wind speed, and solar radiation. The SWAT model simulation was conducted for a 20-year period, covering the years 2001 to 2020. During the development of the SWAT model, in-situ streamflow data from three USGS stations and two TWDB model outputs were utilized for calibration and validation purposes. Six model parameters were selected for updates throughout the calibration and validation phases. To assess the accuracy of the model's results compared to measured data, metrics such as the P-factor, R-factor, R^2, and NS were employed as indicators of the goodness of fit.

The results of the SWAT model indicated that it performed reasonably well in simulating streamflow within the Baffin Bay watershed, with P-factor values ranging from 0.22 to 0.75, R-factor values ranging from 0.13 to 1.28, R^2 values ranging from 0 to 0.78, and NS values ranging from -0.11 to 0.28. It was observed that the model's performance was primarily influenced by factors such as limitations in data availability, the placement of calibration gauges, and the hydrological and topographical characteristics specific to the Baffin Bay watershed.

Based on the model simulations, the average annual precipitation, surface runoff, actual evapotranspiration, and total recharge for the watershed were estimated to be 686 mm, 165 mm (24% of rainfall), 481 mm (70% of rainfall), and 37 mm (5% of rainfall), respectively. Moreover, the average annual total sediment and nitrate loadings (in surface runoff) were estimated to be 3000 kg/ha and 0.9 kg/ha, respectively. The spatial variations in water yield were found to be primarily influenced by rainfall and evapotranspiration patterns as well as LCLU and soil types. The sediment and nutrient loading, however, were mainly controlled by changes in LCLU and soil types.

6.2. Recommendations

To establish a robust monitoring system for tracking the influx of terrestrial freshwater, nutrients, and sediment into Baffin Bay, it is strongly advised to augment the existing monitoring infrastructure by installing supplementary gauges at strategic downstream locations throughout the watershed. In addition to the downstream locations, the SWAT-derived spatial variability in water, sediment, and nutrient yields (e.g., Figures 15a, 16a, and 17a) could be used to map additional optimal locations for these monitoring gauges. When determining the locations for monitoring activities, subbasins or areas that experience higher yields of water, sediment, and nutrients should be given priority. These additional monitoring activities would serve multiple purposes in enhancing data collection, better calibrating and validating the SWAT results, and improving our understanding of the watershed's dynamics.

The installation of additional monitoring gauges is crucial for achieving a comprehensive understanding of the freshwater, nutrient, and sediment dynamics in the Baffin Bay watershed. It allows for a more accurate validation and calibration of the SWAT model, and better assessment of the overall health and sustainability of the ecosystem. Moreover, the collected data serves as a valuable resource for decision-making, enabling policymakers, researchers, and water resource managers to develop targeted strategies for mitigating pollution, improving water quality, and ensuring the long-term ecological integrity of Baffin Bay.

7. References:

Abbaspour, K.C., 2022, User manual for SWATCUP-2019/SWATCUP-Premium/SWATplusCUP Calibration and Uncertainty Analysis Programs. 2w2e Consulting GmbH Publication, Duebendorf, Switzerland:

Abbaspour, K.C., Rouholahnejad, E., Vaghefi, S., Srinivasan, R., Yang, H., and Kløve, B., 2015, A continental-scale hydrology and water quality model for Europe: Calibration and uncertainty of a high-resolution large-scale SWAT model: Journal of Hydrology, v. 524, p. 733–752, doi:10.1016/j.jhydrol.2015.03.027.

Abbaspour, K.C., Vejdani, M., and Haghighat, S., 2007, SWAT-CUP calibration and uncertainty programs for SWAT, *in* MODSIM07 - Land, Water and Environmental Management: Integrated Systems for Sustainability, Proceedings,.

Aibaidula, D., Ates, N., and Dadaser-Celik, F., 2023, Uncertainty analysis for streamflow modeling using multiple optimization algorithms at a data-scarce semi-arid region: Altınapa Reservoir Watershed, Turkey: Stochastic Environmental Research and Risk Assessment, doi:10.1007/s00477-022-02377-x.

Akoko, G., Le, T.H., Gomi, T., and Kato, T., 2021, A review of swat model application in africa: Water (Switzerland), v. 13, doi:10.3390/w13091313.

Aloui, S., Mazzoni, A., Elomri, A., Aouissi, J., Boufekane, A., and Zghibi, A., 2023, A review of Soil and Water Assessment Tool (SWAT) studies of Mediterranean catchments: Applications, feasibility, and future directions: Journal of Environmental Management, v. 326, p. 116799, doi:10.1016/J.JENVMAN.2022.116799.

Anderson, D.M., 1989, Toxic algal blooms and red tides: a global perspective.: Red Tides., p. 11–16.

Anderson, D.M., Glibert, P.M., and Burkholder, J.M., 2002, Harmful algal blooms and eutrophication: Nutrient sources, composition, and consequences: Estuaries, v. 25, doi:10.1007/BF02804901.

Arnold, J.G. et al., 2012, SWAT: Model use, calibration, and validation: Transactions of the ASABE, v. 55, p. 1491–1508.

Arnold, J.G., Srinivasan, R., Muttiah, R.S., and Williams, J.R., 1998, LARGE AREA HYDROLOGIC MODELING AND ASSESSMENT PART I: MODEL DEVELOPMENT1: JAWRA Journal of the American Water Resources Association, v. 34, p. 73–89, doi:10.1111/J.1752-1688.1998.TB05961.X.

Arsenault, R., Brissette, F., and Martel, J.L., 2018, The hazards of split-sample validation in hydrological model calibration: Journal of Hydrology, v. 566, p. 346–362, doi:10.1016/j.jhydrol.2018.09.027.

Ayers, M., Specialist, N.R., Bennis, A., Specialist, P., and Grant, T.S., 2021, Early Phase Watershed Planning for Baffin Bay Early Phase Watershed Planning for Baffin Bay Final Report:

Bacopoulos, P., Tang, Y., Wang, D., and Hagen, S.C., 2017, Integrated Hydrologic-Hydrodynamic Modeling of Estuarine-Riverine Flooding: 2008 Tropical Storm Fay: Journal of Hydrologic Engineering, v. 22, doi:10.1061/(asce)he.1943-5584.0001539.

Barbier, E.B., Hacker, S.D., Kennedy, C., Koch, E.W., Stier, A.C., and Silliman, B.R., 2011, The value of estuarine and coastal ecosystem services: Ecological Monographs, v. 81, doi:10.1890/10-1510.1.

Beecraft, L., and Wetz, M.S., 2022, Temporal Variability in Water Quality and Phytoplankton Biomass in a Low-Inflow Estuary (Baffin Bay, TX): Estuaries and Coasts, doi:10.1007/s12237-022-01145-y.

Bieger, K., Hörmann, G., and Fohrer, N., 2015, Detailed spatial analysis of SWAT-simulated surface runoff and sediment yield in a mountainous watershed in China: Hydrological Sciences Journal, doi:10.1080/02626667.2014.965172.

Bugica, K., Sterba-Boatwright, B., and Wetz, M.S., 2020, Water quality trends in Texas estuaries: Marine Pollution Bulletin, v. 152, p. 110903, doi:10.1016/j.marpolbul.2020.110903.

Buskey, E.J., and Hyatt, C.J., 1995, Effects of the Texas (USA) "brown tide" alga on planktonic grazers: Marine Ecology Progress Series, v. 126, p. 285–292, doi:10.3354/MEPS126285.

Buskey, E.J., Liu, H., Collumb, C., and Bersano, J.G.F., 2001, The decline and recovery of a persistent Texas brown tide algal bloom in the Laguna Madre (Texas, USA): Estuaries, v. 24, p. 337–346.

Campbell, A., Pradhanang, S.M., Kouhi Anbaran, S., Sargent, J., Palmer, Z., and Audette, M., 2018, Assessing the impact of urbanization on flood risk and severity for the Pawtuxet watershed, Rhode Island: Lake and Reservoir Management, v. 34, doi:10.1080/10402381.2017.1390016.

Cira, E.K., Palmer, T.A., and Wetz, M.S., 2021, Phytoplankton Dynamics in a Low-Inflow Estuary (Baffin Bay, TX) During Drought and High-Rainfall Conditions Associated with an El Niño Event: Estuaries and Coasts, v. 44, p. 1752–1764, doi:10.1007/s12237-021-00904-7.

Cira, E.K., and Wetz, M.S., 2019, Spatial-temporal distribution of Aureoumbra lagunensis ("brown tide") in Baffin Bay, Texas: Harmful algae, v. 89, p. 101669.

Cotner, J.B., Suplee, M.W., Chen, N.W., and Shormann, D.E., 2004, Nutrient, sulfur and carbon dynamics in a hypersaline lagoon: Estuarine, Coastal and Shelf Science, v. 59, p. 639–652, doi:10.1016/J.ECSS.2003.11.008.

Dagnew, A., Scavia, D., Wang, Y.C., Muenich, R., Long, C., and Kalcic, M., 2019, Modeling Flow, Nutrient, and Sediment Delivery from a Large International Watershed Using a Field-Scale SWAT Model: Journal of the American Water Resources Association, v. 55, p. 1288–1305, doi:10.1111/1752-1688.12779.

Donmez, C., Sari, O., Berberoglu, S., Cilek, A., Satir, O., and Volk, M., 2020, Improving the applicability of the swat model to simulate flow and nitrate dynamics in a flat data-scarce agricultural region in the mediterranean: Water (Switzerland), v. 12, p. 1–24,

doi:10.3390/w12123479.

Gassman, P.W., Reyes, M.R., Green, C.H., Arnold, J.G., and Gassman, P.W., 2007, The Soil and Water Assessment Tool: Historical Development, Applications, and Future Research Directions: Transactions of the ASABE, v. 50, p. 1211–1250, doi:10.13031/2013.23637.

Ghaith, M., and Li, Z., 2020, Propagation of parameter uncertainty in SWAT: A probabilistic forecasting method based on polynomial chaos expansion and machine learning: Journal of Hydrology, v. 586, p. 124854, doi:10.1016/J.JHYDROL.2020.124854.

Glibert, P.M., Anderson, D.M., Gentien, P., Granéli, E., and Sellner, K.G., 2005, The global, complex phenomena of harmful algal blooms: Oceanography, v. 18, doi:10.5670/oceanog.2005.49.

Grusson, Y., Anctil, F., Sauvage, S., and Sánchez Pérez, J.M., 2017, Assessing the Climatic and Temporal Transposability of the SWAT Model across a Large Contrasted Watershed: Journal of Hydrologic Engineering, v. 22, p. 04017004, doi:10.1061/(ASCE)HE.1943-5584.0001491/SUPPL_FILE/SUPPLEMENTAL_DATA_HE.1943-5584.0001491_GRUSSON.PDF.

Ha, L.T., Bastiaanssen, W.G.M., Van Griensven, A., Van Dijk, A.I.J.M., Senay, G.B., and Ha, L.T., 2017, SWAT-CUP for Calibration of Spatially Distributed Hydrological Processes and Ecosystem Services in a Vietnamese River Basin Using Remote Sensing: Journal of Hydrology and Earth System Sciences, p. 1–35, https://doi.org/10.5194/hess-2017-251.

Hallegraeff, G.M., 1993, A review of harmful algal blooms and their apparent global increase: Phycologia, v. 32, doi:10.2216/i0031-8884-32-2-79.1.

Hargreaves, G.L., Hargreaves, G.H., and Riley, J.P., 1985, Agricultural Benefits for Senegal River Basin: Journal of Irrigation and Drainage Engineering, v. 111, doi:10.1061/(asce)0733-9437(1985)111:2(113).

Heisler, J. et al., 2008, Eutrophication and harmful algal blooms: A scientific consensus: Harmful Algae, v. 8, p. 3–13, doi:10.1016/j.hal.2008.08.006.

Her, Y., Chaubey, I., Frankenberger, J., and Jeong, J., 2017, Implications of spatial and temporal variations in effects of conservation practices on water management strategies: Agricultural Water Management, v. 180, doi:10.1016/j.agwat.2016.07.004.

Her, Y., Frankenberger, J., Chaubey, I., and Srinivasan, R., 2015, Threshold effects in HRU definition of the soil and water assessment tool: Transactions of the ASABE, v. 58, p. 367–378, doi:10.13031/trans.58.10805.

Holvoet, K., van Griensven, A., Gevaert, V., Seuntjens, P., and Vanrolleghem, P.A., 2008, Modifications to the SWAT code for modelling direct pesticide losses: Environmental Modelling and Software, v. 23, doi:10.1016/j.envsoft.2007.05.002.

Homer, C.H., Fry, J.A., and C.A., B., 2012, The National Land Cover Database, U.S. Geological Survey Fact Sheet 2012-3020, 4 p:

Hou, A.Y., Kakar, R.K., Neeck, S., Azarbarzin, A.A., Kummerow, C.D., Kojima, M., Oki, R., Nakamura, K., and Iguchi, T., 2014, The global precipitation measurement mission:

Bulletin of the American Meteorological Society, v. 95, p. 701–722, doi:10.1175/BAMS-D-13-00164.1.

Huffman., G., Bolvin., D., Braithwaite., D., Hsu., K., Joyce., R., and Xie, P., 2014, Integrated Multi-satellitE Retrievals for GPM (IMERG), version 4.4. NASA's Precipitation Processing Center:, ftp://arthurhou.pps.eosdis.nasa.gov/gpmdata/ (accessed September 2021).

Huffman, G.J.., Stocker, E.F.., Bolvin, D.T.., Nelkin, E.J.., and Tan, J., 2019, Gpm Imerg Final Precipitation l3 1 Month 0.1 Degree × 0.1 Degree V06; Goddard Earth Sciences Data and Information Services Center: Greenbelt, MD, USA:, https://disc.gsfc.nasa.gov/datasets/GPM_3IMERGM_06/summary?keywords=%22IMERG final%22.V06.

Kmoch, A., Moges, D.M., Sepehrar, M., Narasimhan, B., and Uuemaa, E., 2022, The Effect of Spatial Input Data Quality on the Performance of the SWAT Model: Water (Switzerland), v. 14, p. 1–18, doi:10.3390/w14131988.

Kouchi, D.H., Esmaili, K., Faridhosseini, A., Sanaeinejad, S.H., Khalili, D., and Abbaspour, K.C., 2017, Sensitivity of calibrated parameters and water resource estimates on different objective functions and optimization algorithms: Water (Switzerland), v. 9, p. 1–16, doi:10.3390/w9060384.

Lam, Q.D., Schmalz, B., and Fohrer, N., 2012, Assessing the spatial and temporal variations of water quality in lowland areas, Northern Germany: Journal of Hydrology, v. 438–439, p. 137–147, doi:10.1016/J.JHYDROL.2012.03.011.

Largier, J., 2010, Low-inflow estuaries: hypersaline, inverse, and thermal scenarios: Contemporary Issues in Estuarine Physics, p. 247–272, doi:10.1017/CBO9780511676567.010.

Li, E.A., Contractor, D.N., Carr, J.C., and Shanholtz, V.O., 1977, GENERATING PRECIPITATION EXCESS BASED ON READILY DETERMINABLE SOIL-VEGETATIVE CHARACTERISTICS., *in* Paper - American Society of Agricultural Engineers,.

Lin, Q., and Zhang, D., 2021, A scalable distributed parallel simulation tool for the SWAT model: Environmental Modelling & Software, v. 144, p. 105133, doi:10.1016/J.ENVSOFT.2021.105133.

Mengistu, A.G., van Rensburg, L.D., and Woyessa, Y.E., 2019, Techniques for calibration and validation of SWAT model in data scarce arid and semi-arid catchments in South Africa: Journal of Hydrology: Regional Studies, v. 25, p. 100621, doi:10.1016/j.ejrh.2019.100621.

Mirchi, A., Watkins, D., and Madani, K., 2010, Modeling for watershed planning, management, and decision making, *in* Watersheds: Management, Restoration and Environmental Impact,.

Monteith, J.L., 1965, Evaporation and environment.: Symposia of the Society for Experimental Biology, v. 19, p. 205–234, https://europepmc.org/article/med/5321565 (accessed June 2023).

Neitsch, S.., Arnold, J.., Kiniry, J.., and Williams, J.., 2011, Soil & Water Assessment Tool Theoretical Documentation Version 2009: Texas Water Resources Institute, p. 1–647,

doi:10.1016/j.scitotenv.2015.11.063.

Nepal, D., and Parajuli, P.B., 2022, Assessment of Best Management Practices on Hydrology and Sediment Yield at Watershed Scale in Mississippi Using SWAT: Agriculture (Switzerland), v. 12, doi:10.3390/agriculture12040518.

Noh, S.J., Weerts, A.H., Rakovec, O., Lee, H., and Seo, D.-J., 2018, Assimilation of Streamflow Observations: Handbook of Hydrometeorological Ensemble Forecasting, p. 1–36, doi:10.1007/978-3-642-40457-3_33-2.

Nyeko, M., 2015, Hydrologic Modelling of Data Scarce Basin with SWAT Model: Capabilities and Limitations: Water Resources Management, v. 29, p. 81–94, doi:10.1007/s11269-014-0828-3.

Ockerman, D.J., and Petri, B.L., 2001, Hydrologic Conditions and Water Quality in an Agricultural Area in Kleberg and Nueces Counties , Texas , 1996 – 98, Water-Resources Investigations Report 01–4101:, https://books.google.com/books?hl=en&lr=&id=9YLuAAAAMAAJ&oi=fnd&pg=PA1&ots=R9YlqrdCuE&sig=1SMRhecm4lMer12mKtyQCm58-WY#v=onepage&q&f=false (accessed June 2023).

Ollivier, C. et al., 2021, An evapotranspiration model driven by remote sensing data for assessing groundwater resource in karst watershed: Science of the Total Environment, v. 781, doi:10.1016/j.scitotenv.2021.146706.

Pendleton, L., 2010, The economic and market value of coasts and estuaries: what's at stake? … Economic and Market Value of Coasts and Estuaries …,.

Pionke, H.B., Gburek, W.J., and Sharpley, A.N., 2000, Critical source area controls on water quality in an agricultural watershed located in the Chesapeake Basin: Ecological Engineering, v. 14, p. 325–335, doi:10.1016/S0925-8574(99)00059-2.

Pisinaras, V., Petalas, C., Gikas, G.D., Gemitzi, A., and Tsihrintzis, V.A., 2010, Hydrological and water quality modeling in a medium-sized basin using the Soil and Water Assessment Tool (SWAT): Desalination, v. 250, p. 274–286, doi:10.1016/J.DESAL.2009.09.044.

Priestley, C.H.B., and Taylor, R.J., 1972, On the Assessment of Surface Heat Flux and Evaporation Using Large-Scale Parameters: Monthly Weather Review, v. 100, doi:10.1175/1520-0493(1972)100<0081:otaosh>2.3.co;2.

Rebich, R.A., Houston, N.A., Mize, S. V., Pearson, D.K., Ging, P.B., and Evan Hornig, C., 2011, Sources and Delivery of Nutrients to the Northwestern Gulf of Mexico from Streams in the South-Central United States1: JAWRA Journal of the American Water Resources Association, v. 47, p. 1061–1086, doi:10.1111/J.1752-1688.2011.00583.X.

Runkel, R.L., Crawford, C.G., and Cohn, T. a, 2004, Load Estimator (LOADEST): A FORTRAN program for estimating constituent loads in streams and rivers. Techniques and Methods Book 4 , Chapter A5. U.S. Geological Survey.:

Santhi, C., Arnold, J.G., Williams, J.R., Dugas, W.A., Srinivasan, R., and Hauck, L.M., 2001, Validation of the SWAT model on a large river basin with point and nonpoint sources: Journal of the American Water Resources Association, v. 37, doi:10.1111/j.1752-

1688.2001.tb03630.x.

Sarrazin, F., Hartmann, A., Pianosi, F., Rosolem, R., and Wagener, T., 2018, V2Karst V1.1: A parsimonious large-scale integrated vegetation-recharge model to simulate the impact of climate and land cover change in karst regions: Geoscientific Model Development, v. 11, doi:10.5194/gmd-11-4933-2018.

Shao, G., Zhang, D., Guan, Y., Xie, Y., and Huang, F., 2019, Application of SWAT Model with a Modified Groundwater Module to the Semi-Arid Hailiutu River Catchment, Northwest China: Sustainability 2019, Vol. 11, Page 2031, v. 11, p. 2031, doi:10.3390/SU11072031.

Shen, J., and Tan, F., 2020, Effects of DEM resolution and resampling technique on building treatment for urban inundation modeling: a case study for the 2016 flooding of the HUST campus in Wuhan: Natural Hazards, v. 104, doi:10.1007/s11069-020-04198-z.

Shen, H., Tolson, B.A., and Mai, J., 2022, Time to Update the Split-Sample Approach in Hydrological Model Calibration: Water Resources Research, v. 58, doi:10.1029/2021WR031523.

Shen, Y., and Xiong, A., 2016, Validation and comparison of a new gauge-based precipitation analysis over mainland China: International Journal of Climatology, v. 36, doi:10.1002/joc.4341.

Shi, W., and Huang, M., 2021, Predictions of soil and nutrient losses using a modified SWAT model in a large hilly-gully watershed of the Chinese Loess Plateau: International Soil and Water Conservation Research, v. 9, doi:10.1016/j.iswcr.2020.12.002.

Smayda, T.J., 1990, Novel and nuisance phytoplankton blooms in the sea: evidence for a global epidemic., *in* Toxic Marine Plankton: Proceedings of the Fourth International Conference on Toxic Marine Phytoplankton, v. 40.

Smith, D.R., Owens, P.R., Leytem, A.B., and Warnemuende, E.A., 2007, Nutrient losses from manure and fertilizer applications as impacted by time to first runoff event: Environmental Pollution, v. 147, p. 131–137, doi:10.1016/j.envpol.2006.08.021.

Srinivasan, V.S., Santos, C., Suzuki, K., and Watanabe, M., 1993, Sediment Yield Observed in a Small Experimental Basin and its Simulation by Runoff-Erosion Modeling: Proceedings of Hydraulic Engineering, v. 37, p. 717–722, doi:10.2208/prohe.37.717.

Stenback, G.A., Crumpton, W.G., Schilling, K.E., and Helmers, M.J., 2011, Rating curve estimation of nutrient loads in Iowa rivers: Journal of Hydrology, v. 396, doi:10.1016/j.jhydrol.2010.11.006.

Street, G.T., Montagna, P.A., and Parker, P.L., 1997, Incorporation of brown tide into an estuarine food web: Marine Ecology Progress Series, v. 152, p. 67–78, doi:10.3354/MEPS152067.

Tan, M.L., Ficklin, D.L., Dixon, B., Ibrahim, A.L., Yusop, Z., and Chaplot, V., 2015, Impacts of DEM resolution, source, and resampling technique on SWAT-simulated streamflow: Applied Geography, v. 63, doi:10.1016/j.apgeog.2015.07.014.

Tan, M.L., Gassman, P.W., Yang, X., and Haywood, J., 2020, A review of SWAT applications,

performance and future needs for simulation of hydro-climatic extremes: Advances in Water Resources, v. 143, doi:10.1016/j.advwatres.2020.103662.

Thomas, T., Ghosh, N.C., and Sudheer, K.P., 2021, Optimal reservoir operation – A climate change adaptation strategy for Narmada basin in central India: Journal of Hydrology, v. 598, doi:10.1016/j.jhydrol.2021.126238.

TPWD Texas Parks and Wildlife Department. “Upper Laguna Madre.”:, https://tpwd.texas.gov/landwater/water/habitats/bays/ulm/ulm_index.phtml.

Tuppad, P., Douglas-Mankin, K.R., Lee, T., Srinivasan, R., and Arnold, J.G., 2011, Soil and Water Assessment Tool (SWAT) Hydrologic/Water Quality Model: Extended Capability and Wider Adoption: Transactions of the ASABE, v. 54, p. 1677–1684, doi:10.13031/2013.39856.

TWDB Coastal Hydrology:, http://www.twdb.texas.gov/surfacewater/bays/coastal_hydrology/index.asp (accessed April 2023).

Uniyal, B., Kosatica, E., and Koellner, T., 2023, Spatial and temporal variability of climate change impacts on ecosystem services in small agricultural catchments using the Soil and Water Assessment Tool (SWAT): Science of the Total Environment, v. 875, doi:10.1016/j.scitotenv.2023.162520.

USDA-NRCS Soil Survey Staff, Natural Resources Conservation Service, United States Department of Agriculture. Web Soil Survey:, https://websoilsurvey.nrcs.usda.gov/ (accessed August 2021).

USGS, 2020, U.S. Geological Survey, 20200409, USGS one meter x65y302 TX South B2 2018: U.S. Geological Survey:, https://www.sciencebase.gov/catalog/item/5ead02a282cefae35a252c95 (accessed August 2021).

Verma, S., Bhattarai, R., Bosch, N.S., Cooke, R.C., Kalita, P.K., and Markus, M., 2015, Climate Change Impacts on Flow, Sediment and Nutrient Export in a Great Lakes Watershed Using SWAT: Clean - Soil, Air, Water, v. 43, doi:10.1002/clen.201400724.

Wetz, M.S., Cira, E.K., Sterba-Boatwright, B., Montagna, P.A., Palmer, T.A., and Hayes, K.C., 2017, Exceptionally high organic nitrogen concentrations in a semi-arid South Texas estuary susceptible to brown tide blooms: Estuarine, Coastal and Shelf Science, v. 188, p. 27–37, doi:10.1016/j.ecss.2017.02.001.

Williams, J.R., 1995, The EPIC Model. In: Singh, V.P., Ed., Computer Models of Watershed Hydrology: Colorado, USA, Water Resources Publications.

Williams, J.R., and Hann, R.W., 1978, Optimal operation of large agricultural watersheds with water quality constraints.: Texas A & M University, College Station, Water Resources Institute, Technical Report,.

Woznicki, S.A., and Nejadhashemi, A.P., 2013, Spatial and Temporal Variabilities of Sediment Delivery Ratio: Water Resources Management, v. 27, doi:10.1007/s11269-013-0298-z.

Zhang, G., 2016, Characteristics of Runoff Nutrient Loss and Particle Size Distribution of Eroded Sediment under Varied Rainfall Intensities, *in* Proceedings of the 2016 4th International Conference on Machinery, Materials and Computing Technology, v. 60, doi:10.2991/icmmct-16.2016.119.

Zhu, C., and Li, Y., 2014, Long-Term Hydrological Impacts of Land Use/Land Cover Change From 1984 to 2010 in the Little River Watershed, Tennessee: International Soil and Water Conservation Research, v. 2, doi:10.1016/S2095-6339(15)30002-2.

8. Appendices:

Appendix 1: Daily maximum and minimum temperature statistics

Appendix 2: Daily rainfall statistics

Appendix (1): Daily maximum and minimum temperature statistics

Station/Parameter	Mean	Standard Error	Median	Mode	Standard Deviation	Sample Variance	Kurtosis	Skewness	Range	Minimum	Maximum	Sum	Count	missing data %
USC00410144_tmp_Max	29.3	0.1	30.6	35.0	7.0	49.3	0.8	-1.0	43.9	0.0	43.9	101792	3474	59
USC00410144_tmp_Min	17.3	0.1	19.4	23.9	6.9	47.3	-0.5	-0.8	31.1	-3.9	27.2	60055	3472	59
USC00410690_tmp_Max	29.1	0.1	30.6	35.6	7.7	59.3	0.6	-0.9	58.3	-13.9	44.4	223166	7666	59
USC00410690_tmp_Min	15.9	0.1	18.3	23.9	8.0	63.2	-0.7	-0.7	43.9	-8.3	35.6	121126	7635	59
USC00410805_tmp_Max	28.4	0.1	29.4	33.3	7.0	49.3	0.6	-0.9	43.9	-1.1	42.8	132807	4674	59
USC00410805_tmp_Min	16.5	0.1	18.9	22.8	7.6	58.0	-0.7	-0.7	33.9	-6.1	27.8	77221	4668	59
USC00411651_tmp_Max	28.2	0.2	28.9	33.9	6.2	39.0	0.7	-0.8	41.7	1.1	42.8	38359	1362	59
USC00411651_tmp_Min	17.0	0.2	18.9	23.3	7.0	48.9	-0.6	-0.6	37.7	-4.4	33.3	23207	1363	59
USC00411932_tmp_Max	29.8	0.2	30.6	33.3	7.2	51.6	0.7	-0.8	43.9	1.1	45.0	35616	1197	59
USC00411932_tmp_Min	16.2	0.2	18.3	22.2	7.2	51.4	-0.2	-0.8	40.5	-13.3	27.2	19395	1194	59
USC00413063_tmp_Max	29.5	0.1	30.6	35.6	7.3	53.9	0.9	-0.9	64.4	-17.8	46.7	157918	5355	59
USC00413063_tmp_Min	15.8	0.1	18.3	22.2	7.8	61.5	-0.6	-0.7	46.7	-17.8	28.9	86667	5476	59
USC00413341_tmp_Max	29.0	0.1	30.6	37.2	7.8	60.1	0.4	-0.8	46.1	0.6	46.7	185669	6404	59
USC00413341_tmp_Min	16.2	0.1	18.3	23.3	7.4	54.3	-0.6	-0.7	39.4	-9.4	30.0	106651	6592	59
USC00414058_tmp_Max	29.4	0.1	30.6	35.6	7.5	55.9	0.5	-0.9	49.5	1.1	50.6	160822	5478	59
USC00414058_tmp_Min	16.3	0.1	18.3	22.8	7.4	54.3	-0.6	-0.7	38.3	-7.2	31.1	88337	5414	59
USC00414810_tmp_Max	28.7	0.1	30.0	35.0	6.9	47.7	0.8	-1.0	43.9	0.0	43.9	231613	8062	59
USC00414810_tmp_Min	17.3	0.1	19.4	24.4	7.3	53.6	-0.6	-0.7	35.6	-5.6	30.0	142447	8212	59
USW00012924_tmp_Max	28.1	0.1	29.4	33.9	6.5	42.4	0.7	-1.0	42.8	0.0	42.8	235113	8358	59
USW00012924_tmp_Min	17.5	0.1	19.4	23.9	7.1	50.2	-0.6	-0.7	34.4	-5.6	28.9	147087	8401	59
USW00012928_tmp_Max	29.0	0.1	30.0	32.8	6.8	46.6	0.7	-0.9	46.7	-0.6	46.1	189517	6535	59
USW00012928_tmp_Min	17.0	0.1	18.9	23.9	7.6	58.0	0.1	-0.8	52.2	-18.3	33.9	114046	6714	59
USW00012932_tmp_Max	29.3	0.1	30.6	34.4	7.2	51.5	0.5	-0.9	43.3	0.0	43.3	207106	7076	59
USW00012932_tmp_Min	16.6	0.1	18.9	23.3	7.2	52.0	-0.7	-0.7	46.7	-17.8	28.9	120657	7258	59

Appendix (2): Daily rainfall statistics

Station/Parameter	Mean	Standard Error	Median	Mode	Standard Deviation	Sample Variance	Kurtosis	Skewness	Range	Minimum	Maximum	Sum	Count
1	1.91	0.09	0.00	0.00	7.87	61.90	81.45	7.70	148.45	0.00	148.45	13985.96	7305.00
2	2.02	0.09	0.00	0.00	8.09	65.40	76.92	7.51	141.72	0.00	141.72	14750.45	7305.00
3	1.87	0.09	0.00	0.00	7.64	58.34	80.44	7.61	147.75	0.00	147.75	13672.22	7305.00
4	1.90	0.09	0.00	0.00	7.70	59.21	80.90	7.61	155.15	0.00	155.15	13843.12	7305.00
5	1.94	0.09	0.00	0.00	7.87	61.95	80.13	7.62	155.92	0.00	155.92	14147.63	7305.00
6	1.98	0.09	0.00	0.00	7.91	62.52	73.52	7.37	144.88	0.00	144.88	14434.44	7305.00
7	2.01	0.09	0.00	0.00	7.93	62.86	67.35	7.15	138.55	0.00	138.55	14647.12	7305.00
8	2.03	0.09	0.00	0.00	8.03	64.52	71.38	7.30	148.13	0.00	148.13	14863.18	7305.00
9	2.06	0.09	0.00	0.00	8.01	64.18	73.26	7.34	150.16	0.00	150.16	15073.18	7305.00
10	1.81	0.09	0.00	0.00	7.43	55.28	72.88	7.40	134.94	0.00	134.94	13215.54	7305.00
11	1.84	0.09	0.00	0.00	7.54	56.87	79.53	7.58	151.49	0.00	151.49	13431.09	7305.00
12	1.87	0.09	0.00	0.00	7.64	58.35	80.67	7.63	149.92	0.00	149.92	13666.83	7305.00
13	1.91	0.09	0.00	0.00	7.71	59.43	75.46	7.41	147.70	0.00	147.70	13970.56	7305.00
14	1.94	0.09	0.00	0.00	7.68	59.02	72.82	7.31	140.10	0.00	140.10	14191.42	7305.00
15	1.97	0.09	0.00	0.00	7.61	57.87	60.90	6.84	126.13	0.00	126.13	14377.76	7305.00
16	2.00	0.09	0.00	0.00	7.85	61.60	70.62	7.25	140.40	0.00	140.40	14640.96	7305.00
17	2.04	0.09	0.00	0.00	7.78	60.51	68.37	7.08	134.95	0.00	134.95	14890.27	7305.00
18	2.08	0.09	0.00	0.00	7.83	61.26	62.36	6.81	134.93	0.00	134.93	15208.38	7305.00
19	2.13	0.09	0.00	0.00	7.79	60.69	51.83	6.37	119.07	0.00	119.07	15578.84	7305.00
20	1.79	0.09	0.00	0.00	7.40	54.72	76.03	7.56	132.57	0.00	132.57	13074.75	7305.00
21	1.84	0.09	0.00	0.00	7.67	58.86	83.06	7.83	147.25	0.00	147.25	13418.45	7305.00
22	1.86	0.09	0.00	0.00	7.62	58.09	83.69	7.75	148.44	0.00	148.44	13572.51	7305.00
23	1.89	0.09	0.00	0.00	7.62	58.13	73.78	7.44	138.22	0.00	138.22	13783.33	7305.00
24	1.92	0.09	0.00	0.00	7.63	58.21	67.14	7.16	128.64	0.00	128.64	14036.72	7305.00
25	1.95	0.09	0.00	0.00	7.58	57.41	61.30	6.89	129.95	0.00	129.95	14247.53	7305.00
26	1.99	0.09	0.00	0.00	7.66	58.74	64.09	6.98	136.67	0.00	136.67	14514.59	7305.00
27	2.03	0.09	0.00	0.00	7.68	58.96	61.84	6.83	123.62	0.00	123.62	14803.87	7305.00
28	2.07	0.09	0.00	0.00	7.70	59.29	60.70	6.72	125.54	0.00	125.54	15124.93	7305.00
29	2.12	0.09	0.00	0.00	7.64	58.33	45.92	6.11	93.67	0.00	93.67	15493.48	7305.00
30	2.16	0.09	0.00	0.00	7.74	59.91	45.99	6.07	110.34	0.00	110.34	15763.53	7305.00
31	1.71	0.08	0.00	0.00	7.15	51.05	76.37	7.61	118.87	0.00	118.87	12487.07	7305.00
32	1.75	0.08	0.00	0.00	7.24	52.47	74.39	7.47	121.21	0.00	121.21	12776.78	7305.00
33	1.78	0.09	0.00	0.00	7.36	54.16	75.42	7.54	127.55	0.00	127.55	13001.52	7305.00
34	1.81	0.09	0.00	0.00	7.44	55.32	75.22	7.45	141.69	0.00	141.69	13222.55	7305.00
35	1.84	0.09	0.00	0.00	7.48	55.92	79.03	7.57	148.91	0.00	148.91	13416.87	7305.00
36	1.87	0.09	0.00	0.00	7.53	56.63	74.70	7.48	132.99	0.00	132.99	13631.02	7305.00
37	1.90	0.09	0.00	0.00	7.68	58.93	73.10	7.49	128.26	0.00	128.26	13861.16	7305.00
38	1.94	0.09	0.00	0.00	7.70	59.32	67.02	7.22	118.95	0.00	118.95	14142.72	7305.00

39	1.97	0.09	0.00	0.00	7.69	59.20	60.44	6.91	119.14	0.00	119.14	14413.89	7305.00
40	2.01	0.09	0.00	0.00	7.60	57.70	55.69	6.62	108.49	0.00	108.49	14663.13	7305.00
41	2.04	0.09	0.00	0.00	7.59	57.56	51.44	6.41	100.31	0.00	100.31	14928.14	7305.00
42	2.10	0.09	0.00	0.00	7.61	57.89	47.91	6.18	114.76	0.00	114.76	15327.27	7305.00
43	2.13	0.09	0.00	0.00	7.68	58.98	43.45	5.97	99.35	0.00	99.35	15570.87	7305.00
44	2.18	0.09	0.00	0.00	7.97	63.54	45.22	6.04	106.46	0.00	106.46	15895.43	7305.00
45	1.66	0.08	0.00	0.00	7.04	49.61	80.35	7.73	130.23	0.00	130.23	12131.34	7305.00
46	1.70	0.08	0.00	0.00	7.26	52.71	79.71	7.80	128.65	0.00	128.65	12399.66	7305.00
47	1.73	0.08	0.00	0.00	7.21	52.02	79.10	7.69	129.90	0.00	129.90	12635.46	7305.00
48	1.75	0.09	0.00	0.00	7.33	53.68	81.28	7.81	129.05	0.00	129.05	12796.10	7305.00
49	1.78	0.09	0.00	0.00	7.43	55.23	86.29	7.95	138.20	0.00	138.20	13000.11	7305.00
50	1.81	0.09	0.00	0.00	7.44	55.34	82.83	7.73	150.65	0.00	150.65	13257.01	7305.00
51	1.86	0.09	0.00	0.00	7.80	60.92	97.19	8.34	161.00	0.00	161.00	13589.95	7305.00
52	1.89	0.09	0.00	0.00	7.68	58.95	71.86	7.44	128.74	0.00	128.74	13817.04	7305.00
53	1.92	0.09	0.00	0.00	7.71	59.51	68.96	7.30	126.00	0.00	126.00	14052.27	7305.00
54	1.95	0.09	0.00	0.00	7.68	58.99	70.31	7.28	135.14	0.00	135.14	14268.82	7305.00
55	1.98	0.09	0.00	0.00	7.71	59.42	65.85	7.08	118.59	0.00	118.59	14492.56	7305.00
56	2.01	0.09	0.00	0.00	7.63	58.26	56.60	6.65	118.32	0.00	118.32	14717.24	7305.00
57	2.07	0.09	0.00	0.00	7.63	58.23	48.07	6.23	99.04	0.00	99.04	15138.25	7305.00
58	2.10	0.09	0.00	0.00	7.68	59.05	48.77	6.24	107.64	0.00	107.64	15332.44	7305.00
59	2.14	0.09	0.00	0.00	7.92	62.65	48.70	6.22	114.44	0.00	114.44	15618.03	7305.00
60	2.17	0.10	0.00	0.00	8.14	66.27	55.81	6.48	144.91	0.00	144.91	15845.87	7305.00
61	1.64	0.08	0.00	0.00	7.04	49.50	83.15	7.85	125.97	0.00	125.97	11963.57	7305.00
62	1.66	0.08	0.00	0.00	7.20	51.86	93.91	8.24	142.16	0.00	142.16	12155.75	7305.00
63	1.70	0.08	0.00	0.00	7.24	52.41	92.88	8.23	140.85	0.00	140.85	12405.77	7305.00
64	1.72	0.09	0.00	0.00	7.32	53.57	85.40	8.01	128.55	0.00	128.55	12556.45	7305.00
65	1.74	0.09	0.00	0.00	7.39	54.61	92.28	8.16	149.29	0.00	149.29	12721.65	7305.00
66	1.79	0.09	0.00	0.00	7.52	56.52	88.24	8.00	142.35	0.00	142.35	13111.78	7305.00
67	1.84	0.09	0.00	0.00	7.62	58.06	79.39	7.74	136.81	0.00	136.81	13436.69	7305.00
68	1.87	0.09	0.00	0.00	7.63	58.19	73.98	7.51	138.54	0.00	138.54	13667.43	7305.00
69	1.90	0.09	0.00	0.00	7.69	59.14	77.70	7.60	135.27	0.00	135.27	13892.45	7305.00
70	1.93	0.09	0.00	0.00	7.74	59.97	74.51	7.47	133.56	0.00	133.56	14109.76	7305.00
71	1.95	0.09	0.00	0.00	7.68	58.94	70.30	7.27	129.73	0.00	129.73	14243.28	7305.00
72	1.98	0.09	0.00	0.00	7.69	59.15	64.29	7.01	130.87	0.00	130.87	14458.49	7305.00
73	2.03	0.09	0.00	0.00	7.63	58.24	52.07	6.45	105.76	0.00	105.76	14798.41	7305.00
74	2.07	0.09	0.00	0.00	7.69	59.15	50.75	6.33	101.86	0.00	101.86	15094.54	7305.00
75	2.11	0.09	0.00	0.00	7.89	62.22	54.68	6.45	136.97	0.00	136.97	15425.14	7305.00
76	2.14	0.10	0.00	0.00	8.13	66.03	64.13	6.82	150.93	0.00	150.93	15649.03	7305.00
77	1.61	0.08	0.00	0.00	6.85	46.97	91.24	8.07	134.29	0.00	134.29	11777.64	7305.00
78	1.65	0.08	0.00	0.00	7.17	51.34	109.58	8.69	153.58	0.00	153.58	12062.11	7305.00
79	1.68	0.08	0.00	0.00	7.11	50.50	93.04	8.14	141.21	0.00	141.21	12248.92	7305.00

80	1.70	0.08	0.00	0.00	7.15	51.19	88.82	8.07	131.95	0.00	131.95	12387.02	7305.00
81	1.73	0.09	0.00	0.00	7.32	53.57	86.10	8.00	130.95	0.00	130.95	12618.28	7305.00
82	1.76	0.09	0.00	0.00	7.40	54.74	81.52	7.82	131.06	0.00	131.06	12876.90	7305.00
83	1.82	0.09	0.00	0.00	7.51	56.46	78.32	7.72	129.07	0.00	129.07	13290.52	7305.00
84	1.85	0.09	0.00	0.00	7.51	56.35	77.56	7.61	131.81	0.00	131.81	13524.54	7305.00
85	1.88	0.09	0.00	0.00	7.54	56.85	76.83	7.52	138.70	0.00	138.70	13727.26	7305.00
86	1.90	0.09	0.00	0.00	7.65	58.51	81.86	7.74	129.78	0.00	129.78	13899.19	7305.00
87	1.92	0.09	0.00	0.00	7.60	57.74	71.91	7.34	120.32	0.00	120.32	14014.16	7305.00
88	1.95	0.09	0.00	0.00	7.66	58.69	66.70	7.16	115.63	0.00	115.63	14217.41	7305.00
89	1.99	0.09	0.00	0.00	7.59	57.66	60.92	6.87	111.22	0.00	111.22	14511.69	7305.00
90	2.05	0.09	0.00	0.00	7.70	59.25	54.29	6.51	111.56	0.00	111.56	14981.07	7305.00
91	2.10	0.09	0.00	0.00	7.78	60.51	78.12	7.03	183.25	0.00	183.25	15323.59	7305.00
92	1.63	0.08	0.00	0.00	7.02	49.30	104.90	8.54	146.81	0.00	146.81	11938.01	7305.00
93	1.66	0.08	0.00	0.00	6.99	48.84	82.78	7.84	132.19	0.00	132.19	12129.39	7305.00
94	1.68	0.08	0.00	0.00	7.03	49.38	88.87	8.01	145.24	0.00	145.24	12283.66	7305.00
95	1.71	0.08	0.00	0.00	7.15	51.12	85.59	7.90	143.24	0.00	143.24	12514.64	7305.00
96	1.74	0.08	0.00	0.00	7.25	52.56	80.36	7.75	140.26	0.00	140.26	12735.87	7305.00
97	1.79	0.09	0.00	0.00	7.39	54.61	77.14	7.63	135.98	0.00	135.98	13077.77	7305.00
98	1.83	0.09	0.00	0.00	7.38	54.45	74.19	7.46	127.39	0.00	127.39	13352.30	7305.00
99	1.85	0.09	0.00	0.00	7.52	56.54	83.63	7.87	131.81	0.00	131.81	13509.57	7305.00
100	1.87	0.09	0.00	0.00	7.51	56.39	78.72	7.65	130.25	0.00	130.25	13691.90	7305.00
101	1.90	0.09	0.00	0.00	7.61	57.92	98.33	8.20	163.84	0.00	163.84	13873.48	7305.00
102	1.94	0.09	0.00	0.00	7.51	56.40	75.23	7.36	145.66	0.00	145.66	14139.76	7305.00
103	1.97	0.09	0.00	0.00	7.47	55.82	63.29	6.90	119.53	0.00	119.53	14378.77	7305.00
104	2.02	0.09	0.00	0.00	7.50	56.30	57.15	6.56	116.49	0.00	116.49	14771.16	7305.00
105	2.08	0.09	0.00	0.00	7.69	59.21	58.76	6.56	137.02	0.00	137.02	15207.65	7305.00
106	1.65	0.08	0.00	0.00	6.80	46.27	82.62	7.67	141.53	0.00	141.53	12085.50	7305.00
107	1.71	0.08	0.00	0.00	7.18	51.62	89.94	8.09	137.79	0.00	137.79	12492.09	7305.00
108	1.72	0.08	0.00	0.00	7.08	50.11	70.62	7.40	118.16	0.00	118.16	12574.17	7305.00
109	1.77	0.08	0.00	0.00	7.26	52.70	84.99	7.87	144.35	0.00	144.35	12901.42	7305.00
110	1.79	0.08	0.00	0.00	7.25	52.57	81.09	7.70	139.11	0.00	139.11	13103.41	7305.00
111	1.82	0.09	0.00	0.00	7.29	53.10	75.26	7.51	123.67	0.00	123.67	13307.18	7305.00
112	1.86	0.09	0.00	0.00	7.43	55.27	74.40	7.50	122.29	0.00	122.29	13551.30	7305.00
113	1.88	0.09	0.00	0.00	7.37	54.32	74.71	7.43	123.60	0.00	123.60	13756.17	7305.00
114	1.92	0.08	0.00	0.00	7.22	52.20	59.11	6.70	112.06	0.00	112.06	14001.70	7305.00
115	1.95	0.09	0.00	0.00	7.33	53.66	57.91	6.61	117.78	0.00	117.78	14225.85	7305.00
116	2.01	0.09	0.00	0.00	7.47	55.79	51.37	6.30	109.55	0.00	109.55	14671.26	7305.00

Task 5:

Education and Outreach

Prepared by:

Michael Wetz, Ph.D.

J. David Felix, Ph.D.

Dorina Murgulet, Ph.D.

Hussain Abdulla, Ph.D.

Mohamed Ahmed, Ph.D.

Task 5 Deliverables:

1. **Results shared through Baffin Bay Stakeholder Group**
   - Mohamed Ahmed provided a land use map to A. Bennis of Texas Sea Grant on 2/9/2021.
   - David Felix shared nutrient source tracking findings with A. Hilmy at the Coastal Bend Bays & Estuaries Program, which was included in his presentation at the 9/28/2022 Baffin Bay Stakeholder Group Meeting.
   - Mohamed Ahmed provided a high-resolution digital elevation model data for Julie Lewey, Deputy Executive Director, Nueces River Authority, on 12/2/2022. Lewey used it to develop a contour map to guide the development of an educational plastic relief model for school kids.
   - Dorina Murgulet provided information on top-soil hydrologic characteristics to A. Bennis on 8/31/2021

2. **Data submission to GRIIDC**

   Wetz: https://doi.org/10.7266/z00h6b2x

   Felix & Qiu: https://doi.org/10.7266/3jzxecp8

   Ahmed: https://doi.org/10.7266/zzfm44t2; https://doi.org/10.7266/fmz6065v; https://doi.org/10.7266/vwry1w58

   Murgulet: https://doi.org/10.7266/x36ex5j7; https://doi.org/10.7266/tydfsncd

   Abdulla: https://doi.org/10.7266/xs9w27j4; https://doi.org/10.7266/a1na953z; https://doi.org/10.7266/e9kjrn2r; https://doi.org/10.7266/dk7wzg8f; https://doi.org/10.7266/dz59wkcc

3. **Baffin Bay Research Symposium**
   - A Baffin Bay Research Symposium was held on May 9th, 2022, in Corpus Christi, Texas. A total of 66 guests signed in for the event. Three of the P.I.'s spoke at the event (Wetz, Murgulet, Felix).

4. **Graduate and undergraduate student training**

   Students received training in water and air quality sampling and analytical techniques, stable isotope sample preparation, hydrological techniques and solute modeling.

   - 18 graduate students received funding support and/or training through this project; Lucero Barraza (M.S.), Ahmed Eid (Ph.D.), Yixi Qui (Ph.D.), Chrissy Barrera (Ph.D.), Sean Majors (M.S.), Quang Ton (M.S.), Justin Elliott (M.S.), Tony Cox (M.S.), Ramadan Abdelrehim (Ph.D.), Ahmed Omar (Ph.D.), Meghan Bygate (M.S.), Muhamed Elshalkany (M.S.), Lilia Zavala (M.S.), Meraj Soharbi (Ph.D.), Skyler Meehan (M.S.), Christopher Vickers (M.S.), Yuting Xiao (Ph.D.), Bimal Gyawali.
   - 12 undergraduate students received training through this project: Abril Lunar, Kaiya Shealy, Kristen Lincoln, Felipe Urrutia, Sofia Miatello, Paulina Caro, An

Nguyen, Hannah Weber, Jessie Rodriguez, Isabelle Cummings, Cindy Vaquero, Christopher Ashworth.

Findings from the project were presented in multiple classroom settings.

- A complete SWAT exercise was introduced to graduate students from ESCI and CMSS (total 12) during the "Advanced Topic: Environmental and Geological Applications of GIS" class instructed by Dr. Mohamed Ahmed during Fall 2022 (9/2022-11/2022).
- Sean Majors presented the groundwater monitoring well as final project for the GIS graduate class and was submitted as a written report for final grade. (9/23-12/23)
- Wetz included information gleaned from this study in a lecture for his undergraduate class, "Global Change Ecology" (enrollment = 18 students). The lecture title was "Eutrophication – Causes and Symptoms" and was held on 4/6/23.
- Ahmed utilized research findings as a hands-on exercise for the graduate class, "Selected Topic: Geological and Environmental Applications of GIS" (enrollment = 6 students) during Summer 2020 (6/2020-7/2020).
- A presentation was given by students William Wooten (class project for Advanced Hydrogeology GEOL 6444) and a report prepared by William Wolfe (class project for Spatial System Science CMSS 6330). (2/22-12/22)

5. Copies of any presentations and/or publications specific to the project

- Wetz, M. 9/22/2021. Baffin Bay – a Texas treasure in transition. Gulf of Mexico Alliance Mid-Year meeting.
- Wetz, M. 11/1/2021. Phytoplankton blooms during wet and dry conditions – Baffin Bay (Texas) can't catch a break. Coastal & Estuarine Research Federation Meeting.
- Wetz, M. 11/29/2021. Challenges affecting the health of the Texas Laguna Madre ecosystem. Binational workshop titled, "Laguna Madre: Towards a binational conservation project between Texas and Tamaulipas".
  Wetz, M. 8/1/2022. Bringing Baffin Back: Restoring and protecting a Texas treasure. Kenedy Foundation.
- Wetz, M. 8/11/2022. Bringing Baffin Back: Restoring and protecting a Texas treasure. Corpus Christi Rotary Club.
- Dr. Felix presented results of nitrogen emission source apportionment to the Board of Directors of the Coastal Bend Air Quality Partnership. This will help them create informed NOx reduction strategies when creating their ozone action plan. This board consists of several government, industry and community representatives. 9/22/22. Determining NOx Emission Sources in the Coastal Bend Airshed: Strategies to Stay Within Ozone Attainment
- Dr. Mohamed Ahmed presented the SWAT results at the Corpus Christi Geological Society and the Coastal Bend Geophysical Society. Talk title: Vulnerability of Coastal Systems to Natural and Anthropogenic Interventions. Date: 11/18/2022.
- S. Sasidharan, M. Wetz. The impact of drought and floods on biogeochemical dynamics in a lagoonal, low inflow estuary (Baffin Bay, Texas)". Conference Name: Time domain controls on carbon storage, release, and transformation in coastal and estuarine waters following extreme events - an Ocean Carbon &

Biogeochemistry (OCB) Scoping Workshop. Location: North Carolina State University, Raleigh, NC (October 23 to 26, 2022)

- L. Beecraft, M. Wetz. Episodic inflow and salinity changes produce distinct bloom communities in a low-inflow estuary (Baffin Bay, Texas)". Conference Name: 11th U.S. Symposium on Harmful Algae, October 23-28, 2022. Location: Albany, New York.
- M. Wetz, K. Stanzel. "Bringing Baffin Back: Restoring & Protecting a Texas Treasure". Name of conference: Texan By Nature Conservation Summit, 11/2/2022. Dallas, Texas.
- M. Wetz, K. Stanzel. "Bringing Baffin Back: Restoring & Protecting a Texas Treasure". Baffin Bay Stakeholder Group meeting, 9/29/2022, Kingsville, Texas
- M.Wetz. "Baffin Bay – A Texas Treasure in Transition". 4-H Texas Water Ambassadors program, 12/15/2022.
- Qui, Y., Felix., J.D., Murgulet, D., Wetz, M., Abdulla, H. High-resolution Spatial Sampling Reveals DIN and DON Sources and Processing from Groundwaters to Surface Waters in a Semi-arid Estuary and Tributaries. AGU Fall Meeting. Chicago, IL. December 2022.
- Qui, Y., Felix., J.D., Wetz, M., Murgulet, D., Abdulla, H. Atmospheric reactive nitrogen (NH3, NOx, and DON) sources and transport over a north-west Gulf of Mexico air shed. February 2023. TAMU-CC monthly Atmospheric Science Program Seminar
- Dr. Felix presented at the TGLO Clean Coast Texas Lunch and Learn Series. Investigating Nitrogen in Coastal Bend Waters. February 2023.
- Dr. Felix presented at the Coastal Bend Air Quality Partnership Coastal Bend Community Air Action Plan Meeting. Determining NOx Emission Sources in the Coastal Bend Airshed: Strategies to Stay Within Ozone Attainment. March 2023.
- Sean Majors, ESCI MS student presented at the Coastal Bend Bays Foundation, Coastal Issues Forum (CIF), March 6, 2023, "Monitoring Nutrient Distribution in Baffin Bay Groundwater".
- Dr. Felix presented preliminary results at the Texas Watershed Coordinator Roundtable and Coastal Bend Bays Foundation Coastal Issues Forum. Presentation titles:
  "Investigating Nitrogen in Sources in Baffin Bay" 4/19/23
  "Determining NOx Emission Sources in the Coastal Bend Airshed: Strategies to Stay Within Ozone Attainment" 4/10/23
- Yixi Qiu has given two presentations at the University of Pittsburgh Collaboratory for Water Research, Education, and Outreach. Presentation titles:
  "Isotopic compositions of organic and inorganic nitrogen reveal processing and source dynamics at septic influenced and undeveloped estuary sites" 5/30/23
  "High-resolution Spatial Sampling and Stable Isotopes Disclose Dissolved Organic and Inorganic Nitrogen Loading Budget and Processing throughout a Semi-arid Estuary"5/31/23
- Dr. Murgulet, D. 4/19/2023. Groundwater Pollution Mechanisms. The Texas Watershed Coordinator Roundtable.
- Wetz, M. 4/19/2023. Bringing Baffin Back: Restoring and protecting a Texas treasure. Texas Watershed Coordinator's conference.

- Wetz, M. 4/19/2023. Baffin Bay – A Texas treasure in transition. Texas Watershed Coordinator's conference.
- Wetz, M. 3/29/2023. Human and climate-driven water quality challenges affecting the Texas coast. University of Florida Wetlands and Watersheds seminar series.
- Ton, Q. and Abdulla, H. Mechanistic understanding of photo-ammonification of porewater dissolved organic matter in Baffin Bay – Texas. 2022 American Chemical Society meeting, San Diego, CA.
- Abdelrehim, R., Ahmed, M. Assessing the vulnerability of Texas coastal watersheds to climate change and human interventions: Symposium on the Application of Geophysics to Engineering and Environmental Problems (SAGEEP), New Orleans, LA, April 2023.
- Abdelrehim, R., Ahmed, M. Modeling runoff, nutrient, and sediment inputs into Baffin Bay, Texas. American Geophysical Union conference, Chicago, IL, Dec. 2022.
- Ahmed, M., Vulnerability of Coastal Systems to Natural and Anthropogenic Interventions. Coastal Bend Geophysical Society, Nov. 2022.

6. Draft manuscript of research findings

- Beecraft, L., and M.S. Wetz. In press. Temporal variability in water quality and phytoplankton biomass in a low inflow estuary (Baffin Bay, Texas). Estuaries and Coasts DOI: 10.1007/s12237-022-01145-y
- *In revision,* Qui, Y., Felix., J.D., Murgulet, D., Wetz, M., Abdulla, H. Isotopic compositions of organic and inorganic nitrogen reveal processing and source dynamics at septic influenced and undeveloped estuary sites. Environmental Science & Technology.

Management Recommendations

This study provides the most comprehensive dataset on nutrient sources to Baffin Bay, which has undergone eutrophication over the past 3-4 decades. It is our hope that the data collected herein will be useful to resource managers and stakeholders who aim to implement practices that reduce nutrient loadings to Baffin Bay. A comprehensive list of nutrient reduction plans can be found in a soon-to-be released Watershed Protection Plan, which can be found here: https://baffin.twri.tamu.edu/. Based on this study's findings, the following management recommendations should be important priorities:

1. Expand routine monitoring as well as source tracking to the Los Olmos Creek/Laguna Salada tributary, where limited data from this study identified numerous indicators of water quality degradation.
2. Routine monitoring of wastewater treatment plant compliance with regulatory requirements is strongly encouraged and, in cases where sewage treatment is not adequate, repairs and/or replacement of treatment plants may be necessary.
3. Regular inspection of septic tanks, especially where the soil is highly permeable, is strongly encouraged. Conventional septic systems located where there are inadequate soils and/or water table is shallow should be removed or replaced with alternative options such as aerobic treatment units or recirculating sand filter systems.
4. Agricultural producers are encouraged to avoid overfertilization, lowering the probability or degree of N reaching the bay through surface/subsurface runoff and rainfall, and to follow NRCS approved practices wherever practical. Ample riparian buffer zones should be maintained on the edges of drain ways and creeks.
5. Regular vehicle emission testing is encouraged in the local area to examine the operation of catalysts to ensure that N emission is not excessive.
6. Additional study is needed to determine potential sources of nutrients to groundwater in the area, as these may differ from nutrient sources to surface waters.